THE UNIVERSITY of ADELAIDE

Unsteady Loads and Associated Flow Fields on Wings Exposed to High Rotation-Rate Dynamic Stall

Ryan Ross Leknys

School of Mechanical Engineering

The University of Adelaide

South Australia, 5005

A thesis submitted in fulfillment of the requirements for the Degree of Doctor of Philosophy

March 5, 2018

Abstract

Aerodynamics is a facet of engineering that has progressed rapidly since the discovery of flight from as early as the mid-19th century. In recent years, high manoeuvrability aircraft, high-speed helicopters, unmanned-aerial vehicles, micro-aerial vehicles and natural flyers have attracted significant interest due to their potential for military, surveillance and rescue applications. Due to economic and global demand to limit greenhouse gas emissions, the awareness of clean energy resources, such as horizontal-axis and vertical-axis wind turbines, has resulted in the rapid growth of research focusing on improving the performance and operational efficiency of such machines. Although these machines are designed for dissimilar applications, they all suffer from a common problem; the process of dynamic stall.

Dynamic stall is the unsteady aerodynamic phenomenon that occurs on pitching and plunging wings due to transient fluctuations in the operating angle of attack. During the process of dynamic stall, flow separation is delayed to elevated angles of attack. Increasing the angle of attack results in growth of a vortex structure originating at the leading edge. This vortex results in increased lift, drag and moment on the wing. Increased forces and moments continue until the vortex detaches from the wing and convects into the wake. The wing proceeds into deep-stall until the incidence angle is reduced to angles permitting reattachment of the boundary layer.

Dynamic stall results in increased material fatigue, cost and maintenance, and an overall decrease in performance of machine components. In contrast, natural flyers such as birds and insects have evolved to exploit the unsteady phenomenon for sustained flight. While

dynamic stall has been extensively studied for helicopter applications, recent work has focused on the operation of wind turbines. Helicopter rotor blades are exposed to sinusoidal changes in the angle of attack throughout each blade rotation. Whereas, wind turbines blades are subject to multiple variations in angle of attack. In addition, stalled rotor conditions may even be used beneficially to control power output during high wind load conditions.

The purpose of this thesis is to investigate the effects of dynamic stall on wings typically associated with wind turbines, helicopter and micro-aerial vehicle applications. More specifically, the thesis will focus on the study of pitching airfoils. Under the unsteady operating conditions, unsteady aerodynamic forces and flow structure development will be investigated during both pitch-up and post-stall phases of the airfoil motion. This is achieved by replicating unsteady operating conditions in both water-channel and wind-tunnel facilities. Particle image velocimetry and surface pressure measurements were utilised to identify key flow structure events, and the associated forces generated on wings during unsteady motion.

Constant-pitch-rate motion at a Reynolds number of 20,000 was applied to similar airfoils of different thicknesses, and includes a NACA 0012 and a NACA 0021. The aim of the investigation was to determine the flow structure variation between both thick and thin airfoil profiles during dynamic stall. Separation was shown to occur at earlier stages of the dynamic stall process for the thinner airfoil section when exposed to low rotation-rate dynamic stall. Increasing the rotation rate resulted in higher inertial loads, which in turn led to delayed stall and increased force generation at higher angles of attack. Fluctuations in forces were correlated with periodic vortex shedding at the trailing edge during airfoil

ramp-up. Under steady-state conditions, the presence of separation bubbles on both surfaces of the airfoil resulted in a negative lift-curve slope prior to the collapse of both bubbles and subsequent recovery of lift. Deep stall was delayed with an increased rotation rate due to the initial delay in formation of the leading-edge vortex. However, once separation of the vortex occurred, post-stall characteristics were not influenced by airfoil geometry, with both airfoils exhibiting bluff-body separated-flow characteristics.

For post-stall conditions following dynamic stall, increasing the reduced frequency delayed separation in some instances up to an angle of attack of 60°. Low surface pressure on the upper surface of the airfoil was linked to vortex structure developed during dynamic stall and in post-stall conditions. The centre of pressure was shown to shift with the development of the leading-edge vortex, and move aft of the quarter-chord location during fully-separated flow conditions. The change in centre of pressure leads to increased moment, which is transferred and linked to increases in torsional loading and fatigue of rotor blades and power transmission components or rotary machines.

For investigation of a boundary layer control method, a simplified leading-edge trip wire was implemented on two airfoils experiencing dynamic stall conditions. NACA 0012 and NACA 0021 airfoils were fitted with leading-edge trip wires of varying diameters, located at a fixed displacement from the airfoil leading edge. The Reynolds number was 20,000. The trip wires were shown to decrease the maximum lift, although the stall angle of attack was not observed to change with variations in the trip wire diameter. Geometric superposition was observed between the trip wire and the airfoil body when the diameter of the wire exceeded 1.6% of the airfoil chord length. This led to increases in lift and drag during the pitch-up motion.

Constant-pitch-rate rotation was utilised to investigate the effects of half-saddle movement and vortex formation on the aerodynamic characteristics of a pitching flat plate. A combination of round, square and triangular leading-edge and trailing-edge extensions were alternated during testing on a flat plate with a thickness-to-chord ratio of 0.1. The Reynolds number was 20,000. The half-saddle point, located on the upper surface, was linked to leading-edge vortex attachment. Detachment of the leading-edge vortex resulted once the position of the half-saddle point reached the trailing edge of the flat plate. Similarly, the rate of aft motion of the half-saddle point was shown to increase as a function of airfoil chord length, rotation rate and free-stream velocity. No benefit to overall force generation was observed once a critical angle of attack was reached. Maximum aerodynamic efficiency was shown to occur at angles of attack significantly below the angle of attack where maximum lift force was observed.

The research in the current dissertation enhances knowledge of the dynamic-stall process, and provides information that can improve methods of boundary layer control on wings exposed to dynamic stall. Moreover, research reported herein provides critical information on the deep-stall process, which occurs after the event of dynamic stall. With the information acquired in this thesis, increased awareness of dynamic stall and deep-stall characteristics can be achieved and utilised for the development of blades which are lighter, perform more efficiently and require lower costs to develop and maintain.

Declaration

I, Ryan Ross Leknys, certify that this work contains no material which has been accepted for the award of any other degree or diploma in my name in any university or other tertiary institution and, to the best of my knowledge and belief, contains no material previously published or written by another person, except where due reference has been made in the text. In addition, I certify that no part of this work will, in the future, be used in a submission in my name for any other degree or diploma in any university or other tertiary institution without the prior approval of the University of Adelaide and where applicable, any partner institution responsible for the joint award of this degree. I give consent to this copy of my thesis when deposited in the University Library, being made available for loan and photocopying, subject to the provisions of the Copyright Act 1968. I acknowledges that copyright of published works contained within this thesis resides with the copyright holder(s) of those works. I also give permission for the digital version of my thesis to be made available on the web, via the University's digital research repository, the Library Search and also through web search engines, unless permission has been granted by the University to restrict access for a period of time. I acknowledge the support received for my research through the provision of the Australian Government Research Training Program Scholarship.

Signed:

___ ___

Ryan Ross Leknys

Date: March 5, 2018

Acknowledgements

The very thought of attempting to complete a Doctoral research degree is one which is full of excitement, nerve and contempt. The seed that grew into the current work was first planted by my wife, Sharon – who initially encouraged me to undertake the degree, as she knew I would embrace the challenge of a Doctoral degree. Since the beginning of this thesis, she has been by my side throughout the challenges of the research project. Her support, admiration and experience are things what I will always value and cherish.

I would also like to acknowledge the support of my supervisor, Associate Professor Maziar Arjomandi. The experience, determination and support received throughout the duration of this thesis have allowed me to grow into a person that interprets life, and its challenges, from multiple angles and from different points of view. His honest and direct opinion are sometimes what is needed to begin and finish a project of this nature.

I am also grateful to my co-supervisor, Associate Professor Richard Kelso. His depth of knowledge and professionalism within the engineering discipline is something that I greatly respect and admire. His knowledge of the area of fluid mechanics, thermodynamics and other interdisciplinary fields of engineering alongside this acute attention to detail and comprehension of the English language are all things that I aspire towards as a student under his supervision.

I would also like to thank my second co-supervisor, Dr Cristian Birzer, for his support and guidance within the project. His experience and knowledge of the experimental test facility and laser diagnostics systems made it possible for me to independently conduct the required laboratory work needed for completion of the research project. His straight

forward, yet professional, attitude are things that allow him to “get to the point” whilst respecting and teaching students values and thoughts.

I would also like to acknowledge the support of Professor Benjamin Cazzolato, Mr Marc Simpson, instrumentation personnel: Mr Philip Schmit, Mr Norio Itsumi, Mr Derek Franklin, Mrs Lydia Zhang, Mechanical engineering technical staff members: Mr Gary Clark, Mr Pascal Symons, Mr Bill Finch, Mr Anthony Herzich and Mr Stephen Kloeden. Their skills and experience within each of their respective areas of expertise has made it possible to successfully design, construct and implement the required mechanical and electrical components of this project.

I would like to thank members of Kathleen Lumley College, and especially Mrs Allyson Sandham, for the emotional and financial support provided whilst completing this thesis.

I acknowledge the support I have received for my research through the provision of an Australian Government Research Training Program Scholarship, the Sir Ross and Sir Keith Smith Fund (www.smithfund.org.au), the Cowan Grant Bursary and the Harrold J Rodda Memorial Scholarship. The financial support received is greatly appreciated.

Finally, I would like to recognise the love and support of my parents, closest friends and family who have been by my side throughout the duration of this degree.

Thank You!

Nomenclature

Acronyms

PIV	Particle image velocimetry

Symbols

α	Angle of attack	$degree$ °
$\alpha_{critical}$	Critical stall angle of attack	$degree$ °
$\dot{\alpha}$	Angular velocity	$degree°/s$
c	Airfoil chord length	m
C_C	Maximum chord force coefficient	$-$
C_D	Drag coefficient	$-$
C_L	Lift coefficient	$-$
C_M	Pitching moment coefficient	$-$
C_μ	Jet moment coefficient	$-$
C_N	Normal airfoil force coefficient	$-$
C_P	Pressure coefficient	$-$
f	Frequency	Hz
h	Boundary layer thickness	m
κ	Reduced frequency, $\omega C/2U_\infty$	$-$
μ	Fluid dynamic viscosity	$N.s/m^2$

ω	Angular velocity	rad/s
ω_Z	Span-wise vorticity	$1/s$
r	Blade radius	m
Re	Chord based Reynolds number, $\rho U_\infty C/\mu$	$-$
ρ	Fluid density	kg/m^3
t	Time	s
τ	Period	s
U'	Free-stream velocity fluctuation	m/s
U_C	Vortex convection velocity	m/s
U_f	Resultant unsteady velocity	m/s
$U_{Forward}$	Helicopter forward velocity	m/s
U_∞	Free-stream velocity	m/s
U_N	Normalised vortex convection velocity	$-$
V'	Operational velocity fluctuation	m/s
X	Distance from the airfoil leading edge	m

Table of Contents

List of Figures

Chapter 1.

Introduction to Dynamic Stall

1.1. Background and Motivation

Modern engineering requires complex problems to be analysed in detail in order to fully comprehend the task at hand, design solutions and engineer fixes to problems that arise in everyday situations. The study of aerodynamics on rotor blades and wings has progressed from a point of steady-state analysis through to unsteady analysis, where induced forces are developed as a result of fluctuating operating conditions on machines such as gas turbines, wind turbines, fixed wing aircraft, helicopters and micro-aerial vehicles. In addition, aerodynamic unsteadiness is associated with natural flyers including birds, bats and insects, where the generated transient lift is critical for sustained flight, avoidance and hunting manoeuvres, and perching during landing (Ellington, 1984, Ellington et al., 1996, Sane, 2003, Birch, Dickson and Dickinson, 2004, Shyy et al., 2007, Choudhry et al., 2014). With an increase in demand for renewable energy resources, a quest for more efficient and quiet operation of aerial vehicles and wind turbines, and a trend towards micro-aerial vehicle and flapping wing applications, the need for a in-depth research of the unsteady aerodynamics is highly warranted. This thesis seeks to provide new knowledge relating to the unsteady aerodynamic behaviour of such machines. In this thesis, wings will be subjected to pure-pitch motion and high rotation rates, in order to simulate and reproduce dynamic stall behaviour. These conditions are linked to increased material fatigue, operational cost and loss of efficiency during the operation of modern

rotary machines, whilst contributing to enhanced lift on micro-aerial vehicles and natural flyers.

Dynamic stall is the unsteady process of delayed stall developed on wing subjected to transient fluctuations in the effective operating angle of attack or reverse flow conditions (Datta, Yeo and Norman, 2013, Hodara et al., 2016, Lind and Jones, 2016). Typically, dynamic stall is characterised by a delay in airfoil stall, where the airfoil stalls at a higher angle of attack in comparison to steady-state stall. Following delayed stall, generation of a vortex structure originated at the leading edge occurs. The vortex structure grows in strength whilst moving downstream over the airfoil upper surface. It is during this time, whilst the vortex remains in proximity to the airfoil surface, that enhanced lift is possible (McCroskey, 1981). The process of dynamic stall is completed via shedding of the leading-edge vortex, which leads to a dramatic decrease in lift and increase in drag until the return of the wing to an angle of attack where flow re-attachment can occur. This process is illustrated in Figure 1.1, which shows the progressive flow structure development and associated forces generated during the dynamic stall cycle.

The process of delayed separation and dynamic stall was first described by Kramer (1932) who described transient lift generation resulting from gusts on aircraft wings during flight. The lift developed led to in-flight instabilities and passenger discomfort during operation. It was not until the early 1960s that a considerable research undertaking of the dynamic stall process occurred, motivated by the development of unsteady flows on the rotor blades of helicopters operating at high speeds and during manoeuvring. Harris and Pruyn (1968) were among the first to identify significant differences between operational rotor loads and conventional steady-state aerodynamics.

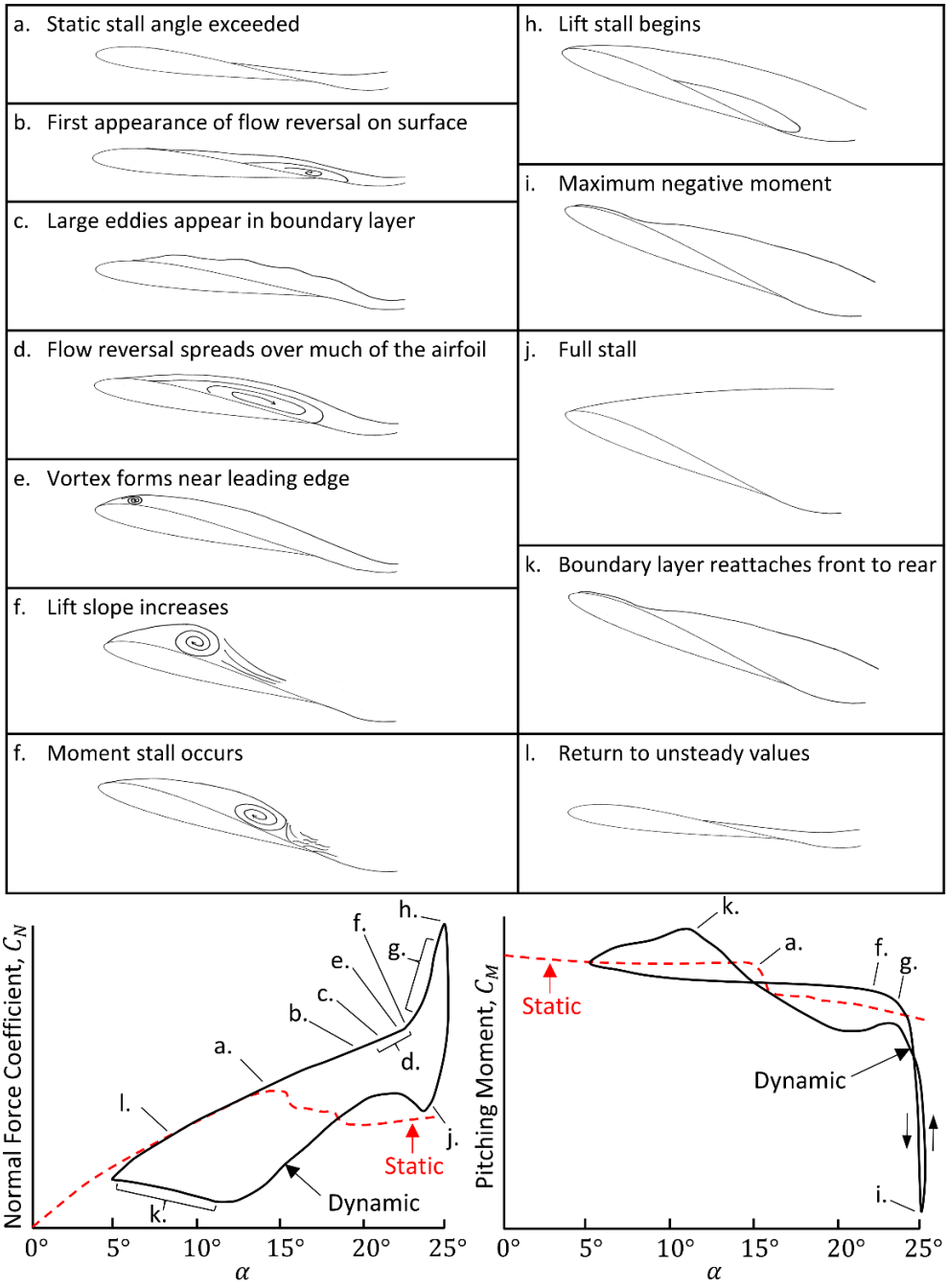

Figure 1.1. Dynamic stall development on an airfoil undergoing cyclic pitching motion, indicating the critical phases of the stall process and associated forces. Image reproduced from Carr (1988).

In addition, Liiva (1969) discussed the difficulties in predicting the applied rotor loads on helicopters at high speed using theoretical strip methods, due to unsteady aerodynamic effects imposed on the rotor by dynamic stall.

The dynamic stall process, and its recognition as a large inhibitor to the performance of high speed helicopters, were highlighted in detailed studies that identified the variation in force generation and flow characteristics with respect to operating parameters including, Reynolds number (*Re*), airfoil rotation rate, Mach number, airfoil geometry, pitch location, and airfoil motion type (McCroskey, Carr and McAlister, 1976, Carr, McAlister and McCroskey, 1977, Carr et al., 1982, McCroskey et al., 1982). Since these extensive studies were conducted, investigation of dynamic stall has become a major topic in rotorcraft aerodynamics. Recent analysis of modern helicopter operation has revealed that blades operate in conditions where even reversed flow can be generated (Datta, Yeo and Norman, 2013, Hodara et al., 2016). In such conditions, the sharp trailing edge of the airfoil is considered to be the leading edge, which limits the lift capabilities of the helicopter and reduces its operational performance due to the unconventional aerodynamics developed during flow separation on the rotor blades. Owing to the limiting performance factors associated with dynamic stall, the continued study of unsteady aerodynamics is necessary to improve the performance and efficiency of machines and vehicles operating in transient unsteady environments. The experimental methods to study unsteady aerodynamics on helicopters laid the foundation for development of analytical models for stall prediction and force modelling (Beddoes, 1976, McAlister, Lambert and Petot, 1984, Leishman and Beddoes, 1989, Hansen, Gaunaa and Madsen, 2004, Larsen, Nielsen and Krenk, 2007). These models could be utilised by engineers and scientists alike to predict the lift characteristics of pitching wings, and to subsequently

design and implement mechanical components that are better suited for operation in unsteady environments.

The dynamic stall process is not only limited to rotorcraft applications. The phenomenon has also been linked with the operation of both vertical-axis and horizontal-axis wind turbines (Butterfield et al., 1991, Leishman, 2006). Installation of horizontal-axis wind turbines has seen a surge in growth where, in 2016, an estimated 487,000MW of capacity was installed, compared to approximately 25,000MW installed in 2001 (World Wind Energy Association, 2016).

Historically the power generation capacity and size of wind turbines shows that future reliance on wind energy will lead to further increases in turbine size and power output. This is reinforced by the current need to reduce greenhouse gases emitted from non-renewable resources such as gas, oil and coal. The increase in wind energy capacity has closely been followed by a gradual increase wind turbine size. Figure 1.2 shows the average increase in horizontal-axis wind turbine size, whilst also indicating future projections of their rotor diameter based on future power demands (Serrano-González and Lacal-Arántegui, 2016). The increase in size not only places additional loads on the turbine blades, but also makes them more susceptible to dynamic stall due to tower shadow, turbine yaw and atmospheric turbulence. The generated unsteady loading resulting from dynamic stall, leads to increased blade vibration, material fatigue, power variation and cost of operation and maintenance(Veers et al., 2003).

Therefore, knowledge of the dynamic stall process is of significant importance to ensure that future wind turbines can be developed to combat the unsteady aerodynamic forces. As a consequence, blades on rotary machines can be designed to have increased life-

spans, and perform more efficiently in environments containing increased turbulence or asymmetric and unsteady blade inflow conditions.

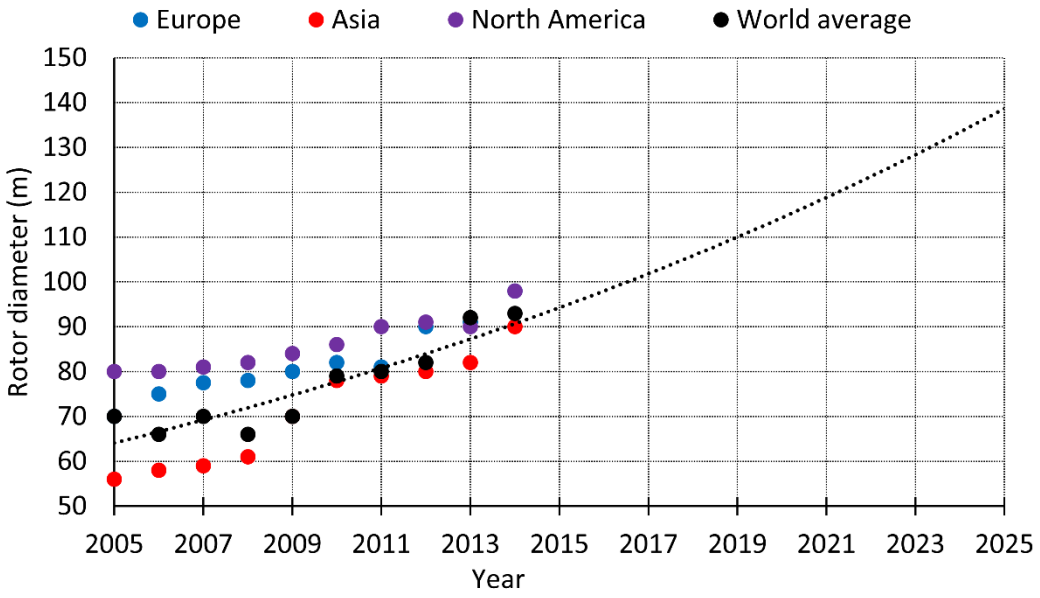

Figure 1.2. Approximation of horizontal axis wind turbine rotor diameter for past and forecasted growth in order to sustain demand for wind energy (Serrano-González and Lacal-Arántegui, 2016).

The motivation of the current research is focused on developing fundamental scientific knowledge of the fluid structure development and load generation characteristics of airfoils undergoing dynamic stall and which are associated with blades of rotary machines, such as helicopters and wind turbines. Development of dynamic stall has previously been shown to vary significantly between airfoil motion types and rotation rates. Furthermore, due to fluctuations in in-flow conditions and turbulent operating conditions of blades of helicopters and wind turbines, extreme angles of attack and reversed flow conditions are possible. Thus, this research is focused on comprehending the aerodynamic behaviour and properties of the dynamic-stall process developed in extreme weather conditions. As

such, the thesis aims to comprehend the impact of extreme operating conditions by utilising constant-pitch-rate airfoil motion to investigation the aerodynamic behaviour during both pitch-up and post-stall operating conditions. Understanding of aerodynamics associated with these operating conditions will allow for the development of lighter blade structures in order to increase the performance, efficiency and blade life-cycles, and to lower operational and maintenance costs of rotary machine blades.

1.2. Research Aims

The overall aim of the current research is to understand the unsteady separation process of dynamic stall on airfoils subject to atmospheric conditions representative of gust-like environments for applications including helicopters and wind turbines. Moreover, the thesis investigates the fluid-structure interaction and force development developed during unsteady dynamic stall. Additionally, the thesis aims to identify the forces and relaxation times required to reach steady-state operating conditions once dynamic stall has occurred. A greater awareness of delayed stall, flow separation, vortex development and post-stall behaviour is important to determine the load characteristics on airfoils subject to unsteady aerodynamics. The research seeks to identify the velocity and vorticity fields associated with dynamic stall, such that more in-depth analysis of force development over a pitching airfoil can be obtained. Furthermore, this thesis focuses on analysing measurements of load generation and flow structure, in order to develop methods to suppress or mitigate the resulting force fluctuations due to dynamic stall. This will ultimately satisfy the project motivation of reducing the costs associated with rotary machine component design and maintenance, whilst increasing overall machine

performance and efficiency. In order to achieve the research aims, the following summarised research objectives are addressed:

1. Determine, using well-resolved flow visualisation measurements, the flow structure development generated about multiple airfoil profiles, including a NACA 0012 airfoil and a NACA 0021 airfoil, subjected to high rotation-rate constant-pitch-rate motion.

2. Identify the flow structures and loads developed about airfoils that undergo dynamic stall, and which also continue to operate in post-stalled conditions.

3. Evaluate the potential of applying a passive flow control device to regulate the dynamic-stall process under highly unsteady operating conditions.

4. Develop fundamental knowledge of the flow separation process and pressure distribution resulting from dynamic stall through the utilisation of a flat plate subjected to unsteady constant-pitch-rate motion.

Full project aims and objectives will be summarised in detail in the conclusion of the literature review, in section 2.8.

1.3. Thesis Outline

This thesis consists of an introduction to the current dissertation (Chapter 1), a literature review on dynamic stall (Chapter 2), four journal articles (Chapter 3 through to Chapter 6) focusing on the analysis of dynamic stall, and a conclusion summarising research outcomes and future work (Chapter 7).

Chapter one provides the research background and motivation underlying the study. Within this section, aims and objectives are introduced to provide the grounding for the remainder of the research work to be conducted.

Chapter two provides a comprehensive review of the dynamic-stall process. This chapter discusses the occurrence of dynamic stall on machinery including helicopters, wind turbines, gas turbines, micro-aerial vehicles and fixed wing aircraft, through to its necessity on natural flyers including birds, bats and insects. Moreover, the review details the effect of multiple performance parameters on the development of dynamic stall, where significant load generation and fluctuation occur. The literature review brings forth the current state of research associated with dynamic stall, and concludes by presenting gaps in literatures which are still required to further advance our knowledge of the dynamic stall phenomenon.

Chapter three utilises the application of particle image velocimetry (PIV) to determine the flow structure development created on two airfoils applicable to helicopter and wind turbine operation. The airfoils include a NACA 0012 and a NACA 0021, which are subjected to high rotation rates and constant-pitch-rate motion profiles. In addition, high reduced frequencies and elevated angles of attack are applied to the airfoils to represent gust-like operating conditions. Flow visualisation, through obtained velocity and vorticity fields, provides details of each individual stage of the dynamic-stall process. These include (a) delayed stall to an angle of attack significantly greater than the steady-state angle of attack, (b) formation of the leading-edge vortex, (c) growth of the leading-edge vortex, and (d) final separation of the leading-edge vortex and transition into deep stall. The chapter also investigates the development of laminar separation bubbles generated over

the rear portion of each airfoil prior to leading-edge vortex formation. This work is significant for rotor designs utilising variable thickness airfoils between the blade root and its tip. With such blade designs, the lift and power generation directly depends on the associated flow patterns and separation properties developed along the entire length of the blade. As such, the characteristics of dynamic stall are presented for two dissimilar airfoils with significant thickness ratio variations to highlight the effects of extreme unsteady motion to elevated angles of attack. The work highlights the differences and similarities in load and flow structure to increase the knowledge with respect to the occurrence of dynamic stall on rotary machine blades.

Chapter four endeavours to investigate the post-stall characteristics following dynamic stall. Particle image velocimetry and surface pressure measurements are utilised to study the pitch-up and post-stall flow structure developed about a NACA 0012 and a NACA 0021. Within the study, the reduced frequency was shown to effect the angle of attack at which deep stall was initiated. For the maximum reduced frequency, deep stall was not observed to occur until $\alpha = 60°$. The results from surface pressure were linked to vortex structures developed during the pitch-up process and during the post-stall configuration. The study also showed the movement of the centre of pressure during post-stall flow conditions. The movement of the centre of pressure shifted between 30% and 55% over the complete range of reduced frequencies and maximum angles of attack evaluated. The movement of the centre of pressure is linked to increased torsional fatigue of wind turbines and helicopter rotor blades exposed to gust-like atmospheric conditions.

Chapter five is developed to focus on the control of the dynamic-stall process through the application of a passive flow control device in the form of a leading-edge trip wire. In this

study, multiple trip wires were fixed at a constant distance from the leading edge of a NACA 0012 airfoil in order to promote boundary layer mixing and attempt to disperse the momentum transferred into the leading-edge vortex. Comparable studies utilised a similar method at low rotation rates, however, in the current chapter the application of the trip wire was extended to high rotation rates, where high fluid inertia is induced through rotation. Surface pressure measurements allowed for the resulting aerodynamic forces to be evaluated. The trip wire was shown to have a minimal influence on the angle of attack at which maximum lift was generated. However, the trip wire was shown to reduce the maximum lift when compared to the airfoil not fitted with the trip wire. The trip wire did not have a significant influence on the dissipation of the large-scale von Karman vortex structures developed during deep stall, and where increased vibration occurs.

Chapter six presents an investigation into the development of the leading-edge vortex generated over a simplified flat-plate model. The model comprises of three parts which include (a) an interchangeable leading-edge extension, where round, square and triangular profiles are employed; (b) a flat-plate body, which encloses the surface pressure sensors; and (c) a trailing-edge extension, where round, square and triangular profiles are employed. The three different geometries for the leading-edge and trailing-edge extensions were selected to decrease curvature effects generated by standard airfoil profiles, and to promote the formation of laminar separation bubbles and leading-edge vortex structures at low angles of attack during the pitch-up process. Surface pressures generated from the tests indicate key flow features developed from the dynamic-stall process via regions of localised low pressure on the upper surface of the flat plate. Features include (a) the leading-edge vortex, recognised as regions of low pressure

coefficient; and (b) a half-saddle point, identified due to a severe pressure gradient aft of the leading-edge vortex and at the location approximated by $C_P = 0$ on the upper surface of the flat plate.

Chapter seven outlines and summarises the major findings of the research developed within this thesis. In addition, the chapter discusses future work that can be continued, with respect to dynamic stall, to facilitate the design and operation of more cost effective rotary machine blades exposed to dynamic stall.

Finally, the appendix includes a conference article, outlining the velocity fields and effects of unsteady separation on a NACA 0012 and NACA 0021 airfoil.

1.4. Publication Arising From This Thesis

The thesis is presented in a manuscript format as a result of the research herein being utilised for the generation of scientific journal manuscripts and a peer-reviewed conference article. The work of each manuscript and conference paper tie in closely with the aims and objectives of the current thesis. Listed below are the outcomes of the publishable material that has either been published, or submitted for publication and peer-review.

1.4.1. Journal Articles

1. Leknys, R., Arjomandi, M., Kelso, R. & Birzer, C. 2017. Dynamic- and post-stall characteristics of pitching airfoils at extreme conditions. Proceedings of the Institution of Mechanical Engineers, Part G: Journal of Aerospace Engineering.

2. Leknys, R., Arjomandi, M., Kelso, R. & Birzer, C. Dynamic stall Flow Structure and Forces on Symmetrical Airfoils at High Angles of Attack and Rotation Rates. Journal of Fluids Engineering (Submitted for publication).

3. Leknys, R., Arjomandi, M., Kelso, R. & Birzer, C. Wind Turbine Unsteady Load Control Using Leading-Edge Trips. Journal of Wind Energy and Industrial Aerodynamics (Submitted for publication).

4. Leknys, R., Arjomandi, M., Kelso, R. & Birzer, C. Leading-Edge Vortex Development on a Pitching Flat Plate with Multiple Leading Edge Geometries. Experimental Thermal and Fluid Science (Accepted for publication).

1.4.2. Refereed Conference Papers

Leknys, R., Arjomandi, M., Kelso, R. & Birzer, C. Dynamic stall on airfoils exposed to constant pitch-rate motion. 20th Australasian Fluid Mechanics Conference, Perth, Western Australia, December 2016.

1.5. Thesis Format

The current thesis has been submitted as a portfolio of the above journal manuscripts according to the formatting requirements of the University of Adelaide. The printed and online versions of the thesis are identical. The online version of the thesis is available as a PDF and can be viewed in its original format using Adobe Reader 11.

1.6. References

Beddoes, T. 1976. A synthesis of unsteady aerodynamic effects including stall hysteresis. *Vertica,* 1**,** 113-123.

Birch, J. M., Dickson, W. B. & Dickinson, M. H. 2004. Force production and flow structure of the leading edge vortex on flapping wings at high and low Reynolds numbers. *Journal of Experimental Biology,* 207**,** 1063-1072.

Butterfield, C., Simms, D., Scott, G. & Hansen, A. 1991. Dynamic stall on wind turbine blades. United States: National Renewable Energy Laboratory.

Carr, L., McCroskey, W., McAlister, K., Pucci, S. & Lambert, O. 1982. An Experimental Study of Dynamic Stall on Advanced Airfoil Sections. Volume 3; Hot-Wire and Hot Film Measurements. United States: National Aeronautics and Space Administration.

Carr, L. W. 1988. Progress in analysis and prediction of dynamic stall. *Journal of Aircraft,* 25**,** 6-17.

Carr, L. W., McAlister, K. W. & McCroskey, W. J. 1977. Analysis of the development of dynamic stall based on oscillating airfoil experiments. United States: National Aeronautics and Space Administration

Choudhry, A., Leknys, R., Arjomandi, M. & Kelso, R. 2014. An insight into the dynamic stall lift characteristics. *Experimental Thermal and Fluid Science,* 58**,** 188-208.

Datta, A., Yeo, H. & Norman, T. R. 2013. Experimental investigation and fundamental understanding of a full-scale slowed rotor at high advance ratios. *Journal of the American Helicopter Society,* 58**,** 1-17.

Ellington, C. 1984. The aerodynamics of hovering insect flight. I. The quasi-steady analysis. *Philosophical Transactions of the Royal Society of London B: Biological Sciences,* 305**,** 1-15.

Ellington, C. P., Van Den Berg, C., Willmott, A. P. & Thomas, A. L. 1996. Leading-edge vortices in insect flight. *Nature,* 384**,** 626.

Hansen, M. H., Gaunaa, M. & Madsen, H. A. 2004. A Beddoes-Leishman type dynamic stall model in state-space and indicial formulations. Denmark: Riso National Laboratory.

Harris, F. D. & Pruyn, R. R. 1968. Blade stall-half fact, half fiction. *Journal of the American Helicopter Society,* 13**,** 27-48.

Hodara, J., Lind, A. H., Jones, A. R. & Smith, M. J. 2016. Collaborative investigation of the aerodynamic behavior of airfoils in reverse flow. *Journal of the American Helicopter Society,* 61**,** 1-15.

Kramer, M. 1932. Increase in the Maximum Lift of an Airplane Wing due to a Sudden Increase in its Effective Angle of Attack Resulting from a Gust. United States: National Advisory Committee for Aeronautics.

Larsen, J. W., Nielsen, S. R. & Krenk, S. 2007. Dynamic stall model for wind turbine airfoils. *Journal of Fluids and Structures,* 23**,** 959-982.

Leishman, G. J. 2006. *Principles of helicopter aerodynamics*, Cambridge university press.

Leishman, J. G. & Beddoes, T. 1989. A Semi-Empirical Model for Dynamic Stall. *Journal of the American Helicopter Society,* 34**,** 3-17.

Liiva, J. 1969. Unsteady aerodynamic and stall effects on helicopter rotor blade airfoil sections. *Journal of Aircraft,* 6**,** 46-51.

Lind, A. H. & Jones, A. R. 2016. Unsteady aerodynamics of reverse flow dynamic stall on an oscillating blade section. *Physics of Fluids,* 28**,** 077102.

McAlister, K. W., Lambert, O. & Petot, D. 1984. Application of the ONERA model of dynamic stall. United States: National Aeronautical and Space Administration.

McCroskey, W., McAlister, K., Carr, L. & Pucci, S. 1982. An experimental study of dynamic stall on advanced airfoil sections. Volume 1, 2 & 3. NASA.

McCroskey, W. J. 1981. The phenomenon of dynamic stall. United States: National Aeronautical and Space Administration.

McCroskey, W. J., Carr, L. W. & McAlister, K. W. 1976. Dynamic stall experiments on oscillating airfoils. *AIAA Journal,* 14**,** 57-63.

Sane, S. P. 2003. The aerodynamics of insect flight. *Journal of Experimental Biology,* 206**,** 4191-4208.

Serrano-González, J. & Lacal-Arántegui, R. 2016. Technological evolution of onshore wind turbines - a market-based analysis. *Wind Energy,* 19**,** 2171-2187.

Shyy, W., Lian, Y., Tang, J., Viieru, D. & Liu, H. 2007. *Aerodynamics of low Reynolds number flyers*, Cambridge University Press.

Veers, P. S., Ashwill, T. D., Sutherland, H. J., Laird, D. L., Lobitz, D. W., Griffin, D. A., Mandell, J. F., Musial, W. D., Jackson, K. & Zuteck, M. 2003. Trends in the design, manufacture and evaluation of wind turbine blades. *Wind Energy,* 6**,** 245-259.

World Wind Energy Association 2016. WWEA Half-year Report 2016. World Wind Energy Association.

Chapter 2.

Literature Review

2.1. Dynamic Stall Occurrence and Characteristics

Aerodynamics is a challenging field of engineering. Dynamic stall is no exception. Unlike steady-state aerodynamics, the process of dynamic stall occurs when a dynamic change in the angle of attack leads to significant increases in aerodynamic force and delayed separation, well beyond steady-state values. The dependency of the phenomenon on transient operating conditions generates complex flows and unsteady loads, which in turn lead to challenges in modelling and control of the dynamic stall process on rotary machine blades. The following chapter highlights the historical progression of research conducted to identify and explain the phenomenon of dynamic stall.

2.1.1. Development of Unsteady Separation and Causes

Unsteady aerodynamics is a complex field within fluid mechanics, which has presented multiple challenges to scientists, engineers and operators of rotary machines. As described in Liebe (2006), unsteady aerodynamics has been investigated from as early as 1925. Due to the effects of vertical wind shear on ride stability of aircraft noted by pilots, Kramer (1932) performed experimental wind tunnel tests to evaluate the effects of vertical gusts on the wings of aircraft, and to determine the loads developed as a result of transient increases in the angle of attack. In these tests, Kramer was able to show that when an airfoil is exposed to rapid pitching motions, the maximum angle of attack (and associated lift) significantly exceeds that of typical steady-state values (Kramer, 1932). The

phenomenon has become of significant importance in modern aerodynamics due to its potential to develop increased lift, and due to the negative effects leading to increased fatigue and structural damage of mechanical components. Significant research of the dynamic stall phenomenon has since occurred as a result of the limiting performance imposed on retreating rotor blades of helicopters and on highly manoeuvrable rotorcraft (McCroskey, Carr and McAlister, 1976, Carr, McAlister and McCroskey, 1977, McCroskey et al., 1982, Robinson and Luttges, 1983, Francis and Keesee, 1985, Walker, Helin and Chou, 1985, Walker, Helin and Strickland, 1985, Jumper, Schreck and Dimmick, 1987, Carr, 1988, Robinson and Wissler, 1988, Green and Galbraith, 1995, Coton and Galbraith, 2003, Buchner, Honnery and Soria, 2017). Additionally, due to the push for greener energy production, research focusing on efficient methods for clean power generation has prompted investigations focusing on the drawbacks of dynamic stall associated with the operation of wind turbines. For a wind turbine, blade-tower interaction, yaw and operation in turbulent atmospheric boundary layers all lead to dynamic stall conditions on the blades of the turbine (Butterfield et al., 1991, Hansen and Butterfield, 1993, Munduate, Coton and Galbraith, 2004). Due to the unsteady operating conditions of the turbines, increased fluctuations in aerodynamic forces are transferred through the rotor blades and concentrated at key components of the turbine, including the power transmission and braking systems. In contrast to the negative effects, a flourishing research field has evolved in part to discover the means of locomotive force of flapping birds and insects, and also, to develop micro-air vehicles that utilise this form of locomotion for disaster recovery and observation purposes.

Unsteady environmental conditions and self-induced flow fields developed by the operation of rotary machines significantly impact the operation of both helicopters and

wind turbines. Designs of airfoils and analysis of rotor disk loading have previously been evaluated using simple blade element techniques, where a single input velocity vector determines the direction, magnitude and resultant angle of attack experienced by the airfoil. In reality, environmental factors such as wind gusts, boundary layer velocity variations and atmospheric turbulence all contribute to the total velocity vector to which a blade is exposed to. The variation between both steady-state and unsteady-state can be represented as shown in Figure 2.1.

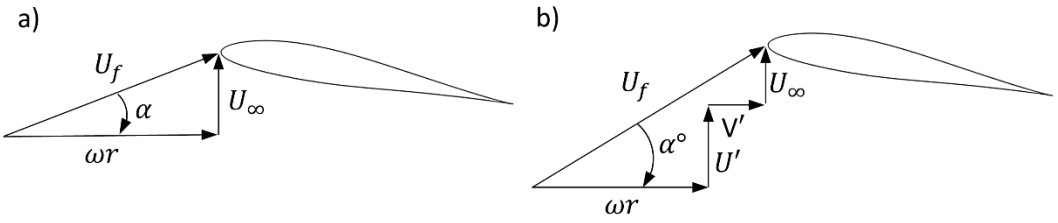

Figure 2.1. Velocity vector representation of (a) steady-state and (b) unsteady operating conditions experienced by rotor blades.

In Figure 2.1, ω is angular velocity, r is blade radius, U_∞ is the steady-state free-stream velocity and $U'$and $V'$are the time varying fluctuating component of velocity developed as a result of transient instabilities. The resultant unsteady velocity component, U_f, imparted onto the airfoil can be expressed as the vector addition of the magnitude and direction of the atmospheric free-stream velocity, rotation velocity and fluctuating velocity component, as shown in *Equation 1*.

$$U_f{}^2 = (\omega r + V')^2 + (U_\infty + U')^2 \qquad \text{Equation 1}$$

Due to the random nature of U' and V', prediction of aerodynamic loads resulting from velocity fluctuations presents a challenge in the design of rotor blades on both wind turbines and helicopters. In addition to atmospheric velocity fluctuations, operational instabilities also impose unsteady fluctuations on the blades of wind turbines and helicopters. Machine operation induced instabilities imposed on the blades exist as either vertical wind shear, for the case of wind turbines, or cyclic velocity fluctuations as experienced by helicopters. For the case of a vertical wind shear on wind turbine blades, as indicated in Figure 2.2a, the varying velocity component can be represented as a boundary layer effect, where the velocity distribution over the vertical axis of the turbine varies according to $U'(h)$.

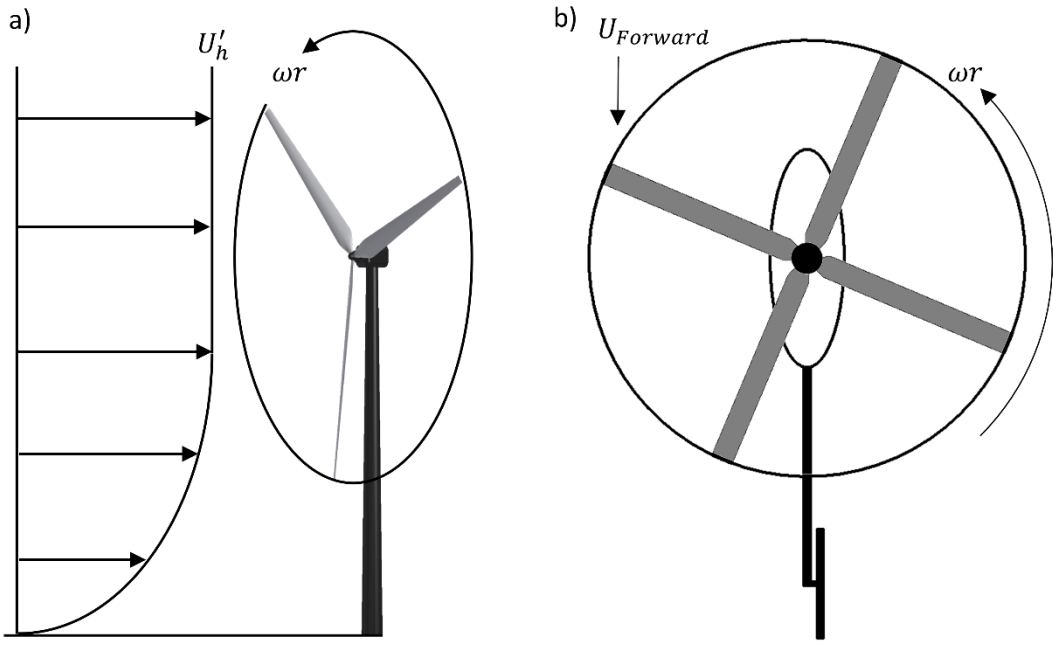

Figure 2.2. Vertical wind shear of a wind turbine due to atmospheric boundary layer development (a) and cyclic variation in velocity created by the combination of helicopter rotor velocity and the helicopter forward velocity (b).

Furthermore, as shown in Figure 2.2b, the rotary motion of a helicopter rotor blade generates a cyclic variation in velocity and angle of attack over the rotor disk, due to the combination of forward speed, $U_{Forward}$, and rotor velocity, ωr. The variation in velocity profile between advancing and retreating blades is typically considered to be sinusoidal due to the cyclic behaviour of the rotor motion.

The effect of tower shadow on the immediate flow field behind the tower of a horizontal-axis wind turbine has been shown to significantly reduce the operational capabilities of the turbine, and increase local blade velocity fluctuations (Snyder and Wentz Jr, 1981, Hansen and Butterfield, 1993, Munduate, Coton and Galbraith, 2004).

As shown in Leishman (2006), the wake generated by the wind turbine tower can be modelled as the wake of a simple cylinder, and as expressed in Figure 2.3. The periodic vortex shedding in the wake of the tower creates a flow field that is non-uniform, and which is highly three dimensional. As a result, the wind turbine blade is not only exposed to a significant velocity fluctuation throughout its azimuth, but also along the total span of the blade. This results in an increase in load fluctuation, decreased fatigue life and difficulties in controlling the power output of large-scale wind turbines.

As the blade passes through this region of chaotic flow structure, the resultant effective velocity and angle of attack change significantly. Due to the turbulent aerodynamics of the tower wake and far-wake, analysis of unsteady flow structure and loading must take into account multiple motion types, including sinusoidal, constant pitch and heave. Moreover, modern wind turbines must factor into their design new design standards that include the possibility of gust-like conditions (Richards, Griffith and Hodges, 2017).

Motions types including cyclic and constant-pitch-rate rotation will be further discussed in later section of this literature review.

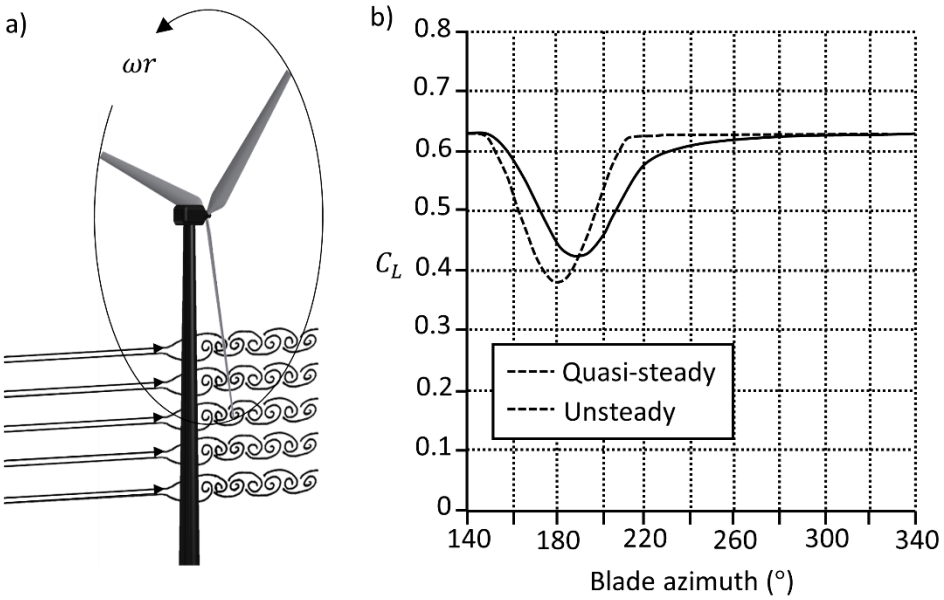

Figure 2.3. Representation of (a) the flow field development downstream of the tower of a horizontal axis wind turbine and (b) resultant lift coefficient developed as a result of the unsteady operating conditions and blade-tower interaction (image reproduced from Leishman (2006)).

Operation of horizontal-axis wind turbines in extreme weather conditions, and also wind turbines using stall for power regulation, are subject to elevated angles of attack and continuous operation in post-stall conditions (Butterfield et al., 1991, Hansen and Butterfield, 1993, Bossanyi, 2003, Tangler and Kocurek, 2005, Lanzafame and Messina, 2013). As such, motion profiles including constant-pitch-rate angular velocity can be utilised to represent gust-like conditions, and to simulate the pitch-up process created by instabilities generated by unsteady operating conditions. From the literature, the random nature of turbulence associated with the operation of rotary machines has been shown

(Butterfield et al., 1991, Hansen and Butterfield, 1993, Bossanyi, 2003, Tangler and Kocurek, 2005, Lanzafame and Messina, 2013). However, much of the work linked to the unsteady behaviour is often completed using airfoils exposed to sinusoidal velocity profiles. Therefore, to represent extreme weather conditions, further research must be conducted to determine the aerodynamics of airfoils undergoing dynamic stall with constant-pitch-rate angular velocity, and to elevated angles of attack. Additionally, research needs to be conducted to evaluate the behaviour of the airfoils which have been exposed to dynamic stall, and which continue to proceed into post-stalled conditions as a result of sustained elevated angles of attack.

2.1.2. Dynamic Stall Forces and Flow Structure Development

Dynamic stall is characterised by multiple stages of flow development and load generation. The critical stages of the unsteady separation process on a pitch-up airfoil are expressed in Figure 2.4, and include: (a) the attached flow phase, (b) boundary layer reversal, (c) shear layer roll-up, (d) dynamic stall onset, (e) fully separated flow and (f) flow reattachment (Carr, 1988, Shih et al., 1992, Mulleners and Raffel, 2012).

During the initial pitch-up motion, the airfoils exhibit properties similar to steady-state airfoils, where the boundary layer remains attached and increased suction pressure continues to develop steadily at the leading edge. This results in a linear increase in lift similar to that of the steady-state counterpart (Mulleners and Raffel, 2012, Gharali and Johnson, 2013). Over the rear section of the airfoil, a recirculation zone forms with similar characteristics to steady-state trailing edge stall. However, its forward detachment point progresses towards the leading edge with an increased angle of attack, whilst its

reattachment point remains fixed at the trailing edge (Lee and Gerontakos, 2004, Gharali and Johnson, 2013).

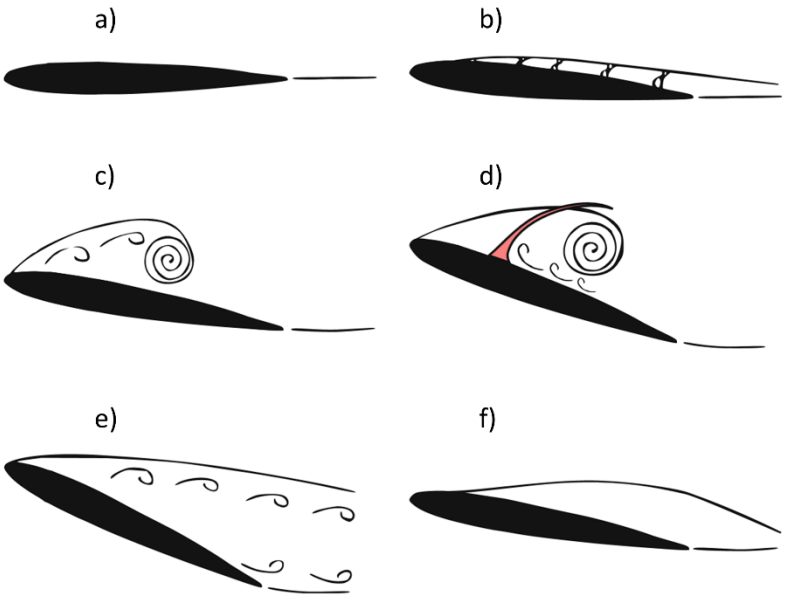

Figure 2.4. Schematic representation of the critical flow stages of the ramp-up phase of dynamic stall showing: a) attached flow, b) flow reversal, c) shear layer roll-up, d) dynamic stall onset, (f) full stall and (e) flow reattachment. (Image adapted from Mulleners and Raffel (2013).

As the airfoil is pitched to a higher angle of attack, the trailing-edge recirculation zone breaks down and is replaced by the growth of two distinct recirculation zones (the leading-edge vortex and the shear layer vortex) that form on the upper surface (Visbal and Shang, 1989). This phase resembles the onset of the dynamic stall development. It is worth noting that resulting flow structures vary according to the applied rotation rate leading to differences in the dynamic stall development stage. Numerical simulations by

Visbal and Shang (1989) showed the formation of two distinct vortices, as described above, for high rotation rate motion. However, for a low rotation rate airfoil motion, the upper shear layer was observed to encapsulate multiple, regularly-spaced vortices, which were transported downstream by the external flow (Mulleners and Raffel, 2012). This indicates that the resulting dynamic stall flow structure is greatly influenced by the rotation rate, and associated induced accelerated flows. Regardless of the rotation rate, roll-up of vorticity originating completely at the leading edge resulted in the formation of the leading-edge vortex and subsequent increased lift (Shih et al., 1992).

At the initiation of leading-edge separation, abrupt and rapid growth of the leading-edge vortex occurs while it remains attached and bound to the airfoil surface, as shown in Figure 2.4c. With the increased vorticity concentrated over the upper surface, the leading-edge vortex induces localised velocity at the airfoil surface which, in turn, contributes to an increase in suction pressure on the airfoil surface. The influence of the leading-edge vortex further induces the formation of a secondary counter-rotating vortex pair, forward of the leading-edge vortex, which aids in the growth and advancement of separation of the leading-edge vortex (Shih et al., 1992).

With the presence of the vortex structures above the airfoil surface, rapid increases in the lift force occur, as the leading-edge vortex grows and begins its journey across the chord of the airfoil (McCroskey and Puccif, 1982). The increase in lift can be either a positive attribute, for the case of high manoeuvrability; or a negative attribute, due to increased blade loading and vibration. Stall onset quickly follows with the passage of the vortex and occurrence of moment stall of the airfoil (McCroskey and Puccif, 1982, Carr, 1988, Visbal and Shang, 1989).

Studies show that the onset of stall can be classified by multiple physical occurrences. For example, using critical events in the dynamic stall process, represented by force, moment and pressure development, can be utilised as criterions to predict dynamic-stall onset (Sheng, Galbraith and Coton, 2006, 2008). These events included: (a) deviation in the airfoil normal force, C_N, and drag C_D coefficients; (b) collapse of both the airfoil moment coefficient, C_M, and leading-edge pressure coefficient, C_P; (c) reaching the maximum airfoil lift coefficient, C_L; and (d) variation in the pressure coefficient at the airfoil quarter-chord location. The stall criterion identifies the point at which the leading-edge vortex translates over the chord to a point where aerodynamic forces and moments combine to create loss of lift force, increased drag and a reduction in airfoil moment. However, the criterion does not provide a good indication of the precise moment where separation of the leading-edge vortex, from the trailing edge, occurs. A method for analysing the progression of the leading-edge vortex and its subsequent separation using other physical properties, such as surface pressure, is therefore required for greater awareness of the leading-edge vortex transition over the upper surface of the airfoil.

The translation velocity of the leading-edge vortex over the airfoil was highlighted in Panda and Zaman (1994), where the shed vortex is shown to translate at a rate according to $0.6 < U_N < 0.8$, where $U_N = U_C/U_\infty$, where U_C is the vortex convection velocity. In the report, the centre of vortex is tracked using the resulting velocity profiles generated from hot-wire measurements. In a similar study, Shih et al. (1992) proposed that the convection velocity is $U_N \approx 0.39$ based on the trajectory of the centroid of the vorticity of the primary leading-edge vortex captured using PIV. Both examples show that the convection velocity is dependent on the proximity of the leading-edge vortex to the airfoil surface, the size and position of the vortex relative to the free-stream, where effects of

shadowing by the airfoil is reduced. These effects are also shown in Rival, Prangemeier and Tropea (2009), who conducted PIV measurements to track the vortex position with time. The normalised convection velocity is shown to range from $U_N \approx 0.15$, at initial formation, through to $U_N \approx 1$ once the vortex has passed approximately 3.5 chord lengths into the free-stream.

Three dimensional interactions of substructures vortices created in the shear layer at the leading edge, in conjunction with wing tip interaction during dynamic stall were discussed in Garmann and Visbal (2017) using high fidelity large-eddy simulations. They showed that the separation bubble prior to dynamic-stall vortex formation was susceptible to instabilities in the boundary layer, which led to rapid breakdown of the separation bubble and generation of small vortex substructures over the upper surface of the airfoil. For an unswept wing, a laminar boundary layer and separation bubble was demonstrated to form uniformly on the upper surface and along the span of the wing. Minor variations in boundary layer development at the tip were observed in their simulation due to the interaction of the wing tip vortex and impinging free-stream flow. In a similar study, Visbal (2014) used large-eddy simulations and a non-swept wing to analyse the formation of separation bubbles and the dynamic-stall vortex. They showed that the interaction between the leading-edge and trailing-edge vortexes was significant in altering span-wise three-dimensional instabilities within the vortex cores. The net effects of three-dimensionality of the developed flow structure is shown to have a minimal influence on the developed force and moment coefficients, although the span-wise flow within the vortex cores was present.

Although much work has been conducted to detail the flow structure development and force generation properties of the dynamic-stall process, there remains a gap in literature detailing systematic differences between airfoils of significant thickness ratios and their performance when subjected to high-rotation-rate angular velocities. Furthermore, details of post-stall flow structure and the impact of unsteady rotation on post-stall behaviour is lacking.

2.2. Performance Parameters Influencing Dynamic Stall

2.2.1. Effects of Reynolds Number

The Reynolds number, a representation of the ratio of inertial to viscous forces acting on a body moving through a fluid medium is defined as:

$$Re = \frac{\rho U_\infty c}{\mu} \qquad \text{Equation 2}$$

where, ρ is the fluid density, U_∞ is the free-stream velocity, C is the chord length of the airfoil, and μ is the dynamic viscosity of the fluid.

The Reynolds number can be classified into three categories: (1) laminar Reynolds numbers, where $Re < 10^5$ and viscous forces dominate the boundary layer and where separation bubbles heavily impact the resulting aerodynamic forces; (2) transitional Reynolds numbers, where $Re = 10^5 - 5 \times 10^6$ and the boundary layer is highly susceptible to boundary layer instabilities and adverse pressure gradients; and (3) turbulent Reynolds numbers, where increased boundary layer mixing results in thickening

of the boundary layer (Cimbala and Çengel, 2014). This process is shown in Figure 2.5, where the growth of the boundary layer over a flat plate indicates the respective Reynolds number and its impact on boundary layer development.

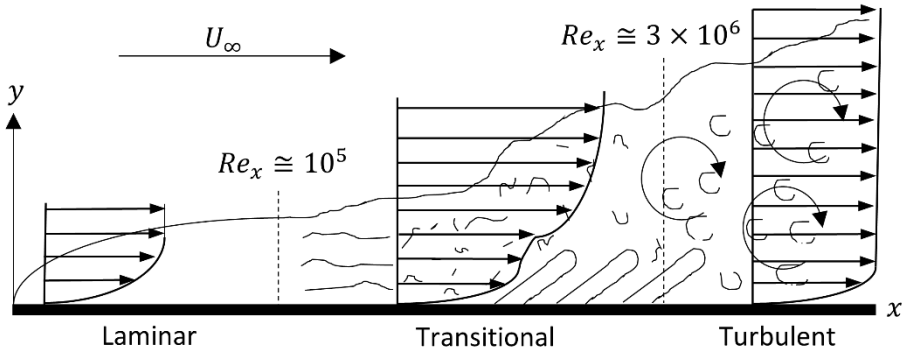

Figure 2.5. Boundary layer development over a flat plate indicating the transition in boundary layer thickness due to the increased Reynolds number along the length of the plate (Cimbala and Çengel, 2014).

Under steady-state operating conditions, the impact of changing the Reynolds number has been heavily investigated and well documented (Sheldahl and Klimas, 1981, Laitone, 1997). With an increase in Reynolds number, the steady-state stall angle of attack is observed to increase. This leads to delayed stall characteristics and an overall increase in aerodynamic efficiency of the airfoil. For steady-state operation, these characteristics are typically preferred for the operation of aircraft and wind turbines, where operation close to the maximum stall angle of attack delivers increased aerodynamic performance. With emerging micro-aerial vehicle development, where wings and rotors are operating at extremely low Reynolds numbers, the need to understand the aerodynamic performance is critical for increased performance and control of the micro-aerial vehicles. Laitone (1997) compared the performance of thin plate-like airfoils with thicker airfoils using a

wind tunnel, where $Re < 70{,}000$. The results showed that the maximum aerodynamic efficiency was far greater for the thin, cambered plate by comparison with a traditional NACA 0012 airfoil. The performance of the airfoils was shown to be susceptible to both wind tunnel turbulence intensity and variations in the Reynolds number.

For higher Reynolds number applications, relevant to the operation of helicopters where $Re > 10^6$, studies of the effects of Reynolds number on the dynamic-stall process have generally been shown to be minor (McCroskey, 1982, Robinson and Wissler, 1988, Choudhuri and Knight, 1996, Schreck, Faller and Helin, 1998, Kang et al., 2009, Ol et al., 2009). McCroskey (1982) discussed the significance of Reynolds number as a critical performance parameter dictating the extent of flow separation. However, the impact of varying the Reynolds number was reported to be insignificant when compared to other parameters, such as the reduced frequency. Minor variation in the surface pressure was noted by Robinson and Wissler (1988), who performed surface pressure measurements on a pitching NACA 0015 airfoil. In this study, the overall vortex dynamics and normal force coefficients were observed to be similar across the range of Reynolds number evaluated ($Re = 59{,}000$, $118{,}000$ and $223{,}000$). Similar surface pressure studies using a NACA 0015 airfoil were performed in Schreck, Faller and Helin (1998), which showed an independent influence of the Reynolds number on the boundary layer reversal and transition. Flow structures, including the leading-edge, secondary and tertiary vortices, were noted to decrease in length scale and form more rapidly in a numerical study presented in Choudhuri and Knight (1996). These results, which relate to a pitching NACA 0012 airfoil, showed that the formation of the leading-edge vortex developed closer to the leading edge with increased Reynolds number. However the overall effects of increasing the Reynolds number on the dynamic-stall process were still considered minor.

In addition to experimental methods that shown similar dynamic-stall characteristics between multiple Reynolds number, Visbal (2014) investigated the boundary layer and substructure vorticity development during the pitch-up process using large-eddy simulations at Reynolds numbers of $Re = 200{,}000$ and $Re = 500{,}000$. He showed that the effects of decreasing Reynolds number led to elevated pressures at the leading edge, earlier bursting of the laminar separation bubble, longer separation bubble development and aft movement of the separation point defining the onset of dynamic-stall vortex formation. Although these effects were evaluated at Reynolds numbers in the range of $Re > 1 \times 10^5$, the effect of boundary layer development at lower Reynolds numbers still requires investigation to assess the viscous-inertial interaction between the impinging flow and the airfoil. Differences in Reynolds number exist, the effects of Reynolds number variations on the overall unsteady separation process was discussed in Shih, Lourenco and Krothapalli (1995). In (Shih, Lourenco and Krothapalli, 1995), the Reynolds number is discussed as it has a limited influence on the overall unsteady separation process. However, they state that differences in the length and time scales of the laminar separation bubble, boundary layer and developed vortex structures are to be expected. As such, investigations using low Reynolds numbers can be utilised to develop knowledge of the overall dynamic stall process, which in turn can be inferred to higher Reynolds number applications.

2.2.2. Effect of Pitch Rate and Motion Type

The pitch rate and motion type have a significant impact on the stall characteristics of a rotating airfoil. The reduced frequency, used to describe the ratio between the freestream

and airfoil leading edge velocity, can be defined as shown in Equation 3 for an airfoil pitched about its mid-chord location.

$$\kappa = \frac{\omega c}{2U_\infty} \qquad \text{Equation 3}$$

Here, ω is the airfoil angular velocity, c is the airfoil chord length, and U_∞ is the free-stream velocity. The reduced frequency is utilised as a non-dimensional measure of flow steadiness. In a steady-state environment, airfoil geometry is primarily responsible for the overall force generation, due to upper and lower surface pressure differentials. However, for a pitching airfoil undergoing dynamic motion, the reduced frequency is recognised as being a highly influential parameter dictating the resulting forces. This is due to the induced inertial effects, created by airfoil rotation, and its influence on delaying flow separation and stall (Carr, McAlister and McCroskey, 1977, McCroskey, 1982, Leishman, 1990). As discussed in Leishman (2006) the extent of steadiness can be classified as either quasi-steady, where $\kappa = 0 - 0.05$; or unsteady, where $\kappa > 0.05$ and accelerated flows become dominant in dictating resulting flow fields and associated forces. Both helicopters and wind turbines can be exposed to quasi-steady rotation rates $(\kappa < 0.05)$ and unsteady rotation rates $(\kappa > 0.05)$ during normal operating conditions. Such conditions may include varying wind speed, velocity gradients in the wind, yawed flow, unsteady wake interaction, sweep effects and rotor-fuselage or turbine-tower interactions. Explicitly constraining the reduced frequency to a specific value would be unrealistic due to the complexity of the system operating conditions. As a result of rotation rate of the airfoil, maximum lift is increased with higher reduced frequencies, and hence rotation rates. This characteristic was established and observed by Harper and

Flanigan (1950), who conducted wind tunnel testing on a rotating wing model and concluded that a linear increase in maximum lift was possible with increased rotation rate. Figure 2.6 shows the lift coefficient, C_L, for constant-pitch rate (Jumper, Schreck and Dimmick, 1987) and sinusoidal (McCroskey, 1981) airfoil motion types.

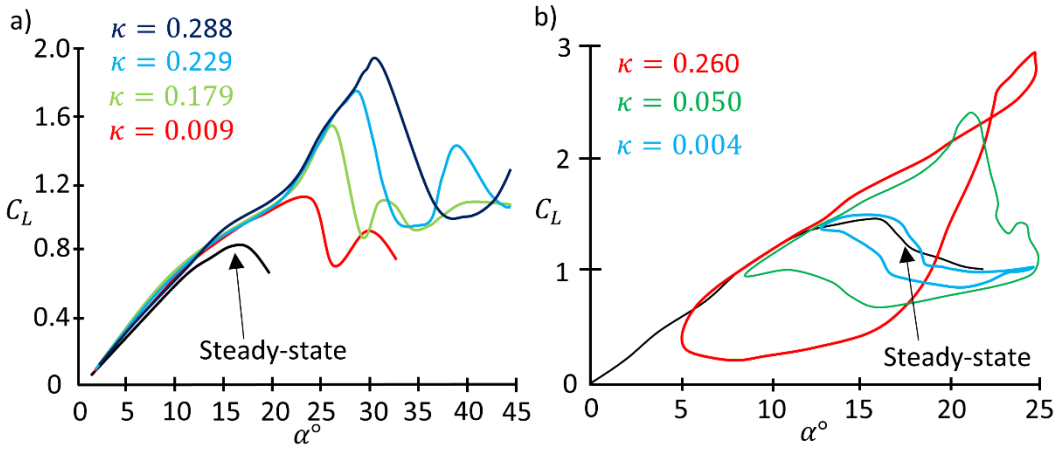

Figure 2.6. Influence of increasing reduced frequency on the overall maximum lift for a (a) constant-pitch rate velocity profile (Jumper, Schreck and Dimmick, 1987), and (b) for a sinusoidal airfoil velocity profile (McCroskey, 1981).

Figure 2.6a shows that constant pitch-rate motion causes an increase in the maximum lift coefficient when the airfoil is rotated beyond steady-state stall angles. The increase in lift is possible until the leading-edge vortex separates, resulting in fully separated flows and deep-stall behaviour. The effects of increasing the rotation rate on the airfoil performance led to a delayed collapse of the initial suction peak and further decreases in the minimum pressure coefficient at the leading edge. As such, increased lift and delayed stall to a higher angle of attack were possible (Liiva, 1968, Conger and Ramaprian, 1994, Corke and Thomas, 2015).

The reduction in pressure at the leading edge can be linked to the development of the leading-edge vortex (Amiralaei, Alighanbari and Hashemi, 2010), where its formation is delayed with increased reduced frequency (Choudhuri and Knight, 1996). Once the leading-edge vortex sheds into the wake, the airfoil proceeds into a state of deep stall until the angle of attack returns to a suitable level to permit flow reattachment.

For the sinusoidal case, a broadening in the lift hysteresis loop occurs with increased reduced frequency, where differences in maximum and minimum lift increases between flow separation and flow re-attachment respectively (Amiralaei, Alighanbari and Hashemi, 2010). Broadening of the lift coefficient curve is also highlighted in Figure 2.6b, and shows an increase in the lift coefficient of a NACA 0012 airfoil undergoing sinusoidal rotation, and where the angle of attack is represented according to the equation $\alpha(t) = 15° + 10° \sin(\omega t)$ (McCroskey, 1981).

The difference between the maximum and minimum lift coefficients during post-stall is shown to increase due to delayed separation resulting from elevated rotation rates. This difference was defined in Choudhry et al. (2014) as the stall intensity factor for a constant-pitch rate velocity profile. Furthermore, the broadening of the hysteresis loop for a sinusoidal velocity profile is classified as light stall, where flow separation and reattachment occur; or as deep stall, where the vortex shedding occurs (McCroskey and Puccif, 1982). Although the maximum lift can significantly increase, minimal impact on the lift-curve slope is observed through increases in the reduced frequency (Amiralaei, Alighanbari and Hashemi, 2010).

Although the effects of increasing reduced frequency are well known, there remains little knowledge regarding the causes to the increased lift during the pitch-up motion. The

question remains as to what underlying mechanics are responsible for the delays in separation prior to the development of the dynamic-stall vortex. For post-stalled conditions, there remains a gap in knowledge associated with the impact of reduced frequency on the forces developed about an airfoil that undergoes constant-pitch-rate motion and which proceeds into a fully-stalled state. Is there a relaxation time to achieve steady-state flow conditions? What are the effects of varying the reduced frequency on critical topological features of the airfoil? These questions still remain and require further investigation.

2.2.3. Effect of Airfoil Geometry

Engineering designs and aeronautical applications heavily rely on the overall geometry of an airfoil to achieve high lift, high efficiency and delayed stall characteristics. For steady-state stall, the application of the airfoil geometries greatly varies depending on the intended use of the wing or blade structure. Similarly, the effect of changing the airfoil geometry on the dynamic-stall process must also be determined to accurately predict the associated loads created during operation. Airfoil profiles studied for dynamic stall characteristics are often associated with helicopters or wind turbines due to their consistent steady-state operating performance. However, these airfoils were observed to underperform in their intended application when subjected to unsteady operating environments. As such, studies to determine the effect of airfoil profiles and their resistance to separation and dynamic stall is critical for the analysis of machines operating in dynamic stall conditions.

Liiva (1968) conducted wind tunnel tests on a modified NACA 0012 and a Vertol 23010 airfoil undergoing dynamic stall and fitted with differential surface pressure sensors. It was determined that airfoils with larger camber performed better than symmetrical airfoils. This was due to an increase in maximum force generation and a delay in negative pitching moment at higher angles of attack. In a similar study, McCroskey, Carr and McAlister (1976) and McCroskey et al. (1982) conducted a series of detailed investigations to determine and compare the effects of parameters such as camber and thickness on dynamic stall. A NACA 0012 airfoil and seven contemporary helicopter airfoil designs were examined in a low speed wind tunnel facility to evaluate their performance under dynamic stall conditions. It was shown that airfoil profile shapes could significantly affect dynamic stall, because of the ability to achieve higher maximum lift and angles of attack prior to the occurrence of stall. In addition, airfoils that exhibited good static-stall behaviour also performed more favourably when operating in dynamic stall conditions (McCroskey et al., 1981).

Much of the research conducted to analyse the effects of airfoil geometry on dynamic stall has been directed towards helicopter applications with sinusoidal motion profiles. Under these conditions, the mean angle of attack is defined within the steady-state limits of the airfoil, and the oscillatory component varied by, $\alpha = \pm 10°$. The effects of the airfoil geometry on the post-stall characteristics of an airfoil that has undergone constant-pitch-rate motion dynamic stall is limited.

A study by Choudhry et al. (2014) utilised three airfoils, a NACA 0012, a NACA 4418, and a NREL-S809, used hydrogen-bubble flow visualisation techniques to show minor flow structure variation in post-stall conditions and when the airfoil was subjected to a

maximum angle of attack of $\alpha = 50°$ and constant-pitch rate motion. From the flow visualisation studies, the dynamic-stall vortex was shown to form further aft of the leading edge for airfoils with increased camber, such as the NACA 4418. No force data was available from the experiments in Choudhry et al. (2014). However, it may be speculated that increased negative moment for airfoils with increased camber and thickness may occur due to the further aft location of the dynamic-stall vortex initiation. Results presented in McCroskey et al. (1981) also concluded that under deep-stalled conditions, the influence of airfoil geometry was negligible, and that other performance parameters were more influential to the dynamic-stall process.

2.2.4. Compressibility Effects on Dynamic Stall

Compressibility of the flow around the tips of rotor blades operating at high speeds results in significant increases in tip load and rotor noise. Due to the occurrence of dynamic stall on rotor blades of helicopters, the effects of compressibility on the development of dynamic stall must be considered.

Early studies (Sankar and Tassat, 1981, Chandrasekhara and Carr, 1990, Chandrasekhara, Ahmed and Carr, 1993) investigating the compressibility effects demonstrate the behaviour of airfoils exposed to dynamic stall operating conditions and also experiencing variations in local Mach number, M. From these studies, it was concluded that increasing the Mach number resulted in the formation and development of the dynamic stall process at lower angles of attack, therefore initiating dynamic stall characteristics earlier in the pitch-up cycle of the airfoil. This was more evident for Mach numbers above 0.3. In addition, the strength of the leading-edge vortex was shown to be lowered with increased

Mach numbers (Chandrasekhara and Carr, 1990). Carr and Chandrasekhara (1996) details the effects of compressibility in a comprehensive review outlining the variation in dynamic stall vortex formation with increased Mach number. In the review, it was shown that the leading-edge suction pressure was decreased as a result of localised shocks at the leading edge. This effect was also noted in a study by Choudhuri and Knight (1996) who showed that adverse pressure gradients and peak suction were reduced through increased compressibility effects. In addition, Choudhuri and Knight (1996) discussed the delay in formation of the recirculation zone on the upper surface of a NACA 0012 airfoil, whilst also showing its formation further from the surface with elevated Mach numbers. Numerical simulations by Sankar and Tassat (1981) showed that increased Mach number can lead to an increase in lift force prior to the development of the leading-edge vortex.

In more recent studies assessing the effects of compressibility, Corke and Thomas (2015) confirm the effects of compressibility in lowering the strength of the leading-edge vortex. In addition, their results showed that for high-enough Mach numbers, the leading-edge vortex is formed downstream of the shockwave on the airfoil upper surface, whilst its topology is altered by comparison to lower Mach numbers. Similarly, Sangwan, Sengupta and Suchandra (2017) utilised implicit large-eddy simulations to show that both lift and moment stall occur at lower angles of attack with an increase in the Mach number. Their study also introduced the effects of compressibility on the hysteresis loops and maximum load generation, where the hysteresis is shown to decrease in magnitude with an increase in Mach number.

2.3. Experimental Methods to Analyse Dynamic Stall

Experimental techniques remain significant for determining the performance characteristics and flow patterns of many fluid mechanics phenomena. Contrary, advances in computing power have led to a growth in modelling of the dynamic-stall process through numerical simulations. Computing systems and numerical modelling schemes can evaluate fluid behaviours and forces associated with dynamic stall with reasonable accuracy. However fundamentally, numerical models must be validated with experimental data in order to determine the accuracy and practicality of the generated data sets.

Numerical schemes were utilised in a series of work investigating the stages of the dynamic stall process and deep-stall characteristics in both subsonic and supersonic flow conditions for multiple airfoils including a NACA 0012, a NACA 0015 and a SD-3007 airfoil (Visbal and Shang, 1989, Visbal, 1990, Visbal, 2011, 2014). In this work, the dependency of the dynamic-stall process on the pitch-rate and pitch axis locations was shown. Furthermore, detailed flow structure and formation of Kelvin-Helmholtz instabilities within the leading-edge shear layer were discussed and linked to span-wise vortex breakdown during dynamic stall. Using a similar numerical model, the control of the dynamic stall vortex at low Reynolds numbers using a moving wall and boundary layer suction was explored in Visbal (1991). For the NACA 0015 airfoil utilised, both methods of boundary layer control were shown to delay flow reversal and prolong the formation of the dynamic-stall vortex.

Variation in unsteady free-stream inflow conditions and its effects on the dynamic stall process has been previously investigated (Spentzos et al., 2005, Amiralaei, Alighanbari and Hashemi, 2010, Gharali and Johnson, 2013, Lu, Xie and Zhang, 2013, Lu et al., 2013). In these studies, a comparison between unsteady force and flow development data resulting from uniform free-stream inflow condition and unsteady inflow conditions were presented. They showed an aerodynamic coupling due to the unsteady free-stream and the dynamic-stall process, which led to an increase in circulation of both the leading-edge and trailing-edge vortices.

Numerical schemes using unsteady Reynolds averaged Navier-Stokes (URANS) equations have been shown to falsely predict the load and flow structure development during pitch-down motion and when the airfoil is pitched to a high angle of attack (Martinat et al., 2008, Wang et al., 2012). They show that the inherent nature of the averaging schemes utilised within the URANS models leads to significant loss of turbulent structures resulting in failure to accurately model force during highly unsteady flow conditions. Due to these errors, higher order schemes including direct eddy simulation, organised eddy simulations and large eddy simulations have been utilised to capture the generation of smaller vortex structures, separation bubbles and force augmentation during dynamic stall (Martinat et al., 2008, Wang et al., 2012, Visbal and Garmann, 2017). Although these models generate significant amounts of data pertaining to the onset of dynamic stall and the detailed flow structure, the work has not shed any light on the processes and flow behaviour occurring at extreme angles of attack and following dynamic-stall vortex separation. Therefore, the need to use experimental techniques still remains necessary for validation of modern numerical schemes, and for situations were high performance computing facilities are not available.

2.3.1. Flow Visualisation

Flow visualisation techniques are utilised to provide insight into flow patterns resulting from external and internal flow disturbances. For an airfoil exposed to dynamic stall conditions, flow visualisation allows detailed information to be obtained with respect to flow separation, vortex formation and observation of critical topological features. These features include the formation of the rear separation bubble, leading edge separation, the development of the dynamic-stall vortex and vortex structures resulting from fully-separated flows. The principles of flow visualisations are applicable in determining, visualising and interpreting the development of fluid flows. Simple methods to obtain fast and effective visualisation of flow features created during dynamic stall include hydrogen-bubble wire techniques, smoke-wire visualisation, dye injection and precipitation methods.

A hydrogen-bubble wire was utilised in McAlister and Carr (1979) to generate flow patterns over a NACA 0012 airfoil undergoing dynamic stall. Coupling the hydrogen-bubble wire and surface-mounted electrodes, flow structure development within the shear layer on the upper surface of the airfoil was obtained. From their hydrogen-bubble wire results, McAlister and Carr (1979) concluded that the onset of dynamic stall was established by the presence of a fast-moving reverse-flow region on the upper surface that progressed towards the leading edge. This unsteady reversed flow region broke down into multiple vortex structures leading to the formation of the leading-edge vortex.

The hydrogen-bubble wire technique was also presented in Choudhry et al. (2014) who showed significant differences in the vortex development phase of dynamic stall with

three airfoils of dissimilar thickness and camber. Their results showed that thicker airfoils delayed stall to higher angles of attack, whilst higher-cambered airfoils moved the formation of the dynamic-stall vortex further aft of the leading edge, as indicated in Figure 2.7.

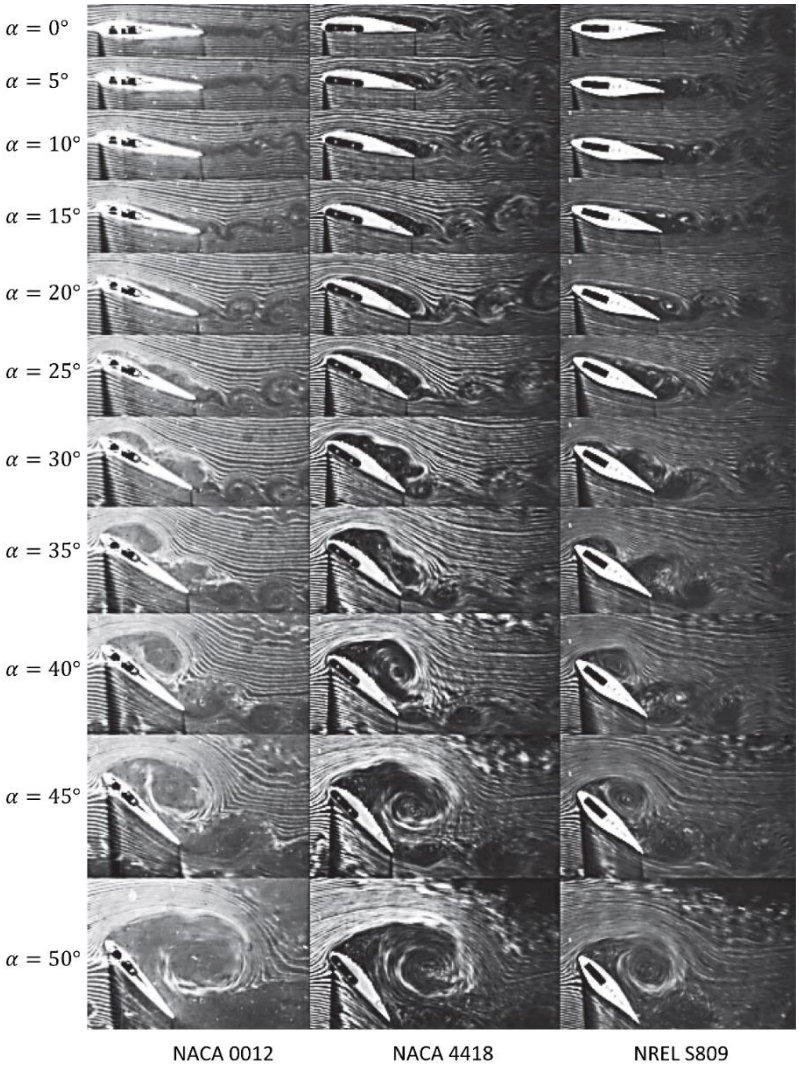

Figure 2.7. Flow visualisation showing vortex structure development about a NACA 0012, a NACA 4418 and a NREL-S809 airfoil undergoing dynamic stall conditions and pitching to a maximum angle of attack where $\alpha = 50°$. $Re = 10{,}000$, whilst $\kappa = 0.1$. (Choudhry et al., 2014).

Similar flow structure development, using smoke visualisation, was utilised to identify flow structure interaction and the dependency of the dynamic-stall process on performance parameters including Reynolds number and reduced frequency (Helin and Walker, 1985, Albertson et al., 1987). The effect on flow development as a result of two different motion types was investigated in Rival and Tropea (2010). In their study, a direct comparison between a pitching and a plunging asymmetric SD-7003 airfoil showed that similar flow topology and growth of the leading-edge vortex occurred in each case. Smoke visualisation showed the development of the leading-edge vortex and transition of the wake structure, from multiple vortex pairs (under bluff body conditions) to a 'mushroom' profile, at increased rotation rates (Rival and Tropea, 2010). The tests performed by Rival and Tropea (2010) were, however, limited to angles of attack of $\alpha < 25°$. As such, flow structures in deep stall and at elevated angles of attack were not observed.

The influence of elevated angles of attack and pitching rate on the wake flow structure development of a pitching NACA 0012 and elliptical body is presented in Ohmi et al. (1990) and Ohmi et al. (1991). Their testing utilised solid particle tracers in a water channel to observe global streamlines of the developed flow fields about the pitching wings. In addition, streaklines were obtained using the tellurium method to observe the vorticity at the airfoil surface and in the wake (Ohmi et al., 1990). Vorticity within the shear layer was also presented in a study that investigated the application of upper-surface blowing (Weaver, McAlister and Tso, 1998) and upper-surface suction (Ahsanul Karim and Acharya, 1994). Furthermore, outer flow field visualisation was presented in Post and Corke (2004), where the application of plasma actuators for means of flow control during dynamic stall is suggested. However, the angular displacement was shallow ($\alpha < 35°$) and specific to the application of helicopter operations, and as such, did not detail the vortex

structures developed at high angles of attack and during deep-stall conditions (Post and Corke, 2004).

Similar studies, investigating the flow structure and dynamic stall process using smoke-wire visualisation, are presented in Albertson et al. (1987). This study detailed events in the dynamic-stall process including the breakdown of the upper surface shear layer, leading edge separation and roll-up of the leading-edge vortex. Their results showed that the dynamic-stall vortex was a consequence of the unsteady motion and not a fundamental mechanism for lift generation, as significant lift is observed prior to its formation (Albertson et al., 1987). Although this study successfully highlighted the development phase of the dynamic-stall process, no details of the post-stall flow behaviour are presented. Details of the effects of rotation rate and airfoil geometry for high angle of attack dynamic stall are still required during deep stall operating conditions.

A study that investigates dynamic stall and post-stall behaviour showed the influence of the leading-edge vortex and separated flows on the surface flow of a NACA 0015 airfoil (Helin and Walker, 1985). Figure 2.8 shows smoke-wire visualisation of the dynamic-stall process about the NACA 0015 airfoil and highlights the effects of delayed growth of the leading-edge vortex due to increased angular velocity on the airfoil. In Figure 2.8a, where $\dot{\alpha} = 460°/s$, the leading-edge vortex is shown to have commenced its translation into the wake of the airfoil. Similarly, for the angular velocity of $\dot{\alpha} = 920°/s$, as shown in Figure 2.8b, the leading-edge vortex has also shed into the wake, resulting in fully separated flow. However, as the angular velocity is increased to $\dot{\alpha} = 1380°/s$, the leading-edge vortex and recirculation zone over the upper surface of the airfoil is shown to stay fixed to the airfoil surface, without separating into the free-stream.

This observation is critical as it indicates a dependence of the dynamic-stall process on the angular velocity, which subsequently delays the development of post-stall flow due to the delay in formation of the leading-edge vortex.

a. $\alpha = 60°, \omega = 460°/s$ b. $\alpha = 60°, \omega = 920°/s$ c. $\alpha = 60°, \omega = 1380°/s$

Figure 2.8. Smoke visualisation of a NACA 0015 airfoil at $\alpha = 60°$, and for (a) $\omega = 460°/s$, (b) $\omega = 920°/s$ and (c) $\omega = 1380°/s$ showing the variation in flow structure resulting from increased pitch rate (Helin and Walker, 1985).

The effects of both pitch rate and plunge motion is presented in OI et al. (2009), which makes use of dye injection methods to show the effects of increasing Reynolds number and three-dimensional diffusion on the leading-edge vortex during dynamic stall development around a SD-7003 airfoil. This work was conducted where the maximum angle of attack was limited to $\alpha = 25°$, and as such, the behaviour of the dynamic-stall process could not be determined for higher angles of attack, where $\alpha > 30°$.

All of the flow visualisation techniques detailed above generate qualitative results that can only be used for visualisation of the flow structure during dynamic stall. Quantitative details regarding the flow velocity and pressure fields require more advanced measurement techniques, such as PIV, in order to further understand the physical interaction between the fluid and wing body undergoing dynamic stall.

2.3.2. Hot-Wire Anemometry and Hot-Film Measurement

Hot-wire anemometry allows for the measurement of local flow velocities and their fluctuation, with respect to time, at high frequency ranges. Hot-wire anemometry utilises the electrical resistance of a conductive wire fixed between two or more probes to sense flow velocity via the degree of cooling created by the impinging flow. Similarly, hot films can also be utilised to provide velocity fluctuation within the boundary layer. Due to the hot-wire operation, directionality of flow measurement is limited as the flow speed can only be measured in the plane perpendicular to the wire axis. A diagram of a simplified hot-wire and hot-film probe is shown in Figure 2.9, which includes details of the arrangement of the wire electrode and hot-wire supports in conjunction with the hot-film flush-mounted probe, typically mounted level with the airfoil surface.

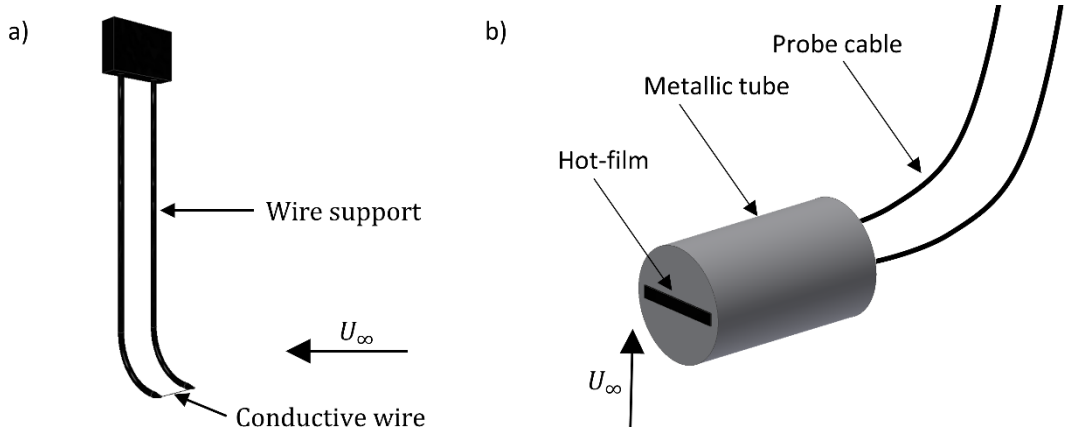

Figure 2.9. Diagram of (a) a simplified hot-wire probe and (b) a hot-film flush-mount probe used for measurement of wall shear stress, localised velocity and boundary layer reversal.

Analysis of the velocity profile using both hot-wire anemometry and hot-film measurements has allowed for a more in-depth comprehension of the dynamic-stall

process. This has been achieved through a greater understanding of the separation characteristics at the boundary layer and on the surface of the airfoil where increased shear and reversed flow at elevated angles of attack occurs. McAlister, Carr and McCroskey (1978), using multiple hot-wire probes mounted at the leading edge of a NACA 0012 airfoil, demonstrated the transition of laminar to turbulent flow resulting from dynamic stall occurring on an airfoil undergoing oscillatory motion. In addition, re-attachment of the separation bubble developing at the leading edge of the airfoil was demonstrated through a sequential reduction in voltage of each hot-wire placed along the chord of the airfoil. Detailed studies of multiple airfoil profiles were investigated in Carr et al. (1982), where both hot-wire anemometry and hot-film analysis were conducted. In Carr et al. (1982), the presence of flow reversal was analysed through the interpretation of shear stresses within the boundary layer, to show the effect of airfoil geometry and pitch motion on the development of dynamic stall process and boundary layer transition. In this study, insight to the behaviour of the boundary layer under unsteady motion was gained. However, the behaviour of the boundary layer and its reversal for high rotation rates, and in post-stall flow regions at elevated angles of attack was not investigated.

A study performed by Helin and Walker (1985) employed seven hot-wire probes mounted on the suction side of a pitching NACA 0015 airfoil to assess the near-surface flow field at elevated angles of attack. Their results showed a near linear increase in normalised flow velocity at the leading edge with increased rotation rate and until initiation of the leading-edge vortex. Once the leading-edge vortex had begun its formation, higher velocities at the leading edge were identified to correlate with increased rotation rate, and a subsequent increase in the magnitude of the circulation of the vortex. This is significant

as it shows a direct comparison between the near surface flow strength and the airfoil rotation rate, whilst also linking the dynamic-stall vortex to an increase in flow velocity at the surface of the airfoil.

Increases in vortex circulation were also observed in experiments performed in Lorber and Carta (1987) and Lorber and Carta (1988). In their experiments, they utilised hot-wire anemometry to study the separation process of a Sikorsky SSC-A09 helicopter airfoil undergoing dynamic-stall conditions. In the reports, increasing the reduced frequency was indicated to influence the location of boundary layer transition, from laminar to turbulent, where the transition point moved forward along the chord. These results were applicable for angles of attack of $\alpha < 30°$ and for reduced frequencies of $\kappa = 0.001$ through to $\kappa = 0.02$. For reduced frequencies in the unsteady range, where $\kappa > 0.1$ and inertial loads dominate flow structure development, there remains a gap in the literature detailing behaviour of boundary layer separation and post-stall flows when subjected to high rotation rate and high angle of attack operating conditions.

Shear stress behaviour within the boundary layer was investigated in Schreck, Faller and Helin (1998), where the influence of increased rotation rates and Reynolds numbers was presented for a NACA 0015 airfoil undergoing constant-pitch-rate motion to a maximum angle of attack of $\alpha = 60°$. The results from fifteen hot-wire shear stress sensors concentrated on the forward portion of the airfoil ($X/c < 0.2$) demonstrated that both reduced frequency and Reynolds number influence the vortex initiation and separation process. However, both of these parameters were shown to act independently on the dynamic stall process, although both were shown to decrease the time required before unsteady boundary layer reversal.

Although the application of hot-wire anemometry for the measurement of unsteady boundary layer flow reversal and its separation can be utilised, measurements are typically focused on regions of high shear stress – such as at the leading-edge where the dynamic-stall vortex is generated. Studies utilising hot-wire techniques typically focus on the flow at low angles of attack, and which are associated with dynamic-stall vortex onset. There remains a gap in the literature detailing the dynamic stall process at high angles of attack, and during post-stall flow phases. In these conditions, the application of the hot-wire technique becomes difficult due to highly separated and reversed flows, and increased fluctuation of surface velocity, resulting in increased signal noise and difficulty when interpreting the generated signals.

2.3.3. Surface Pressure Analysis

Unlike both flow visualisation and hot-wire anemometry, surface pressure measurements offer the advantage of being able to observe the resulting pressures caused through dynamic motion of a pitching airfoil. The variation in surface pressure can be utilised to identify features, such as reversed flow, the existence of separation bubbles and regions of increased suction within the flow field. The pressure distribution surrounding an object can further be integrated to resolve the overall forces acting on the wing body.

Under dynamic stall conditions, increased suction at the leading edge is observed. With an increased angle of attack, the formation of the leading-edge vortex further increases the suction on the upper surface (Leishman, 1990). The surface pressure distribution is observed to broaden and reduce in magnitude as the vortex grows in strength and size until its eventual separation and departure from the upper surface of the airfoil.

The surface pressure distributions on airfoil surfaces resulting from the dynamic-stall process have been heavily investigated (McAlister, Carr and McCroskey, 1978, Carta, 1979, McCroskey, 1981, McCroskey et al., 1982, Daley and Jumper, 1984, Jumper, Schreck and Dimmick, 1987, Lorber and Carta, 1987, Robinson and Wissler, 1988, Jumper, Dimmick and Allaire, 1989, Acharya and Metwally, 1992, Currier and Fung, 1992, Conger and Ramaprian, 1994, Geissler, Dietz and Mai, 2005, Mulleners and Raffel, 2012). In these studies, performance parameters including Reynolds number, reduced frequency, Mach number, airfoil geometry and pitch motion were shown to influence the pressure distribution through changes in induced inertial flows, delayed separation and the presence of the dynamic-stall vortex.

The effect of increased angle of attack, vortex development and turbulence in the free-stream on the pressure distribution about an airfoils exposed to dynamic-stall conditions was discussed in Carr (1988). As a result of delayed stall, increased suction is observed at the leading edge prior to formation of the dynamic stall vortex. As the dynamic-stall vortex passes over the airfoil upper surface, a region of low pressure exists at the airfoil surface as a result of localised low pressure within the vortex. Similar observations detailing the surface pressure interaction with the dynamic stall vortex showed the relationships between the dynamic-stall vortex and overall force (Pierce, Kunz and Malone, 1976, Dadone, 1977, McCroskey et al., 1981). Dynamic stall remains to be a multi-stage flow phenomenon where increased lift is obtained during both pre-vortex formation and post-vortex formation stages.

In Leishman (1990) it was identified that multiple vortex shedding patterns could exist during dynamic stall and, that there was a lack of experimental data for airfoils specific to

helicopter applications. As a result, surface pressure measurements were conducted to determine the forces applied to a NACA 23012 airfoil pitching about its quarter-chord location. In this work, the effects of delayed stall, leading-edge vortex formation and secondary vortex formations were presented using surface pressure coefficients for multiple angles of attack, as indicated in Figure 2.10 (Leishman, 1990).

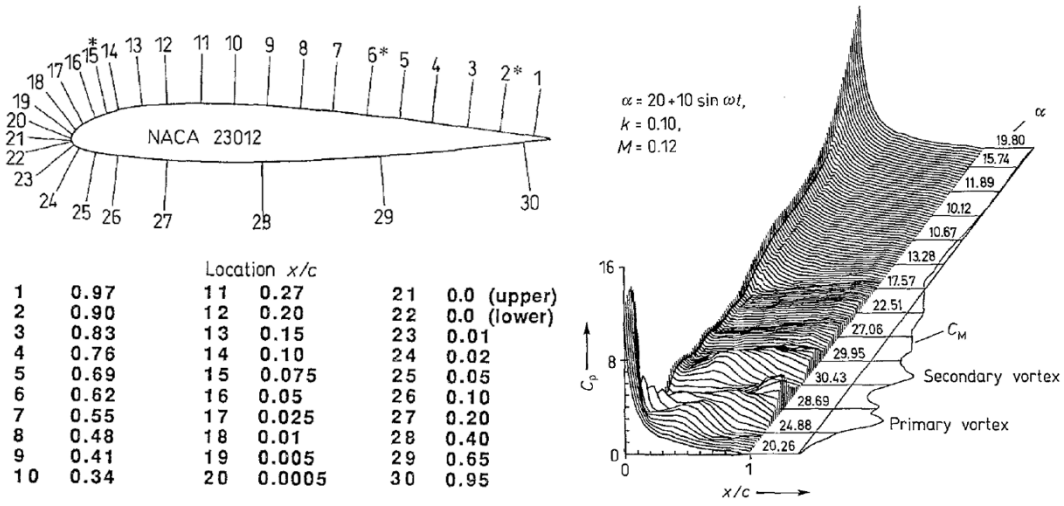

	Location x/c				
1	0.97	11	0.27	21	0.0 (upper)
2	0.90	12	0.20	22	0.0 (lower)
3	0.83	13	0.15	23	0.01
4	0.76	14	0.10	24	0.02
5	0.69	15	0.075	25	0.05
6	0.62	16	0.05	26	0.10
7	0.55	17	0.025	27	0.20
8	0.48	18	0.01	28	0.40
9	0.41	19	0.005	29	0.65
10	0.34	20	0.0005	30	0.95

Figure 2.10. Increased suction resulting from the pitch-up motion of a NACA 23012 airfoil indicating the influence of the leading-edge vortex on the overall airfoil pressure distribution (Image adapted from Leishman (1990)).

Figure 2.10 shows that for an angle of attack of $\alpha < 21°$, delayed stall leads to a dramatic increase in leading-edge suction. Pressure soon drops as a result of the onset of the leading-edge vortex growth between $\alpha = 22°$ and $\alpha = 24°$ and due to its convection over the airfoil chord. A secondary vortex is then observed to form and develop between $\alpha = 30°$ and $\alpha = 27°$ during the airfoil pitch-down process, as shown in Figure 2.10. These results indicate the interaction between the vortex dynamics and associated surface pressure on the airfoil, although only for shallow angles of attack, where $\alpha_{max} = 30°$, and

for reduced frequencies where $\kappa = 0.01$ through to $\kappa = 0.2$. Further conclusions about the extent of vortex interaction with the airfoil at higher angles of attack, and where the motion is of a constant pitch-rate type could not be drawn due to the limited surface pressure data.

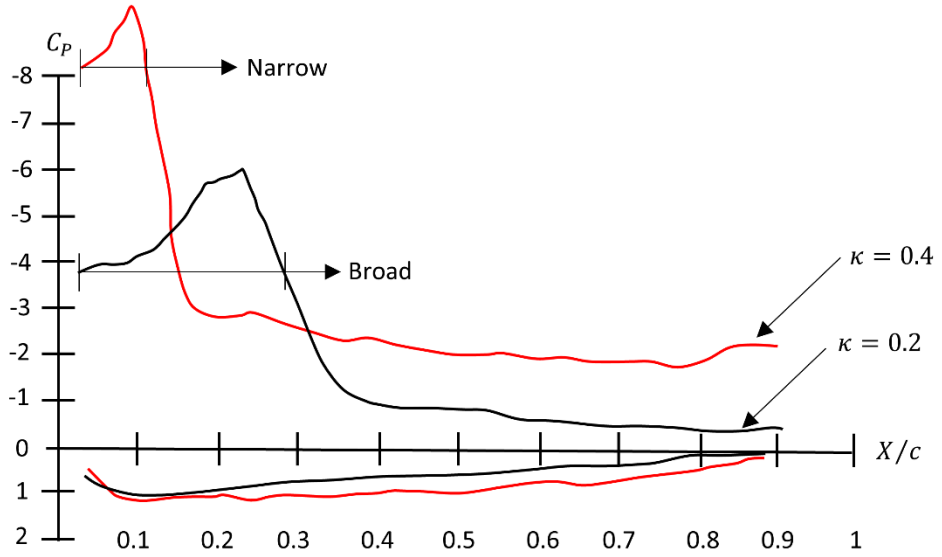

Figure 2.11. Variation in surface pressure at an angle of attack of $\alpha = 30°$, and with varying reduced frequency, indicating increased magnitude and narrowing of the peak suction due to increased rotation rate (Image adapted from Walker, Helin and Chou (1985)).

Results from experiments using constant-pitch-rate motion to a maximum angle of attack of $\alpha = 60°$ are presented in Walker, Helin and Chou (1985), which showed a significant increase in lift coefficient and delayed separation resulting from the increased rotation rate. Shown in Figure 2.11 are the surface pressure results for multiple rotation rates, and to a maximum angle of $\alpha = 30°$. Here, the effect of increased rotation rate is shown to

raise and narrow the peak suction pressure curve, focusing it further towards the leading edge of the airfoil.

Similar studies utilising surface pressure were discussed in Jumper, Dimmick and Allaire (1989) and Conger and Ramaprian (1994), where both articles investigated the surface pressure about a NACA 0015 airfoil undergoing constant-pitch-rate motion. Both studies showed that increasing the pitch rate increases the minimum pressure coefficient, and delays the collapse of the initial pressure peak, prior to dynamic-stall vortex formation, and until higher angles of attack (Conger and Ramaprian, 1994).

The application of surface-mounted pressure sensors has been successfully utilised for decades to identify different stages of flow development in the dynamic stall process. The measurement system is both simple to implement and install, whilst providing data that can be directly related to flow structure and forces developed on wings undergoing unsteady motions. Many of the previous studies have investigated dynamic stall behaviour using parameters defined by typical operating conditions of helicopters and wind turbines. However, this has somewhat limited the knowledge of the post-stall flow behaviour and the associated forces resulting from the dynamic stall process. Examples include a rotor blade exposed to significant gusts and variations in atmospheric turbulence, such as that experienced by wind turbines (Shipley, Miller and Robinson, 1995); and high speed helicopter rotors, where exposure to reversed flow conditions can occur (Raghav et al., 2014, Granlund, Ol and Jones, 2016, Hodara et al., 2016). Under such operating conditions, further analysis of the dynamic-stall process is required to increase knowledge of high angle-of-attack flows, deep-stalled flows and fully-separated flows resulting from dynamic stall.

2.3.4. Particle Image Velocimetry

The experimental techniques discussed above provide quantitative details of fluid properties including the velocity and pressure, which in turn can be resolved as force acting on a wing undergoing dynamic stall. Quite often these measurement techniques are performed independently, thus limiting *in-situ* data recording. Whilst traditional flow visualisation techniques provide overall flow structure development, and valuable representations of boundary layers flow and development, overall flow field velocity and pressure cannot be obtained. For this reason, the technique of PIV can be utilised as a means of non-intrusive flow measurement in order to deduce details including flow velocity, vorticity, circulation and pressure distribution within the flow field. Particle image velocimetry is an attractive flow measurement tool to analyse dynamic stall due to the unsteady motion and variability in operating conditions often replicated on wings during experimental processes.

A method of PIV analysis includes freely suspending small tracer particles in a fluid medium and shinning a high-intensity light sheet through the region of analysis. A digital camera can then be used to capture synchronised images of the tracer particles, and their movements as the flow develops. Individual interrogation windows within the images are then used to correlate the respective particle motion, leading to the determination of the local flow velocity of the fluid. Numerical schemes, correlation and interpretation methods, and limitations of each method are well documented (Lourenco, Krothapalli and Smith, 1989, Willert and Gharib, 1991, Westerweel, 1993, Prasad, 2000, Merzkirch, 2001, Adrian and Westerweel, 2011, Raffel et al., 2013). A simplified representation of the PIV test arrangement is shown in Figure 2.12 (Raffel et al., 2013).

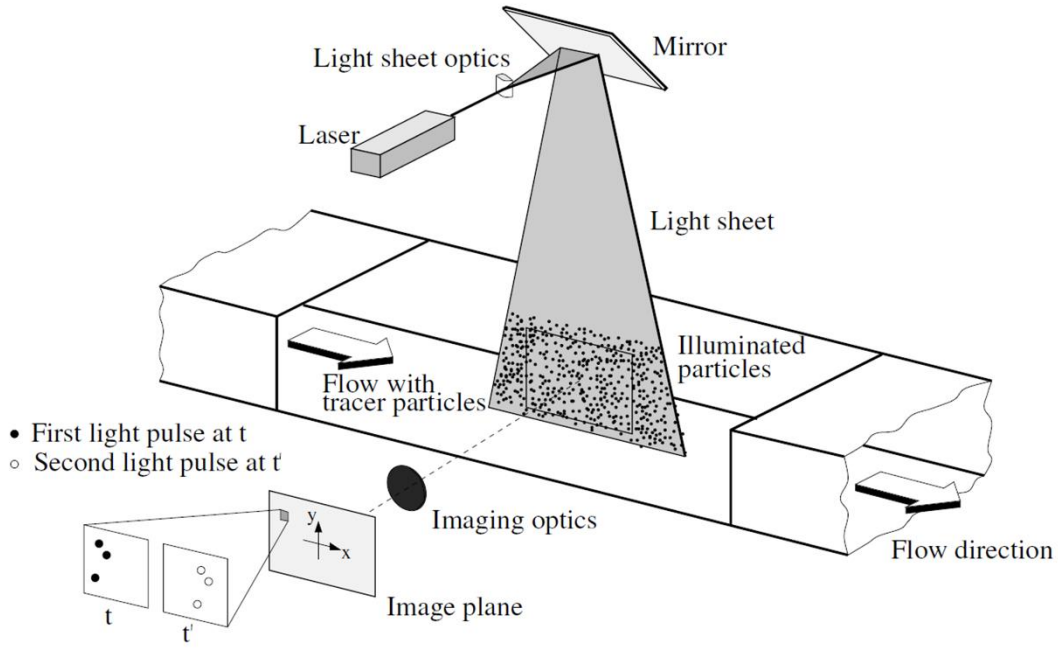

Figure 2.12. Diagram of the basic PIV experimental arrangement for external flow fields about pitching airfoils. (Image acquired from Raffel et al. (2013)).

The implementation of PIV, as a suitable flow measurement tool for rotor craft applications, was comprehensively reviewed and summarised in Raffel et al. (2017). Within the review, insight into methods of PIV analysis for dynamic stall on rotorcraft is presented. The advancement of the PIV concept, as an experimental flow measurement tool, has been shown to increase exponentially since its introduction into the field of unsteady aerodynamics. This indicates that both phase-averaged and time-averaged PIV can and will continue to be a significant tool for analysis of unsteady flow fields developed around airfoils exposed to unsteady motions.

Evaluation of the dynamic-stall flow field was initially identified in Shih et al. (1992) using PIV data from a water channel with $Re = 5000$. Details of the vortex formation stage, vortex convection, stall onset and shear layer properties at the leading edge were

investigated. Using a random walk scheme to process the PIV results, Shih et al. (1992) concluded that the vorticity encapsulated within the dynamic-stall vortex was predominantly generated at the leading edge. The dynamic-stall vortex origin is shown in Figure 2.13a, which displays the concentration of vorticity within the dynamic-stall vortex as a results of vorticity generated at the leading edge (Shih et al., 1992).

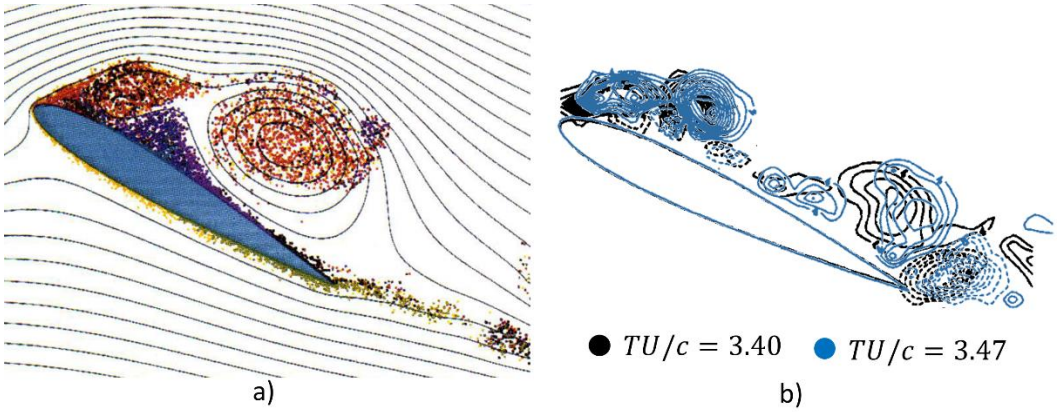

Figure 2.13. Dynamic-stall vortex origin denoted through colour-coded point vortices correlating to alternate regions on the airfoil surface (a), and superimposition of instantiations vorticity plots indicating the repeatability of ensemble-averaged PIV data (b) (Shih et al., 1992).

Shih et al. (1992) proposed that any manipulation of the dynamic-stall vortex should be performed immediately at the leading edge and not at locations below the vortex structure itself. Details for convection velocity and origins of the leading-edge vortex were also presented. In addition, Shih et al. (1992) discussed the repeatability of ensemble averaged PIV. Results from their experiments of instantaneous vorticity fields are superimposed in Figure 2.13b. These results showed similar vortex development and repeatability between test cases. In this study, minor variations between tests were

reported due to 'smearing' created by averaging techniques (Shih et al., 1992). Therefore, the authors proposed that analysis of small vortex structures using ensemble averaged PIV should be performed with care to avoid loss of detailed flow structure resolution.

Another study using PIV to evaluate the boundary layer separation process of a NACA 0015 airfoil undergoing constant-pitch-rate motion is presented in Lourenco et al. (1993), which utilised a similar approach to that presented in Shih et al. (1992). In this study, the effects of rotation rate and Reynolds number were investigated to identify their effect on the developed vortex structures. The dynamic stall process was shown to be insensitive to Reynolds number, with little change occurring to the dominant vortex structures formed during the pitch-up motion (Shih et al., 1992, Lourenco et al., 1993).

To further investigate the separation mechanisms resulting in leading edge separation, Shih, Lourenco and Krothapalli (1995) focused on the formation of both leading-edge and trailing-edge vortices using instantaneous PIV. The research showed that trailing edge flow had an indirect influence on the dynamic-stall process, with the vorticity generated at the trailing edge, prior to complete separation, affecting only the overall circulation. The authors also noted that the completion of the dynamic stall process occurred with the departure of the dynamic stall trailing-edge vortex, due to the presence and aft motion of the primary leading-edge vortex. Although this work provides significant detail with respect to the pitch-up motion of the wing body, a clear definition of the vortex separation mechanism and deep stall characteristics are not presented. The flow features leading to and occurring during separation of the leading-edge vortex still require further investigation. More specifically, knowledge pertaining to the vortex separation process, topological flow feature development and the resulting surface pressure and forces as a

consequence of the dynamic stall and post-stall process is lacking. As such, additional work is required to determine the influence of the dynamic stall and post-stall operating conditions on the fluid-structure interaction and aerodynamic properties of pitching airfoils.

Early research into dynamic stall using PIV was also described in Raffel and Kompenhans (1993), where difficulties performing high-speed PIV are presented for a case study of an oscillating NACA 0012 airfoil at $Re = 373{,}000$. High-speed flows were also investigated using PIV in Crisler (1994), where the effect of compressibility was investigated and shown to have a minor influence on dynamic stall development.

In a similar study, Raffel, Kompenhans and Wernert (1995) used PIV to investigate dynamic stall conditions using sinusoidal motion of a NACA 0012 airfoil in a wind tunnel with $Re = 373{,}000$ and $\kappa = 0.15$. Their work showed the development of the dynamic stall vortex and its associated flows for angles of attack specific to the operation of helicopters, where $\alpha(t) = 15° + 10° \sin(2\pi f t)$. Although overall flow structure development was shown, the research was primarily focused on indicating the limitations of the PIV and providing data for validation of numerical modelling schemes used to simulate dynamic stall. Due to the narrow angle of attack and range of rotation rates investigated, the knowledge of high angle of attack flows, and where the airfoil continues to proceed into deep-stall conditions, remains limited. Clearly research must be performed in deep-stall and post-stall stages of dynamic stall, to better understand how high angles of attack and high rotation rates influence the flow development and forces once the airfoil has completed the dynamic stall process.

Repeated tests using consistent operating conditions were applied using phase-averaged PIV to indicate the difficulties and precautions when determining point velocity measurements about an oscillating NACA0012 airfoil (Wernert et al., 1996, Wernert et al., 1997). The overall major flow field structures developing from the dynamic stall process were captured successfully using this technique.

Mulleners et al. (2009) used time-resolved PIV to develop vortex detection schemes and present details of the delay in boundary layer separation, dynamic-stall onset, and dynamic-stall vortex development for a OA-209 airfoil. However, the material presented was specific for helicopter applications where $Re = 9.2 \times 10^5$, $\kappa = 0.05, 0.075, 0.1$ (where $\kappa = \pi f c / U_\infty$) and to a maximum angle of attack, where $\alpha = 30°$. These conditions, alongside the surface pressure measurements, were also detailed in Mulleners and Raffel (2012) and Mulleners and Raffel (2013). In addition, the dynamic-stall development stage, based on shear layer reversal, is presented.

Development of the laminar separation bubble was presented in Nati et al. (2015) to address the gap in literature associating the behaviour of the laminar separation bubble with varying rotation rate. They utilised both planar PIV and topographic PIV to study the cross-sectional characteristics and three-dimensional flow structure of the laminar separation bubble forming on a SD-7003 airfoil. It was shown that airfoil rotation delayed the formation of the laminar separation bubble at a low angle of attack and during the pitch-up motion. However, rotation rate accelerated the formation of the laminar separation bubble during the pitch-down phase of the airfoil motion. Although providing significant detail on the laminar separation bubble characteristics during both pitch-up and pitch-down motions, the study did not include details of high angle of attack

variations in the laminar separation bubble, due to the shallow angles of attack ($\alpha = 8°$) presented. Therefore, research is required to extend the range of angles of attack to higher values where significant force fluctuation occurs.

Particle image velocimetry has been observed to perform well for studies involving unsteady aerodynamics. Repeatability of experiments is limited when using phase-averaged PIV as it may lead to increased velocity errors and 'smearing' of small-scale vortex structures developed during airfoil rotation. From the literature utilising PIV, a majority of the research has been completed to understand the unsteady separation process specific to normal operation of rotor blades on helicopters. For these cases, the angle of attack is relatively shallow and the motion type is sinusoidal in nature. There remains a large avenue for future research to utilise PIV to study dynamic stall on airfoils exposed to high angles of attack, where $\alpha > 30°$, and which continuing to operate in post-stalled conditions.

2.4. Control Mechanisms of Dynamic Stall

Control of unsteady separation is a major factor for the operation of helicopters and wind turbines. Increased fatigue, lower power generation and higher design and maintenance costs all result from the unsteady separation process developed during dynamic stall. For this purpose, awareness of suitable control devices specific to the operating conditions of rotor blades is critical for improved performance and operation of both helicopters and wind turbines. Methods of dynamic stall control have historically been developed on techniques devised for boundary layer control of steady-state flow, and include both passive flow control and active flow control systems. Reviews of boundary layer control

mechanisms for steady-state flows in Katz, Nishri and Wygnanski (1989) and Lachmann (2014) provide details of boundary layer control devices for both turbulent and laminar flows, whilst reviews in (Yu et al., 1995) and Choudhry et al. (2014) highlight the state of the art in terms of dynamic stall flow control using both passive and active devices.

2.4.1. Passive Control

Passive control techniques use devices that are fixed to the surface of a wing to control boundary layer formation and flow separation, without the addition of momentum from alternative sources to sustain attached flow during normal operating conditions. Although passive control methods offer low-maintenance and cost-effective application, they may be limited in their effectiveness outside of specified operating conditions. Examples utilised for passive control of both steady-state and unsteady operation include the use of leading-edge vortex and perturbation generators, tubercles, cavities, leading-edge trip wires, slats and flaps. All of these techniques rely on their ability to lower and redistribute vorticity and momentum within the boundary layer to sustain flow attachment to higher angles of attack.

Mai et al. (2008) utilised vortex generators, in the form of circular cylinders, mounted to the lower surface of the leading edge, and in close proximity to the stagnation point. The vortex generators were used to decrease the momentum of the dynamic-stall vortex via increased boundary mixing during leading-edge vortex development. In their study, they showed that the dynamic-stall drag could be reduced during dynamic-stall vortex growth, whilst maintaining similar lift to that of a clean airfoil not fitted with vortex generators. This was achieved whilst maintaining similar steady-state performance between the clean

airfoil and the one fitted with the vortex generators. Similar experiments using comparable vortex generators were presented in Geissler, Dietz and Mai (2005) and Heine et al. (2013), who also found positive benefits using vortex generators placed on the lower leading edge.

Under steady-state conditions, modifications to the leading-edge geometry of wings using tubercles (Fish et al., 2011, Hansen, Kelso and Dally, 2011, New, Wei and Cui, 2016) and leading-edge undulations (Rostamzadeh et al., 2013) were shown to provide benefits of delayed separation and reduced drag at elevated angles of attack during steady-state operation. Tubercles and leading-edge undulations utilise chord-wise vortices to introduce momentum into the boundary layer, thus assisting with delayed transition and separation. Investigations of the effectiveness of tubercles under dynamic stall conditions, in Hrynuk (2015), resulted in a greater attenuation of the dynamic-stall process at low angles of attack. However, no significant control of the dynamic-stall vortex was gained at elevated angles of attack and for high rotation rates. Current methods of control are beneficial for the delay of boundary layer separation at low angles of attack and with low rotation-rate airfoils motions. There remains a gap in literature that focuses on effective boundary layer control of airfoils during extreme angles of attack and high rotation rate operation.

Other passive control devices including high-lift devices such as leading-edge slats and trailing-edge flaps have been shown to significantly reduce dynamic stall occurrence and formation of the leading-edge vortex (McAlister and Tung, 1993, Carr et al., 2001, Joo et al., 2006). Figure 2.14 shows the effects of a leading-edge slat fitted to a VR-7 airfoil. The

results indicated that the effects of dynamic stall were eliminated due to the ability of the slat to suppress the formation of the leading-edge vortex (Carr and McAlister, 1983).

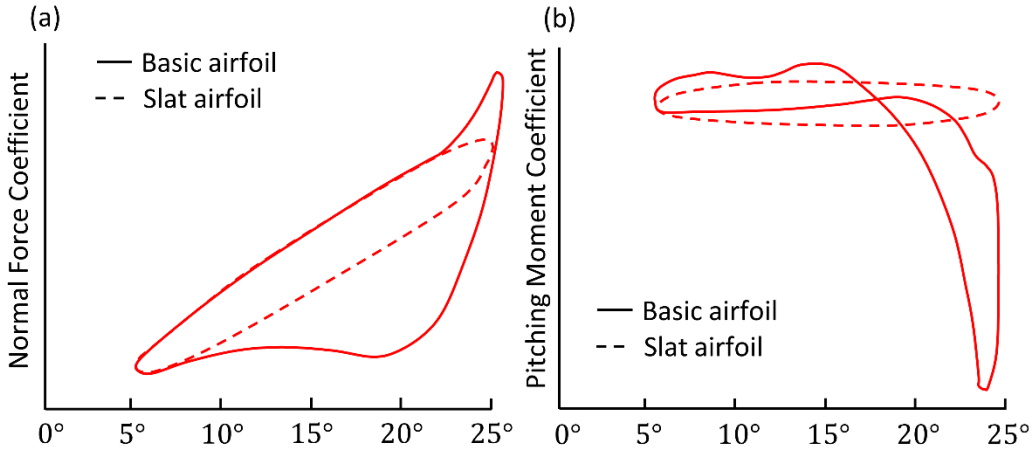

Figure 2.14. Normal force coefficient (a) and pitching moment coefficient (b) generated by a VR-7 airfoil undergoing dynamic stall, with and without the installation of a leading-edge slat (Carr and McAlister, 1983).

The addition of the leading-edge slat resulted in reducing peak lift at the airfoil maximum angle of attack and prior to stall, whilst also reducing significant moment fluctuation at operating angles of attack. However, limitations in boundary layer control systems for dynamic stall exist, due to the mechanical limitations and difficulties in their installation. This has restricted the application of some boundary layer control methods of blades for rotary machine applications (Geissler et al., 2005).

The use of leading-edge trip wires to control dynamic stall was presented in Choudhry, Arjomandi and Kelso (2016). Trip wires were fitted to a wing with a NACA 0021 airfoil profile at multiple fixed displacements from the leading edge, in order to breakdown and dissipate the momentum transferred into the leading-edge vortex through the generation

of span-wise vorticity. Their results showed improvements in stall intensity and post-stall aerodynamics, however the reduced frequency was specific to a quasi-steady operation. Further investigations must be undertaken to confirm the suitability of the trip wire as a means of passive control during unsteady rotation, and to develop a cost function to assess the feasibility of applying the trip wire to current wind turbines.

2.4.2. Active Control

Active control systems require complex feedback devices to monitor and apply suitable responses to behaviour and variations in the boundary layer. A recent active control system for dynamic stall boundary layer separation control includes the utilisation of plasma actuators (Post and Corke, 2006, Lombardi, Bowles and Corke, 2013, Greenblatt, Ben-Harav and Mueller-Vahl, 2014). More traditional methods include adaptive geometry (Yu et al., 1995, Chandrasekhara, Wilder and Carr, 1998b, Chandrasekhara, Martin and Tung, 2004, Feszty, Gillies and Vezza, 2004, Geissler et al., 2004, Lee and Gerontakos, 2006, Kerho, 2007), boundary layer suction (Karim and Acharya, 1994, Alrefai and Acharya, 1996), boundary layer blowing (Weaver, McAlister and Tso, 1996, Sun and Sheikh, 1999, Weaver, McAlister and Tso, 2004, Singh et al., 2006, Müller-Vahl et al., 2014, Müller-Vahl et al., 2016), and periodic excitation of the boundary layer (Yu et al., 1995, Magill and McManus, 1998, Greenblatt et al., 2001, Greenblatt and Wygnanski, 2001, Greenblatt and Wygnanski, 2002, Gardner, Richter and Rosemann, 2011).

Plasma actuators function by inducing external flow into the boundary layer through high voltage ionisation of air near to the surface of the wing. A simplified diagram showing the plasma actuation arrangement is presented in Figure 2.15.

Through activation of the plasma actuator, the region of induced flow can be used to introduce momentum into the boundary layer at the surface. This is beneficial for boundary layer separation control and transition delay. Under dynamic stall, significant reverse flow exists during the formation and development of the leading-edge vortex.

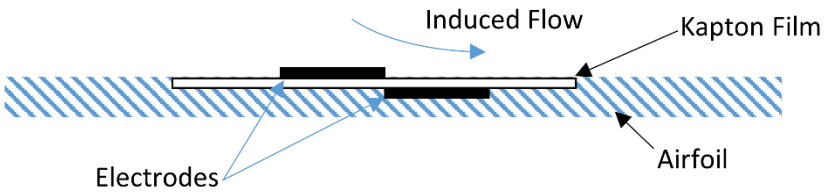

Figure 2.15. Diagram describing the plasma actuator arrangement and induced flow effect created through ionisation of the surrounding air (Post and Corke, 2004).

Placement of the plasma actuator at the location susceptible to flow reversal can potentially assist with delaying separation through local entrainment of flow. Post and Corke (2006) utilise plasma actuators fixed at the leading edge to increase lift and improve cyclic hysteresis of the lift during dynamic stall for a quasi-steady reduced frequency of $\kappa = 0.08$. Additionally, results in Post and Corke (2006) indicated sustained flow attachment and a decreased leading-edge vortex size with the use of plasma actuators. These findings were later confirmed by Lombardi, Bowles and Corke (2013), who also demonstrated complete flow attachment using plasma actuators, for $\kappa = 0.08$, where $\kappa = \omega c/U_{\infty}$. This is shown in Figure 2.16 which compares both control-off and control-on states of a NACA 0015 airfoil undergoing dynamic stall. As indicated in Figure 2.16c and Figure 2.16d, complete recovery of the boundary layer can be achieved through induced flow entrainment generated via activation of the plasma actuator. Without boundary layer control, the flow is seen to separate (Figure 2.16a and Figure 2.16b)

leading to fully-stalled conditions. Although the plasma actuation method shows positive outcomes with respect to controlling boundary layer separation and leading-edge vortex development, research into its effect on the aerodynamic force at unsteady reduced frequencies ($\kappa > 0.1$) and at high angles of attack ($\alpha > 30°$) remains limited. Future work needs to be completed to assess the effectiveness of the actuators as a boundary layer control method under highly unsteady flow conditions.

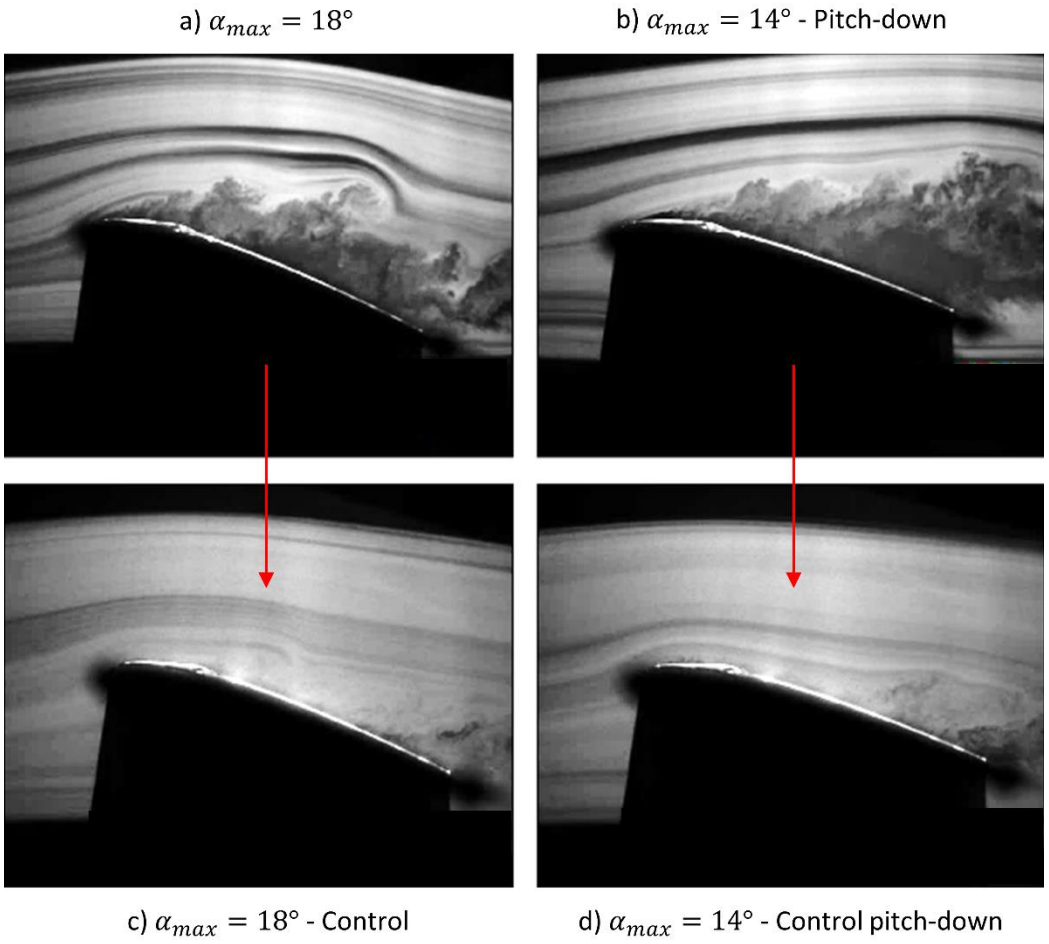

Figure 2.16. Flow visualisation of a NACA 0015 airfoil (a and b) without flow control and (c and d) using plasma actuation for control and reattachment of the boundary layer during dynamic stall (Lombardi, Bowles and Corke, 2013).

Adaptive airfoil geometry has also been shown to improve the performance and reduce the force fluctuations of airfoils undergoing dynamic stall. To overcome dynamic stall developed through increased acceleration and subsequent deceleration of flow at the leading edge, Chandrasekhara, Wilder and Carr (1998b) proposed to modify the leading edge radius and curvature through adaptive changes to the airfoil chord during the pitch-up motion. Although the maximum angle of attack was $\alpha = 20°$, it was reported that a complete elimination of the leading-edge vortex was possible.

A variable-droop leading edge was later used in Chandrasekhara, Martin and Tung (2004) to eliminate dynamic stall of an airfoil in compressible flow. By drooping the leading edge, Chandrasekhara, Martin and Tung (2004) were able to reduce the adverse pressure gradient and suction pressure at the leading edge of the drooped airfoil, thus lowering the force fluctuation generated by dynamic stall. Variations in upper surface pressure distributions between a standard VR-12 airfoil and a VR-12 airfoil adapted with leading-edge droop is shown in Figure 2.17.

In a similar study, Geissler et al. (2004) utilised a variable-droop leading edge to increase the maximum angle of attack at which maximum lift was obtained for a DLR-A1510 airfoil exposed to dynamic stall conditions. The resulting increase in lift can be attributed to an increase in camber, thus reducing the susceptibility of flow separation at high angles of attack. These findings were also observed in Kerho (2007) where the maximum lift was increased by 9% and stall delayed by $\alpha = 2.5°$, when comparing a SSC-A09 airfoil and a variable-camber SSC-A09 airfoil at $Re = 4.25 \times 10^6$ and $\kappa = 0.075$. The influence of increasing camber, during the pitch-up motion, resulted in removal of high pressure gradients, resulting in shock induced separation, at the leading edge. This allowed for the

development of trailing-edge separation and late formation of the leading-edge vortex (Kerho, 2007).

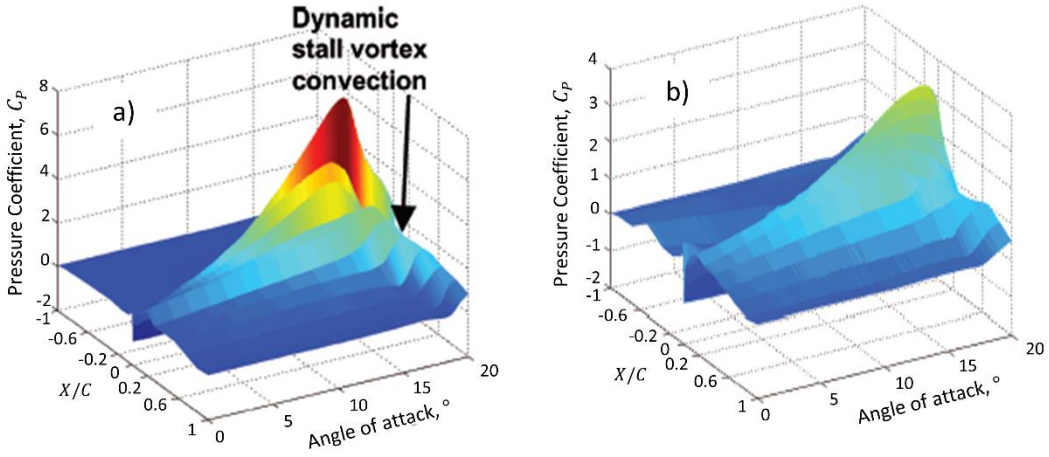

Figure 2.17. Variation in surface pressure distribution between (a) a VR-12 airfoil and (b) an VR-12 airfoil adapted with leading edge droop. Note that maximum suction is reduced due to increased leading-edge droop (Chandrasekhara, Martin and Tung, 2004).

Other methods of adaptive control include blowing, suction and periodic excitation of the boundary layer. These methods all use a similar concept to either remove or add fluid to a low momentum region of the boundary layer in order to prevent early flow separation (Sun and Sheikh, 1999). Using numerical modelling, Sun and Sheikh (1999) were able to reduce the lift, drag and pitching moment through the application of tangential blowing at multiple locations from the leading edge. The effects of tangential blowing on the aerodynamic load generation are presented in Figure 2.18 which shows reduced lift and drag as a result of increasing jet momentum coefficient, C_μ, indicating an addition of boundary layer momentum and reduced flow separation. From Figure 2.18, by increasing the jet momentum coefficient, an increased control of the separation process was demonstrated for $\kappa = 0.25$, and for $Re = 10^6$. This led to delayed separation at the

leading edge, whilst in turn delaying the formation of the dynamic-stall vortex to higher angles of attack (Sun and Sheikh, 1999). The addition of blowing significantly reduced the load hysteresis of both lift and drag indicating that control through the means of steady blowing can successfully be used for dynamic stall control.

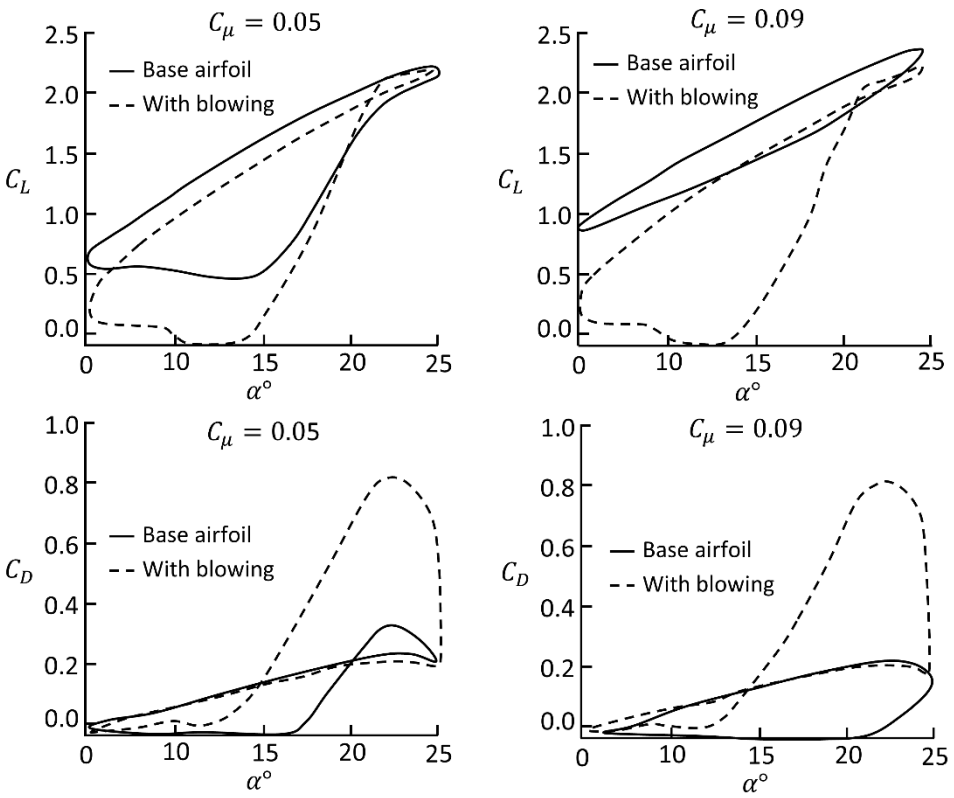

Figure 2.18. Lift and drag coefficient of a standard NACA 0012 airfoil and a NACA 0012 airfoil with steady leading-edge blowing showing reduced lift hysteresis and decreased drag fluctuation with increased jet momentum coefficient (Sun and Sheikh, 1999).

McCloud, Hall and Brady (1960) demonstrated the ability to delay retreating blade stall on full-scale helicopter blades through careful placement of tangential jets located near the leading edge. However, the effect was less successful as the jets were moved aft of the leading edge, to a location positioned at $x/c = 0.4$. The effect of jet momentum

strength for the control of boundary layer separation on a thick NACA 0018 airfoil undergoing sinusoidal motion with $\kappa = 0.074$, and for a Reynolds number ranging from $Re = 1.25 \times 10^5$ to $Re = 5 \times 10^5$, was discussed in Müller-Vahl et al. (2014) and Müller-Vahl et al. (2016). In both studies, a jet located near to the leading edge, where $x/c = 0.05$, was shown to promote early separation using a low-momentum jet injection. Conversely, control of flow separation and elimination of the formation of the leading-edge vortex was achieved using a high momentum jet.

In a similar manner to boundary layer jet blowing, which introduces momentum into the boundary layer, the use of suction removes low momentum fluid for flow control on pitching airfoils. Limiting the build-up of low momentum and reversed flow fluid within the shear layer during the pitch-up motion was the basis of work in Karim and Acharya (1994). Karim and Acharya (1994) utilised five suction ports within a NACA0012 airfoil to completely suppress the leading-edge vortex. The influence of the rotation rate, angle of attack and Reynolds number were all shown to vary the suction rate required to sustain attached boundary layer conditions. Likewise, higher lift and delayed stall were also reported in Alrefai and Acharya (1996), who used leading-edge suction to determine the required flow rate to completely suppress the leading-edge vortex, delay detachment of the vortex and maximise lift on a NACA 0012. Figure 2.19 presents the lift coefficient results obtained by Alrefai and Acharya (1996), where multiple suction flow rates were utilised to increase maximum lift and delay airfoil stall to elevated angles of attack. Their results showed that suction applied on the upper surface inhibited the formation of the dynamic-stall vortex. However, the suction rate of the actuators was shown to be dependent on the airfoil angle of attack and rotation rate (Alrefai and Acharya, 1996).

From Figure 2.19, it is clear that significant gains in aerodynamic load generation can be obtained, and stall behaviour manipulated through the use of both suction and blowing mechanisms. However, as stated in Alrefai and Acharya (1996), the sensitivity of the suction flow rate was only specific to the operating conditions applied in their investigation.

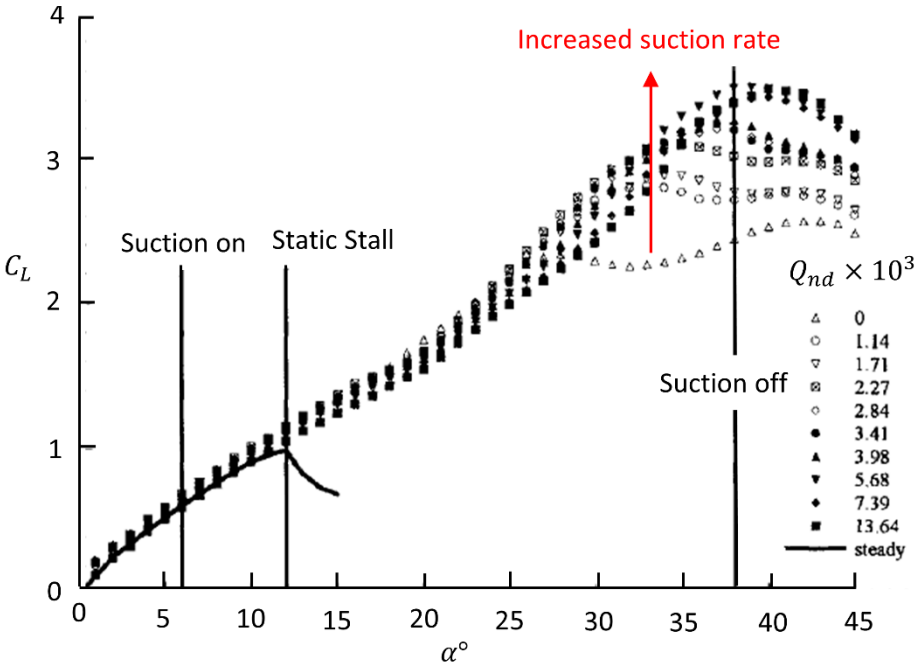

Figure 2.19. Effect of increasing leading edge suction rate, Q_{nd}, on the maximum lift and stall angle of attack for a NACA 0012 airfoil undergoing constant-pitch-rate motion, and with $\kappa = 0.075$ (Alrefai and Acharya, 1996).

The feasibility of both boundary layer injection and suction for active control in highly unsteady flow and at extreme angles of attack remains a topic for future investigation. For this reason, it is recommended to further investigate boundary layer control using suction and blowing under highly unsteady operating conditions, similar to that experienced on horizontal-axis wind turbines during extreme weather conditions. A

summary of the methods of dynamic stall control are presented in Table 1. Both passive and active control methods are presented alongside each respective investigator.

Table 1: Summary of passive and active dynamic stall control methods.

Control Type	Method of control	Article
Passive	Vortex Generator	Mai et al. (2008)
		Geissler, Dietz and Mai (2005)
		Heine et al. (2013)
	Tubercles	Fish et al. (2011)
		Hansen, Kelso and Dally (2011)
		Hrynuk (2015)
		New, Wei and Cui (2016)
	Leading-edge Undulations	Rostamzadeh et al. (2013)
	Leading- and Trailing-edge Slat	Carr and McAlister (1983)
		McAlister and Tung (1993)
		Carr et al. (2001)
		Geissler et al. (2005)
		Joo et al. (2006)
	Leading-edge Trip Wire	Choudhry, Arjomandi and Kelso (2016)
		Chapter 5
Active	Plasma Actuators	Post and Corke (2006)
		Lombardi, Bowles and Corke (2013)
		Greenblatt, Ben-Harav and Mueller-Vahl (2014)
	Adaptive Geometry	Yu et al. (1995)
		Chandrasekhara, Wilder and Carr (1998b)
		Chandrasekhara, Martin and Tung (2004)
		Feszty, Gillies and Vezza (2004)
		Geissler et al. (2004)
		Lee and Gerontakos (2006)
		Kerho (2007)
	Boundary Layer Suction	Karim and Acharya (1994)
		Alrefai and Acharya (1996)
	Boundary Layer Blowing	McCloud, Hall and Brady (1960)
		Weaver, McAlister and Tso (1996)
		Sun and Sheikh (1999)
		Weaver, McAlister and Tso (2004)
		Singh et al. (2006)
		Müller-Vahl et al. (2014)
		Müller-Vahl et al. (2016)
	Periodic Boundary Layer Excitation	(Yu et al., 1995,
		Magill and McManus (1998)
		Greenblatt et al. (2001)
		Greenblatt and Wygnanski (2001)
		Greenblatt and Wygnanski (2002)
		Gardner, Richter and Rosemann (2011)

2.5. Dynamic Stall on Pitching Plates

Using pitching flat plates, the underlying mechanism of lift generation and flow structure developed during dynamic stall can be evaluated. With regards to the control of the dynamic stall process, it is necessary to develop knowledge of the stall process to allow more efficient means of flow control to be developed and implemented. By utilising flat plates, elimination of geometric effects associated with airfoils (and the associated variable pressure gradients) is possible (Widmann and Tropea, 2017). The following section reviews literature that focuses on the study of dynamic stall applied to pitching flat plates, in order to increase knowledge of the topological flow structure and load developed as a result of unsteady separation.

Flat plate aerodynamics has often been investigated for its application on birds, bats and insects. All of these natural flyers utilise the unsteady processes to create sufficient lift to sustain flight, increase manoeuvrability and perform flight techniques such as perching. In recent years, the development of micro-aerial vehicles have led to deeper investigations of flapping flight. Interaction of separation bubbles and vortex structures formed through the unsteady separation process allows for periods of enhanced lift required to sustain flight (Ellington, 1984, Sane, 2003, Shyy et al., 2007). Flat plates have been shown (Pelletier and Mueller, 2000) to provide an increased aerodynamic efficiency over thicker airfoil geometries at low Reynolds numbers. Flat plates can also be utilised in unsteady environments where generation of the leading-edge vortex can be utilised for enhanced lift to higher angles of attack.

Using PIV and force measurements in a water channel with $Re = 10{,}000$, Rival et al. (2013) showed the lift development and its variation with time for four dissimilar leading edge and trailing edge configurations. Furthermore, the study made comparisons to a NACA 0012 airfoil undergoing similar pure-plunge motion. The shapes of the leading edge and trailing edge included sharp, blunt, round and ramp geometries. The flow structure developed for each leading edge and trailing edge configuration was shown to be similar between all four cases. However, variation in leading edge geometry was shown to influence the delay in leading-edge vortex development. In a similar study, using a flat plate with a sharp leading edge and near constant-pitch-rate motion, Widmann and Tropea (2017) discussed the variation in shear layer thickness and its role in feeding the leading-edge vortex for $Re = 10{,}000$ to $Re = 80{,}000$ and for $\kappa = \pi cf/U_\infty = 0.25$. The changes in shear layer thickness were linked to variations in Reynolds number, where decreasing Reynolds number generated thicker shear layers.

A major review of flat plate aerodynamics is presented in North Atlantic Treaty Organization (2016), where a parametric evaluation of flat plate motion type, Reynolds number and reduced frequency were presented, using direct force measurements and PIV from multiple independent experimental facilities. In this study, the effects of Reynolds number on the lift coefficient were found to be minimal for Reynolds numbers between $Re = 500$ and $Re = 10{,}000$. However, at low Reynolds numbers, the effects of increased skin friction becomes a dominant factor in varying the drag properties of the plate. As such, changes in drag become more significant in low Reynolds number operating conditions. It was found that increasing the rotation rate increases the lift well beyond steady-state values until rotation is ceased. Increasing the rotation rate also introduces a non-circulatory ‘bump’ in the lift curve, which is not present in the low

reduced-frequency cases. Additionally, performance parameters including motion type and amplitude, Reynolds number and reduced frequency were evaluated using a SD-7003 airfoil (Granlund et al., 2010) and a flat plate (Baik et al., 2012, Granlund, Ol and Bernal, 2013, Jones et al., 2016) undergoing unsteady motion to show the resulting variation in lift, drag and flow structure with respect to each performance parameter. In these studies, and similarly in the studies by North Atlantic Treaty Organization (2016), the effects of Reynolds number were shown to be insignificant for Reynolds numbers between 5,000 and 25,000. The rotation rate significantly increases the peak lift during rotation and is therefore shown to be the major parameter governing flow development.

The effect of pivot location on the resulting inertial forces and flow structure was explored in Yu and Bernal (2013) and Yu (2014), where PIV and force measurements were correlated to evaluate the inertial load generated as a result of pitching at reduced frequencies of $\kappa = 0.022$ through to $\kappa = 0.394$. It was shown that a leading-edge pivot point generated a greater normal force coefficient. The normal force coefficient subsequently decreased when the pivot location moved towards the trailing edge. Similarly, Stevens and Babinsky (2017) provide experimental data to show the influence of rotation on inertial flows and leading-edge vortex circulation. The study concluded that the effect of pivot location, in this case positioned at the leading edge and the mid-chord, generated similar convection velocities, where $U_{conv} = 0.5\ m/s$ and $U_{conv} = 0.6\ m/s$ for the leading and mid-chord pitch locations respectively. Furthermore, the mid-chord pivot location was demonstrated to generate several additional trailing-edge vortices when compared to the leading edge pivot location. Although these studies are beneficial in increasing the knowledge of force development of a flat plate exposed to unsteady

motion types, little detail is provided on the control and interaction of critical topological flow features developed during progression of the dynamic stall process.

Using time-resolved PIV, Buchner and Soria (2015) provided details of the vortex development process of a pure-pitch-motion flat plate for $Re = 1500$ to $Re = 10{,}000$ and for a highly unsteady rotation rate where $\kappa = 0.7$. They showed that the leading-edge vortex grew from the merging of multiple smaller coherent vortex structures developed within the shear layer at the leading edge. This is demonstrated in Figure 2.20, which shows the mean and fluctuating vorticity of the leading-edge vortex as a result of the smaller vortex structures.

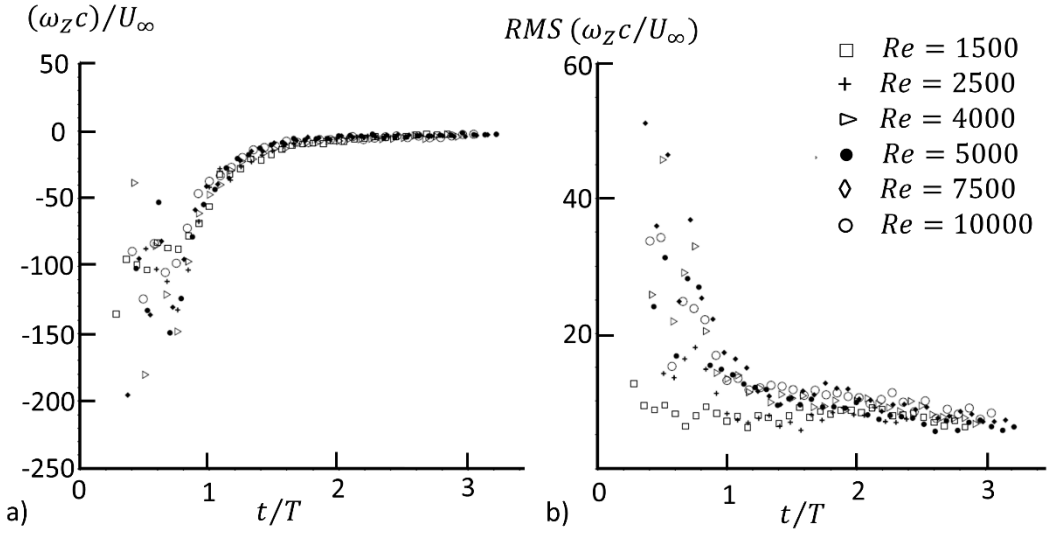

Figure 2.20. Mean normalised vorticity (a) and RMS fluctuation (b) in vorticity of a pitching flat plate indicating the influence of Reynolds number on the development of the leading-edge vortex (Buchner and Soria, 2015).

In their study, the time scale of the leading-edge vortex is shown to be similar for all Reynolds numbers evaluated. However, during the pitch-up process, significant scatter in

the leading-edge vortex vorticity is presented and characterised by the ongoing vorticity shedding and merging process at the leading-edge vortex.

In a similar study evaluating the effect of Reynolds number on the vortex development process of a flat plate, Garmann and Visbal (2011) concluded that increasing the Reynolds number resulted in many more discrete vortex structures emanating from the leading edge and trailing edge of the flat plate. Results from their numerical simulations for $Re = 5{,}000$ to $Re = 40{,}000$ and for a pitch rate of $\kappa = 0.4$ are shown in Figure 2.21.

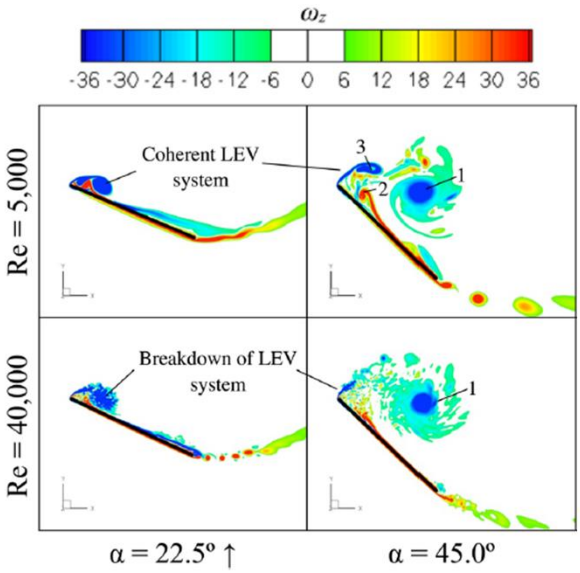

Figure 2.21. Vorticity contours of a pitching flat plate indicating the effect of increasing the Reynolds number on the vortex shedding frequency at the leading edge and trailing edge (Image adapted from Garmann and Visbal (2011)).

This figure shows the vorticity contours about a flat plate undergoing pitch-up motion. It is clear from the vorticity contours that increasing the Reynolds number promotes increased vortex production at the leading edge and the trailing edge. Similar observations of increased vortex shedding with an increase in Reynolds number, were

also provided in Buchner and Soria (2015). The results showing the formation and interaction of vortex structures are critical for the development of understanding of the lift generation process of the flat plate. However, for the control of the vortex, a gap in literature remains regarding on the identification and tracking of the movement of the leading-edge vortex with time. Further details of topological flow features distinguishing the leading-edge vortex are required in order to identify the vortex motion, for control purposes, whilst it remains over the upper surface of the flat plate.

A study to evaluate the motion of the leading-edge and trailing-edge vortex as a result of unsteady separation over a flat plate was presented in Rival, Prangemeier and Tropea (2009). However, only the displacement and velocity were reported for the respective vortex cores. No information was provided with respect to the pressure variations on the upper surface of the plate, as a result of the vortex-wall interaction. The convection rate of the leading-edge vortex and the trailing-edge vortex were established to be $0.5U_\infty$ and $0.6U_\infty$ for leading-edge and mid-chord pivot points respectively (Stevens and Babinsky, 2017). These convection velocities however, cannot be utilised for the identification of critical features on the surface of the plate for boundary layer control purposes. A study which utilises topological flow features was presented in Rival et al. (2013). Within this investigation, PIV was utilised to determine the relative velocity and vorticity profiles of the unsteady flow field surrounding a flat plate undergoing pure-plunge motion. Their results define a half-saddle point bounded to the upper surface of the pitching plate, and which also coexists at the bifurcation between forward and reverse flow located on the rear of the leading-edge vortex as shown in Figure 2.22. Movement of this half-saddle location into the wake via the 'lift-off' process was defined as the critical transition point leading to development of fully separated flows (Perry and Fairlie, 1975, Perry and

Steiner, 1987, Rival et al., 2013). It is also notable that a definition of the leading-edge vortex growth was suggested in Widmann and Tropea (2017) using similar notation and representation of the half-saddle point.

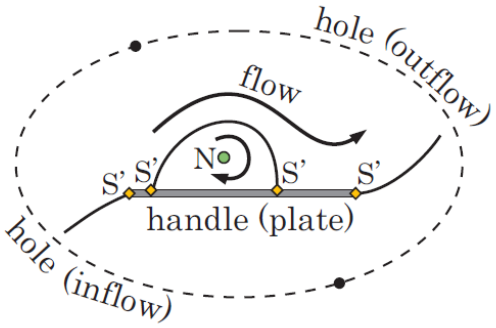

Figure 2.22. Definition of the half-saddle forming aft of the leading-edge vortex at the bifurcation between forward and reverse flow on the upper surface of the pitching plate (Rival et al., 2013).

Past literature has provided a wealth of information with respect to the lift and drag associated with vortex-induced lift developed on pitching plates. Furthermore, performance parameters such as reduced frequency, Reynolds number, pitch-axis location and pitching motion have all been heavily analysed for their impact on the dynamic-stall process. In addition, methods of quantifying the process of leading-edge vortex separation has been presented through investigations studying the process of dynamic stall.

A possibility for active boundary layer control includes sensing the location of the half-saddle point, through the use of internal pressure sensors, to provide suction or blowing in order to control the formation of the leading-edge vortex. A gap in literature exists

since minimal data is available for use of tracking and positioning the location of the half-saddle point on the upper surface of a flat plate during pitch-up motions. Moreover, the variation and rate of movement of the half-saddle point location with respect to performance parameters has not been documented. For this reason, further research must be undertaken in order to fully comprehend the relationship between the half-saddle point location and the overall flow structure and lift. This will allow more efficient application of active control boundary layer devices on both flat plates and airfoils subject to unsteady separation.

2.6. Summary of Literature and Research Still Required

Rotary machines operate in severe environments that place the blades in unsteady conditions allowing for the development of dynamic stall. This leads to an increase in force and power fluctuation, whilst decreasing material lifetime. A challenge currently facing designers of rotary machine components is having adequate knowledge to design and predict the onset and aerodynamic characteristics of the unsteady separation process. Current literature focuses on the operation of helicopter and wind turbine blades typically operating at angles of attack of $\alpha < 30°$, and where the motion type is sinusoidal about a mean angle of attack. For a wind turbine, such conditions may lead to false evaluation of force in situations where the blade is exposed to an extreme and prolonged gust or weather event. Under these conditions, the unsteady motion of the blade can be characterised using constant-pitch-rate conditions.

Furthermore, operation in post-dynamic stall conditions, where the angle of attack is held fixed at the maximum angle of attack to enable post-stall flow conditions, is critical for

the understanding of post-stall flow behaviour resulting from significant wind shear and gust-like operating conditions.

Although significant research has been completed with respect to dynamic stall, there remains a gap in knowledge specifically relating to the understanding of vortex generation and fluid-structure interaction leading to force fluctuations on airfoils operating in highly unsteady flow conditions where unsteady constant-pitch-rate dynamic stall at extreme angles of attack occur. Furthermore, there is a lack of information detailing the process of separation and development of vortex structures in high-rotation-rate operating conditions. This may lead to the under-prediction of force development on rotary machine blades. For this reason, there remains a scope to further investigate and compare multiple airfoil geometries operating in conditions, where accelerated flow conditions become a dominant factor in the overall force generation. Understanding the flow structure behaviour in high angle of attack, high rotation-rate motions and during post stall can ultimately lead to improved methods of boundary layer control. This may reduce and mitigate machine vibration, increase material life cycles, lower the overall cost and improve the machine efficiency.

In order to control the dynamic-stall process, researchers have applied multiple methods of active and passive control systems that have been applied in steady-state conditions. Examples of such control devices include turbulence generators, tubercle leading-edge modifications, undulating leading edges, addition of flaps and slats, active blowing and suction and more recently the application of plasma actuators. Literature has shown significant benefits towards the control of dynamic stall at quasi-steady reduced frequencies and moderate angles of attack. However, there remains a large gap in the

literature regarding the control of dynamic stall under unsteady operating conditions. Moreover, the effectiveness of applying leading-edge trip wires to airfoils operating in highly unsteady conditions remains unknown.

To further apply active control methods, and to increase their effectiveness, details of the pressure field and critical flow features developed during unsteady operation must be understood. By using flat plates, effects of airfoil geometry can be omitted to allow the flow separation to develop immediately at the leading edge. Literature using flat plates for the study of dynamic stall sheds light on the dynamic stall process and critical topological flow features, such as the half-saddle located aft of the leading-edge vortex. The importance of understanding such critical flow features has also been discussed for applications of boundary layer control. Nonetheless, from the current literature review, there remains a gap in knowledge regarding the development and progression of the half-saddle point from the leading edge rearwards toward the trailing edge. By better knowing the motion characteristics of the half-saddle point, more selective and efficient control methods can be adapted to either inhibit vortex formation or control its growth to achieve specific load characteristics.

2.7. Summary of Performance Parameters and Investigation Type

The following section summarises the performance parameters associated with dynamic stall from historical experimental and numerical investigations. Performance parameters include the reduced frequency, Reynolds number, pivot location (x_P), airfoil geometry and the operating angle of attack. The results of the summary combined with the parameters of the current thesis are shown in Table 2.

Table 2: Performance parameters and investigation type associated with the study of dynamic stall.

Article	Method	Re	$\kappa\ (\omega C/2U_\infty)$	x_P/c	Airfoil	$\alpha°$
Acharya and Metwally (1992)	Experimental	$8.8 \times 10^4 \rightarrow 1.2 \times 10^5$	$0.018 \rightarrow 0.385$	0.25	NACA 0012	$0 \rightarrow 40$
Albertson et al. (1987)	Experimental	6.35×10^4	$0.05 \rightarrow 0.1$	0.25	NACA 0015	$0 \rightarrow 60$
Amiralaei, Alighanbari and Hashemi (2010)	Numerical	$0.5 \times 10^3 \rightarrow 5 \times 10^3$	$0.05 \rightarrow 0.125$	0.50	NACA 0012	$-10 \rightarrow 10$
Baik et al. (2012)	Experimental	$5 \times 10^3 \rightarrow 2 \times 10^4$	$0.314 \rightarrow 1$	0.25	Flat Plate	$-6 \rightarrow 22$
Buchner, Honnery and Soria (2017)	Experimental	$1 \times 10^3 \rightarrow 1 \times 10^4$	0.7	0.00	Flat Plate	$0 \rightarrow 40$
Carr, McAlister and McCroskey (1977)	Experimental	$1 \times 10^6 \rightarrow 3.5 \times 10^6$	$0.02 \rightarrow 0.25$	0.25	NACA 0012	$1 \rightarrow 29$
Chandrasekhara, Wilder and Carr (1998a)	Experimental	$0.54 \times 10^6 \rightarrow 1.1 \times 10^6$	$0.0125 \rightarrow 0.05$	0.25	NACA 0012	$0 \rightarrow 20$
Choudhuri, Knight and Visbal (1994)	Numerical	1×10^4	0.1	0.25	NACA 0012	$0 \rightarrow 25$
Conger and Ramaprian (1994)	Experimental	$5.2 \times 10^5 \rightarrow 2.2 \times 10^5$	$0.018 \rightarrow 0.1$	0.25	NACA 0015	$0 \rightarrow 40$
Crisler (1994)	Experimental	$2.8 \times 10^5 \rightarrow 6.2 \times 10^5$	$0.005 \rightarrow 0.03$	0.25	NACA 0012	$0 \rightarrow 30$
Dadone (1977)	Experimental	$3.1 \times 10^6 \rightarrow 7 \times 10^6$	$0.16 \rightarrow 0.18$	0.25	NLR 7223-62	$-10 \rightarrow 30$
Daley and Jumper (1984)	Experimental	$7.8 \times 10^4 \rightarrow 3.01 \times 10^5$	$0 \rightarrow 0.270$	0.25	NACA 0015	$0 \rightarrow 31$
Francis and Keesee (1985)	Experimental	$7.7 \times 10^4 \rightarrow 1.69 \times 10^5$	$0.001 \rightarrow 0.21$	$0.31 \rightarrow 0.37$	NACA 0012 NACA 64A012	$0 \rightarrow 60$
Garmann and Visbal (2011)	Numerical	$5 \times 10^3 \rightarrow 4 \times 10^4$	0.2	0.25	Flat Plate	$0 \rightarrow 45$
Geissler, Dietz and Mai (2005)	Experimental Numerical	$2.1 \times 10^6 \rightarrow 2.8 \times 10^6$	$0.0125 \rightarrow 0.05$	0.25	DLR A1510	$0 \rightarrow 25$
Gharali and Johnson (2013)	Numerical	1.35×10^5	0.05	0.25	NACA 0012	$-5 \rightarrow 25$
Granlund et al. (2010)	Experimental Numerical	5×10^4 2×10^4	0.03 $0.0025 \rightarrow 0.2$	0, 0.25, 0.5, 0.75	SD7003 Flat Plate	$0 \rightarrow 45$ $0 \rightarrow 90$
Green and Galbraith (1995)	Experimental	$2 \times 10^4 \rightarrow 1.5 \times 10^6$	$0.03 \rightarrow 0.048$	0.25	NACA 23012B NACA 21012C NACA 0015	$0 \rightarrow 40$
Helin and Walker (1985)	Experimental	4.5×10^4	$0.1 \rightarrow 0.3$	0.25, 0.5, 0.75	NACA 0015	$0 \rightarrow 60$
Jumper, Schreck and Dimmick (1987)	Experimental	$1.6 \times 10^5 \rightarrow 2.8 \times 10^5$	$0.01 \rightarrow 0.015$	0.50	NACA 0015	$0 \rightarrow 50$
Kang et al. (2009)	Experimental Numerical	$1 \times 10^4 \rightarrow 6 \times 10^4$	0.25	0.25	SD7003	$-6 \rightarrow 22$

	Analytical					
Kim and Chang (2014)	Experimental	$2 \times 10^4 \rightarrow 5 \times 10^4$	0.1	0.25	NACA 0012	$-6 \rightarrow 6$
Lee and Gerontakos (2004)	Experimental	1.35×10^5	$0.0125 \rightarrow 0.3$	0.25	NACA 0012	$-10 \rightarrow 30$
Leishman (1990)	Experimental	$0.8 \times 10^6 \rightarrow 2 \times 10^6$	$0.01 \rightarrow 0.2$	0.25	NACA 23012	$0 \rightarrow 30$
Liiva (1968)	Experimental	$2.6 \times 10^6 \rightarrow 6.6 \times 10^6$	$0.02 \rightarrow 0.36$	0.25	NACA 0012 Vertol 23010	$0 \rightarrow 30$
Lorber and Carta (1988)	Experimental	$2 \times 10^6 \rightarrow 4 \times 10^6$	$0.001 \rightarrow 0.02$	0.25	Sikorsky SSC-A09	$0 \rightarrow 30$
Lourenco et al. (1993)	Experimental	$5 \times 10^3 \rightarrow 2.5 \times 10^4$	$0.02 \rightarrow 0.065$	0.25	NACA 0012	$0 \rightarrow 30$
Lu, Xie and Zhang (2013)	Numerical	1.35×10^4	$0 \rightarrow 3.0$	0.25	NACA 0012	$5 \rightarrow 30$
Martinat et al. (2008)	Numerical	$1 \times 10^5 \rightarrow 1 \times 10^6$	$0.1 \rightarrow 0.188$	0.25	NACA 0012	$5 \rightarrow 25$
McAlister, Carr and McCroskey (1978)	Experimental	2.5×10^6	$0 \rightarrow 0.25$	0.25	NACA 0012	$5 \rightarrow 25$
McCroskey et al. (1982)	Experimental	$4.9 \times 10^5 \rightarrow 4.2 \times 10^6$	$0.01 \rightarrow 0.2$	0.25	NACA 0012 Verton VR-7 NLR-1 NLR7310 Ames A-01 Wortmann FX-098 Sikorsky SC-1095 Hughes HH-02	$-10 \rightarrow 29$
Mulleners et al. (2009)	Experimental	9.2×10^5	$0.025 \rightarrow 0.05$	0.25	OA-209	$10 \rightarrow 30$
Nati et al. (2015)	Experimental	3×10^4	0.1	0.25	SD7003	$4 \rightarrow 8$
Ohmi et al. (1990)	Experimental Numerical	$1.5 \times 10^3 \rightarrow 1 \times 10^4$	$0.5 \rightarrow 1$	0.5	Elliptical Airfoil	$0 \rightarrow 45$
Ol et al. (2009)	Experimental Numerical	$1 \times 10^4 \rightarrow 6 \times 10^4$	0.25	0.25	SD7003	$4 \rightarrow 23$
Panda and Zaman (1994)	Experimental	$2.2 \times 10^4 \rightarrow 4.4 \times 10^4$	$0 \rightarrow 1.6$	0.25	NACA 0012	$5 \rightarrow 25$
(Raffel, Kompenhans and Wernert, 1995)	Experimental	4×10^5	0.15	0.25	NACA 0012	$5 \rightarrow 25$
Rival and Tropea (2010)	Experimental	$3 \times 10^4 \rightarrow 6 \times 10^4$	$0.05 \rightarrow 0.3$	0.25	SD7003	$-8 \rightarrow 24$
Shih, Lourenco and Krothapalli (1995)	Experimental	$5 \times 10^3 \rightarrow 2.5 \times 10^4$	0.06	0.25	NACA 0012	$0 \rightarrow 30$
Spentzos et al. (2005)	Numerical	6.9×10^4	$0.05 \rightarrow 0.1$	$0.25 \rightarrow 0.33$	NACA 0012 Square	$0 \rightarrow 60$
Visbal (1990)	Numerical	3×10^6	$0.022 \rightarrow 0.1$	$0.25 \rightarrow 1$	NACA 0015	$0 \rightarrow 60$
Visbal (2014)	Numerical	6×10^4	0.025	0.25	SD7003	$4 \rightarrow 30$
Wang et al. (2012)	Numerical	1.35×10^5	0.1	0.25	NACA 0012	$-5 \rightarrow 25$

THIS THESIS						
Chapter 3	Experimental	2×10^4	$0.05 \rightarrow 0.2$	0.5	NACA 0012 NACA 0021	$0 \rightarrow 90$
Chapter 4	Experimental	2×10^4	$0.05 \rightarrow 0.2$	0.5	NACA 0021	$0 \rightarrow 90$
Chapter 5	Experimental	2×10^4	$0.025 \rightarrow 0.1$	0.5	NACA 0012	$0 \rightarrow 60$
Chapter 6	Experimental	2×10^4	$0.025 \rightarrow 0.1$	0.5	Flat Plate	$0 \rightarrow 50$

2.8. Conclusions from the Literature Review and Thesis Objectives

The overall aim of the current research is to identify the unsteady behaviour of airfoils undergoing dynamic stall. Moreover, the thesis investigates the application of high airfoil rotation rates and high angles of attack specific to severe weather conditions. Moreover, the thesis will investigate fluid-structure interaction and force development resulting from unsteady separation during dynamic stall. The research will focus on identifying the effects of dynamic stall on the post-stall behaviour of airfoils exposed to such extreme operating conditions. The first objective of this thesis is to identify the variation in flow structure and forces developed as a result of continued rotation of an airfoil exposed to highly unsteady rotation rates and excessive angles of attack. Literature has detailed the flow structure and forces associated with reduced frequencies specific to the normal operation of helicopters. However, the angle of attack is typically limited to a maximum angle of $\alpha = 30°$. In addition, due to the variation in rotor blade thickness of wind turbines, the effects of airfoil thickness on dynamic stall during gust-like conditions remains unclear. The outcomes of the first objective will address this gap in the literature, so that a greater awareness of the variation between thick and thin airfoils operating in highly unsteady environments can be established. For this purpose, and as summarised in the literature review, the use of NACA 0012 and a NACA 0021 airfoil will be utilised for a

comparative analysis of the flow structure and force generation resulting from dynamic stall.

The second objective of the current work focuses on addressing the gap in knowledge regarding the continued operation of wind turbine blades in post-stall environments, representative of stall-regulated wind turbines. Post-stall environments are highly complex flow fields resulting from tower shadow, turbine wake interaction, atmospheric turbulence, turbine yaw and blade elasticity. All of these parameters impose significant unsteady loads on the turbine. The literature does not detail the operation of airfoils exposed to dynamic stall conditions and which then continue to proceed into post-stall operating conditions. The second objective is to address this matter by replicating dynamic stall conditions, although instead of allowing the airfoil to return to an angle of attack where flow reattachment naturally occurs, the airfoil will be held fixed at its maximum angle of attack, allowing for the transition into post-stall to occur. Experimental techniques using PIV and surface pressure measurements will be utilised to identify the major flow structure characteristics, along with the forces associated with the airfoil motion.

The third objective of the thesis is to determine the suitability of passive boundary layer control devices under highly unsteady flow conditions. Literature discusses the application of both passive and active boundary layer control techniques for the control of dynamic stall. The operating conditions of these control devices are typically associated with quasi-steady flows, where inertial loads generated via airfoil rotation are small. Control of dynamic stall at quasi-steady rotation rates are achieved by Choudhry, Arjomandi and Kelso (2016) through the application of a leading-edge trip wire. However,

the rotation rate was significantly lower than that obtained during highly unsteady flow conditions. Therefore, the scope of the third objective is to determine the effectiveness of the trip wire when the airfoil is subjected to increased rotation rates more indicative of severe wind gusts. Surface pressure measurements will be utilised to resolve the unsteady forces developed about a pitching airfoil fitted with a leading-edge trip wire. Analysis of the resulting forces will allow for the determination of the effectiveness of the trip wire under high rotation-rate pitching motions.

The fourth objective of the research is to determine the characteristics of the dynamic-stall process for a flat plate. This will be conducted in order to further increase the knowledge of the unsteady separation process, so that improved methods of flow control can be utilised for reduction or removal of the unsteady loads imposed by dynamic stall. Research using flat plates allows for geometrical properties of the airfoil to be limited. Therefore, inertial effects induced through rotation of the flat plate can be assessed for their influence on the flow structure development and separation behaviour during dynamic stall. Literature has previously discussed the performance of flat plates at low Reynolds numbers. Attempts have also been made to understand the topological flow structures developed during leading-edge vortex development and its transition over the plate. Performance parameters such as the reduced frequency, pitch location, Reynolds number and leading-edge and trailing-edge geometry have been investigated for their influence on the overall aerodynamic performance. In addition, literature discusses the presence of a half-saddle point located on the upper surface of the plate that could potentially be utilised for boundary layer control. This work has provided significant insight into dynamic stall. However, there remains a gap in knowledge of the motion of the half-saddle point during the pitch-up process. Therefore, the fourth objective of the

thesis will focus on investigating the motion of the half-saddle point in order to detect its variation in velocity along the upper surface with respect to parameters such as leading-edge geometry and airfoil rotation rate. The work will identify the half-saddle point through the use of imbedded surface pressure measurements, allowing for trends in its motion to be identified. This will ultimately lead to a greater awareness of the dynamic stall process, so that adaptive boundary layer control techniques can be tuned and refined for increased control of flow separation.

2.9. References

Acharya, M. & Metwally, M. 1992. Unsteady pressure field and vorticity production over a pitching airfoil. *AIAA Journal,* 30**,** 403-411.

Adrian, R. J. & Westerweel, J. 2011. *Particle image velocimetry*, Cambridge University Press.

Ahsanul Karim, M. & Acharya, M. 1994. Suppression of dynamic-stall vortices over pitching airfoils by leading-edge suction. *AIAA Journal,* 32**,** 1647-1655.

Albertson, J., Troutt, T., Siuru, W. & Walker, J. 1987. Dynamic stall vortex development and the surface pressure field of a pitching airfoil. United States: Frank J Seiler Research Laboratory United States Air Force Academy

Alrefai, M. d. & Acharya, M. 1996. Controlled leading-edge suction for management of unsteady separation over pitching airfoils. *AIAA Journal,* 34**,** 2327-2336.

Amiralaei, M., Alighanbari, H. & Hashemi, S. 2010. An investigation into the effects of unsteady parameters on the aerodynamics of a low Reynolds number pitching airfoil. *Journal of Fluids and Structures,* 26**,** 979-993.

Baik, Y. S., Bernal, L. P., Granlund, K. & Ol, M. V. 2012. Unsteady force generation and vortex dynamics of pitching and plunging aerofoils. *Journal of Fluid Mechanics,* 709**,** 37-68.

Bossanyi, E. 2003. Wind turbine control for load reduction. *Wind Energy,* 6**,** 229-244.

Buchner, A.-J., Honnery, D. & Soria, J. 2017. Stability and three-dimensional evolution of a transitional dynamic stall vortex. *Journal of Fluid Mechanics,* 823**,** 166-197.

Buchner, A. & Soria, J. 2015. Measurements of the flow due to a rapidly pitching plate using time resolved high resolution PIV. *Aerospace Science and Technology,* 44**,** 4-17.

Butterfield, C., Simms, D., Scott, G. & Hansen, A. 1991. Dynamic stall on wind turbine blades. United States: National Renewable Energy Laboratory.

Carr, L. 1988. Progress in analysis and prediction of dynamic stall. *Journal of Aircraft,* 25**,** 6-17.

Carr, L., Chandrasekhara, M., Wilder, M. & Noonan, K. 2001. Effect of compressibility on suppression of dynamic stall using a slotted airfoil. *Journal of Aircraft,* 38**,** 296-309.

Carr, L. & McAlister, K. 1983. The effect of a leading-edge slat on the dynamic stall of an oscillating airfoil. *Aircraft Design, Systems and Technology Meeting.* USA: AIAA.

Carr, L., McCroskey, W., McAlister, K., Pucci, S. & Lambert, O. 1982. An Experimental Study of Dynamic Stall on Advanced Airfoil Sections. Volume 3; Hot-Wire and Hot Film Measurements. United States: National Aeronautics and Space Administration.

Carr, L. W. & Chandrasekhara, M. 1996. Compressibility effects on dynamic stall. *Progress in Aerospace Sciences,* 32**,** 523-573.

Carr, L. W., McAlister, K. W. & McCroskey, W. J. 1977. Analysis of the development of dynamic stall based on oscillating airfoil experiments. United States: National Aeronautics and Space Administration

Carta, F. O. 1979. A comparison of the pitching and plunging response of an oscillating airfoil. United States: National Aeronautical and Space Administration.

Chandrasekhara, M., Ahmed, S. & Carr, L. 1993. Schlieren studies of compressibility effects on dynamic stall of transiently pitching airfoils. *Journal of Aircraft,* 30**,** 213-220.

Chandrasekhara, M. & Carr, L. 1990. Flow visualization studies of the Mach number effects on dynamic stall of an oscillating airfoil. *Journal of Aircraft,* 27**,** 516-522.

Chandrasekhara, M., Martin, P. & Tung, C. 2004. Compressible dynamic stall control using a variable droop leading edge airfoil. *Journal of Aircraft,* 41**,** 862-869.

Chandrasekhara, M., Wilder, M. & Carr, L. 1998a. Competing mechanisms of compressible dynamic stall. *AIAA Journal,* 36**,** 387-393.

Chandrasekhara, M., Wilder, M. & Carr, L. 1998b. Unsteady stall control using dynamically deforming airfoils. *AIAA Journal,* 36.

Choudhry, A., Arjomandi, M. & Kelso, R. 2016. Methods to control dynamic stall for wind turbine applications. *Renewable Energy,* 86**,** 26-37.

Choudhry, A., Leknys, R., Arjomandi, M. & Kelso, R. 2014. An insight into the dynamic stall lift characteristics. *Experimental Thermal and Fluid Science,* 58**,** 188-208.

Choudhuri, P. G. & Knight, D. 1996. Effects of compressibility, pitch rate, and Reynolds number on unsteady incipient leading-edge boundary layer separation over a pitching airfoil. *Journal of Fluid Mechanics,* 308**,** 195-217.

Choudhuri, P. G., Knight, D. & Visbal, M. 1994. Two-dimensional unsteady leading-edge separation on a pitching airfoil. *AIAA Journal,* 32**,** 673-681.

Cimbala, J. M. & Çengel, Y. A. 2014. Fluid mechanics: fundamentals and applications. McGraw-Hill.

Conger, R. & Ramaprian, B. 1994. Pressure measurements on a pitching airfoil in a water channel. *AIAA Journal,* 32**,** 108-115.

Corke, T. C. & Thomas, F. O. 2015. Dynamic stall in pitching airfoils: aerodynamic damping and compressibility effects. *Annual Review of Fluid Mechanics,* 47**,** 479-505.

Coton, F. N. & Galbraith, R. A. An examination of dynamic stall on an oscillating rectangular wing. 21st AIAA Applied Aerodynamics Conference, Fluid Dynamics and Co-Located Conferences, 2003 United States.

Crisler, W. P. 1994. PIV investigation of compressibility effects on dynamic stall.

Currier, J. M. & Fung, K. 1992. Analysis of the onset of dynamic stall. *AIAA Journal,* 30**,** 2469-2477.

Dadone, L. U. 1977. Two-dimensional wind tunnel test of an oscillating rotor airfoil, volume 1. United States: National Aeronautics and Space Administraction.

Daley, D. & Jumper, E. 1984. Experimental investigation of dynamic stall for a pitching airfoil. *Journal of Aircraft,* 21**,** 831-832.

Ellington, C. 1984. The aerodynamics of hovering insect flight. I. The quasi-steady analysis. *Philosophical Transactions of the Royal Society of London B: Biological Sciences,* 305**,** 1-15.

Feszty, D., Gillies, E. A. & Vezza, M. 2004. Alleviation of airfoil dynamic stall moments via trailing-edge-flap flow control. *AIAA Journal,* 42**,** 17-25.

Fish, F. E., Weber, P. W., Murray, M. M. & Howle, L. E. 2011. The tubercles on humpback whales' flippers: application of bio-inspired technology. *Integrative and Comparative Biology,* 51**,** 203-213.

Francis, M. & Keesee, J. 1985. Airfoil dynamic stall performance with large-amplitude motions. *AIAA Journal,* 23**,** 1653-1659.

Gardner, A. D., Richter, K. & Rosemann, H. 2011. Numerical investigation of air jets for dynamic stall control on the OA209 airfoil. *CEAS Aeronautical Journal,* 1**,** 69-82.

Garmann, D. J. & Visbal, M. R. 2011. Numerical investigation of transitional flow over a rapidly pitching plate. *Physics of Fluids,* 23**,** 094106.

Garmann, D. J. & Visbal, M. R. 2017. Analysis of Tip Vortex Near-Wake Evolution for Stationary and Oscillating Wings. *AIAA Journal***,** 1-17.

Geissler, W., Dietz, G. & Mai, H. 2005. Dynamic stall on a supercritical airfoil. *Aerospace Science and Technology,* 9**,** 390-399.

Geissler, W., Dietz, G., Mai, H., Bosbach, J. & Richard, H. Dynamic stall and its passive control investigations on the OA209 airfoil section. 31st European Rotorcraft Forum, 2005 Italy.

Geissler, W., Dietz, G., Mai, H., Junker, B. & Lorkowski, T. Dynamic stall control investigations on a full size chord blade section. 30th European Rotorcraft Forum, 2004 France.

Gharali, K. & Johnson, D. A. 2013. Dynamic stall simulation of a pitching airfoil under unsteady freestream velocity. *Journal of Fluids and Structures,* 42**,** 228-244.

Granlund, K., Ol, M., Garmann, D., Visbal, M. & Bernal, L. Experiments and computations on abstractions of perching. 28th AIAA Applied Aerodynamics Conference, 2010 United States. 4943.

Granlund, K. O., Ol, M. V. & Bernal, L. P. 2013. Unsteady pitching flat plates. *Journal of Fluid Mechanics,* 733**,** R5.

Granlund, K. O., Ol, M. V. & Jones, A. R. 2016. Streamwise oscillation of airfoils into reverse flow. *AIAA Journal*.

Green, R. & Galbraith, R. 1995. Dynamic recovery to fully attached aerofoil flow from deep stall. *AIAA Journal,* 33.

Greenblatt, D., Ben-Harav, A. & Mueller-Vahl, H. 2014. Dynamic stall control on a vertical-axis wind turbine using plasma actuators. *AIAA Journal,* 52**,** 456-462.

Greenblatt, D., Nishri, B., Darabi, A. & Wygnanski, I. 2001. Dynamic stall control by periodic excitation, Part 2: Mechanisms. *Journal of Aircraft,* 38**,** 439-447.

Greenblatt, D. & Wygnanski, I. 2001. Dynamic stall control by periodic excitation, Part 1: NACA 0015 parametric study. *Journal of Aircraft,* 38**,** 430-438.

Greenblatt, D. & Wygnanski, I. 2002. Effect of leading-edge curvature and slot geometry on dynamic stall control. *AIAA Journal,* 3271**,** 2002.

Hansen, A. & Butterfield, C. 1993. Aerodynamics of horizontal-axis wind turbines. *Annual Review of Fluid Mechanics,* 25**,** 115-149.

Hansen, K. L., Kelso, R. M. & Dally, B. B. 2011. Performance variations of leading-edge tubercles for distinct airfoil profiles. *AIAA Journal,* 49**,** 185-194.

Harper, P. & Flanigan, R. 1950. The effect of rate of change of angle of attack on the maximum lift of a small model. United States: National Advisory Committee for Aeronautics.

Heine, B., Mulleners, K., Joubert, G. & Raffel, M. 2013. Dynamic stall control by passive disturbance generators. *AIAA Journal,* 51**,** 2086-2097.

Helin, H. E. & Walker, J. M. 1985. Interrelated effects of pitch rate and pivot point on airfoil dynamic stall. *AIAA 23rd Aerospace Sciences Meeting.* United States: AIAA.

Hodara, J., Lind, A. H., Jones, A. R. & Smith, M. J. 2016. Collaborative investigation of the aerodynamic behavior of airfoils in reverse flow. *Journal of the American Helicopter Society,* 61**,** 1-15.

Hrynuk, J. 2015. *The effect of leading edge tubercles on dynamic stall.* Doctor of Philospohy, Clarkson University.

Jones, A. R., Manar, F., Phillips, N., Nakata, T., Bomphrey, R., Ringuette, M. J., Percin, M., van Oudheusden, B. & Palmer, J. Leading edge vortex evolution and lift production on rotating wings. 54th AIAA Aerospace Sciences Meeting, 2016 United States. 0288.

Joo, W., Lee, B.-S., Yee, K. & Lee, D.-h. 2006. Combining passive control method for dynamic stall control. *Journal of Aircraft,* 43**,** 1120-1128.

Jumper, E., Dimmick, R. & Allaire, A. 1989. The effect of pitch location on dynamic stall. *ASME, Transactions, Journal of Fluids Engineering,* 111**,** 256-262.

Jumper, E., Schreck, S. & Dimmick, R. 1987. Lift-curve characteristics for an airfoil pitching at constant rate. *Journal of Aircraft,* 24**,** 680-687.

Kang, C.-k., Baik, Y. S., Bernal, L., Ol, M. V. & Shyy, W. 2009. Fluid dynamics of pitching and plunging airfoils of Reynolds number between 1× 104 and 6× 104. *AIAA Journal,* 536**,** 2009.

Karim, M. & Acharya, M. 1994. Suppression of dynamic-stall vortices over pitching airfoils by leading-edge suction. *AIAA Journal,* 32**,** 1647-1655.

Katz, Y., Nishri, B. & Wygnanski, I. 1989. The delay of turbulent boundary layer separation by oscillatory active control. *Physics of Fluids A: Fluid Dynamics,* 1**,** 179-181.

Kerho, M. F. 2007. Adaptive airfoil dynamic stall control. *Journal of Aircraft,* 44**,** 1350-1360.

Kim, D.-H. & Chang, J.-W. 2014. Low-Reynolds-number effect on the aerodynamic characteristics of a pitching NACA0012 airfoil. *Aerospace Science and Technology,* 32**,** 162-168.

Kramer, M. 1932. Increase in the Maximum Lift of an Airplane Wing due to a Sudden Increase in its Effective Angle of Attack Resulting from a Gust. United States: National Advisory Committee for Aeronautics.

Lachmann, G. V. 2014. *Boundary layer and flow control: its principles and application,* London, Elsevier.

Laitone, E. 1997. Wind tunnel tests of wings at Reynolds numbers below 70 000. *Experiments in Fluids,* 23**,** 405-409.

Lanzafame, R. & Messina, M. 2013. Advanced brake state model and aerodynamic post-stall model for horizontal axis wind turbines. *Renewable Energy,* 50**,** 415-420.

Lee, T. & Gerontakos, P. 2004. Investigation of flow over an oscillating airfoil. *Journal of Fluid Mechanics,* 512**,** 313-341.

Lee, T. & Gerontakos, P. 2006. Dynamic stall flow control via a trailing-edge flap. *AIAA Journal,* 44**,** 469-480.

Leishman, G. J. 2006. *Principles of helicopter aerodynamics with CD extra,* Cambridge, Cambridge University Press.

Leishman, J. 1990. Dynamic stall experiments on the NACA 23012 aerofoil. *Experiments in Fluids,* 9**,** 49-58.

Liebe, R. 2006. *Flow Phenomena in Nature: Inspiration, learning and application*, Wit Press.

Liiva, J. 1968. *Unsteady aerodynamic and stall effects on helicopter rotor blade airfoil sections*, American Institute of Aeronautics and Astronautics.

Lombardi, A. J., Bowles, P. O. & Corke, T. C. 2013. Closed-loop dynamic stall control using a plasma actuator. *AIAA Journal,* 51**,** 1130-1141.

Lorber, P. F. & Carta, F. O. 1987. Unsteady stall penetration experiments at high Reynolds number. United Technology Research Center

Lorber, P. F. & Carta, F. O. 1988. Airfoil dynamic stall at constant pitch rate and high Reynolds number. *Journal of Aircraft,* 25**,** 548-556.

Lourenco, L., Krothapalli, A. & Smith, C. 1989. Particle image velocimetry. *Advances in fluid mechanics measurements.* Springer.

Lourenco, L. M., Krothapalli, A., Van Dommelen, L. & Shih, C. 1993. Unsteady flow past a NACA 0012 airfoil pitching at constant rates. United States: Florida agricultural and Mechanical University

Lu, K., Xie, Y. & Zhang, D. 2013. Numerical study of large amplitude, nonsinusoidal motion and camber effects on pitching airfoil propulsion. *Journal of Fluids and Structures,* 36**,** 184-194.

Lu, K., Xie, Y., Zhang, D. & Lan, J. 2013. Numerical investigations into the asymmetric effects on the aerodynamic response of a pitching airfoil. *Journal of Fluids and Structures,* 39**,** 76-86.

Magill, J. C. & McManus, K. 1998. Control of dynamic stall using pulsed vortex generator jets. *AIAA Journal,* 675**,** 1998.

Mai, H., Dietz, G., Geißler, W., Richter, K., Bosbach, J., Richard, H. & de Groot, K. 2008. Dynamic stall control by leading edge vortex generators. *Journal of the American Helicopter Society,* 53**,** 26-36.

Martinat, G., Braza, M., Hoarau, Y. & Harran, G. 2008. Turbulence modelling of the flow past a pitching NACA0012 airfoil at 105 and 106 Reynolds numbers. *Journal of Fluids and Structures,* 24**,** 1294-1303.

McAlister, K. & Carr, L. 1979. Water tunnel visualizations of dynamic stall. *Journal of Fluids Engineering,* 101**,** 376-380.

McAlister, K. W., Carr, L. W. & McCroskey, W. J. 1978. Dynamic stall experiments on the NACA 0012 airfoil. United States: National Aeronautical and Space Administration.

McAlister, K. W. & Tung, C. 1993. Suppression of Dynamic Stall with a Leading-edge Slat on a VR-7 Airfoil. DTIC Document.

McCloud, J. L., Hall, L. P. & Brady, J. A. 1960. Full-Scale Wind-Tunnel Tests of Blowing Boundary-Layer Control Applied to a Helicopter Rotor. United States: National Aeronautical and Space Administration.

McCroskey, W., McAlister, K., Carr, L. & Pucci, S. 1982. An experimental study of dynamic stall on advanced airfoil sections. Volume 1, 2 & 3. NASA.

McCroskey, W. & Puccif, S. 1982. Viscous-inviscid interaction on oscillating airfoils in subsonic flow. *AIAA Journal,* 20**,** 167-174.

McCroskey, W. J. 1981. The phenomenon of dynamic stall. United States: National Aeronautical and Space Administration

McCroskey, W. J. 1982. Unsteady airfoils. *Annual Review of Fluid Mechanics,* 14**,** 285-311.

McCroskey, W. J., Carr, L. W. & McAlister, K. W. 1976. Dynamic stall experiments on oscillating airfoils. *AIAA Journal,* 14**,** 57-63.

McCroskey, W. J., McAlister, K., Carr, L., Pucci, S., Lambert, O. & Indergrand, R. 1981. Dynamic stall on advanced airfoil sections. *Journal of the American Helicopter Society,* 26**,** 40-50.

Merzkirch, W. 2001. Particle image velocimetry. *Optical Measurements***,** 341-357.

Mulleners, K., Henning, A., Mai, H., Raffel, M., Le Pape, A. & Costes, M. 2009. Investigation of the unsteady flow development over a pitching airfoil by means of TR-PIV. *AIAA Journal,* 3504**,** 2011.

Mulleners, K. & Raffel, M. 2012. The onset of dynamic stall revisited. *Experiments in Fluids,* 52**,** 779-793.

Mulleners, K. & Raffel, M. 2013. Dynamic stall development. *Experiments in Fluids,* 54**,** 1469.

Müller-Vahl, H. F., Nayeri, C. N., Paschereit, C. O. & Greenblatt, D. 2016. Dynamic stall control via adaptive blowing. *Renewable Energy,* 97**,** 47-64.

Müller-Vahl, H. F., Strangfeld, C., Nayeri, C. N., Paschereit, C. O. & Greenblatt, D. 2014. Control of thick airfoil, deep dynamic stall using steady blowing. *AIAA Journal,* 53**,** 277-295.

Munduate, X., Coton, F. N. & Galbraith, R. A. M. 2004. An Investigation of the Aerodynamic Response of a Wind Turbine Blade to Tower Shadow. *Journal of Solar Energy Engineering,* 126**,** 1034-1040.

Nati, A., De Kat, R., Scarano, F. & Van Oudheusden, B. 2015. Dynamic pitching effect on a laminar separation bubble. *Experiments in Fluids,* 56**,** 172.

New, D. T., Wei, Z. & Cui, Y. D. 2016. A time-resolved particle-image velocimetry study on the unsteady flow behaviour of leading-edge tubercled hydrofoils. *18th International Symposium on the Application of Laser and Imaging Techniques to Fluid Mechanics.* Portugal.

North Atlantic Treaty Organization, S. T. O. 2016. Extensions of Fundamental Flow Physics to Practical MAV Aerodynamics. North Atlantic Treaty Organization, Science and Technology Organization.

Ohmi, K., Coutanceau, M., Daube, O. & Loc, T. P. 1991. Further experiments on vortex formation around an oscillating and translating airfoil at large incidences. *Journal of Fluid Mechanics,* 225**,** 607-630.

Ohmi, K., Coutanceau, M., Loc, T. P. & Dulieu, A. 1990. Vortex formation around an oscillating and translating airfoil at large incidences. *Journal of Fluid Mechanics,* 211**,** 37-60.

Ol, M. V., Bernal, L., Kang, C.-K. & Shyy, W. 2009. Shallow and deep dynamic stall for flapping low Reynolds number airfoils. *Experiments in Fluids,* 46**,** 883-901.

Panda, J. & Zaman, K. B. 1994. Experimental investigation of the flow field of an oscillating airfoil and estimation of lift from wake surveys. *Journal of Fluid Mechanics,* 265**,** 65-95.

Pelletier, A. & Mueller, T. J. 2000. Low Reynolds number aerodynamics of low-aspect-ratio, thin/flat/cambered-plate wings. *Journal of Aircraft,* 37**,** 825-832.

Perry, A. & Fairlie, B. 1975. Critical points in flow patterns. *Advances in Geophysics,* 18**,** 299-315.

Perry, A. & Steiner, T. 1987. Large-scale vortex structures in turbulent wakes behind bluff bodies. Part 1. Vortex formation processes. *Journal of Fluid Mechanics,* 174**,** 233-270.

Pierce, G., Kunz, D. & Malone, J. The effect of varying freestream velocity on dynamic stall characteristics. Annual National Forum of the American Helicopter Society, 1976 United States. National Aeronautical and Space Administration.

Post, M. L. & Corke, T. C. 2004. Separation control on high angle of attack airfoil using plasma actuators. *AIAA Journal,* 42.

Post, M. L. & Corke, T. C. 2006. Separation control using plasma actuators: dynamic stall vortex control on oscillating airfoil. *AIAA Journal,* 44**,** 3125-3135.

Prasad, A. K. 2000. Particle image velocimetry. *Current Science,* 79**,** 51-60.

Raffel, M., Bauknecht, A., Ramasamy, M., Yamauchi, G. K., Heineck, J. T. & Jenkins, L. N. 2017. Contributions of Particle Image Velocimetry to Helicopter Aerodynamics. *AIAA Journal*.

Raffel, M. & Kompenhans, J. 1993. PIV measurements of unsteady transonic flow fields above a NACA 0012 airfoil. *Laser Anemometry: Advances and Applications: Fifth International Conference.* Netherlands: SPIE.

Raffel, M., Kompenhans, J. & Wernert, P. 1995. Investigation of the unsteady flow velocity field above an airfoil pitching under deep dynamic stall conditions. *Experiments in Fluids,* 19**,** 103-111.

Raffel, M., Willert, C. E., Wereley, S. & Kompenhans, J. 2013. *Particle image velocimetry: a practical guide*, Springer.

Raghav, V., Mayo, M., Lozano, R. & Komerath, N. 2014. Evidence of vortex-induced lift on a yawed wing in reverse flow. *Proceedings of the Institution of Mechanical Engineers, Part G: Journal of Aerospace Engineering,* 228**,** 2130-2137.

Richards, P. W., Griffith, D. T. & Hodges, D. H. 2017. Aeroelastic design of large wind turbine blades considering damage tolerance. *Wind Energy,* 20**,** 159-170.

Rival, D., Kriegseis, J., Schaub, P., Widmann, A. & Tropea, C. A criterion for vortex separation on unsteady aerodynamic profiles. 51st AIAA Aerospace Sciences

Meeting including the New Horizons Forum and Aerospace Exposition, 2013 United States. AIAA, 836.

Rival, D., Prangemeier, T. & Tropea, C. 2009. The influence of airfoil kinematics on the formation of leading-edge vortices in bio-inspired flight. *Experiments in Fluids,* 46**,** 823-833.

Rival, D. & Tropea, C. 2010. Characteristics of pitching and plunging airfoils under dynamic-stall conditions. *Journal of Aircraft,* 47**,** 80-86.

Robinson, M. & Wissler, J. Pitch rate and Reynolds number effects on a pitching rectangular wing. 6th Applied Aerodynamics Conference, 1988. 2577.

Robinson, M. C. & Luttges, M. W. 1983. Unsteady flow separation and attachment induced by pitching airfoils. United States: Colorade University at Boulder, Department of Aerospace Engineering Sciences.

Rostamzadeh, N., Kelso, R., Dally, B. & Hansen, K. 2013. The effect of undulating leading-edge modifications on NACA 0021 airfoil characteristics. *Physics of Fluids,* 25**,** 117101.

Sane, S. P. 2003. The aerodynamics of insect flight. *Journal of Experimental Biology,* 206**,** 4191-4208.

Sangwan, J., Sengupta, T. K. & Suchandra, P. 2017. Investigation of compressibility effects on dynamic stall of pitching airfoil. *Physics of Fluids,* 29**,** 076104.

Sankar, N. & Tassat, Y. 1981. Compressibility Effects on Dynamic Stall of an NACA 0012 Airfoil. *AIAA Journal,* 19**,** 557-558.

Schreck, S. J., Faller, W. E. & Helin, H. E. 1998. Pitch rate and Reynolds number effects on unsteady boundary-layer transition and separation. *Journal of Aircraft,* 35**,** 46-52.

Sheldahl, R. E. & Klimas, P. C. 1981. Aerodynamic characteristics of seven symmetrical airfoil sections through 180-degree angle of attack for use in aerodynamic analysis of vertical axis wind turbines. United States: Sandia National Laboratory.

Sheng, W., Galbraith, R. M. & Coton, F. 2006. A new stall-onset criterion for low speed dynamic-stall. *Journal of Solar Energy Engineering,* 128**,** 461-471.

Sheng, W., Galbraith, R. M. & Coton, F. 2008. Prediction of dynamic stall onset for oscillatory low-speed airfoils. *Journal of Fluids Engineering,* 130**,** 101204.

Shih, C., Lourenco, L. & Krothapalli, A. 1995. Investigation of flow at leading and trailing edges of pitching-up airfoil. *AIAA Journal,* 33**,** 1369-1376.

Shih, C., Lourenco, L., Van Dommelen, L. & Krothapalli, A. 1992. Unsteady flow past an airfoil pitching at a constant rate. *AIAA Journal,* 30**,** 1153-1161.

Shipley, D. E., Miller, M. S. & Robinson, M. C. 1995. Dynamic stall occurrence on a horizontal axis wind turbine blade. United States: National Renewable Energy Laboratory.

Shyy, W., Lian, Y., Tang, J., Viieru, D. & Liu, H. 2007. *Aerodynamics of low Reynolds number flyers*, Cambridge University Press.

Singh, C., Peake, D. J., Kokkalis, A., Khodagolian, V., Coton, F. N. & Galbraith, R. A. M. 2006. Control of rotorcraft retreating blade stall using air-jet vortex generators. *Journal of Aircraft,* 43**,** 1169-1176.

Snyder, M. H. & Wentz Jr, W. 1981. Dynamics of wakes downstream of wind turbine towers. United States: National Aeronautical and Space Administration.

Spentzos, A., Barakos, G. N., Badcock, K. J., Richards, B. E., Wernert, P., Schreck, S. & Raffel, M. 2005. Investigation of three-dimensional dynamic stall using computational fluid dynamics. *AIAA Journal,* 43**,** 1023-1033.

Stevens, P. & Babinsky, H. 2017. Experiments to investigate lift production mechanisms on pitching flat plates. *Experiments in Fluids,* 58**,** 7.

Sun, M. & Sheikh, S. 1999. Dynamic stall suppression on an oscillating airfoil by steady and unsteady tangential blowing. *Aerospace Science and Technology,* 3**,** 355-366.

Tangler, J. & Kocurek, J. D. Wind turbine post-stall airfoil performance characteristics guidelines for blade-element momentum methods. 43rd AIAA Aerospace Sciences Meeting and Exhibit, 2005 United States. AIAA, 10-13.

Visbal, M. 1990. Dynamic stall of a constant-rate pitching airfoil. *Journal of Aircraft,* 27**,** 400-407.

Visbal, M. & Shang, J. 1989. Investigation of the flow structure around a rapidly pitching airfoil. *AIAA Journal,* 27**,** 1044-1051.

Visbal, M. R. 1991. On the formation and control of the dynamic stall vortex on a pitching airfoil. *AIAA Journal,* 6.

Visbal, M. R. 2011. Numerical investigation of deep dynamic stall of a plunging airfoil. *AIAA Journal,* 49**,** 2152-2170.

Visbal, M. R. 2014. Analysis of the onset of dynamic stall using high-fidelity large-eddy simulations. *AIAA Journal,* 591**,** 2014.

Visbal, M. R. & Garmann, D. J. 2017. Analysis of Dynamic Stall on a Pitching Airfoil Using High-Fidelity Large-Eddy Simulations. *AIAA Journal*.

Walker, J., Helin, H. & Chou, D. 1985. Unsteady surface pressure measurements on a pitching airfoil. United States: Frank J Seiler Research Laboratory, United States Air Force Academy.

Walker, J., Helin, H. & Strickland, J. 1985. An experimental investigation of an airfoil undergoing large-amplitude pitching motions. *AIAA Journal,* 23**,** 1141-1142.

Wang, S., Ingham, D. B., Ma, L., Pourkashanian, M. & Tao, Z. 2012. Turbulence modeling of deep dynamic stall at relatively low Reynolds number. *Journal of Fluids and Structures,* 33**,** 191-209.

Weaver, D., McAlister, K. & Tso, J. 1998. Suppression of dynamic stall by steady and pulsed upper-surface blowing. *AIAA Journal*.

Weaver, D., McAlister, K. & Tso, J. 2004. Control of VR-7 dynamic stall by strong steady blowing. *Journal of Aircraft,* 41**,** 1404-1413.

Weaver, D., McAlister, K. W. & Tso, J. 1996. Suppression of dynamic stall by steady and pulsed upper-surface blowing. National Aeronautical and Space Administration

Wernert, P., Geissler, W., Raffel, M. & Kompenhans, J. 1996. Experimental and numerical investigations of dynamic stall on a pitching airfoil. *AIAA Journal,* 34**,** 982-989.

Wernert, P., Koerber, G., Wietrich, F., Raffel, M. & Kompenhans, J. 1997. Demonstration by PIV of the non-reproducibility of the flow field around an airfoil pitching under deep dynamic stall conditions and consequences thereof. *Aerospace Science and Technology,* 1**,** 125-135.

Westerweel, J. Analysis of PIV interrogation with low pixel resolution. 1993 International Symposium on Optics, Imaging, and Instrumentation, 1993 United States. SPIE, 624-635.

Widmann, A. & Tropea, C. 2017. Reynolds number influence on the formation of vortical structures on a pitching flat plate. *Interface Focus,* 7**,** 20160079.

Willert, C. E. & Gharib, M. 1991. Digital particle image velocimetry. *Experiments in Fluids,* 10**,** 181-193.

Yu, H.-T. 2014. *Unsteady Aerodynamics of Pitching Flat Plate Wings.* Doctor of Philosophy, The University of Michigan.

Yu, H.-T. & Bernal, L. Effect of pivot point on aerodynamic force and vortical structure of pitching flat plate wings. 51st AIAA aerospace sciences meeting including the new horizons forum and aerospace exposition, 2013 United States. AIAA, 792.

Yu, Y. H., Lee, S., McAlister, K. W., Tung, C. & Wang, C. M. 1995. Dynamic stall control for advanced rotorcraft application. *AIAA Journal,* 33**,** 289-295.

Chapter 3.

Thick and Thin Airfoil Dynamic Stall

3.1. Chapter 3 Overview

The following chapter investigates the variation in force and flow structure development between a thick NACA 0021 and a thin NACA 0012 airfoil undergoing constant-pitch-rate motion to elevated angles of attack and at high rotation rates. This is conduced to achieve the first project objective to identify the flow behaviour of airfoils with varying thickness ratios and undergoing highly unsteady flow conditions. An experimental apparatus was created to simulate constant-pitch-rate motion for both airfoils using water channel and wind tunnel testing facilities. Flow structures, identified from vorticity contours, were investigated using phase-averaged PIV, whilst airfoil surface pressures were evaluated using differential pressure sensors embedded within each wings. Results show minimal flow structure variation at angles of attack beyond $\alpha = 40°$. Velocity profiles were published as a conference article and can be referred to in Appendix A. The investigations showed that the highly accelerated flows significantly increased the total lift generation of both wings. The presence of separation bubbles on both surfaces of the airfoils are also shown to negatively influence the lift during steady-state conditions. Fluctuations in force generation were correlated with trailing-edge vortex shedding during pitch-up motions and were observed to intensify with increased rotation rate. The work shows minor variation between the flows produced by the two airfoils, however, differences in the location of vortex development are identified.

3.2. Elevated Angles of Attack and High Rotation Rates

Statement of Authenticity

Title of Paper:	Dynamic Stall Flow Structure and Forces on Symmetrical Airfoils at High Angles of Attack and Rotation Rates
Publication Status:	☐ Published ☐ Accepted for Publication ☑ Submitted for Publication ☐ Unpublished and Unsubmitted work written in manuscript style
Publication Details:	Leknys, R. R., Arjomandi, M., Kelso, R. M. & Birzer, C. H., 2017, Dynamic Stall Flow Structure and Forces on Symmetrical Airfoils at High Angles of Attack and Rotation Rates, *Journal of Fluids Engineering*.

Principal Author

Name of Principal Author:	Ryan Ross Leknys
Contribution to the Paper:	Performed data analysis and interpretation, wrote manuscript and acted as corresponding author.
Overall percentage (%):	70
Certification:	This paper reports on original research I conducted during the period of my Higher Degree by Research candidature and is not subject to any obligations or contractual agreements with a third party that would constrain its inclusion in this thesis. I am the primary author of this paper.

Signature: ____ Date: 05 March 2018

Co-Author Contributions

By signing the Statement of Authorship, each author certifies that:

i. the candidate's stated contribution to the publication is accurate (as detailed above);

ii. permission is granted for the candidate in include the publication in the thesis; and

iii. the sum of all co-author contributions is equal to 100% less the candidate's stated contribution.

Name of Co-Author:	Associate Professor Maziar Arjomandi
Contribution to the Paper:	Supervised the development of the research and contributed in academic discussion and the review process of submitted manuscripts.

Signature: _____ _____ Date: 05 March 2018

Name of Co-Author:	Associate Professor Richard Kelso
Contribution to the Paper:	Supervised the development of the research and contributed in academic discussion and the review process of submitted manuscripts.

Signature: Date: 05 March 2018

Name of Co-Author:	Dr Cristian Birzer
Contribution to the Paper:	Supervised the development of the research and contributed in academic discussion and the review process of submitted manuscripts.

Signature: _____ ___ Date: 05 March 2018

Dynamic Stall Flow Structure and Forces on Symmetrical Airfoils at High Angles of Attack and Rotation Rates

R R. Leknys, M. Arjomandi, R M. Kelso and C H. Birzer

The University of Adelaide, Adelaide, South Australia, 5006

Abstract

This article describes a direct comparison between two symmetrical airfoils undergoing dynamic stall at high, unsteady reduced frequencies under otherwise identical conditions. Particle image velocimetry was performed to distinguish the differences in flow structure between a NACA 0021 and a NACA 0012 airfoil undergoing dynamic stall. In addition, surface pressure measurements were performed to evaluate aerodynamic load and investigate the effect of laminar separation bubbles and vortex structures on the pressure fields surrounding the airfoils. Airfoil geometry is shown to have a significant effect on flow structure development and boundary layer separation, with separation occurring earlier for thinner airfoil sections undergoing constant pitch-rate motion all reduced frequencies. Inertial forces were identified to have a considerable impact on the overall force generation with increasing rotation rate. Force oscillation was observed to correlate with multiple vortex structures shedding at the trailing edge during high rotation rates. The presence of laminar separation bubbles on the upper and lower surfaces were shown to dramatically influence the steady-state lift of both airfoils. Post-stall characteristics are shown to be independent of airfoil geometry such that periodic vortex shedding was observed for all cases. However, the onset of deep stall is delayed with increased non-dimensional pitch rate due to the delay in initial dynamic stall vortex.

Nomenclature

α Angle of attack (deg)

b Wing span (m)

c Airfoil chord length (m)

CI Confidence interval $(C_L \pm Z\sigma/\sqrt{n})$

C_L Lift coefficient

dl Control volume vector spacing (m/s)

f_s Sample rate (Hz)

Γ Circulation (m^2/s)

κ Non-dimensional pitch rate $(\omega C/2U_\infty)$

L Lift Force (N)

n Number of samples

ω Angular velocity (rad/s)

ω_z Normalised vorticity

Re_C Chord based Reynolds number

ρ Fluid density (kg/m^3)

S Theoretical span (m)

σ Force coefficient standard deviation

Tu Turbulence intensity $(\%)$

T Time (s)

T^* Non-dimensional time (TU_∞/c)

u Horizontal velocity (m/s)

U_∞ Freestream velocity (m/s)

v Vertical velocity (m/s)

V Velocity (u, v) of control volume boundary (m/s)

Introduction

Dynamic stall is a phenomenon whereby the angle of attack can temporarily exceed typical steady-state values without the occurrence of deep stall, therefore increasing the lift coefficient (C_L). The increase in C_L has been attributed to the delay in separation and formation of a dominant vortex structure that originates at the leading edge and convects over the upper surface of the airfoil [1-5]. Surface pressure measurements show a decreased pressure coefficient at the leading edge as a result of delayed separation and vortex presence on the airfoil upper surface [6-10]. As the leading edge vortex grows and begins to move across the upper surface, a broadening of the low-pressure region is observed which coincides with increased lift coefficient prior to vortex shedding.

For the case of flapping machines, birds and insects, this behaviour is beneficial and critical for sustained flight. For rotary machines, such as vertical- and horizontal-axis wind turbines, dynamic stall can significantly reduce the performance output and impose increased fatigue and loads on rotor blades during operation at low flow speeds and during start-up. Therefore, the need to further understand the dynamic stall process is critical for optimisation of the performance, whilst also reducing operation and maintenance costs of rotary machine parts exposed to increased fluctuating loads.

Wind turbine blades are frequently exposed to a high degree of oscillatory and gust-like conditions which are characterised by rapid changes in flow angle to high angles of attack

(i.e. high rotation rates). Tower shadow, atmospheric turbulence and turbine-turbine wake interaction for horizontal-axis wind turbines [11-14], and wake interaction for vertical-axis wind turbines [15], place varying unsteady flow conditions on wind turbine blades. In addition, the control of dynamic stall can assist with power generation and reduced load fluctuation resulting in increased lifetime and lowered maintenance costs [16-18].

The unsteady operating conditions of these machines typically lead to transient variations in the angles of attack, which in turn result in dynamic-stall conditions and increased load fluctuation. In order to design wind turbine structures to cope with or minimise the effects of these conditions, we must first understand the underlying flow mechanisms and the influence of basic design parameters.

Blades of wind turbines are designed to meet a range of requirements, including blade structural load limits, aerodynamic efficiency, and hub integration. All of these factors impact the overall thickness of the blade structure, resulting in variable aerodynamic performance characteristics along the span of the blade. Thickness ratios of wind turbine blades may vary as much as from 27% at the root to 15% at the tip [19]. Due to this variation in airfoil thickness, deviation in aerodynamic performance and flow behaviour along a blade is expected under dynamic stall conditions. It has been shown that the blades of horizontal axis wind turbines can experience dynamic stall conditions on up to 80% of their blade length, or potentially operate continuously in stalled conditions for the majority of their operation [11]. To achieve optimal performance of rotary machines in low flow speed conditions, it is therefore essential to understand the effects of the blade thickness ratio with respect to dynamic stall development across a wide range of airfoil

profile thicknesses. Although thick and thin airfoils have been compared comprehensively at steady-state conditions, there have been no studies that specifically focus on the unsteady flow field development and forces produced by thick and thin airfoils operating in identical, highly-unsteady conditions and at extreme angles of attack, i.e. gust like operating conditions. A comprehensive, systematic and direct comparison between thick and thin airfoils undergoing dynamic stall at high (unsteady) reduced frequencies is therefore warranted in order to distinguish the differences in flow structure and force characteristics. For unsteady flows, where $\kappa > 0.05$, the effects of rotation are considerable and induced inertial flow effects cannot be ignored. Similarly, for $\kappa < 0.05$, the flow is considered quasi-steady with only minor inertial effects influencing the resulting force generation [20].

Panda and Zaman [21] and Panda and Zaman [22] successfully conducted wake surveys of an unsteady oscillating NACA 0012 airfoil at Reynolds numbers of 22,000 and 44,000, and deduced the effect of increasing the non-dimensional pitch rate on the delay in formation of the dynamic stall. The velocity profiles in the wake were utilised to estimate the lift with a good agreement with their PIV experimental data, however only for low angles of attack and rotation rates. Similar studies of the flow structure development at low Reynolds numbers (5,000 and 25,000) and for angles of attack between $0°$ and $30°$ were also performed using particle image velocimetry (PIV) in a water towing tank facility [23, 24]. Formation of the leading-edge vortex and roll-up of a shear layer vortex on the suction side of the airfoil are highlighted, whilst the convection and separation of the leading-edge vortex is suggested to be associated with the accumulation of fluid ahead of the leading-edge vortex, which induces the leading-edge vortex away from the airfoil surface and into the faster moving free-stream [24].

Detailed numerical investigations of the dynamic stall process are presented in a large body of work focusing on addressing dynamic stall flow structure development at low Reynolds numbers and for multiple rates of constant-pitch-rate motion and to elevated angles of attack [25-29]. Visbal and Shang [26] present the effects of pitch rate and pitch axis on the induced forces and vortex development of a pitching NACA 0015 airfoil. Here the maximum angle of attack is $\alpha = 60°$, whilst the Reynolds number ranged between $Re = 0.2 \times 10^4$ and $Re = 1 \times 10^4$. The results show that the formation of the leading-edge vortex, in conjunction with an upper-surface separation region over the rear of the airfoil, was directly dependent on both rotation rate and pitch axis location. Continued rotation of the airfoil to elevated angles of attack resulted in the separation of the upper-surface separation region prior to its amalgamation with the leading-edge vortex. In a similar study using a NACA 0015 airfoil, Visbal [25] provided the results of local Mach number development for a constant-pitch-rate motion, and for $Re = 0.6 \times 10^6$ through to $Re = 3 \times 10^6$. Although a parametric study of the rotation rate, pitch axis location and Reynolds number were performed to assess their impact on Mach number, the flow structure formation at the higher Reynolds numbers is not available for comparison to presented force data.

Low Reynolds number dynamic stall about a SD-7003 airfoil undergoing plunging and oscillating motion is investigated in Visbal [28]. In the study, detailed flow structure developed on the upper surface of the airfoil is presented for an unsteady reduced frequency of $\kappa = 0.25$, where $\kappa = \pi f c / U_\infty$, $Re = 1 \times 10^3$ through to $Re = 1.2 \times 10^5$, and where the effective range of the angle of attack, during airfoil pitch-up motions, was between $\alpha = -6°$ and $\alpha = 22°$. The results indicated a significant variation in flow

structure, with higher force coefficients and increased vortex breakdown occurring with increased Reynolds number. Although this material provides invaluable details of the vortex formation and shedding process, the results presented are for a singular airfoil geometry and for shallow angles of attack. As such, there remains a gap in the knowledge of unsteady aerodynamics that address the difference between flow structure development of both thick and thin airfoils operating at high angles of attack (beyond $\alpha = 60°$) and at high rotation rates. Further studies are therefore required for identification of variations in flow structure with respect to airfoil thickness ratio, angles of attack, where $\alpha > 30°$, and high rotation rate operating conditions.

A study using high fidelity large-eddy simulations in Visbal [29] was used to assess the impact of the upper surface laminar separation bubble on dynamic stall development for a NACA 0012 airfoil subject to constant-pitch-rate motion. In the numerical models the maximum angle of attack was $\alpha = 30°$, whilst the non-dimensional rotation rate was fixed at $\kappa = 0.05$. Although Visbal [29] discusses the critical role of the laminar separation bubble in initiating the events contributing to leading-edge vortex formation, further research is required to determine whether these mechanisms apply to a broader range of rotation rates and airfoil thickness.

Consequently, to address the identified gap in the literature, the current article presents a study of both a thick and a thin airfoil geometries subject to highly unsteady, high angle of attack, constant-pitch-rate dynamic stall conditions that are typically associated with gust-like atmospheric conditions about wind-turbine blades and perching manoeuvres of MAV's and natural flyers. The article focuses on two similar airfoil geometries, namely the NACA 0021 and a NACA 0012, operating in identical, highly-unsteady conditions and at

extreme angles of attack. This work will further extend the knowledge of highly unsteady aerodynamics, similar to work performed in Visbal [26, 27, 29]. However, the work herein will focus on a difference performance parameter space which investigates highly unsteady operating conditions to extreme angles of attack. Direct comparison of these flow cases provides insights into the effects of thickness variations on the lift and the flow patterns, including the development of the dynamic stall vortex, and more specifically, the separation bubble observed prior to the formation of the leading-edge dynamic stall vortex.

Materials and Methods

Experimental investigations were conducted in two test facilities located at the University of Adelaide. A water channel was utilised to determine major flow structure development using phase-averaged PIV, whilst a wind tunnel was utilised to evaluate forces generated during the dynamic stall process. Two symmetrical airfoils of differing thickness ratios (NACA 0021 and a NACA 0012) were assessed using similar rotation rates and Reynolds numbers between each test facility.

To simulate dynamic-stall motion during PIV analysis, a brushless direct-current motor with internal position encoder was directly coupled to the wing section with $c = 0.07m$, and $b = 0.45m$, and an aspect ratio of 6.4. The water channel had a working cross-section of $0.5m \times 0.45m$. To isolate the aerodynamic forces and to minimise inertial effects, the pivot axis of the wing was positioned at the half-chord location in order to reduce virtual mass effects, as proposed in Stevens and Babinsky [30]. Angles of attack ranged between $\alpha = 0° \text{ and } 90°$, with PIV images being acquired every $10°$ of airfoil rotation throughout

the pitch-up motion until the maximum angle of attack was reached. The non-dimensional pitch rate, κ, was set to values of 0.05, 0.1 and 0.2, such that quasi-steady and unsteady flow conditions are replicated. Although most of the applications experiencing dynamic stall occur at higher Reynolds numbers, the unsteady separation and external flow developed under unsteady rotation conditions have been shown to be independent of Reynolds number [23]. Therefore, due to the limitations in scale of the test facilities, the Reynolds number was maintained at a constant value of 20,000 for all test cases. A smooth transition to constant angular velocity was achieved by limiting the motor acceleration phase to the first 5°, and the deceleration to the last $5°$ of the total angular displacement of the airfoil. The position of the airfoil was controlled to within $\alpha = \pm 0.25°$ of the target study angle of attack. The angular displacement with respect to non-dimensional time, T^*, is shown in Fig. 1.

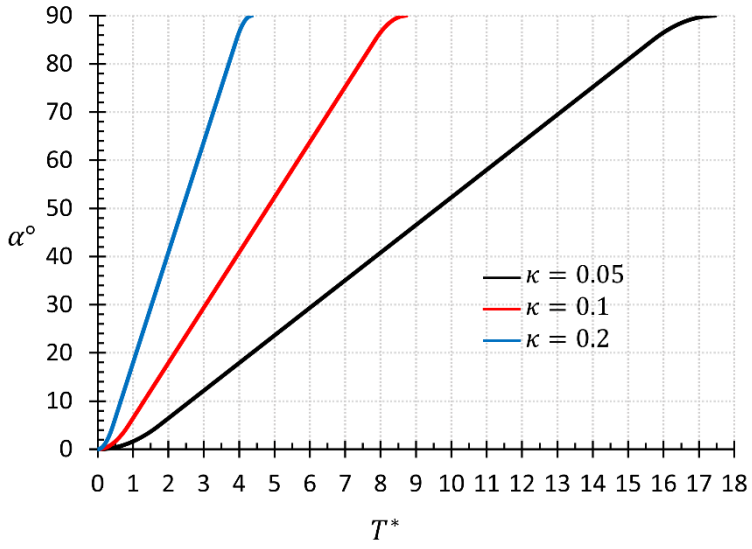

Fig. 1 Airfoil angular displacement with respect to non-dimensional time for reduced frequencies of $\kappa = 0.05$, $\kappa = 0.1$ and $\kappa = 0.2$.

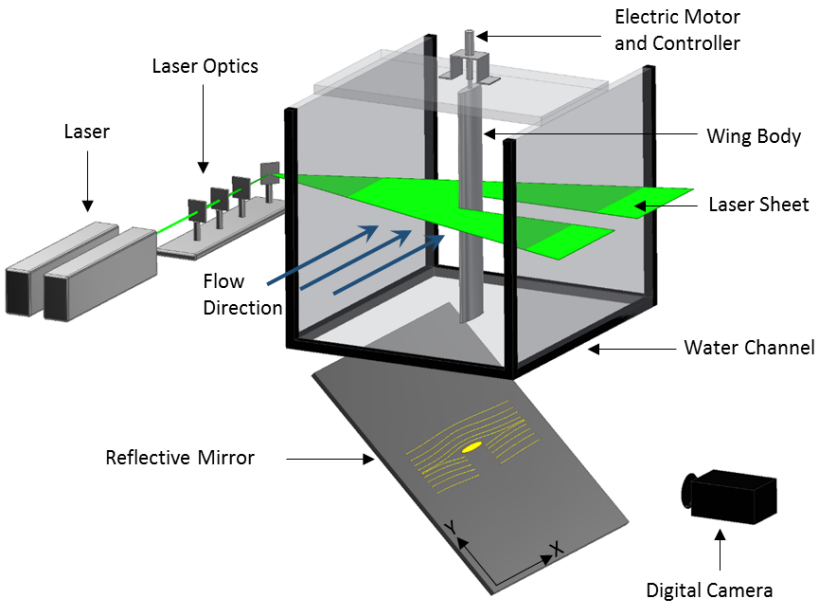

Fig. 2 Schematic diagram of the water channel test facility used to conduct the constant pitch-rate experiments, showing the orientation of the digital camera, laser sheet and dynamic stall test apparatus.

The arrangement of the water channel, test apparatus and PIV setup is indicated in Fig. 2. The test wing was clamped in a fixture located below the free surface of the water channel, and which acted as an end plate in order to reduce three-dimensional effects. A similar arrangement is utilised in Conger and Ramaprian [8] who performed similar water tunnel PIV experiments using a NACA 0015 airfoil. Three-dimensional effects at the tip of a heaving and pitching wing were shown to have a significant influence on the flow structure development during unsteady motion, although these effects only had a minor impact on the flow field development at the mid-span location [31]. As such, three-dimensional flows created at the intersection of the test wing and the free-surface of the water channel could be considered to be minor in the current investigation, where the plane of analysis is located at the mid-span position. The wing was directly coupled to the

motor and gear box arrangement. To limit bending of the wing, the lower end of the wing was located at a fixed position in the floor of the water channel tunnel using a locator pin fixed at the mid-chord position. The gap between the airfoil and the water channel floor was 1.6mm, sufficiently small (less than $0.005 \times \mathrm{span}$) to avoid leakage effects at the wing tip and water tunnel junction [32].

PIV images were captured using a Kodak MegaPlus ES1.0 CCD digital camera with 1008×1018 pixel resolution. A digital control system was developed to phase-lock the camera trigger and airfoil position to consecutive 10Hz laser pulses generated from a frequency-doubled Nd-YAG laser. To alleviate airfoil shadow in the obtained images, phase-averaged data were superimposed from both above and below the airfoil such that complete flow field velocity vectors could be obtained. A total of 200 image pairs was used for phase averaging to ensure statistical convergence of the velocity fields. Lighting was such that a 3mm thick horizontal sheet penetrated the mid-chord location of the water channel to minimise three-dimensional effects. Spherical polyamide particles with a specific gravity of 1.03 and diameter of $50\mu m$ were used for flow seeding. Combined with a magnification factor of 7.3 on the camera, particle pixel diameters of 1-3 pixel units were achieved in order to reduce peak-detection bias errors during image correlation [33, 34]. The PIV velocity vectors were established using a 32×32 pixel interrogation window, resulting in approximately 2.19mm between each velocity vector at 50% overlap. A 3-point Gaussian peak-detection method with Nyquist filtering was implemented and interrogated three times using a multi-pass analysis within PIVView V1.7. Streamlines were computed using the streamline function within Matlab®, whilst normalised vorticity fields were evaluated according to Equation 1. Using the phase-averaged PIV data, an averaged velocity flow field was established to capture the major dynamic-stall and post-stall flow structures.

$$\omega_z = \left[\frac{\delta v}{\delta x} - \frac{\delta u}{\delta y}\right] \cdot \frac{c}{U_\infty} \quad (1)$$

For assessment of the aerodynamic force, a series of separate tests were performed using an open-return wind tunnel with a test section opening of $0.5m \times 0.5m$ and a turbulence intensity of $\sim 0.8\%$ [35]. A similar study using two independent test facilities, for evaluation of external flow fields and force measurement, was undertaken to investigate the response of a cavity on the upper surface of an airfoil undergoing dynamic stall conditions [36]. In these experiments, a turbulence intensity of the wind tunnel was 0.2%, whilst no details of the water channel turbulence intensity was provided. In addition, the blockage of the wind tunnel was 11.1% at $\alpha = 20°$, whilst the blockage of the water tunnel was 5.5% at only $\alpha = 6°$. In the current investigation, two wing bodies, with similar airfoil profiles to those used in PIV testing, were constructed such that $c = 0.1$m and $b = 0.5$m. Corrections for tip effects of the wing were not necessary for the wind tunnel tests due to the installation of end plates positioned within $2mm$ of the wing tip. Surface pressures were evaluated using a series of $50 \pm 1\%\ Pa$ Honeywell Truestability® differential pressure sensors imbedded in each of the NACA 0012 and NACA 0021 wing bodies. The sensors incorporated temperature self-calibration and internal amplification. The sensors produced an error in the evaluated pressure of the current operating range of $\pm 2.5\%$. Analogue signals were collected using a National Instruments NI-6210 data acquisition module, with a sample rate of $f_s = 10{,}000Hz$ for all of the 100 individual ramp-up cases performed for each dimensionless pitch rate. The sample frequency was determined to be sufficient to capture all vortex structures occurring during the pitch-up process. Axial and tangential force coefficients were evaluated through trapezoidal integration of the measured surface pressure distribution, whilst net forces in the airfoil

coordinate system were transferred to the local wind tunnel coordinate system using standard coordinate transformation techniques.

A schematic representation of the sensor locations within the NACA 0012 wing is shown in Fig. 3, whilst details of the sensor orifice positions on the surface of the NACA 0021 were similar to those described in Choudhry et al. [37] and Jumper, Schreck and Dimmick [9].

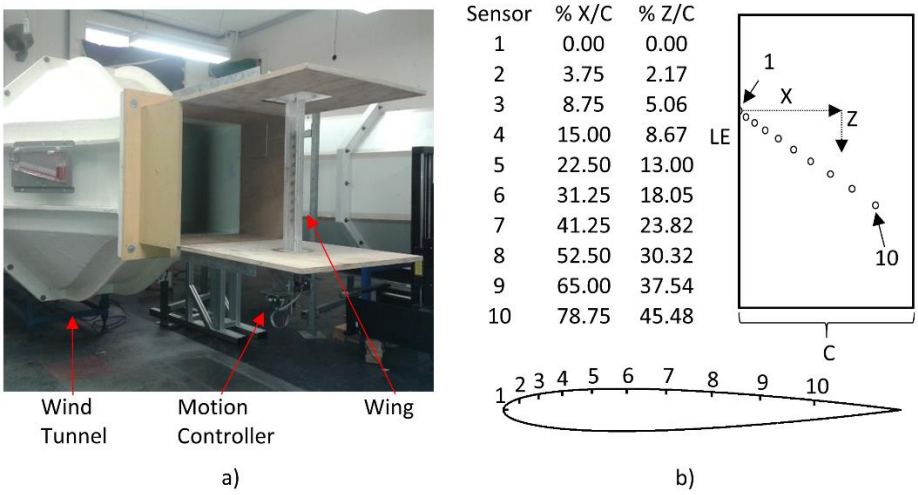

Fig. 3 Wind tunnel and motion controller arrangement (a) and details of the NACA 0012 wing body showing the orientation and locations of the imbedded differential surface pressure sensors

The non-dimensional rotation rate and Reynolds number were consistent with those of the PIV measurements performed in the water channel, such that $\kappa = 0.05, 0.1, 0.2$ and $Re = 20{,}000$. The location of the rotation axis was maintained at the wing half-chord location.

Due to the use of different test facilities, the effects of blockage and turbulence intensity, Tu, were important due to their impact on promoting early transition of the boundary layer and altering the forces during the pitch-up motion. Maximum blockage within the water channel was limited to 14%, whilst the maximum blockage of the open jet wind tunnel was 20%. Maximum blockage occurred periodically for both facilities as the airfoil reached its maximum angle of attack. After reaching $\alpha = 90°$, the airfoil was rotated back to $\alpha = 0°$ and held fixed for 30 chord length of flow travel prior to the beginning of subsequent test cycles. The impact of blockage on the flow structure development of pitching wings is described in Granlund et al. [38]. From their findings, short periods of high blockage were not observed to have a significant influence on the resulting forces during the dynamic stall process. Consequently, in the current investigation, where only short durations of elevated angles of attack are achieved, the influence of blockage on the flow structure development was considered to be minor.

The wing was positioned $250mm$ downstream of the wind tunnel opening, allowing for the free expansion of the wind tunnel streamlines [39]. This reduced blockage effects allowing the airfoil aerodynamics to be evaluated with confidence. In addition, due to the absence of side walls on the wind tunnel, wake blockage effects were considered to be negligible [32]. Therefore, no corrections for solid body or wake blockage were applied.

The impact of flow facility turbulence intensity has been demonstrated to influence both flow separation and the development of separation bubbles about airfoils exposed to various Reynolds numbers and pitch rates [32, 8]. In the current analysis, the turbulence intensity of the wind tunnel flow was $Tu = 0.85\%$ at $Re = 20{,}000$ [35], whilst the

turbulence intensity of the water channel flow was approximately $Tu = 2\%$ [40] for $Re = 20{,}000$.

If these differences in turbulence intensity are significant, they will be seen in the flow structures such as laminar separation bubbles on the airfoil surfaces and the unsteady separation process itself. Firstly, at *Re* = 20,000 it is expected that laminar separation bubbles will occur, and that differences in free-stream turbulence intensity will affect the location and size of these separation zones. However, with variations in turbulence intensity between the facilities of only 1.15% and the high rotation rates applied, these differences are expected to be minor. Secondly, as discussed by Lourenco et al., 1993, the unsteady separation process is relatively universal and substantially independent of the Reynolds number and external flow conditions. Thus, at the low Reynolds numbers and relatively similar turbulence intensities considered herein, differences between the two test facilities can be considered to be minimal.

Results and Discussion

Constant pitch-rate dynamic stall was investigated using a thick NACA 0021 and a thin NACA 0012 airfoil. The PIV data for each airfoil was collected at $\kappa = 0.05$, $\kappa = 0.1$ and $\kappa = 0.2$, where both airfoils showed dynamic-stall characteristics at these reduced frequencies. To study the post-stall flow characteristics, the airfoils were allowed to rotate through to $\alpha = 90°$ prior to cessation of PIV data collection. This ensured that deep-stall characteristics were achieved and development of the shedding vortex structures was well established.

Pre-Vortex Formation

The dynamic-stall vortex is shown to develop at the leading edge for all non-dimensional pitch rate cases investigated ($\kappa = 0.05$, $\kappa = 0.1$ and $\kappa = 0.2$). In addition, increasing the non-dimensional pitch rate is found to delay the onset of leading-edge vortex formation to higher angles of attack. Fig. 4 shows the streamline patterns and normalised vorticity magnitudes for three respective test cases where formation of the dynamic-stall leading-edge vortex begins. It can be seen that for $\kappa = 0.05$, the beginning of vortex formation occurs at $\alpha = 20°$. Although $\kappa = 0.05$, which is indicative of high quasi-steady flow conditions [20], a comparison with the steady-state stall angle of attack, where $\alpha = 10°$, suggests that under the current test conditions, the airfoil rotation has a significant impact on the overall flow structure and force generation characteristics of the wing. It can also be seen that the angle of attack at which leading-edge vortex formation occurs increases with non-dimensional pitch rate, so for $\kappa = 0.1$, $\alpha = 30°$ and $\kappa = 0.2$, $\alpha = 40°$.

Prior to leading-edge vortex formation, the presence of a displaced shear layer above the upper surface of the airfoil can be observed. The shear layer extends to the trailing edge of the airfoil where a second stagnation point is observed, as indicated in Fig. 4. Within this region, bound between the shear layer and upper surface of the airfoil, there exists a region of low-velocity flow with clockwise vorticity representative of a separation bubble. Unlike trailing-edge stall, where the flow begins to separate at the trailing edge and continues towards the leading edge with increased angle of attack, the pitch-up motion inhibits this trailing edge separation and prevents flow detachment to elevated angles of attack.

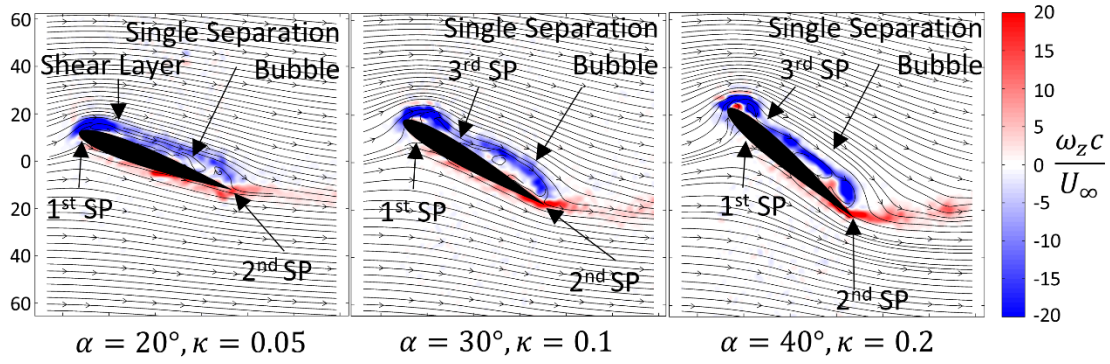

Fig. 4 Initiation of the leading edge vortex showing its delay in formation to higher angles of attack as the non-dimensional pitch rate is increased from $\kappa = 0.05 - 0.2$ for a NACA 0012 airfoil. Also observed is the detached shear layer and additional stagnation points (SP) on the upper surface of the airfoil during the pitch-up motion.

Increasing the non-dimensional pitch rate delayed the breakdown of the separation bubble over the rear of the airfoil, until higher angles of attack. This allowed flow to be drawn back towards the surface of the airfoil and to a second stagnation point located at the trailing edge. The presence of the separation bubble delays separation of the boundary layer, allowing increased suction and lift to form prior to its breakdown [41].

For the unsteady reduced frequencies, $\kappa = 0.1$ and $\kappa = 0.2$, where unsteady effects become significant in dictating flow separation characteristics [20], the existence of the separating vortex structures, resulting from the breakdown of the separation bubble above the upper surface, are not observed at low angles of attack. Increasing rotation rate is shown to reduce the effects of the minor vortex structure development, allowing the rear separation bubble to maintain its presence until higher angles of attack and until formation of the leading-edge vortex. The airfoil rotation, as seen in Fig. 4, is shown to

suppress flow separation until the leading-edge vortex forms. Only once the leading-edge vortex forms are further increases in lift achieved, beyond steady-state lift values.

Vortex Development Flow Structure

Critical flow structures and topological flow features developed during dynamic stall include minor vortex structures on the upper-rear surface of the airfoil, a rear separation bubble, a half-saddle point (HSP) and stagnation points (SP) attached to the airfoil surface, and the leading-edge vortex, as indicated in Fig. 4 and Fig. 5.

After leading-edge vortex development, minor changes to the vortex shedding process occur with increasing non-dimensional pitch rate. At extreme angles of attack, vortex growth and size become more dependent on the location of the leading-edge vortex, behind the airfoil, and the maximum airfoil angle of attack. Once the leading-edge vortex separates, the wake of the airfoil exhibits periodic von-Karman vortex shedding, representing bluff-body separation [42, 43]. Fig. 5 shows PIV contour plots of normalised vorticity for both airfoils at increasing angles of attack but similar non-dimensional pitch rate, where $\kappa = 0.05$. Both airfoils exhibit dynamic stall characteristics such that delayed leading-edge separation and formation of a dynamic-stall vortex are observed. The flow patterns at $\alpha = 10°$ in Fig. 5 show a clockwise (negative vorticity) closed separation bubble over the rear half of each airfoil, with reattachment occurring at the trailing edge. The separation bubble is observed not to burst, leading to delayed flow separation and increased lift. In contrast, a difference in flow structure is observed at $\alpha = 20°$. For the NACA 0012, a region of high vorticity develops at the leading edge in conjunction with a closed separation bubble located above the rear of the airfoil. With the presence of the

leading-edge vortex, a half-saddle point is produced behind the vortex at the airfoil surface.

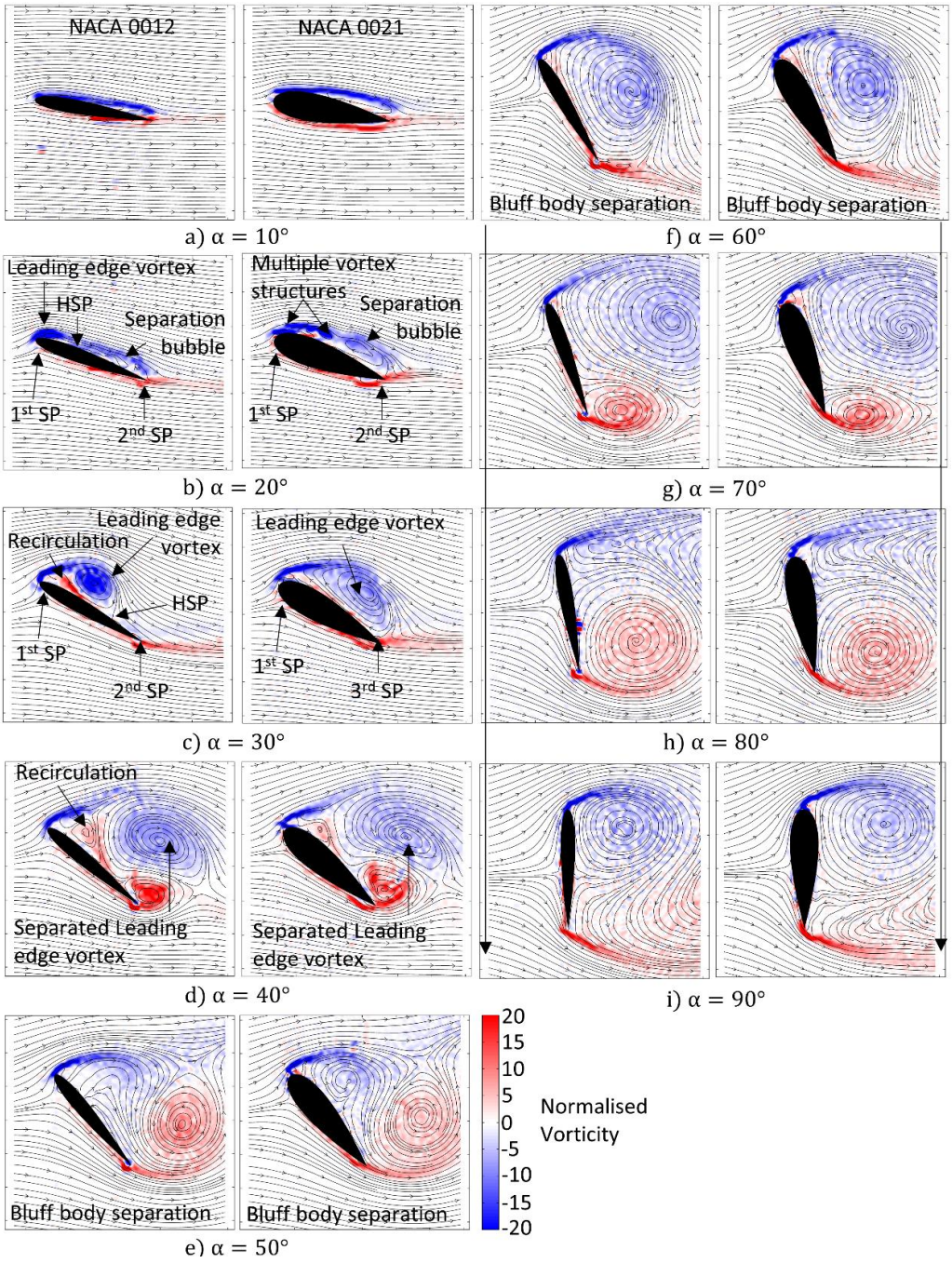

Fig. 5 Normalised vorticity contours and streamlines developed during dynamic stall of a NACA 0012 (left) and NACA 0021 (right) airfoil. $\kappa = 0.05$.

This half-saddle point divides the initial separation bubble into two zones of clockwise vorticity, including a leading-edge vortex and a trailing-edge vortex. With comparison to the NACA 0021 at $\alpha = 20°$, observation of a region of negative vorticity at the leading edge indicates the breakdown in attached flow and onset of leading-edge vortex formation. A similar vortex development process was indicated in Shih, Lourenco and Krothapalli [23], however only a NACA 0012 airfoil rotating under quasi-steady reduced frequencies was investigated. Under the current test conditions, leading-edge vortex development is shown to be highly dependent on the airfoil thickness, with a much broader recirculation zone occurring above the NACA 0021 in comparison to the NACA 0012, as seen in Fig. 5b and Fig. 5c, which developed a concentrated leading-edge vortex over the forward 50% of the airfoil suction side.

The differences in the position of the separation bubble on the upper surface suggests that under the highly unsteady flow conditions in the current investigation, airfoil thickness can significantly alter the surface pressure distribution, due to the separation bubble, varying the overall lift, drag and moment prior to leading-edge vortex formation.

As both airfoils reach $\alpha = 30°$, growth of the leading-vortex structures continues. The NACA 0012 leading-edge vortex is shown to occupy approximately 0.7 of the airfoil chord, and is terminated by the half-saddle point (HSP) aft of the vortex and located on the airfoil upper surface. For the NACA 0021 airfoil, under the same operating conditions, the leading-edge vortex occupies the entire upper surface of the airfoil, as shown in Fig. 5. Also noted in Fig. 5(d) is a recirculation zone with positive vorticity bounded by the leading-edge shear layer and positioned immediately aft of the leading edge, but ahead of the leading-edge vortex. This recirculation zone is generated as a result of the fluid

ejection produced by the viscous interaction between the wall and the primary leading-edge vortex, as discussed in Rival et al. [44] and Choudhuri, Knight and Visbal [45].

At $\alpha = 30°$, the negative-vorticity separation bubble over the trailing edge is drawn into the leading-edge vortex, where it develops into a single vortex that extends to the airfoil trailing edge. For the NACA 0021 the leading-edge vortex is shown to have grown to an extent that the HSP is located at the trailing edge, whereas in the NACA 0012 case, the outer streamline stagnates at a point approximately 0.7 chord lengths from the leading edge At $\alpha = 40°$, the streamline patterns for both airfoils show that the leading-edge vortex becomes detached from the airfoil, since none of their bounding streamlines are attached to the airfoil surface [46].

Once the leading-edge vortex separates and the airfoil transitions into deep stall, similar vortex structures develop about both airfoils. This suggests that although airfoil geometry has little influence on post-stall flow conditions, it has a significant effect on the onset of delayed separation and dynamic-stall at low pitch rates. This observation is in agreement with previous studies which identify the minimal influences of airfoil geometry in deep stall conditions [47].

Increasing the non-dimensional pitch rate to $\kappa = 0.1$ and $\kappa = 0.2$ results in both airfoils exhibiting similar vortex separation processes. Under such conditions, high-speed rotation of the airfoil delays vortex formation resulting in abrupt and sudden vortex rollup at elevated angles of attack. The flow structure development at these higher reduced frequencies is shown in Fig. 6, for $\kappa = 0.1$, and Fig. 7 for $\kappa = 0.2$.

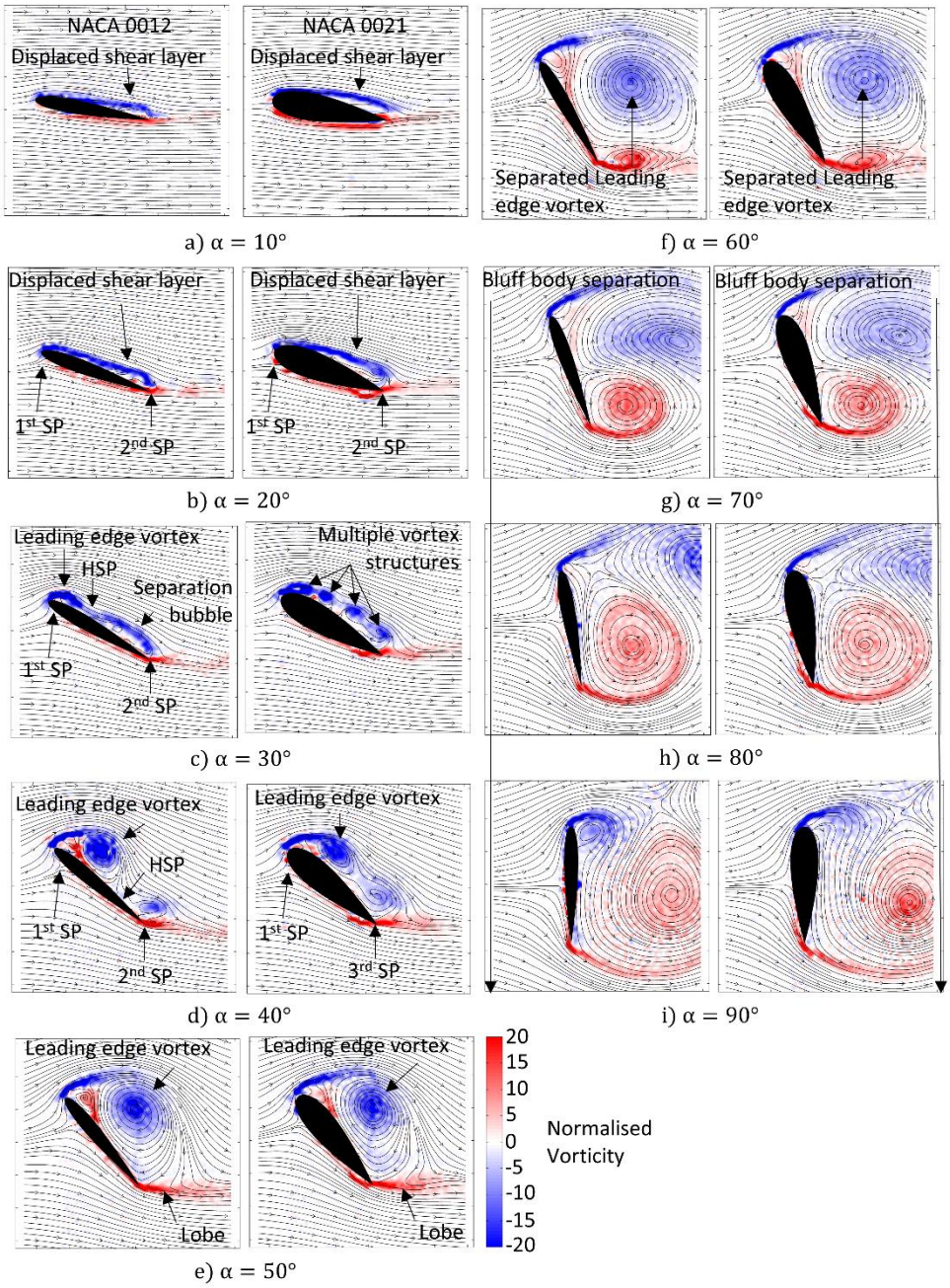

Fig. 6 Normalised vorticity contours and streamlines of a NACA 0012 (left) and NACA 0021 (right) airfoil undergoing dynamic stall where $\kappa = 0.1$.

Fig. 6 shows normalised vorticity contours and streamline patterns developed for both airfoils when pitching during the dynamic stall process for $\kappa = 0.1$. Both airfoils generate a negative vorticity rear separation bubble that extends to the trailing edge, as indicated

in Fig. 6(a-b). Due to the expansion of the separation bubble, the shear layer moves away from the airfoil surface and into the freestream. The shear layer is shown to re-attach at the trailing edge at $\alpha = 10°$. For shallow angles of attack, the flow structure development for a non-dimensional pitch rate of $\kappa = 0.1$ is similar to that for tests with the non-dimensional pitch rate, $\kappa = 0.05$, although delayed by approximately $10°$. For $\kappa = 0.1$, the separation bubble remains positioned over the rear upper surface of both airfoils throughout the pitching movement and until the angle of attack reaches $\alpha = 30°$. During this period of rotation, thickening of the separation bubble due to the inclusion of multiple minor vortices with negative vorticity can be observed. Similar vortex structures were observed in Shih, Lourenco and Krothapalli [23], however in their tests the non-dimensional pitch rate was $\kappa = 0.065$ and quasi-steady. Under the unsteady rotation rates, where $\kappa = 0.1$ and $\kappa = 0.2$, in the current investigation, minor impact of the non-dimensional pitch rate and airfoil geometry on the formation of the rear separation bubble and its enclosed vortex structures are observed.

As the airfoils approach $\alpha = 30°$ (Fig. 6(c)), both airfoils show signs of initial leading-edge vortex development. This stage represents the initiation of dynamic stall where abrupt leading edge vortex growth is imminent. For the NACA 0012 airfoil, separation at the leading edge begins whilst the rear separation bubble remains attached over the trailing edge of the airfoil. However, the NACA 0021 appears to generate multiple vortex structures within the rear separation bubble in conjunction with the initiation of the leading-edge vortex. In Fig. 6(d), at $\alpha = 40°$, both airfoils have developed a distinct leading-edge vortex. This vortex continues to develop until $\alpha = 50°$, where the leading-edge vortex engulfs the negative vorticity regions that are present over the rear of the airfoil. From $\alpha = 50°$ to $\alpha = 90°$ (Fig. 6(e-i)) the trailing-edge stagnation point gradually

detaches from the airfoil and transitions into the free-stream, indicating the initiation of deep-stall and fully separated flow [46]. Whilst the trailing-edge stagnation point remains attached to the airfoil, increases in lift generation of the airfoil are possible [8, 9, 48].

For $\kappa = 0.2$, similar flow development to $\kappa = 0.1$ is evident, as indicated in Fig. 7. However, for $\kappa = 0.2$, the process of dynamic stall and leading-edge vortex development is delayed due to the increase in rotation rate. Both airfoils exhibit similar flow behaviour, where a separation bubble of negative vorticity develops over the upper surface of the airfoil and with reattachment taking place at the trailing edge.

The leading-edge vortex formation is delayed until $\alpha = 40°$ for the NACA 0012 and $\alpha = 50°$ for the NACA 0021 (Fig. 7(d)). Fig. 7(e-g) shows that between $\alpha = 50°$ and $\alpha = 70°$ engulfment of the rear vortex structures by the leading-edge vortex occurs. Beyond $\alpha = 70°$ (Fig. 7), both airfoils are seen to develop a positive vorticity trailing-edge vortex, representing early stages of bluff-body separation.

Through PIV measurements and under the high reduced frequencies tested, the present study highlights the strong dependency of dynamic stall on inertial based flows around pitching airfoils. Although earlier work discusses the influence of the inertial loads on aerodynamic force generation [26, 20], the current article highlights the significance of rotation rate, and its effects on the flow structure and load characteristics developed during dynamic stall of dissimilar airfoil geometries at elevated angles of attack and highly unsteady rotation rates.

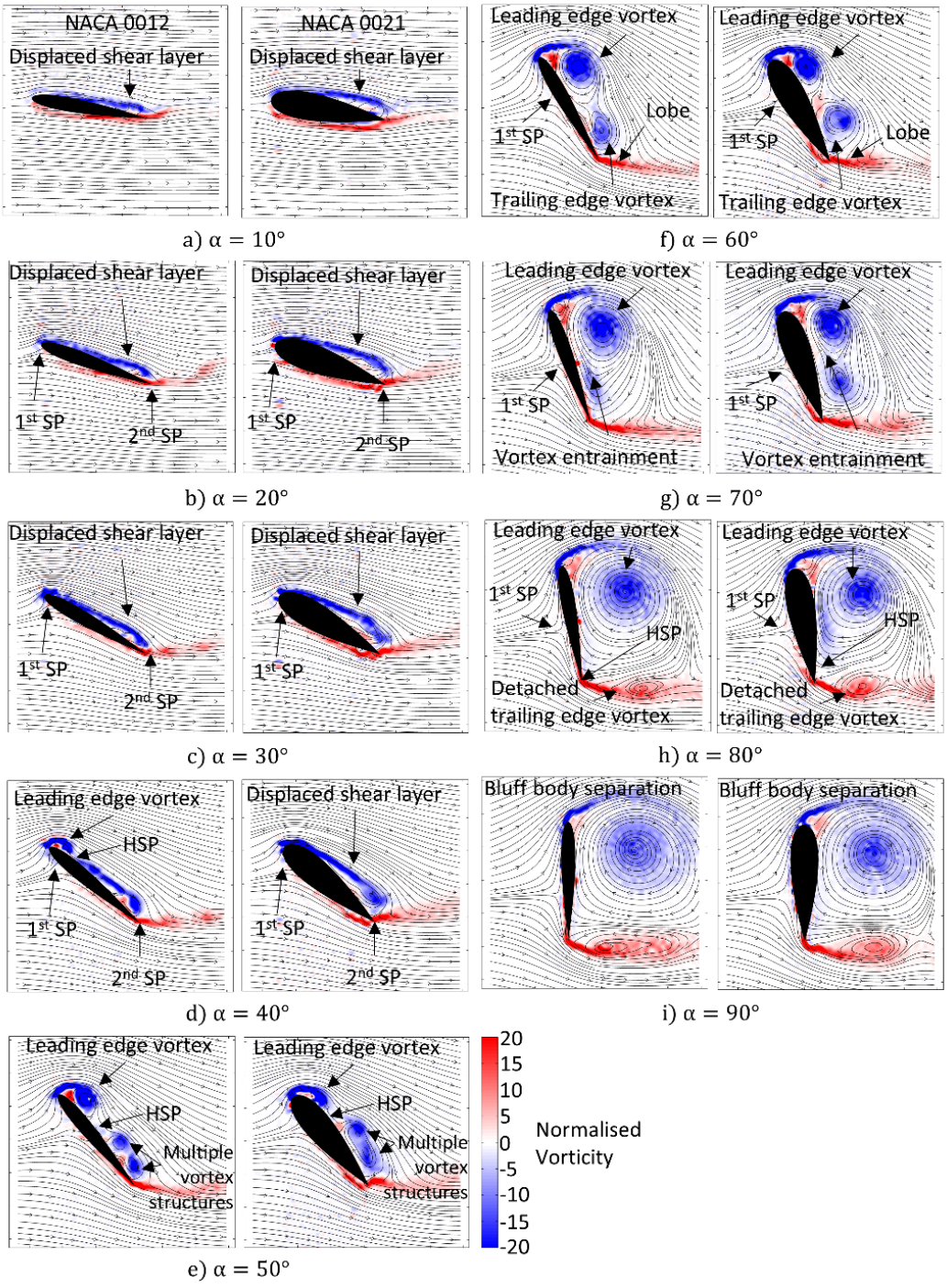

Fig. 7 Normalised vorticity contours and streamline development of a NACA 0012 (left) and NACA 0021 (right) airfoil undergoing dynamic stall where $\kappa = 0.2$.

Force Generation

Determination of the aerodynamic loads indicated significant differences between the unsteady dynamic stall and steady-state tests. Fig. 8 shows the lift coefficient for the NACA 0012 and NACA0021 airfoils for both steady-state and dynamic-stall conditions over the range of reduced frequencies investigated. Fig. 8 and Fig. 12 also show the maximum and minimum fluctuation in force response due to unsteady separation and experimental uncertainty evaluated during the cycle-to-cycle pitch-up motion. The precision of the obtained force results was determined to have a maximum standard deviation of $\sigma = 6\%$ about the mean over the 100 samples of the pitch-up motion recorded during the highly separate and unsteady periods in the dynamic-stall process. The fluctuations are related to the formation of vortex structures and separation bubbles developed on the airfoil upper surface leading to increased surface pressure variation. Similar fluctuations in force results were also observed for highly unsteady flow generated about a OA209 airfoil undergoing dynamic stall, which resulted in a standard deviation of approximately $\sigma = 10\%$ [49]. For the obtained force results, a confidence level of $CI = 95\%$ resulted in a variability of the mean force coefficients of $\pm 1.2\%$ during peak force generation and fluctuation.

Increase in steady-state lift is observed to be delayed until $\alpha = 5°$ for the NACA 0012. Further increasing the angle of attack led to a sudden increase in lift until the airfoil stalled at an angle of attack of approximately $\alpha = 10°$. The current results for the steady-state case were compared to the data presented in Zhou et al. [50], where wind tunnel tests were performed on a NACA 0012 airfoil using a similar Reynolds number of $Re = 50000$. In addition, viscous solutions using XFOIL were generated for the current test

configurations for both NACA 0012 and NACA 0021 airfoils. Similarly, unsteady results from Conger and Ramaprian [8] show the lift generation for a NACA 0015 airfoil operating at $\kappa = 0.2$ and a Reynolds number of $Re = 120{,}000$. A good correlation between the current tests and experiments in Conger and Ramaprian [8], although using a NACA 0012 in the current investigation, indicates that the unsteady force generation is comparable between high Reynolds number and that vortex shedding at the trailing edge significantly influences the unsteady lift during the pitch-up process.

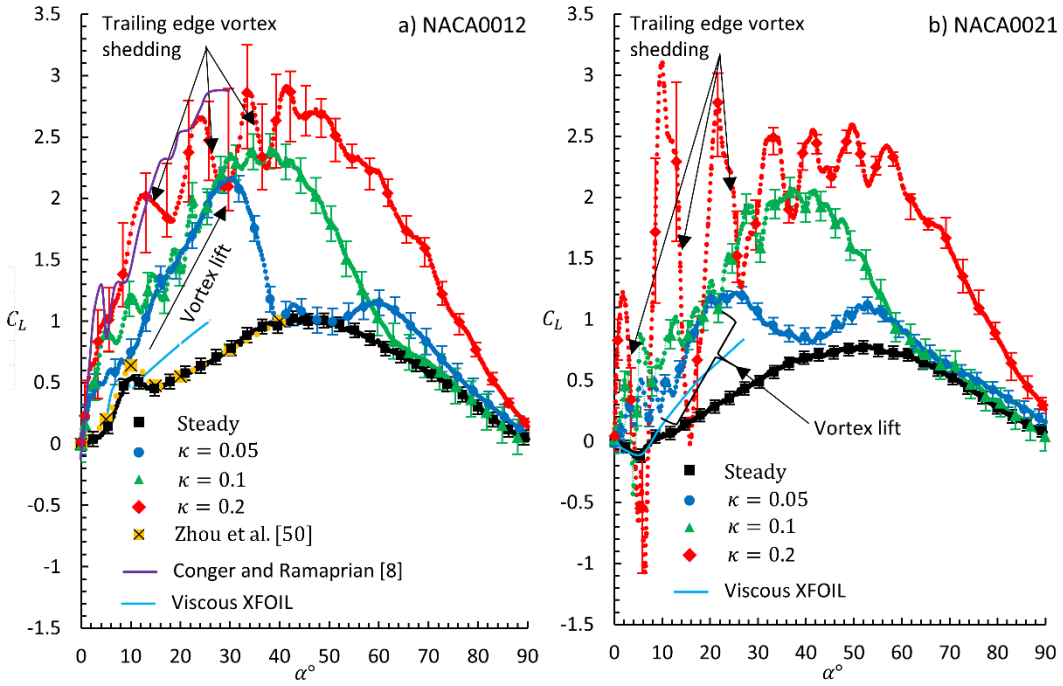

Fig. 8 NACA 0012(a) and NACA 0021(b) lift coefficient comparing the dynamic stall and steady-state test cases. Initial lift delay is observed for the steady-state case, whilst inertial and vortex lift is evident in dynamic stall conditions. Error bars indicate maximum and minimum fluctuation in force coefficient evaluated, whilst an error of 1.2% was established about the mean to achieve a 95% confidence level.

A reduction in lift, prior to $\alpha = 5°$, can be attributed to a separated shear layer, which becomes turbulent and reattaches to form a separation bubble at $\alpha = 10°$ [51-53], and reduced pressure on the lower side of the airfoil, as identified in Anyoji et al. [54]. For the NACA 0021, negative lift was developed for an angle of attack, where $\alpha < 8°$ and under steady-state conditions, as shown in Fig. 8. Similar conditions have also been reported in Hansen, Kelso and Dally [55], where negative lift was produced by a NACA 65-021 airfoil, as a result of a laminar separation bubble on the rear lower portion of the airfoil. The influence of the separation bubble on the surface pressure distribution of the NACA 0021 is shown in Fig. 9.

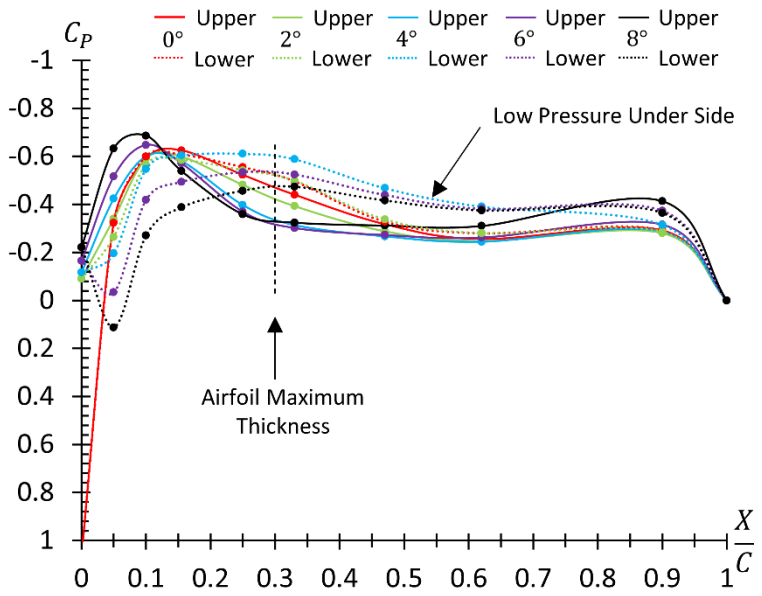

Fig. 9 NACA 0021 surface pressure distribution highlighting the increased suction on the lower surface resulting from the formation of a separation bubble at low angles of attack, and over the rear of the airfoil at low Reynolds numbers.

In Fig. 9, the presence and influence of the separation bubble developed on the surface pressure distribution of a NACA 0021 airfoil is presented. With increased angle of attack, the separation bubble on the lower side is observed to increase in length, as shown by

decreases pressure coefficient, and transition towards the trailing edge until $\alpha = 5°$. As the angle of attack is further increased, the pressure distribution flattens as the flow becomes fully attached. This continues until $\alpha = 10°$, where stall occurs. Similar results of negative lift for the initial $10°$ of airfoil rotation under steady state conditions was calculated using the viscous XFOIL predictions. However, results from XFOIL are observed to over predict the lift coefficient for both test airfoils when stall is reached. This anomaly could be attributed to the low sensor density on the upper surface of the wing combined with three-dimensional effects generated by the wing aspect ratio limiting pure two-dimensional results as utilised in XFOIL.

For all dynamic stall cases, the plateau in lift at $\alpha = 10°$, as seen for the NACA 0012 (Fig. 8) under steady-state conditions, was not observed. By contrast, an increase in lift coefficient was observed to occur until approximately $\alpha = 2°$. From $\alpha > 2°$, a divergence of the lift coefficient for all non-dimensional pitch rate test cases is observed with increasing rotation rate. This is attributed to an increase in rotation rate and associated unsteadiness resulting from induced inertia developed through the airfoil pitch-up motion.

As the angle of attack reaches $\alpha = 10°$, for $\kappa = 0.05$, a sudden increase in lift coefficient results. From Fig. 5, the presence of a thick separation bubble over the rear of the airfoil begins to break down, leading to the formation of the leading-edge vortex. Due to the position of the leading-edge vortex above the airfoil surface, a significant increase in lift occurs until the half-saddle point on the upper surface reaches the trailing edge. At this point, maximum lift coefficient occurs, where $C_L = 2.15$ at $\alpha = 30°$. The NACA 0021 was shown to exhibits similar aerodynamic and flow structure properties, although the

maximum lift coefficient was less, such that $C_L = 1.3$ at $\alpha = 22°$. With the shedding of the leading-edge vortex, significant lift reduction results for both airfoils, as observed, Fig. 8. The lift coefficient curves for both airfoils then approach the steady-state curves until the maximum angle of attack of $\alpha = 90°$.

Increasing the non-dimensional pitch rate to $\kappa = 0.1$ and $\kappa = 0.2$ delayed the leading-edge vortex formation on both the NACA 0012 and NACA 0021 airfoils, and prevented the early reduction in lift-curve slope. Maximum lift, prior to leading-edge vortex formation where $\alpha = 30°$ for $\kappa = 0.1$ (Fig. 6) and $\alpha = 40°$ for $\kappa = 0.2$ (Fig. 7), is attributed to increased inertial loads generated through airfoil rotation. The leading-edge vortex was shown to increase the period of maximum lift by broadening of the lift coefficient curve for increased non-dimensional pitch rates. The difference between the performance of the two airfoils was such that the NACA 0012 generated a maximum $C_L = 2.4$ and $C_L = 2.7$ for $\kappa = 0.1$ and $\kappa = 0.2$ respectively, whilst for the NACA 0021 maximum lift coefficients of $C_L = 1.9$ and $C_L = 2.3$ occurred for $\kappa = 0.1$ and $\kappa = 0.2$ respectively. The increase in lift is attributed to the more concentrated leading-edge vortex generated on the NACA 0012 in comparison to the NACA 0021 airfoil, as shown in Fig. 7c. As observed for $\kappa = 0.05$, once the leading-edge vortex separated from the airfoil, the airfoil proceeded into a state of deep-stall with the reduction in lift coefficient until α_{max} was reached. The increase in lift, beyond steady-state values, is shown to be only lightly influenced by the Reynold number (as shown through comparison of results by Conger and Ramaprian [8]) and airfoil geometry during highly unsteady operating conditions. The physics of the system and resulting forces developed at the unsteady rotation rates examined herein are shown to be significantly influenced by the rotation rate and presence of the leading-edge vortex. Airfoil geometry was only shown to effect the

magnitude of lift fluctuation during the pitch-up phase, which in turn can be linked to trailing-edge vortex shedding.

For all unsteady test cases, an oscillation in the lift-curve slope occurred at angles of attack between $\alpha = 0°$ and $45°$, becoming increasingly larger at higher non-dimensional pitch rates. The oscillation in force coefficient and its frequency was related to a series of vortex structures shedding at the trailing edge during the pitch-up motion, as shown in Fig. 10 using instantaneous flow visualisation of a NACA 0012 during ramp-up dynamic stall.

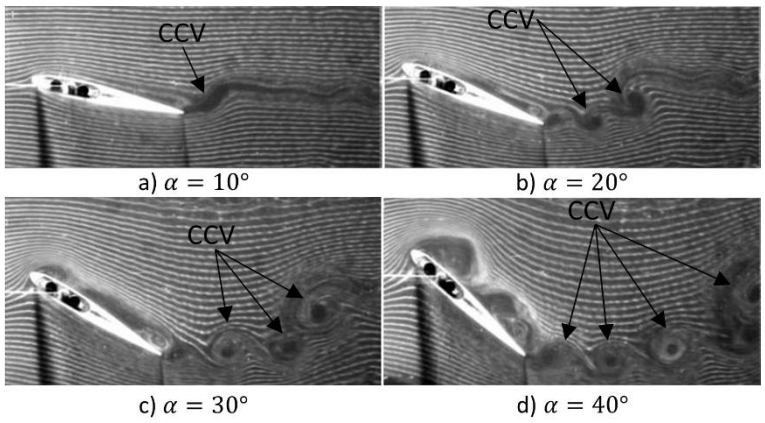

Fig. 10 Vortex patterns observed, using the hydrogen-bubble wire technique, at the trailing edge of the NACA 0012 airfoil resulting in force oscillation during ramp-up dynamic stall [56].

The vortex structures resembled Kelvin-Helmholtz instabilities forming in the shear layer separating the upper airfoil surface flows from the lower surface flows at the trailing edge. Similar observations were also made in Visbal [29], who attributed the force oscillation and decreased the upper surface suction pressure coefficient to the formation of Kelvin-Helmholtz instabilities within the shear layer and originating at the leading edge. By contrast, in the current investigation the leading-edge instabilities are not observed (as

shown in Fig. 10), although the presence of the trailing-edge vortices are identified and linked to the force evolution during the airfoil pitch-up motion.

The authors propose that the shedding of the trailing-edge vortex results in sudden decreases in the bound circulation of the airfoil, which in turn periodically reduces the airfoil lift. The effect of increasing the non-dimensional pitch rate was shown to increase the magnitude of vortex shedding strength. From the results in Fig. 9, higher rotation rates led to more significant oscillations in lift as the vortex structures separated from the trailing edge. This indicates that the strength of the shedding vorticity could potentially be directly related to the non-dimensional pitch rate, however further studies are required for validation.

Although the leading-edge vortex has been shown to increase the overall lift, the higher rotation rates were also observed to augment the lower surface pressure distribution of the airfoil prior to the formation of the leading-edge vortex [57, 10, 58]. Surface pressure distributions around the NACA 0012 airfoil are shown in Fig. 11 for multiple reduced frequencies at various angles of attack to highlight the significance of rotation and also vortex lift on the airfoil.

The airfoil rotation rate is shown to significantly influence the lower-surface pressure distribution prior to formation of the leading-edge vortex. Surface pressure was shown to decrease at the leading edge, whilst simultaneously increasing over the rear underside of the airfoil for $\alpha < 8°$, as indicated in Fig. 11c and Fig. 11d. Also observed is the development of a laminar separation bubble over the rear of the airfoil. The combined effect of the laminar separation bubble and increasing rotation rate is such that the lift-curve slope increases due to manipulation of the airfoil surface pressure coefficient.

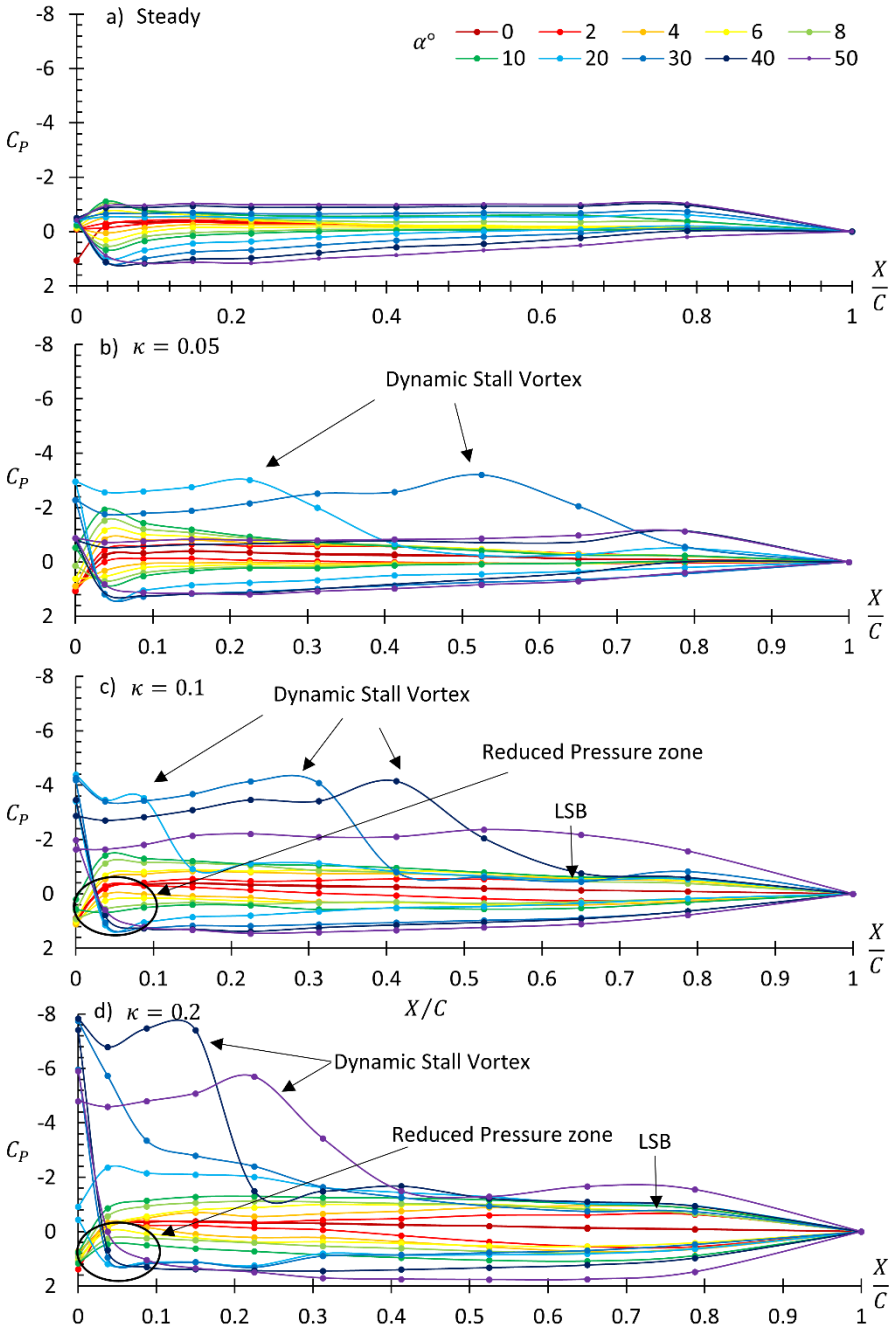

Fig. 11 Surface pressure distribution around the NACA 0012 airfoil experiencing constant-pitch-rate motion to $\alpha_{max} = 90°$ and for multiple unsteady reduced frequencies showing effects of the leading-edge vortex and airfoil rotation rate on both the upper and lower pressure distribution.

Assessment of the drag indicated significant increases in force due to the formation of the leading-edge vortex. Fig. 12 shows the drag coefficient of the NACA 0012 and NACA 0021 airfoil at steady-state and dynamic stall conditions.

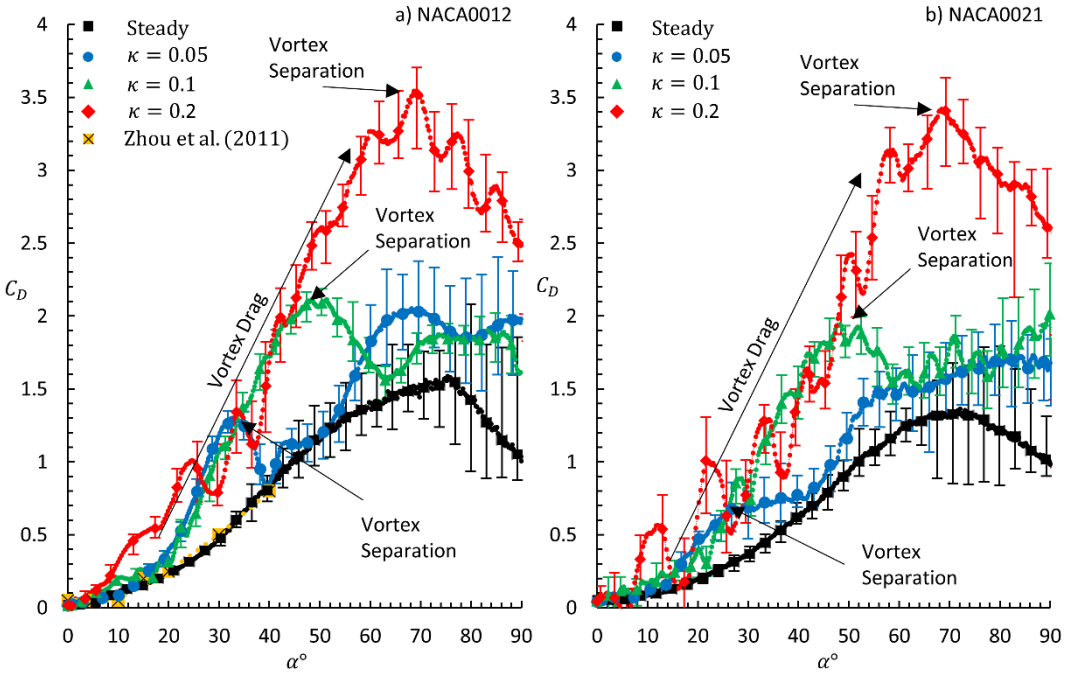

Fig. 12 Pressure drag coefficient of both the NACA 0012 and NACA 0021 airfoil for steady and dynamic stall conditions indicating increased drag coefficient with leading-edge vortex formation and increased non-dimensional pitch rate. Error bars indicate maximum and minimum drag force coefficient values recorded, whilst the error of 1.2% was established about the mean to achieve a 95% confidence level.

From Fig. 12, it can be seen that the formation of the leading-edge vortex significantly increase the drag prior to its separation. Under steady-state conditions, the drag was shown to be consistent with wind tunnel tests reported in Zhou et al. [50] over the narrow angle of attack range presented. As expected, drag was observed to grow steadily to a maximum of $C_D = 1.5$ at $\alpha = 78°$ for the NACA 0012 and $C_D = 1.3$ at $\alpha = 72°$ for the

NACA 0021 under steady-state conditions. Prior to formation of the leading-edge vortex, drag profiles were similar between all test cases, indicating minor influence of the separation bubbles on drag. However, with the development of the leading-edge vortex, significant drag increases are observed. The NACA 0012 generated larger drag in comparison with the NACA 0021 for $\kappa = 0.05$, where $C_D = 1.3$ and $C_D = 0.7$ respectively. Inspection of the vorticity contours in Fig. 5b, for the NACA 0012, and Fig. 5c, for the NACA 0021, show a more concentrated leading-edge vortex over the NACA 0012 resulting in higher pressure gradients at the airfoil surface and subsequent increased drag. The decay in drag reduction, on separation of the leading-edge vortex, was shown to be less compared with the NACA 0021. This suggests that thicker airfoils would be more beneficial to reduce force oscillation under post-stall dynamic stall conditions. Increasing the non-dimensional pitch rate to $\kappa = 0.1$ and $\kappa = 0.2$ showed similar drag development for both airfoils, which highlights the dominance of increased loads induced through airfoil rotation during high rotation rates. The drag was shown to rise with increased non-dimensional pitch rate due to the proximity of the leading-edge vortex to the airfoil surface until high angles of attack. This resulted in a region of low pressure on the rear of the airfoil, as indicated by the increased suction on the upper surface in Fig. 11d, and vorticity contours in Fig. 7h and Fig. 7i. Maximum drag for $\kappa = 0.1$ was shown to reach $C_D = 2.0$ at $\alpha = 50°$, for the NACA 0012, and $C_D = 1.9$ at $\alpha = 50°$ for the NACA 0021. Maximum drag for $\kappa = 0.2$ was shown to increase to $C_D = 3.4$ at $\alpha = 70°$, for both the NACA 0012 and NACA 0021 airfoils.

Conclusions

An investigation of the flow field and force generation for airfoils undergoing dynamic stall at significantly high angles of attack and rotation rates has been performed using PIV and surface pressure analysis in both water channel and wind tunnel facilities respectively. The study compares the effects of thickness ratio, using a NACA 0012 and a NACA 0021 airfoils, to determine the variation in flow structure and force development at high rotation rates and angles of attack, specific to gust-like conditions. The two airfoils exhibit similar flow patterns, in terms of vortex formation, although the flow structure and location of the dynamic-stall vortex above the airfoils is shown to be dependent on airfoil pitch rate and thickness. Increasing the rotation rate resulted in the delay of flow separation and leading-edge vortex onset until higher angles of attack. This resulted in increases in the lift of up to three times that of steady-state values recorded at equivalent angles of attack. Similar observations were also observed for the airfoil drag, where the presence of the leading-edge vortex, and its delayed separation resulted in significant force development for $\alpha > 60°$.

Airfoil thickness was shown to have a significant effect on the onset of delayed separation and the growth of the leading edge vortex in all of the unsteady flow cases. For the NACA 0012 airfoil, the leading edge vortex formed at a lower angle of attack than in the thicker-airfoil, whereas in the NACA 0021 case the initiation of the leading-edge vortex was preceded by the formation of multiple vortex structures within the rear separation bubble. In contrast, once formed, the rate of growth of the leading-edge vortex was greater for the thicker foil. The results also showed that, whilst the thinner foil produced

more unsteady lift, the lift force fluctuations were markedly higher for the thicker airfoil at the highest rotation rate.

Once deep stall was established, however, the airfoil thickness was shown to have a minor impact on the flow structure, which was initiated by the detachment of the trailing-edge stagnation point into the wake. In post-stall scenarios and under unsteady rotation rates, both airfoils display similar vortex formations, representative of bluff-body separation.

Increasing the non-dimensional pitch rate was shown to impact the pressure distribution on the lower surface of the airfoil such that decreased pressure at the leading edge and increased the pressure over the rear of the airfoil occurred. This effect, combined with the generation of a separation bubble resulted in an increase in the lift-curve slope prior to leading-edge vortex formation.

For all dynamic stall cases, a periodic fluctuation in the ramp-up lift curve was observed and related to the shedding frequency of vortex structures developed at the trailing edge of the airfoil, and shed into the wake. Increasing the non-dimensional pitch rate resulted in amplification of the force fluctuation, suggesting that the circulations of the trailing-edge vortex structures separating into the wake are linked to increased pitch rate. Further analysis of this hypothesis is however required to determine a quantitative relationship between pitch rate and trailing edge vortex circulation.

The ability to operate at large reduced frequencies and angles of attack is critical for the efficient operation of vertical axis wind turbines, and during perching manoeuvres of MAVs and natural flyers where blades and wings are exposed to strong, rapid or prolonged changes in effective angle of attack. The evidence presented in this study

suggests that, in order to achieve enhanced lift under high pitch-rate conditions, a thin airfoil is advantageous, due to initiation of the leading-edge vortex at lower angles of attack and higher maximum lift. However, to decrease the detrimental effects of dynamic stall, a thicker foil is generally advantageous, with later leading-edge vortex formation and lower lift overall. However, at high rotation rates, the present study found that lift force fluctuations due to vortex shedding can be substantially larger in the thicker foil case.

Acknowledgments

I acknowledge the support I have received for my research through the provision of an Australian Government Research Training Program Scholarship. In addition, research undertaken for this report has been assisted with a grant from the Sir Ross and Sir Keith Smith Fund (www.smithfund.org.au). The support is acknowledged and greatly appreciated.

References

[1] Sangwan, J., Sengupta T. K., and Suchandra P., 2017, "Investigation of Compressibility Effects on Dynamic Stall of Pitching Airfoil," Physics of Fluids, 29 (7):076104.

[2] Tangler, J. L., 2004, "Insight into Wind Turbine Stall and Post-Stall Aerodynamics," Wind Energy, 7 (3):247-260.

[3] Ericsson, L. E., and Reding J. P., 1988, "Fluid Mechanics of Dynamic Stall Part 1. Unsteady Flow Concepts," Journal of Fluids and Structures, 2:1-33. doi: 10.1016/S0889-9746(88)90116-8.

[4] Francis, M. S., and Keese J. E., 1985, "Airfoil Dynamic Stall Performance with Large-Amplitude Motions," AIAA Journal, 23 (11):1653-1659. doi: 10.2514/3.9146.

[5] McAlister, K. W., and Carr L. W., 1979, "Water Tunnel Visualisations of Dynamic Stall," J Fluid Eng, 101 (3):376-380. doi: 10.1115/1.3448981.

[6] Lee, T., and Su Y., 2015, "Surface Pressures Developed on an Airfoil Undergoing Heaving and Pitching Motion," J Fluid Eng, 137 (5):051105.

[7] Poels, A., Rudmin D., Benaissa A., and Poirel D., 2015, "Localization of Flow Separation and Transition over a Pitching Naca0012 Airfoil at Transitional Reynolds Numbers Using Hot-Films," J Fluid Eng, 137 (12):124501.

[8] Conger, R. N., and Ramaprian B. R., 1994, "Pressure Measurements on a Pitching Airfoil in a Water Channel," AIAA Journal, 32 (1):108-115. doi: 10.2514/3.11957.

[9] Jumper, E. J., Schreck S. J., and Dimmick R. L., 1987, "Lift-Curve Characteristics for an Airfoil Pitching at Constant Rate," Journal of Aircraft, 24 (10):680-687. doi: 10.2514/3.45507.

[10] McAlister, K., Pucci S., McCroskey W., and Carr L., 1982, "An Experimental Study of Dynamic Stall on Advanced Airfoil Section. Volume 2: Pressure and Force Data": NASA.

[11] Butterfield, C. P., Hansen A. C., Simms D., and Scott G., 1991, "Dyanamic Stall on Wind Turbine Blades": National Renewable Energy Laboratory.

[12] Munduate, X., and Coton F. N., 2000, "Identification of Dynamic Stall Regions on Horizontal Axis Wind Turbines," 19th ASME Wind Energy Symposium, AIAA paper.

[13] Schreck, S. J., Robinson M. C., Maureen Hand M., and Simms D., A, 2001, "Blade Dynamic Stall Vortex Kinematics for a Horizontal Axis Wind Turbine in Yawed Conditions," Journal of Solar Energy Engineering, 123 (4):272-281. doi: 10.1115/1.1408307.

[14] Shipley, D. E., Miller M. S., and Robinson M. C., 1995, "Dynamic Stall Occurance on a Horizontal Axis Wind Turbine": National Renewable Energy Laboratory.

[15] Laneville, A., and Vittecoq P., 1986, "Dynamic Stall: The Case of the Vertical Axis Wind Turbine," Journal of Solar Energy Engineering, 108 (2):140-145. doi: 10.1115/1.3268081.

[16] Müller-Vahl, H. F., Nayeri C. N., Paschereit C. O., and Greenblatt D., 2016, "Dynamic Stall Control Via Adaptive Blowing," Renewable Energy, 97:47-64.

[17] Müller-Vahl, H. F., Strangfeld C., Nayeri C. N., Paschereit C. O., and Greenblatt D., 2014, "Control of Thick Airfoil, Deep Dynamic Stall Using Steady Blowing," AIAA journal, 53 (2):277-295.

[18] Tadjfar, M., and Asgari E., 2018, "Active Flow Control of Dynamic Stall by Means of Continuous Jet Flow at Reynolds Number of 1× 106," J Fluid Eng, 140 (1):011107.

[19] Schubel, P. J., and Crossley R. J., 2012, "Wind Turbine Blade Design," Energies, 5 (9):3425-3449. doi: 10.3390/en5093425.

[20] Leishman, J. G., 2000. *Principles of Helicopter Aerodynamics*. 2 ed. New York: Cambridge Aerospace Press.

[21] Panda, J., and Zaman K., 1992, "Experimental Investigation of the Flowfield of an Oscillating Airfoil," 10th Applied Aerodynamics Conference.

[22] Panda, J., and Zaman K., 1994, "Experimental Investigation of the Flow Field of an Oscillating Airfoil and Estimation of Lift from Wake Surveys," Journal of Fluid Mechanics, 265:65-95.

[23] Shih, C., Lourenco L., and Krothapalli A., 1995, "Investigation of Flow at Leading and Trailing Edges of Pitching-up Airfoil," AIAA Journal, 33 (8):1369-1376.

[24] Shih, C., Lourenco L., Van Dommelen L., and Krothapalli A., 1992, "Unsteady Flow Past an Airfoil Pitching at a Constant Rate," AIAA Journal, 30 (5):1153-1161.

[25] Visbal, M., 1990, "Dynamic Stall of a Constant-Rate Pitching Airfoil," Journal of Aircraft, 27 (5):400-407.

[26] Visbal, M., and Shang J., 1989, "Investigation of the Flow Structure around a Rapidly Pitching Airfoil," AIAA Journal, 27 (8):1044-1051.

[27] Visbal, M. R., 1991, "On the Formation and Control of the Dynamic Stall Vortex on a Pitching Airfoil," AIAA Paper.

[28] Visbal, M. R., 2011, "Numerical Investigation of Deep Dynamic Stall of a Plunging Airfoil," AIAA Journal, 49 (10):2152-2170.

[29] Visbal, M. R., 2014, "Analysis of the Onset of Dynamic Stall Using High-Fidelity Large-Eddy Simulations," AIAA Paper, 591:2014.

[30] Stevens, P., and Babinsky H., 2017, "Experiments to Investigate Lift Production Mechanisms on Pitching Flat Plates," Experiments in Fluids, 58 (1):7.

[31] Garmann, D. J., and Visbal M. R., 2017, "Analysis of Tip Vortex near-Wake Evolution for Stationary and Oscillating Wings," AIAA Journal.

[32] Barlow, J. B., Rae W., and Pope A., 1999, "Low-Speed Wind Tunnel Testing, 1999," John Wiley & Sons, Canada.

[33] Raffel, M., Willert C., Wereley S., and Kompenhans J., 2007. *Particle Image Velocimetry: A Practical Guide*. 2 ed. Berlin: Springer.

[34] Westerweel, J., 2000, "Theoretical Analysis of the Measurement Precision in Particle Image Velocimetry," Experiments in Fluids, 29:S003-S012. doi: 10.1007/s003480070002.

[35] Gibson, B. A., 2012, "Laminar Flow Control of a Flat Plate Boundary Layer Using Dielectric Barrier Discharge Plasma," Doctor of Philosophy, School of Mechanical Engineering, The University of Adelaide.

[36] Olsman, W., Willems J., Hirschberg A., Colonius T., and Trieling R., 2011, "Flow around a Naca0018 Airfoil with a Cavity and Its Dynamical Response to Acoustic Forcing," Experiments in fluids, 51 (2):493-509.

[37] Choudhry, A., Leknys R., Arjomandi M., and Kelso R., 2014, "An Insight into the Dynamic Stall Lift Characteristics," Experimental Thermal and Fluid Science, 58:188-208.

[38] Granlund, K., Ol M., Garmann D., Visbal M., and Bernal L., 2010, "Experiments and Computations on Abstractions of Perching," 28th AIAA Applied Aerodynamics Conference.

[39] Sayers, A., and Ball D., 1983, "Blockage Corrections for Rectangular Flat Plates Mounted in an Open Jet Wind Tunnel," Proceedings of the Institution of Mechanical Engineers, Part C: Journal of Mechanical Engineering Science, 197 (4):259-263.

[40] Hansen, K. L., 2012, "Effect of Leading Edge Tubercles on Airfoil Performance," Doctor of Philosophy, School of Mechanical Engineering, The University of Adelaide.

[41] Katz, J., and Plotkin A., 2001. *Low-Speed Aerodynamics*. Edited by Second Edition. Vol. 13: Cambridge University Press.

[42] Gharib, M., and Roshko A., 1987, "The Effect of Flow Oscillations on Cavity Drag," Journal of Fluid Mechanics, 177:501-530. doi: 10.1017/S002211208700106X.

[43] Hudy, L. M., Naguib A., and Humphreys W. M., 2007, "Stochastic Estimation of the Separation-Flow Field Using Wall-Pressure-Array Measurements," Physics of Fluids, 19. doi: 10.1063/1.2472507.

[44] Rival, D., Kriegseis J., Schaub P., Widmann A., and Tropea C., 2013, "A Criterion for Vortex Separation on Unsteady Aerodynamic Profiles," 51st AIAA Aerospace Sciences Meeting including the New Horizons Forum and Aerospace Exposition.

[45] Choudhuri, P. G., Knight D., and Visbal M., 1994, "Two-Dimensional Unsteady Leading-Edge Separation on a Pitching Airfoil," AIAA journal, 32 (4):673-681.

[46] Perry, A., and Steiner T., 1987, "Large-Scale Vortex Structures in Turbulent Wakes Behind Bluff Bodies. Part 1. Vortex Formation Processes," Journal of Fluid Mechanics, 174:233-270. doi: 10.1017/S0022112087000119.

[47] McCroskey, W., McAlister K., Carr L., Pucci S., Lambert O., and Indergrand R., 1981, "Dynamic Stall on Advanced Airfoil Sections," Journal of the American Helicopter Society, 26 (3):40-50. doi: 10.4050/JAHS.26.40.

[48] Leishman, J., 1990, "Dynamic Stall Experiments on the Naca 23012 Aerofoil," Experiments in Fluids, 9 (1-2):49-58. doi: 10.1007/BF00575335.

[49] Heine, B., Mulleners K., Joubert G., and Raffel M., 2013, "Dynamic Stall Control by Passive Disturbance Generators," AIAA journal.

[50] Zhou, Y., Alam M. M., Yang H., Guo H., and Wood D., 2011, "Fluid Forces on a Very Low Reynolds Number Airfoil and Their Prediction," International Journal of Heat and Fluid Flow, 32 (1):329-339.

[51] Huang, R. F., and Lin C. L., 1995, "Vortex Shedding and Shear-Layer Instability of Wing at Low-Reynolds Numbers," AIAA Journal, 33 (8):1398-1403.

[52] Kim, D.-H., Chang J.-W., and Chung J., 2011, "Low-Reynolds-Number Effect on Aerodynamic Characteristics of a Naca 0012 Airfoil," Journal of Aircraft, 48 (4):1212-1215.

[53] Lin, J.-C., and Rockwell D., 1996, "Force Identification by Vorticity Fields: Techniques Based on Flow Imaging," Journal of Fluids and Structures, 10 (6):663-668.

[54] Anyoji, M., Nonomura T., Aono H., Oyama A., Fujii K., Nagai H., and Asai K., 2014, "Computational and Experimental Analysis of a High-Performance Airfoil under Low-Reynolds-Number Flow Condition," Journal of Aircraft.

[55] Hansen, K. L., Kelso R. M., and Dally B. B., 2011, "Performance Variations of Leading-Edge Tubercles for Distinct Airfoil Profiles," AIAA journal, 49 (1):185-194.

[56] Leknys, R. R., 2013, "Investigations into the Dynamic Stall Characteristics of Airfoils Used in the Wind Turbine Industry Using Flow Visualisation Techniques," Masters, School of Mechanical Engineering, The University of Adelaide.

[57] Carr, L. W., and Chandrasekhara M., 1996, "Compressibility Effects on Dynamic Stall," Progress in Aerospace Sciences, 32 (6):523-573. doi: 10.1016/0376-0421(95)00009-7.

[58] McCroskey, W. J., Carr L. W., and McAlister K. W., 1976, "Dynamic Stall Experiments on Oscillating Airfoils," AIAA Journal, 14 (1):57-63. doi: 10.2514/3.61332.

Chapter 4.

Deep Stall Effects

4.1. Chapter 4 Overview

This chapter investigates the effects of dynamic stall on the post-stall characteristics of an airfoil exposed to high rotation rate, high angle of attack operating conditions. Wind turbines frequently operate in post-stall conditions for power regulation and during start-up. The current chapter shows the results from surface pressure and PIV measurements to identify the performance of a NACA 0021 airfoil experiencing dynamic stall, and continuing to operating in post-stall conditions. Dynamic stall using constant-pitch-rate motion is experimentally investigated to a maximum angle of attack of $\alpha = 20°$, $\alpha = 40°$ and $\alpha = 60°$. The Reynolds number was $Re = 20{,}000$ and the reduced frequency was $\kappa = 0.05$, 0.1 and 0.2. Increasing the rotation rate resulted in delayed stall and continued lift generation until $\alpha = 37°$, for $\kappa > 0.1$. The presence of the leading-edge vortex during dynamic stall resulted in increased suction on the airfoil upper surface, significantly shifting the centre of pressure. Significant load fluctuation was noted once the airfoil motion had ceased, and increasing the rotation rate was shown to increase load fluctuation in the post-stall region. This resulted in an increase in time required to reach steady-state flow conditions. The results show that rotor blades exposed to high rotation-rate dynamic stall can exhibit large force fluctuations for increased duration once the maximum angle of attack is obtained.

4.2. Post-Stall Operation of Airfoils Undergoing Dynamic Stall

Statement of Authenticity

Title of Paper:	Dynamic and Post-Stall Characteristics of Pitching Airfoils at Extreme Conditions
Publication Status:	☑ Published ☐ Accepted for Publication ☐ Submitted for Publication ☐ Unpublished and Unsubmitted work written in manuscript style
Publication Details:	Leknys, R. R., Arjomandi, M., Kelso, R. M. & Birzer, C. H., 2017, Dynamic and Post-Stall Characteristics of Pitching Airfoils at Extreme Conditions, *Proceedings of the Institution of Mechanical Engineers, Part G: Journal of Aerospace Engineering*.

Principal Author

Name of Principal Author:	Ryan Ross Leknys
Contribution to the Paper:	Performed data analysis and interpretation, wrote manuscript and acted as corresponding author.
Overall percentage (%):	70
Certification:	This paper reports on original research I conducted during the period of my Higher Degree by Research candidature and is not subject to any obligations or contractual agreements with a third party that would constrain its inclusion in this thesis. I am the primary author of this paper.

Signature: _ Date: 05 March 2018

Co-Author Contributions

By signing the Statement of Authorship, each author certifies that:

iv. the candidate's stated contribution to the publication is accurate (as detailed above);

v. permission is granted for the candidate in include the publication in the thesis; and

vi. the sum of all co-author contributions is equal to 100% less the candidate's stated contribution.

Name of Co-Author:	Associate Professor Maziar Arjomandi
Contribution to the Paper:	Supervised the development of the research and contributed in academic discussion and the review process of submitted manuscripts.

Signature: _____ _____ Date: 05 March 2018

Name of Co-Author:	Associate Professor Richard Kelso
Contribution to the Paper:	Supervised the development of the research and contributed in academic discussion and the review process of submitted manuscripts.

Signature: Date: 05 March 2018

Name of Co-Author:	Dr Cristian Birzer
Contribution to the Paper:	Supervised the development of the research and contributed in academic discussion and the review process of submitted manuscripts.

Signature: _____ _____ Date: 05 March 2018

Original Article

Institution of MECHANICAL ENGINEERS | Journal of AEROSPACE ENGINEERING

Proc IMechE Part G:
J Aerospace Engineering
0(0) 1–15

DOI: 10.1177/0954410017710274
journals.sagepub.com/home/pig
SAGE

Dynamic- and post-stall characteristics of pitching airfoils at extreme conditions

RR Leknys, M Arjomandi, RM Kelso and C Birzer

Abstract

Post-stall flow structure and surface pressures are evaluated to determine the effects of large angles of attack, perching like manoeuvres on the flow about a NACA 0021 airfoil exposed to dynamic stall. Phase-averaged particle image velocimetry was performed to assess the load development during the constant angular velocity pitch-up motion and in post-stall conditions. Evaluation of the resultant aerodynamic loads indicates that initial airfoil rotation generates significant delays in force response. Furthermore, the reduced frequency is shown to influence the angle of attack at which deep stall is initiated, to the extent that fully separated flows are delayed to an angle of attack of 60°. Vortex structures are linked to lower surface pressures with increased angle of attack and also for post-stall flow conditions. Likewise, the presence of the vortex structures shifts the centre of pressure significantly along the airfoil chordline immediately after cessation of the airfoil rotation. At the maximum angle of attack, the centre of pressure is shown to move aft for fully separated flow conditions. The variation in location of the centre of pressure, not only changes the moment generation and aero-elastic characteristics of the airfoil, but also increases structural torsional loading and fluctuations that result in increased fatigue of helicopter rotor shafts and horizontal-axis wind turbines.

Keywords

Dynamic stall, post-stall, vertical axis wind turbine, perching, particle image velocimetry, surface pressure, airfoil

Date received: 24 February 2017; accepted: 24 April 2017

Introduction

For the period of start-up and operation during off-peak conditions of wind turbines, and for high-speed forward flight and manoeuvres of helicopters, the blades of such machines can be exposed to severe dynamic stall, or even reversed flow conditions.[1,2] In addition, dynamic stall is associated with natural flyers where manoeuvres, such as perching, often rely on the increased lift to sustain or control flight. Dynamic stall is the phenomenon of delayed stall on pitching airfoils accompanied by the rapid growth of a vortex originating at the leading edge.[3] This vortex has been attributed to increased lift and drag whilst in proximity to the upper surface of the airfoil. To date, work on dynamic stall continues to be conducted due to its detrimental effects on rotary-machine blades and wind turbines as well as the benefits it offers flapping-wing flyers.

The dynamic-stall phenomenon has been of concern, and has been deliberated for many years. Past research has focused on its mitigation, for the case of helicopters and wind turbines, where excessive loads lead to decreased performance and increased material fatigue. Alternatively, the development of microaerial vehicles has recently spurred increased interest into dynamic stall due to the aerodynamic properties generated from pitching, flapping wings, where unsteady lift can be advantageous for sustained flight and manoeuvring. Of these studies, many discuss the loads created during the pitch-up motion for constant pitch rate and sinusoidal motion, and for cases where cyclic hysteresis of the airfoil results in the airfoil oscillating above and below a mean angle of attack that represents a steady-state stall angle of attack. For helicopters, wind turbines and perching natural flyers, the residual after-effects of dynamic stall and the associated loading, for cases where the airfoil remains in a stalled condition, is still not

School of Mechanical Engineering, The University of Adelaide, Adelaide, South Australia, Australia

Corresponding author:
RR Leknys, School of Mechanical Engineering, The University of Adelaide, Adelaide, South Australia 5005, Australia.
Email: ryan.leknys@adelaide.edu.au

understood or represented. Research into the lift and drag generation during post-stall is a topic requiring further investigation, as increased loading ultimately leads to blade vibration and damage to mechanical components, such as gearboxes and drive units, due to torsional load fluctuations. Although much work has been performed to analyse the dynamic-stall process, the post-stall behaviour of a constant pitch rate motion airfoil is still poorly understood. As such, the motivation for the current article is the need to understand the dynamic-stall and post-stall characteristics leading to aerodynamic load fluctuations on airfoils operating at extreme angles of attack and under high rotation rates.

Load fluctuations are attributed to the development of vortex structures, and formation of separation bubbles on the upper surface of wings.[4,5] During the dynamic-stall process, a delay in flow separation and formation of both a trailing-edge separation bubble and a leading-edge vortex has a net effect of periodically increasing the aerodynamic force. Surface pressure measurements at low Mach numbers in Leishman[6] indicate that increased suction generated by the leading-edge vortex, results in an overall increase in lift coefficient. These changes are not only restricted to the leading-edge region. As the vortex passes over the airfoil surface, a subsequent shift in minimum pressure coefficient also follows the trajectory of the vortex.[6] Once the vortex detaches from the airfoil, a decrease in lift and increase in drag occurs, resulting in deep-stall conditions prior to the airfoil returning to angles of attack where attachment of the flow can be established. During the period of deep stall, the transition of the leading-edge vortex over the upper surface leads to sudden changes in surface pressure resulting in the intense changes to the pitching moment denoted as moment stall.[3] All of these aerodynamic characteristics lead to large load fluctuations that ultimately increase material fatigue and reduce the performance of the helicopter or wind turbine.

In an attempt to reduce the negative effects, which include excessively fluctuating lift and drag, of dynamic stall for the case of helicopters, studies sought to identify the effects of performance parameters and their influence on lift generation characteristics about pitching airfoils. For example, Lorber and Carta,[7] Dimmick,[8] Jumper and Dimmick[9] and Jumper and Schreck[10] investigated the changes in the pitch rate and pitch axis, where it was demonstrated that increasing the reduced frequency, $\kappa = \omega C/2U_\infty$ (where ω is the angular velocity, C is the airfoil chord and U_∞ is the freestream velocity) and moving the pitch axis aft of the leading edge resulted in greater lift coefficients and increased angles of attack prior to deep-stall conditions. Likewise, other studies detailed the effect of performance parameters including Reynolds number,[11,12] Mach number[13–15] and airfoil geometry.[16,17] These primary studies all shed light on the characteristics of dynamic stall, with their focus predominantly based upon the mitigation of the dynamic-stall force production about rotor blades of helicopters where pitch angles are low and the pitch angle varies sinusoidally. Similar problems with the unsteady loading on blades, due to dynamic stall, are also evident on the horizontal-axis wind turbines.[18] Variations in the atmospheric turbulence, gusts, tower shadow and wake interaction all lead to dynamic-stall conditions.[19]

Previous literature has shown the pressure and load fluctuations generated from airfoils with motions operating over narrow ranges of pitch angles and for multiple motion types. Airfoils typically pitch about an angle of attack within the steady-state operating region and oscillate $\pm 20^\circ$ about this mean value; however, other motion types such as constant pitch rate motion to elevated angles of attack is still required. Moreover, a knowledge gap remains with regard to the understanding of the deep dynamic-stall process and post-stall relaxation time of airfoils exposed to high angles of attack, and which experience continued operation in post-stall conditions. This gap in knowledge is more applicable to airfoils exposed to gust-like or start-up conditions, for the case of vertical axis wind turbines, or for perching manoeuvers of natural flyers where the airfoil is exposed to very large angles of attack, and motion types representative of constant angular velocity. As such, the remainder of the current study is focused on the post-stall behaviour of airfoils under deep dynamic stall where large amplitude, constant pitch rate motion occurs.

Ol and Bernal[20] investigated deep-dynamic-stall conditions about a SD7003 airfoil undergoing pitch and heave motions using numerical techniques, flow visualisation and direct force measurements, although the maximum angle of attack was limited to $\alpha = 20^\circ$. Likewise, particle image velocimetry (PIV) data are presented for a NACA 0012 airfoil in Raffel and Kompenhans,[21] although, the maximum angle of attack for deep stall in the experiments was $\alpha = 25^\circ$. The effects of boundary layer blowing at the leading edge on a NACA 0018 airfoil exposed to deep-dynamic-stall conditions are shown in Mueller-Vahl and Strangfeld[22] for sinusoidal motion and to maximum angles of attack of $\alpha = 35^\circ$. In this study, PIV data and surface pressure measurements were utilised to correlate the surface pressure with vortex structures generated during the pitching motion. Shih and Lourenco[23] investigated, using PIV, the unsteady flow about a NACA 0012 airfoil rotating to $\alpha = 30^\circ$ and at $Re = 5000$ under ramp-up motions. In this study, flow topology including the leading-edge vortex and trailing-edge vortex development were identified. Furthermore, a description of the dynamic-stall process and interaction between the leading-edge and trailing-edge vortices is provided

for the vortex formation, vortex convection, stall onset and stalled stages. Although beneficial for the understanding of the dynamic-stall process, further work to identify the ramp-up and hold aerodynamics in post-stall configurations is still required.

Analytical methods, for the case of a specifically developed wind turbine S809 airfoil are shown in Gupta and Leishman.[24] Here, a version of the Leishman–Beddoes dynamic-stall model was applied for $\alpha = 40°$ with success during attached flow conditions, although it was shown that over-prediction of the thrust coefficient was evident for deep-dynamic-stall conditions. Deep-dynamic-stall investigations using numerical techniques were also presented in Visbal[25] and in Wang and Ingham.[26] Visbal[25] applied large eddy simulation technique to show the boundary layer and dynamic-stall vortex structures developed about a plunging, oscillating SD7003 airfoil. In this study, it was shown that deep-stall phases became highly sensitive to the numerical scheme, with large errors occurring between experimental data and the generated numerical data. Likewise, Wang and Ingham[26] compared unsteady Reynolds-averaged Navier–Stokes (URANS) and direct eddy simulations (DES) schemes to an oscillating NACA 0012 airfoil undergoing deep dynamic stall to $\alpha = 25°$. The numerical methods in this study were also shown to break down, by over or underprediction of the forces at elevated angles of attack where the leading edge vortex development occurred. The numerical studies highlight their suitability to estimate dynamic-stall loading during attached flow conditions, but also highlight their limitations to adequately predict deep, post-stall loads where large-scale separation occurs.

Limited studies have been conducted for deep-stall flow conditions above $\alpha = 40°$. Although, exceptions to this include the work reported in Jumper and Schreck,[10] where $\alpha = 90°$, and in Francis and Keesee,[27] where $\alpha = 60°$. In these investigations, surface pressure sensors were utilised to show the initiation, development and progression of the leading-edge vortex during dynamic stall. Although they discuss deep-stall loading, post-stall load development was not reported. A comprehensive review of MAV wing kinematics conducted in Ol and Babinsky[28] details the flow dynamics of a flat plate undergoing multiple motions types and to elevated angles of attack; however, the influence of geometry on the flow behaviour and separation process ramp-up stage of dynamic stall is limited due to the simplified and fundamental application of the flat plate.

Literature has comprehensively described the fundamental aspects of the dynamic-stall process, whilst also investigating operational parameters and their influence on the aerodynamic performance of airfoils of different geometries. However, for the case of an airfoil undergoing ramp-and-hold constant pitch rate motion, which closely models wind turbine start-up and perching manoeuvres of natural flyers, insight into the stall process and post-stall aerodynamics at elevated angles of attack is currently lacking. To address this gap, the present article reports an investigation into the deep-stalled flow conditions about a pitching airfoil. Additionally, the article shows the effects of wake development resulting from dynamic stall, and then links the associated flow patterns with post-stall load and the movement of the centre of pressure about airfoils in deep-dynamic-stall conditions. This work enhances our understanding of the force characteristics of airfoils exposed to dynamic-stall and post-stall flow conditions, which are relevant to increased rotor-blade fatigue and the manoeuvring of natural flyers and micro-aerial vehicles. This can lead to improved methods of flow control and blade design such that power generation, material life-cycle and flight performance can all be increased.

Methodology

Studies to determine the effects of dynamic-stall and post-stall load and torsional variation were conducted using a combination of PIV and surface pressure measurements. This enabled a correlation to be generated linking the respective dynamic-stall events with load fluctuations generated during rotation of the airfoil. This was achieved using two flow facilities, a water tunnel and a wind tunnel of the same cross-sectional dimensions, operating at the same Reynolds number and using similar models. Dynamic stall about a NACA 0021 airfoil was investigated using phase-averaged PIV in a water channel located at the University of Adelaide with a test section of 0.5 m × 0.5 m and a maximum blockage ratio of 14% at the maximum angle of attack of $\alpha = 60°$. The Reynolds number was set such that $Re_C = 20000$, based on the airfoil chord, $C = 70$ mm and freestream velocity, $U_\infty = 0.27$ m/s. Reduced frequencies of 0.05, 0.1 and 0.2 were studied with the airfoil behaviour such that constant pitch rate motion was established about the mid-chord pitch axis, to maximum angles of attack of 20°, 40° and 60°. The equivalent angular velocity, ω, relating to the test reduced frequency was $\omega = 0.41$, 0.82 and 1.64 rad/s and $\omega = 2.94$, 5.88 and 11.75 rad/s in both water and wind tunnel tests respectively. A brushless DC motor with an embedded position encoder coupled to a reduction gearbox was utilised to provide motion to the airfoil to within 0.5° of the respective study angle during the pitch-up motion. To achieve smooth motor start and stop transitions, acceleration and deceleration was set to 5° each of the total airfoil angular displacement. Post-stall flow structure, using PIV, was investigated using the nondimensional time, $T^* = (TU_\infty)/C$, where $T^* = 0.2 - 1.4$. PIV was conducted using a 1008 × 1018 pixel Kodak MegaPlus ES1.0 CCD digital camera and respective EPIX-PIXCI image acquisition software. To account for airfoil shadow,

multiple images were captured for both upper and lower surface of the airfoil. Upper and lower images were then combined using an in-house image processor before post-processing using PIVView V1.7. A total of 200 image sets were recorded to establish statistical convergence of the velocity fields for both the upper and lower sides of the airfoil. Both the upper and lower phase-averaged data was then superimposed to eliminate the shadow from the airfoil. A light sheet was provided through the combination of two Nd-YAG lasers arranged such that a 3 mm thick light sheet projected through the mid-chord plane of symmetry of the wing bounded by end plates with 1.5 mm end gaps such that leakage and three-dimensional effects were minimal.[29] Seeding was achieved using 50 μm polyamide particles with a specific gravity of 1.03. The camera used a magnification factor of 7.3 with the images being de-focused such that particle image diameters ranged between 1 and 3 pixels per particle in order to reduce bias errors associated with peak detection during image interpolation and correlation.[30,31] A schematic diagram of the test apparatus is for PIV measurement is shown in Figure 1.

Velocity vectors were calculated using 32×32 pixel interrogation windows with a 50% overlap, creating a grid spacing of 2.19 mm between each velocity vector. The three-point Gaussian peak detection was implemented with three-pass interrogation and Nyquist frequency filtering being applied for interrogation window correlation and peak detection. Vorticity fields were evaluated and normalised according to $\omega_z = \left[\frac{\delta v}{\delta x} - \frac{\delta u}{\delta y}\right]\frac{C}{U_\infty}$, whilst streamlines were estimated using Matlab's® Streamline function.

Due to an inability to obtain direct force measurements using the water channel facility, forces were computed by integrated surface pressure measurements obtained in an open-jet wind tunnel at the same Reynolds number, $Re_C = 20{,}000$, and using the same reduced frequencies and airfoil motion profiles. The wind tunnel has an open-jet test section of cross section 0.5×0.5 m and a turbulence intensity of ~0.85%. The technique of using dissimilar test facilities to generate flow structure and surface pressure measurements, was successfully applied in Erm[32] and in Hansen and Kelso,[33] the latter using the same facilities as the present work where the differences between the flows was shown to be minimal. The key difference between the facilities is in the blockage effects in the open and closed tunnel sections, although this will be relevant only at the end of the ramp-up process where the blockage exceeds 10%. Therefore, variations between the generated PIV flow fields and pressure measurements in this study are considered to be minor, and the velocity and pressure data can be used for a direct comparison of the dynamic-stall process.

Surface pressure distributions were recorded using nine Honeywell differential-pressure sensors mounted within a 100 mm chord length polycarbonate wing, with a similar configuration to Jumper and Schreck[10] and in Choudhry and Leknys.[5] Internal tubing connecting the surface orifice and the pressure sensor was kept to a minimum in order to decrease damping effects and system response times; however, a 50 ms response time was evaluated and correlated to the pressure sensors utilised in the experimental setup and subsequently corrected for in the final results. The wing was located 250 mm upstream of the wind tunnel exit and generating 17% blockage at the maximum angle of attack, $\alpha = 60°$. Blockage corrections were not applied to either the PIV or the pressure measurements due to the minor variation in load as detailed in Sayers and Ball[34] and in Grunlund and Ol.[35] The configuration of the wind tunnel and test setup is shown in Figure 2, whilst the orientation of the surface pressure sensors are indicated in Figure 3.

The chordwise distribution of the pressure sensors is according to Choudhry and Leknys.[5] Due to the

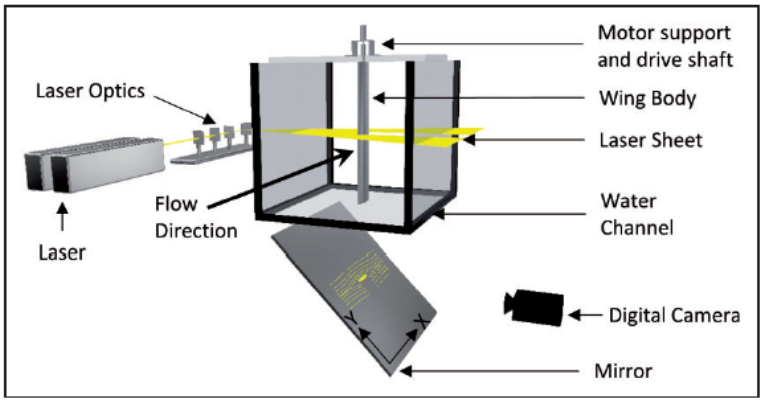

Figure 1. Water channel, motion mount, drive axis and arrangement of lighting and camera orientation used for PIV.

sensors being on one side of the airfoil, measurements in both pitching directions were used to obtain the upper and lower surface pressure readings. A total of 120 tests were averaged for both the upper surface and lower surface of the airfoil respectively. Within each test, a total of 1000 samples were collected for the pitching duration, whilst 2000 individual samples were recorded during the post-stall periods of $T^* = 10$. This ensured that the sample frequency was sufficient to capture all major flow events occurring during the pitch-up motion at the highest reduced frequency. Global aerodynamic force was evaluated using trapezoidal-rule integration over the airfoil surface such that

$$L = \oint P\mathrm{d}x \sin\alpha + \oint P\mathrm{d}z \cos\alpha \quad (1)$$

$$D = \oint P\mathrm{d}x \cos\alpha + \oint P\mathrm{d}z \sin\alpha \quad (2)$$

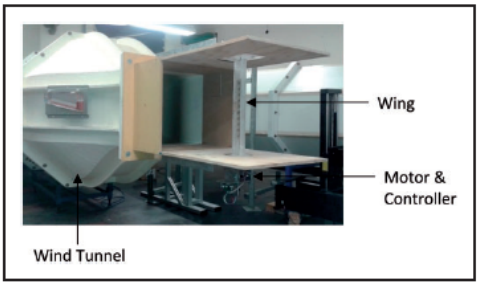

Figure 2. The open-return wind tunnel used to simulate dynamic stall and evaluate post-stall behaviour of the NACA 0021 airfoil.

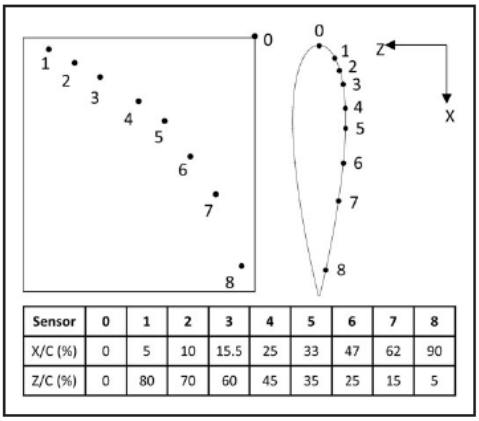

Sensor	0	1	2	3	4	5	6	7	8
X/C (%)	0	5	10	15.5	25	33	47	62	90
Z/C (%)	0	80	70	60	45	35	25	15	5

Figure 3. Orientation of the surface pressure sensors located on the NACA 0021 airfoil.

In equations (1) and (2), L and D represent the global pressure lift and drag forces generated during the pitch-up process, P is the recorded surface pressure, whilst $\mathrm{d}x$ and $\mathrm{d}z$ are the displacements between each of the pressure port locations positioned in the airfoil surface, as indicated in Figure 3.

Results and discussion

Error analysis of pressure measurements

Force evaluation is critical for airfoils undergoing unsteady motion due to the practical implications and force generation resulting from the development of an unsteady aerodynamics. Results from the current PIV and surface pressure testing indicate that significant load generation during post-stall flow conditions is possible, based on the input maximum angle of attack and reduced frequency. Analysis of the pressure measurements used for evaluation of the airfoil force coefficients indicates minor deviations in pressure variation due to the minimal change in force coefficient from the mean. Where high vortex shedding occurred, such as during shedding of the dynamic-stall vortex, a resulting increase in force coefficient was also obtained and can be related to the fluctuating pressure coefficient generated during the unsteady motion. The errors in force coefficient resulting from vortex induced pressure fluctuations are shown in Figure 4.

Figure 4 shows the lift coefficient for ramp-up dynamic stall where the maximum angle of attack was $\alpha_{max} = 60°$, and for multiple reduced frequencies. Also indicated is the range of variation in the force coefficient resulting from the fluctuation in pressure generated by the dynamic-stall process. A maximum

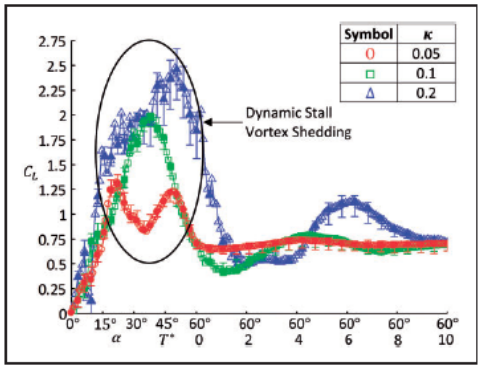

Figure 4. Lift coefficient generated by integration of the surface pressure indicating the variation in force coefficient as a function of angle of attack and also normalised time. Regions of dynamic vortex shedding show greater force variation with comparison to ramp-up and post-stall stages where lower vortex fluctuation occurs.

variation in C_L of 6%, from the mean force coefficient indicated in Figure 4 at $T^* = 1$, was obtained based on the pressure data filtered to within one standard deviation of the mean for each surface pressure sensor during the dynamic-stall vortex shedding process. Lower variations from the mean C_L were evaluated for the ramp-up and post-stall conditions where no vortex formation is observed, or increased stability in the vortex shedding process occurs. Similar results were also observed for cases where $\alpha_{max} = 20°$ and $\alpha_{max} = 40°$; however, the observed errors were lower than for the case of $\alpha_{max} = 60°$. Furthermore, the limited number of the surface pressure sensors at the location of high-pressure fluctuation around the leading edge would ultimately lead to a slight loss of resolution with respect to pressure variation at the leading edge. This issue was also discussed in Hansen,[36] where variations between resolved forces, from surface pressures, at angles of attack approaching and exceeding stall were less then direct force measurements recorded under similar test conditions. However, earlier testing conducted on pitching airfoils,[4,5,10–12] using similar pressure sensor arrangements to that of the current setup, were shown to capture the major flow structure development and adequately resolve the aerodynamic forces generated during dynamic stall, and at angles of attack well beyond steady-state stall. As such, the variation in surface pressure, and resolution of the surface pressure sensors at the leading edge, could therefore be considered to have a minor influence on the resulting data sets indicating the overall flow structure and force patterns.

Lift characteristics, $\alpha_{Max} = 20°$

Increasing the reduced frequency is shown to delay initial lift generation of the airfoil at the beginning of airfoil rotation. The delay angle, α_D, is defined as the angle of attack at which force generation is observed over the NACA 0021 airfoil as a result of the airfoil input rotation. The resultant lift coefficient for dynamic-stall tests where the maximum angle of attack is $\alpha_{max} = 20°$, is shown in Figure 5. In order to directly compare each reduced frequency case, results for force coefficient are plotted against angle of attack, as the respective development time is dissimilar between the various ramp-up cases. Also shown in Figure 4 are the corresponding normalised vorticity contours and streamline plots generated from PIV data resulting from dynamic stall about the NACA 0021 airfoil.

In Figure 5, for each of the test cases with varying reduced frequency, maximum lift occurred at $\alpha = 20°$, except $\kappa = 0.2$ where maximum lift was delayed by approximately $T^* = 0.2$ after the maximum angle of attack was reached. Similar force magnitudes are observed to occur between the cases of $\kappa = 0.1$ and $\kappa = 0.05$. However, for $\kappa = 0.1$, the lift coefficient is slightly less, $|C_{LMax} = 1.1$, and consists of a boarder lift characteristic such that the lift is sustained for a longer duration prior to a rapid drop in force generation. The reduction in lift for the case of $\kappa = 0.1$ is believed to be due to the detachment of the minor vortical structures on the upper surface of the airfoil resulting from the breakdown of the separation bubble present prior to airfoil rotation ending.

From the normalised vorticity plots indicated in Figure 5, the effect of pitch rate on flow structure, for the case of $\alpha = 20°$, includes the delay in upper separation bubble breakdown as the reduced frequency is increased. For $\kappa = 0.05$, a large separation bubble (SB) forms over the entire upper surface (Figure 5(a) to (d), $\kappa = 0.05$). The separation bubble is identified through the observation of a detachment point at the leading edge and re-attachment point of the shear layer at the trailing edge. The expansion of the separation bubble, at $\kappa = 0.05$, is shown to decrease lift with a broadening of the pressure coefficient towards the trailing edge of the airfoil. Figure 6 shows the simplified flow structures and their respective pressure distributions. As the separation bubble expands post airfoil rotation, a decrease in suction at the leading edge on the upper surface is observed, whilst the pressure recovery at the trailing edge remains relatively constant. This decrease correlates in pressure at the leading edge correlates to the overall reduction in lift as shown in Figure 6.

Increasing the rotation rate to $\kappa = 0.1$ resulted in significant changes in the development of the large separation bubble observed on the upper surface of the airfoil for the case of $\kappa = 0.05$. At the higher reduced frequency of $\kappa = 0.1$, the separation bubble is not present. In this case, breakdown of the upper-surface separation bubble is observed through the formation of multiple clockwise vortical structures that are distributed over the chord of the airfoil as indicated in Figure 5 for $\kappa = 0.1$ and $T^* = 0.6$. The occurrence of the localised vortical structures over the upper surface is shown to increase the velocity in the immediate vicinity of the airfoil wall, leading to a temporary increase in suction prior to their amalgamation into two dominant vortical structures at the leading edge and trailing edge, as indicated in Figure 5 for $\kappa = 0.1$ and $T^* = 1.4$.

Figure 7 describes the flow fields generated for $\kappa = 0.1$ and for a maximum angle of attack of $\alpha = 20°$ comparing the generated surface pressure surrounding the airfoil at multiple time intervals after cessation of airfoil rotation. For the case of $T^* = 0.6$, leading-edge suction is maintained, although maximum suction peak is observed to occur at approximately $X/C = 0.3$, as the separation bubble begins to divide into multiple vortical structures above the airfoil. These structures subsequently amalgamate into a leading-edge vortex (LEV) and a secondary region of vorticity (V2) at $T^* = 1.4$. The existence of these two isolated vortical structures can be observed in Figure 7(c), where the two

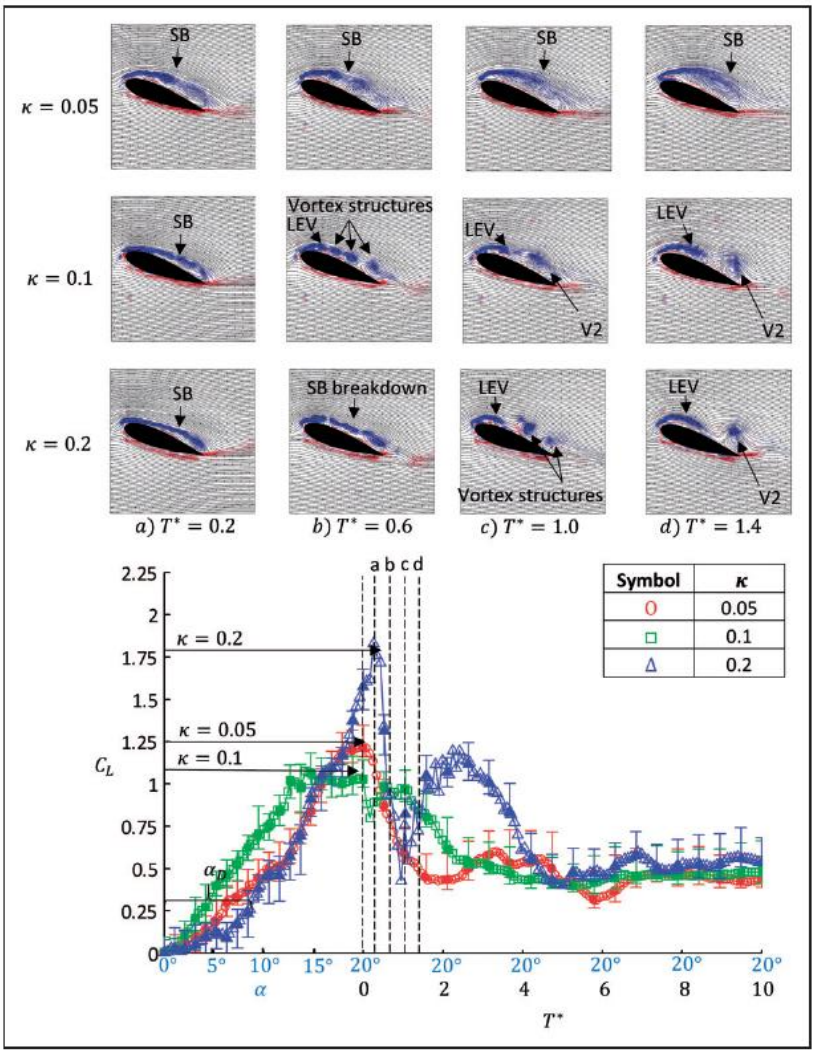

Figure 5. Lift coefficient of a NACA 0021 undergoing constant pitch rate motion to a maximum angle of attack, $\alpha_{max} = 20°$. Shown is the progressive stage of dynamic stall with post-stall load development becoming dependent on the pitch rate. Lift coefficient can be correlated to the observed vortex structures for each reduced frequency and normalised time value.
SB: separation bubble; LEV: leading-edge vortex; V2: secondary vortex.

distinctive peaks in suction pressure are found at approximately $X/C = 0.4$ and $X/C = 0.65$.

Similar flow structure, to $\kappa = 0.1$, is also observed for $\kappa = 0.2$ with a separation bubble forming, followed by its breakdown into multiple vortical structures that eventually amalgamate to form the single trailing-edge vortex. Maximum lift coefficient for $\kappa = 0.2$ was seen to reach $C_{LMax} = 1.8$ followed by a rapid loss in lift at $T^* = 0.6$ resulting from the generation of both leading and trailing-edge vortices.

Lift characteristics, $\alpha_{Max} = 40°$

Force measurements and flow structure are evaluated for the case of $\alpha_{max} = 40°$ and displayed in Figure 8, which shows normalised vorticity contours and streamline plots for the NACA 0021 airfoil undergoing constant pitch rate dynamic stall where $\alpha_{max} = 40°$. For $\kappa = 0.05$, complete separation is observed after the angle of attack exceeds $\alpha = 20°$, with the maximum lift coefficient being measured to be $C_L = 1.2$. As indicated in Figure 8(a) to (d) for

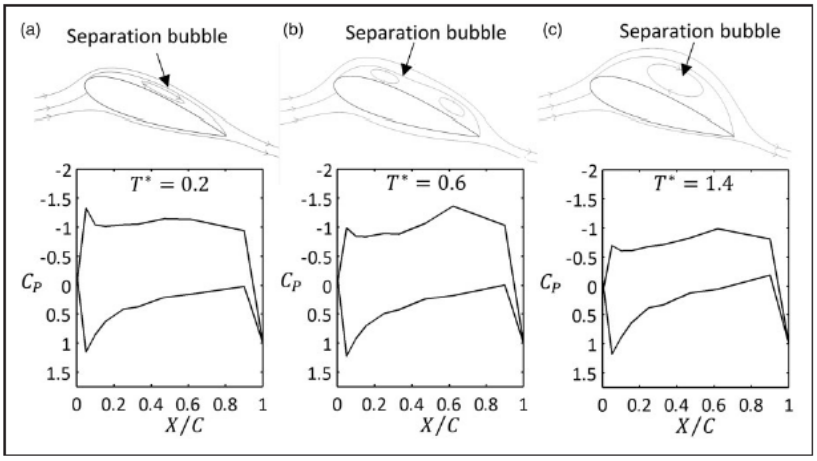

Figure 6. Schematic representation of the flow structure and surface pressure, and the influence of the upper separation bubble on the pressure distribution over the upper surface of the airfoil for the case of $\kappa = 0.05$ and $\alpha = 20°$.

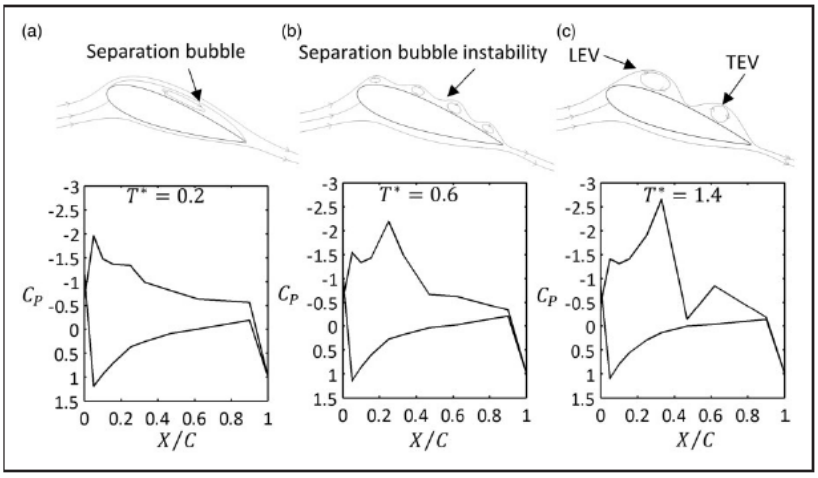

Figure 7. Schematic representation of the flow structure and surface pressure, and the influence of the upper separation bubble on the pressure distribution over the upper surface of the airfoil for the case of $\kappa = 0.1$ and $\alpha = 20°$.

$\kappa = 0.05$, the leading edge vortex is observed to have passed into the free stream, resulting in fully separated flow, representative of bluff body separation. With $\kappa = 0.1$ and $\kappa = 0.2$, lift is maintained until $\alpha = 40°$ with $C_L \approx 1.95$ and $C_L \approx 2.15$ respectively. Maximum lift is generated for $\kappa = 0.1$ when the leading-edge vortex is positioned over the entire upper surface, Figure 8(a) ($\kappa = 0.1$). Once the second trailing-edge vortex (TEV2) begins to form, initiation of leading-edge vortex detachment from the airfoil occurs. This leads to a reduction in lift coefficient as the leading-edge vortex sheds from the airfoil and transitions into its wake. Similar lift generation characteristics are observed for $\kappa = 0.2$, where the maximum lift coefficient, $C_L = 2.15$ occurs at $\alpha = 40°$, although the leading-edge vortex is not observed until $T^* = 0.6$ for $\kappa = 0.2$. Prior to this, a separation bubble is located over the rear of the airfoil with separation at the leading edge forming a minor leading-edge vortex, as shown in Figure 8(a) ($\kappa = 0.2$). Lift continues to grow until $T^* = 0.6$, where the leading-edge and secondary vortical structures (V2) are observed to increase in size. With the formation of the secondary trailing-edge vortex (TEV2), a sharp decrease in lift results, which in turn initiates deep-stalled conditions.

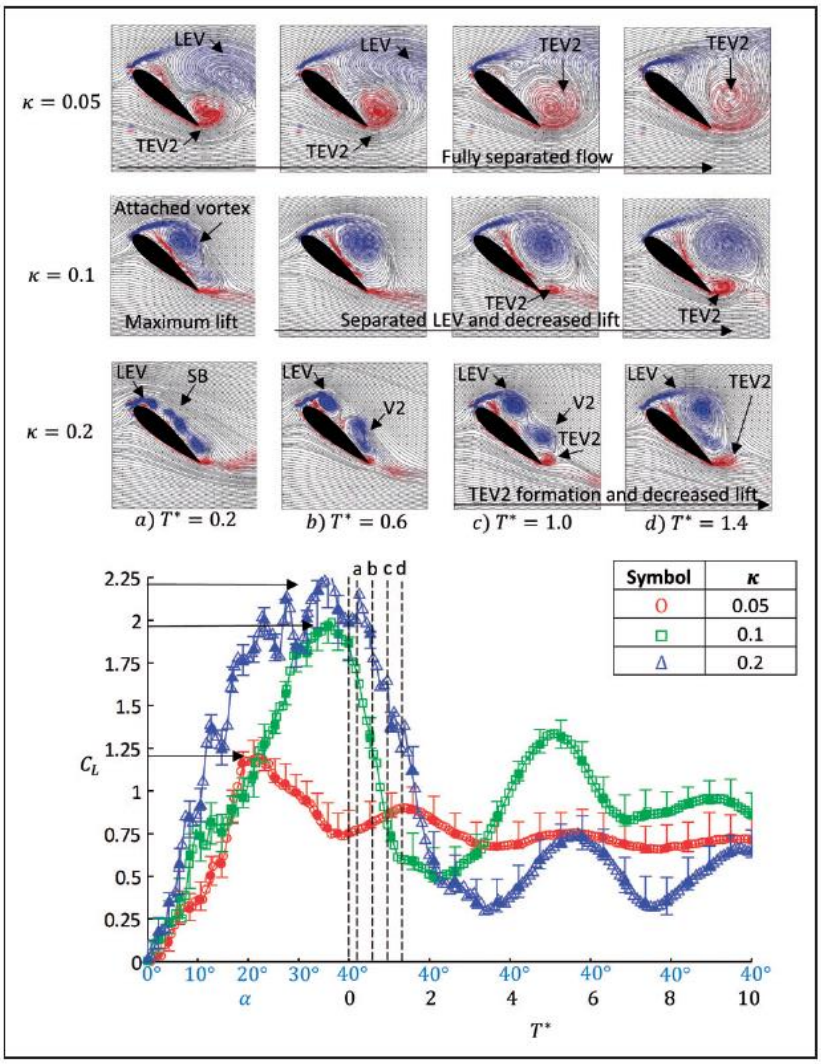

Figure 8. Lift coefficient of a NACA 0021 undergoing constant pitch rate motion to a maximum angle of attack, $\alpha_{max} = 40°$. Detachment of the attached vortex structures and lift reduction for $\kappa = 0.05$ is observed to occur at $\alpha \approx 20°$. Alternatively, lift increases with the presence of the leading-edge vortex (LEV) where $\kappa = 0.1$ and $\kappa = 0.2$, but decreases when the second trailing-edge vortex (TEV) forms.

Lift characteristics, $\alpha_{Max} = 60°$

The lift characteristics for pitch angles up to $\alpha_{Max} = 60°$ were investigated. PIV data and surface pressure measurements were again utilised to assess the dynamic-stall and post-stall loads of the NACA 0021 airfoil undergoing constant pitch rate dynamic stall. Shown in Figure 9 are the normalised vorticity and streamline plots of the post-stall vortex development proceeding ending of airfoil rotation.

From analysis of the vorticity contours for $T^* = 0.2 - 1.4$ and for both $\kappa = 0.05$ and $\kappa = 0.1$ of Figure 9, it is shown that the NACA 0021 exhibits fully separated flow before the airfoil reached the specified maximum angle of attack of $\alpha = 60°$. For $\kappa = 0.05$, separated flow is initiated by $\alpha_{max} \approx 20°$ and $\kappa = 0.05$, whilst for $\kappa = 0.1$, separated flow is observed at $\alpha \approx 40°$. For $\kappa = 0.05$, bluff body separation results for post-stall flow with periodic vortex shedding occurring and a maximum lift coefficient, $C_L \approx 0.75$. The lift created by the initial pitching and the presence of the leading-edge vortex is seen, through inspection of the generated lift coefficient in Figure 9, to decrease substantially for $\kappa = 0.1$ over the

period of $T^* = 0.2 - 1.4$. From Figure 9(a) to (d) for $\kappa = 0.1$, the shedding of the leading edge vortex away from the airfoil surface and into the freestream is observed and leads to bluff body separation. Enhanced lift is maintained for $\kappa = 0.2$ until approximately $\alpha = 55°$, after which formation of a secondary trailing-edge vortex (TEV2) promotes separation of the initial leading-edge and vortical structures (V2) as indicated in Figure 9(a) for $\kappa = 0.2$. Separation of the leading-edge vortex results in deep-stall where $C_L \approx 0.95$; however, convergence of the lift coefficient to a values similar to both $\kappa = 0.05$ and $\kappa = 0.1$ was not observed within the test period of $T^* = 10$.

The results from the elevated angles of attack indicate that the post-stall load is dependent on both the reduced frequency, or pitch rate, and also the maximum angle of attack. Results show that separation is delayed, until higher angles of attack, and that enhanced lift is possible with increased reduced frequency. Additionally, the maximum lift coefficient is limited at approximately $C_L = 2.2$ for $\kappa = 0.2$ and for both $\alpha = 40°$ and $\alpha = 60°$.

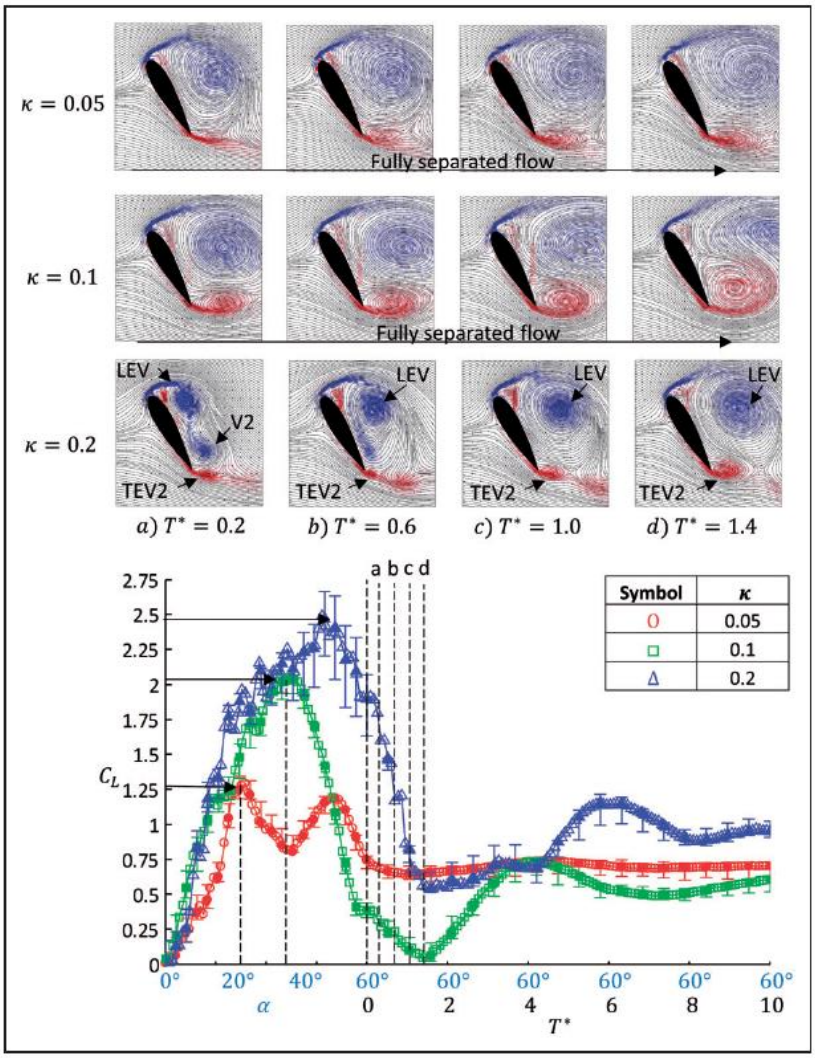

Figure 9. Lift coefficient of a NACA 0021 undergoing constant pitch rate motion to a maximum angle of attack, $\alpha_{max} = 50°$ indicating delayed lift generation at rotation start-up and dynamic lift generation as a result of delayed boundary layer separation, vortex detachment and vortex induced lift. Additionally, the post stall load is dependent on the pitch rate and periodic vortex shedding.

Drag characteristics

The maximum drag coefficient is primarily dependent on the maximum angle of attack of the airfoil with associated vortex-induced forces contributing to random spikes in force generation. As boundary layer separation is delayed to higher angles of attack through increases in reduced frequency, the resulting drag also subsequently increases. For $\alpha_{max} = 20°$, drag is shown to increase steadily until motion is ceased, and the airfoil is allowed to transition into a state of deep stall. Figure 10 shows the cases where $\alpha_{max} = 20°$ and $\kappa = 0.05$, $\kappa = 0.1$ and $\kappa = 0.2$, at $\alpha_{max} = 20°$ with increased reduced frequency.

The PIV vorticity plots in Figure 10 show the lack of any leading-edge vortex and the presence of a separation bubble, with the separation point at the leading edge, and re-attachment point at the trailing edge. The presence of the displaced shear layer and underlying separation bubble significantly influences the drag force generated prior to dynamic-stall vortex formation.

As the maximum angle of attack is increased to $\alpha_{max} = 40°$, a rise in drag coefficient during post-stall

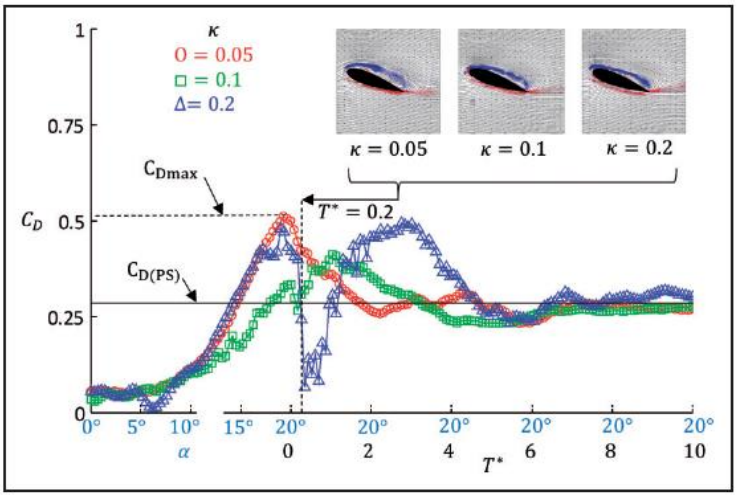

Figure 10. Drag coefficient of a NACA 0021 airfoil undergoing constant-pitch-rate motion with $\alpha_{max} = 20°$ and $T^*_{max} = 10$.

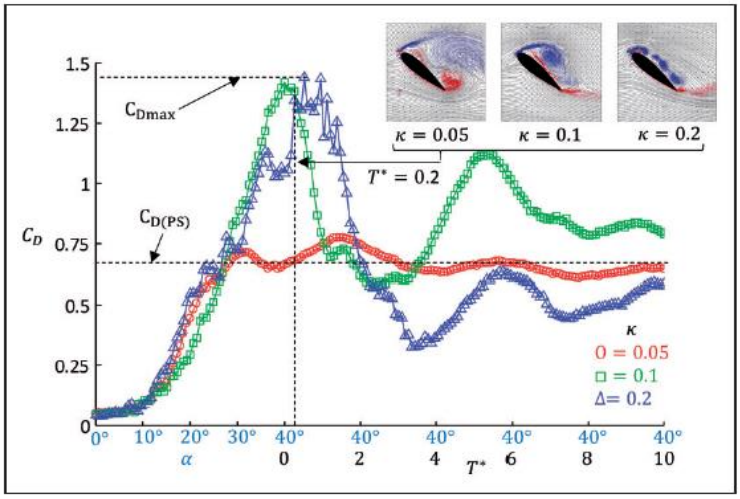

Figure 11. Drag coefficient of a NACA 0021 airfoil undergoing constant pitch rate motion wither $\alpha_{max} = 40°$ and $T^*_{max} = 10$.

flow conditions from $C_D \approx 0.3$ for $\alpha_{max} = 20^\circ$ to $C_D \approx 0.7$ for $\alpha_{max} = 40^\circ$, is also noted for all reduced frequencies tested, which can be attributed to the overall maximum angle of attack. However, with the presence of the dynamic-stall vortex, as shown in Figure 11 for $\kappa = 0.1$, a substantial peak in vortex-induced drag is formed. The peak in drag is also associated with the breakdown of the separation bubble resulting in a broadening of the drag coefficient curve for $\kappa = 0.2$.

The case of $\alpha_{max} = 60^\circ$ leads to similar force generation characteristics to $\alpha_{max} = 40^\circ$ case as a result of the presence of the leading-edge vortex. However, only the drag coefficient values for $\kappa = 0.2$ are seen to increase due to the growth of the leading-edge

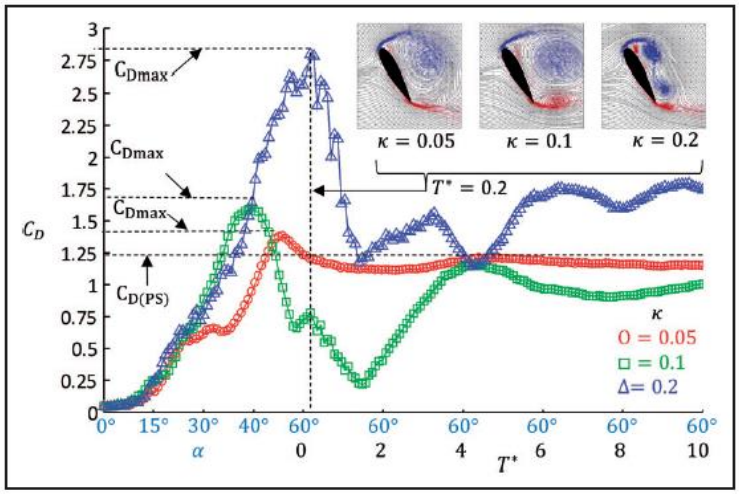

Figure 12. Drag coefficient of a NACA 0021 airfoil undergoing constant pitch rate motion wither $\alpha_{max} = 60^\circ$ and $T^*_{max} = 10$.

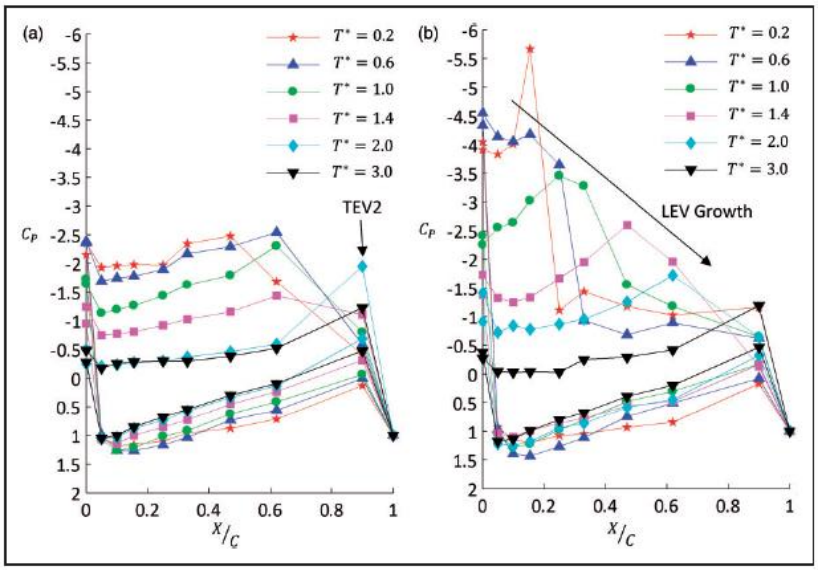

Figure 13. Surface pressure distributions of the NACA 0021 airfoil held at 40° once constant pitch rate motion had ceased. (a) Increased suction pressure at the trailing edge as a result of the secondary formation of a trailing-edge vortex (TEV2), $\kappa = 0.1$. (b) The influence of the leading-edge vortex (LEV) on surface pressure as it grows in size and transitions towards the trailing edge, $\kappa = 0.2$.

vortex. Figure 12 shows drag coefficient values for the NACA 0021 airfoil rotating at multiple reduced frequencies with the maximum angle of attack, $\alpha_{max} = 60°$. Within Figure 12, for the case of $\kappa = 0.1$ and $\kappa = 0.05$, the drag associated with the leading-edge vortex occurs prior to the airfoil reaching the maximum angle of attack, with fully stalled conditions being established whilst the airfoil is rotating. This is confirmed by the detachment and shedding of the leading-edge vortex into the wake.

As shown through the surface pressure investigations, the effect of the leading-edge vortex on the drag is similar to its effect on the lift characteristics, such that force generation from the presence of the vortex structure results in increased drag on the airfoil. Also evident is the similar trend of delayed force generation at the beginning of rotation due to the rapid rotation of the airfoil, as noted through observation of the trends of both lift and drag coefficient.

Surface pressure, load and vortex correlation

The vortex structures on the upper surface heavily influence the pressure distribution and centre of pressure (COP), resulting in increased moment fluctuation during rotation. The existence of the vortex structures over the upper surface is demonstrated to increase suction and broaden the low-pressure peak over the airfoil. This, in effect, alters the lift generation and changes the COP, shifting its location further aft of the airfoil leading edge. Figure 13(a) indicates the results of surface pressure for $\alpha = 40°$ after cessation of rotation and the flow is allowed to transition into deep-stall conditions. Multiple measurements points at the airfoil leading edge are a result of minor variation in the airfoil angular displacement due to experimental limitations to individually record both upper and lower surface pressures. The presence of the trailing-edge vortical structures (V2), highlighted in Figure 8(c) for $\kappa = 0.1$, are shown to increase suction whilst in proximity to the airfoil surface. Similarly, when $\kappa = 0.2$, the growth of the leading-edge vortex and its motion over the upper surface of the airfoil are shown, in Figure 13(b), to influence the pressure distribution such that peak suction moves aft of the leading edge as the vortex continues to grow. The magnitude of the suction peak is reduced as the vortex core expands and the flow progresses into the deep-stall condition. Also observed is the increased broadening of the maximum suction peak which is attributed to increased leading edge vortex growth and the amalgamation of the primary trailing-edge vortex and upper surface vortical structures, as indicated in Figure 8(c) for $\kappa = 0.2$.

Due to the movement of the maximum suction peak towards the trailing edge, and the effects of secondary vortex structures altering the airfoil surface pressure, subsequent changes to the airfoil COP are also noted to occur.

Figure 14 shows the location of the airfoil's COP, X_{CP}, normalised by the airfoil chord, once the rotation of the airfoil had ceased, plotted with respect to normalised time, maximum angle of attack and reduced frequency. For $\alpha_{max} = 20°$ (Figure 14(a)), once fully separated flow conditions are established, the effects of leading-edge and trailing-edge vortex growth, are shown to move the COP forward and aft respectively. For the test cases shown in Figure 14, large shifts in the location of the COP are indicated during deep-post-stall conditions and with the presence of the generated vortex structures. The magnitude of the change in COP location is similar between each reduced frequency, indicating that that force generation is dependent on the maximum angle

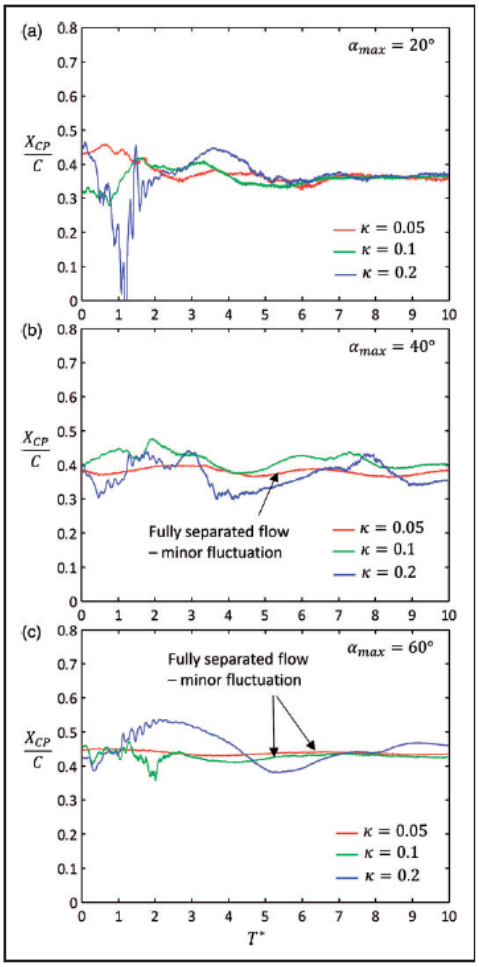

Figure 14. Change in COP, X_{CP}, of the NACA 0021 airfoil as a function of normalised time once the airfoil maximum angle of attack is reached. (a) $\alpha_{max} = 20°$; (b) $\alpha_{max} = 40°$; (c) $\alpha_{max} = 60°$.

of attack and the maximum size of the vortex structures developing during separation. The movement of the COP aft of the leading edge occurs for all reduced frequency values tested. Similar motion of the COP is observed for $\alpha_{max} = 40°$ and $\alpha_{max} = 60°$. However, if the airfoil has already developed bluff-body separated flow prior to reaching the maximum angle of attack, minor changes to the COP are observed. The overall location of the COP is shifted rearward with increased α_{max}, although large fluctuations in its location resulting from initial vortex shedding are not observed. This is indicated in Figure 14(a) for $\kappa = 0.05$, Figure 14(b) for $\kappa = 0.1$ and Figure 14(c) for $\kappa = 0.2$ where the COP is shifted aft with increased angle of attack. Increasing α_{max} is shown only to move the COP aft from approximately 0.38 to 0.45 for $\alpha_{max} = 40°$ and $\alpha_{max} = 60°$, respectively.

Whilst the initial vortex structures developed during dynamic stall are present over the airfoil, significant fluctuations in the location of the COP are noted. For the case of deep dynamic stall, the COP is observed to move up to 55% of the airfoil chord, between $X_{CP} = 0$ at the lowest reduced frequency, $\kappa = 0.05$ (Figure 14(a)), and the maximum value, $X_{CP} = 0.55$, for $\kappa = 0.2$ (Figure 14(c)). This change significantly alters the magnitude of the resultant torque generated by the airfoil, which equates to exacerbated fatigue on rotor shafts of helicopters and wind turbines.

Conclusions

Dynamic-stall conditions were simulated using constant pitch rate motion of a NACA 0021 airfoil, demonstrating its effects on the aerodynamic properties and flow structure. All test cases resulted in the formation of the dynamic-stall vortex, which forms as a result of the amalgamation of the leading-edge vortex and the primary trailing-edge vortex. A clockwise vortical structure develops on the upper surface as a result of the breakdown of the separation bubble observed during initial airfoil rotation. It was shown that this vortical structure initiates the separation of the dynamic-stall leading-edge vortex, triggering bluff body separation. The pitch rate is shown to influence the angular delay in initial force response, where increased reduced frequency resulted in high delay times prior to aerodynamic load generation. Post-stall flow characteristics are demonstrated to be minimally affected by the maximum angle of attack and reduced frequency, with fully separated flows developing once separation of the dynamic-stall vortex occurs. Bluff body flow characteristics are established after approximately six chord length of flow. Prior to this, large fluctuation in force generation are possible due to the unsteady nature and vortex shedding of the airfoil proceeding initial dynamic-stall separation.

Surface pressure measurements were shown to be influenced by the presence of the generated vortex structures on the upper surface of the airfoil where increased suction results. Passage of the dynamic-stall vortex, and the occurrence of the vortical structures over the trailing edge, decrease pressure and increase lift periodically until their separation from the airfoil. In addition, for post-stall flows, the motion of the vortex structures towards the trailing edge was shown to significantly move the centre of pressure and increase the moment generation immediately post dynamic-stall vortex separation, indicating the negative attributes of dynamic stall post dynamic-stall separation. If the airfoil is well established in deep-stall conditions, where bluff body separation occurs, fluctuations in the position of the centre of pressure are shown to be minimal. The location of the centre of pressure is shown to move aft along the airfoil chord with increases in the airfoil's maximum angle. Post-stall load is shown to be influenced by the reduced frequency and maximum angle of attack, with significant force fluctuation occurring after cessation of the airfoil motion. The current work highlights the significant load fluctuation created by an airfoil experiencing high rotation rate, high angle-of-attack dynamic stall. The results show that, although the airfoil may be stalled, for immediate post-stall flows, large fluctuations in force are possible. This is significant for the efficient operation of power-generation machines, such as wind turbines, and for the study of perching manoeuvers of natural flyers.

Acknowledgements

I acknowledge the support I have received for my research through the provision of an Australian Government Research Training Program Scholarship. In addition, research undertaken for this report has been assisted with a grant from the Sir Ross and Sir Keith Smith Fund (www.smithfund.org.au). The support is acknowledged and greatly appreciated.

Declaration of Conflicting Interests

The author(s) declared no potential conflicts of interest with respect to the research, authorship, and/or publication of this article.

Funding

The author(s) received no financial support for the research, authorship, and/or publication of this article.

References

1. Carr LW. Progress in analysis and prediction of dynamic stall. *J Aircraft* 1988; 25: 6–17.
2. Lind AH and Jones AR. Unsteady aerodynamics of reverse flow dynamic stall on an oscillating blade section. *Phys Fluids* 2016; 28: 077102.
3. McCroskey WJ, Carr LW and McAlister KW. Dynamic stall experiments on oscillating airfoils. *AIAA J* 1976; 14: 57–63.

4. Choudhry A, Arjomandi M and Kelso R. A study of long separation bubble on thick airfoils and its consequent effects. *Int J Heat Fluid Flow* 2015; 52: 84–96.
5. Choudhry A, Leknys R, Arjomandi M, et al. An insight into the dynamic stall lift characteristics. *Exp Therm Fluid Sci* 2014; 58: 188–208.
6. Leishman J. Dynamic stall experiments on the NACA 23012 aerofoil. *Exp Fluids* 1990; 9: 49–58.
7. Lorber PF and Carta FO. Airfoil dynamic stall at constant pitch rate and high Reynolds number. *J Aircraft* 1988; 25: 548–556.
8. Dimmick RL. Pitch-location effects on dynamic stall. DTIC Document, 1985.
9. Jumper E, Dimmick R and Allaire A. The effect of pitch location on dynamic stall. *J Fluids Eng* 1989; 111: 256–262.
10. Jumper E, Schreck S and Dimmick R. Lift-curve characteristics for an airfoil pitching at constant rate. *J Aircraft* 1987; 24: 680–687.
11. Carr LW, McAlister KW and McCroskey WJ. Analysis of the development of dynamic stall based on oscillating airfoil experiments. NASA, 1977.
12. Robinson MC and Wissler JB. Pitch rate and Reynolds number effects on a pitching rectangular wing. *AIAA Paper 1988–2577*. 1988.
13. Carr LW and Chandrasekhara M. Compressibility effects on dynamic stall. *Prog Aerosp Sci* 1996; 32: 523–573.
14. Chandrasekhara M, Wilder M and Carr L. Boundary-layer-tripping studies of compressible dynamic stall flow. *AIAA J* 1996; 34: 96–103.
15. Choudhuri PG and Knight D. Effects of compressibility, pitch rate, and Reynolds number on unsteady incipient leading-edge boundary layer separation over a pitching airfoil. *J Fluid Mech* 1996; 308: 195–217.
16. McCroskey WJ. The phenomenon of dynamic stall. DTIC Document, 1981.
17. Wilby P. An experimental investigation of the influence of a range of aerofoil design features on dynamic stall onset. In: *10th European rotorcraft forum*. The Netherlands, 1984.
18. Shipley DE, Miller MS and Robinson MC. Dynamic stall occurrence on a horizontal axis wind turbine blade. *National Renewable Energy Laboratory*. Golden, CO, USA, 1995.
19. Leishman JG. *Principles of helicopter aerodynamics*. Cambridge, NY: Cambridge University Press, 2006.
20. Ol MV, Bernal L, Kang C-K, et al. Shallow and deep dynamic stall for flapping low Reynolds number airfoils. *Exp Fluids* 2009; 46: 883–901.
21. Raffel M, Kompenhans J and Wernert P. Investigation of the unsteady flow velocity field above an airfoil pitching under deep dynamic stall conditions. *Exp Fluids* 1995; 19: 103–111.
22. Mueller-Vahl H, Strangfeld C, Nayeri C, et al. Thick airfoil deep dynamic stall and its control. AIAA Paper, 2013.
23. Shih C, Lourenco L, van Dommelen L, et al. Unsteady flow past an airfoil pitching at a constant rate. *AIAA J* 1992; 30: 1153–1161.
24. Gupta S and Leishman JG. Dynamic stall modelling of the S809 aerofoil and comparison with experiments. *Wind Energy* 2006; 9: 521–547.
25. Visbal MR. Numerical investigation of deep dynamic stall of a plunging airfoil. *AIAA J* 2011; 49: 2152–2170.
26. Wang S, Ingham DB, Ma L, et al. Turbulence modeling of deep dynamic stall at relatively low Reynolds number. *J Fluids Struct* 2012; 33: 191–209.
27. Francis M and Keesee J. Airfoil dynamic stall performance with large-amplitude motions. *AIAA J* 1985; 23: 1653–1659.
28. Ol M and Babinsky H. *Extensions of fundamental flow physics to practical MAV aerodynamics*. North Atlantic Treaty Organization, 2016.
29. Rae WH and Pope A. *Low-speed wind tunnel testing*. New York: John Wiley, 1984.
30. Raffel M, Willert CE, Wereley ST, et al. *Particle image velocimetry: A practical guide*. Dordrecht: Springer, 2007.
31. Westerweel J. Theoretical analysis of the measurement precision in particle image velocimetry. *Exp Fluids* 2000; 29: S003–S12.
32. Erm L. Measurement of flow-induced pressures on the surface of a model in a flow visualization water tunnel. *Exp Fluids* 2003; 35: 533–540.
33. Hansen KL, Kelso RM and Dally BB. Performance variations of leading-edge tubercles for distinct airfoil profiles. *AIAA J* 2011; 49: 185–194.
34. Sayers A and Ball D. Blockage corrections for rectangular flat plates mounted in an open jet wind tunnel. *Proc IMechE, Part C: J Mechanical Engineering Science* 1983; 197: 259–263.
35. Granlund K, Ol M, Garmann D, et al. Experiments and computations on abstractions of perching. In: *28th AIAA applied aerodynamics conference*, Chicago, Illinois, 2010, p. 4943.
36. Hansen KL. Effect of leading edge tubercles on airfoil performance. The University of Adelaide, Australia, 2012.

Chapter 5.

Passive Control of Dynamic Stall

5.1. Chapter 5 Overview

Control of the dynamic-stall process at high rotation rates and elevated angles of attack are explored in this chapter to address the third objective and to identify the suitability of a leading-edge trip as a passive flow control method in highly unsteady flow conditions. In the current work, the behaviour of the trip wire as a method of boundary layer control is explored. The trip-wire was fixed at varying distances from the leading edge of a NACA 0012 airfoil undergoing constant-pitch-rate rotation, where $Re = 20{,}000$ and $\kappa = 0.025$, 0.5 and 0.1. The trip-wire was observed to reduce the lift prior to dynamic stall onset. The control device was also shown to lower post-stall load fluctuation, however, the wire was more successful in reducing the build-up of the laminar separation bubble developed at low Reynolds numbers and prior to dynamic stall. Results from the work indicate that the influence of inertial flows, generated via the high rotation-rate motion of the airfoil, dominated the force and flow characteristics of the wing. As the diameter of the trip wire was increased, a superposition of the two bodies was observed, where the two bodies acted as one, leading to increased lift and drag. It is concluded that alternative flow control methods should be utilised for the control of dynamic stall at unsteady rotation rates, and where the wings are exposed to elevated angles of attack.

5.2. Elevated Trip Wires for Unsteady Dynamic Stall Control

Statement of Authenticity

Title of Paper:	Wind Turbine Load Control During Post-Stall and Extreme Weather Conditions Using Leading-Edge Trips
Publication Status:	☐ Published ☐ Accepted for Publication ☑ Submitted for Publication ☐ Unpublished and Unsubmitted w ork w ritten in manuscript style
Publication Details:	Leknys, R. R., Arjomandi, M., Kelso, R. M. & Birzer, C. H., 2017, Wind Turbine Load Control During Post-Stall and Extreme Weather Conditions Using Leading-Edge Trips, *Journal of Wind Energy and Industrial Aerodynamics*

Principal Author

Name of Principal Author:	Ryan Ross Leknys
Contribution to the Paper:	Performed data analysis and interpretation, wrote manuscript and acted as corresponding author.
Overall percentage (%):	70
Certification:	This paper reports on original research I conducted during the period of my Higher Degree by Research candidature and is not subject to any obligations or contractual agreements with a third party that would constrain its inclusion in this thesis. I am the primary author of this paper.

Signature: ___ Date: 05 March 2018

Co-Author Contributions

By signing the Statement of Authorship, each author certifies that:

vii. the candidate's stated contribution to the publication is accurate (as detailed above);

viii. permission is granted for the candidate in include the publication in the thesis; and

ix. the sum of all co-author contributions is equal to 100% less the candidate's stated contribution.

Name of Co-Author:	Associate Professor Maziar Arjomandi
Contribution to the Paper:	Supervised the development of the research and contributed in academic discussion and the review process of submitted manuscripts.

Signature: _____ _____ Date: 05 March 2018

Name of Co-Author:	Associate Professor Richard Kelso
Contribution to the Paper:	Supervised the development of the research and contributed in academic discussion and the review process of submitted manuscripts.

Signature: Date: 05 March 2018

Name of Co-Author:	Dr Cristian Birzer
Contribution to the Paper:	Supervised the development of the research and contributed in academic discussion and the review process of submitted manuscripts.

Signature: __ _____ Date: 05 March 2018

Wind Turbine Load Control During Post-Stall and Extreme Weather Conditions Using Leading-Edge Trips

Leknys R. R.*, Arjomandi M., Kelso R. M., Birzer C. H.

The University of Adelaide

School of Mechanical Engineering, Adelaide, South Australia, 5005

*Corresponding author email: ryan.leknys@adelaide.edu.au

Abstract

Dynamic stall significantly impacts the performance of horizontal-axis wind turbines where unsteady blade loading is generated. This article describes the effects of a passive flow-control device in the form of a leading-edge trip wire applied to a NACA 0012 airfoil at high angle of attack and dynamic stall conditions and where the Reynolds Number is 20,000. For determination of unsteady lift, surface pressure measurements were conducted. The benefit of the trip wire at high reduced frequencies was shown to be minimal due to the large accelerated flows induced by airfoil rotation, and decreases in maximum force and stall intensity were observed. The trip wires were shown to decrease maximum lift, although the stall angle of attack was not observed to change with trip wire diameter. Increasing the trip wire diameter beyond 1.6% of the airfoil chord led to geometric superposition of the trip wire and wing body, leading to subsequent increases in force. Under post-stall flow conditions, the leading-edge trip wire was shown to have

little impact on the large-scale von Karman vortex structure development, where load oscillation and vibration occurred.

Keywords

Wind Turbine; Dynamic-stall Control; Unsteady Reduced Frequency; Boundary Layer; Vortex Shedding

Introduction

Ever-increasing requirements for clean energy production have led to a greater demand for renewable energy resources, including the application of horizontal-axis wind turbines (HAWT). Maximising the energy output of a HAWT requires detailed analysis of the environmental operating conditions in conjunction with the imposed aerodynamic loads created through its unsteady operation. Dynamic stall is one such unsteady phenomenon generated during the operation of a HAWT exposed to high yaw angles, unsteadiness in the atmospheric boundary layer and turbine-wake interaction. Such conditions lead to the formation of a characteristic leading-edge vortex, which has been widely investigated due to the excessive loads it imposes on the mechanical components and blades of HAWTs. Previous studies [1-3] highlighted the necessity to study the dynamic-stall and post-stall aerodynamic characteristics of the turbine blades when exposed to high yaw angles, tower shadow and upwind turbine wakes.

Under dynamic-stall conditions, delayed separation occurs, which is subsequently followed by the formation of a leading-edge vortex structure as the angle of attack is further increased [4]. The formation of dynamic-stall vortex structures is linked to adverse pressure gradients at the leading edge and typically results from geometric discontinuities or loss of momentum within the attached boundary layer at elevated angles of attack,

well beyond steady-state angles of attack. The leading-edge vortex leads to increased force generation, which itself has been shown to vary with performance parameters such as Reynolds number, pitch rate, Mach number and airfoil geometry [5-13]. Control and manipulation of the leading-edge vortex can therefore be used to delay the onset of dynamic stall and force generation characteristics. However, practical methods of doing so are limited. Furthermore, increasing operation of rotor blades in post-stall conditions requires accurate analysis of the aerodynamic behaviour such that blades can be developed to withstand the applied loads.

As the majority of research conducted on dynamic stall is focused on low angles of attack, where attempts to avoid airfoil stall are sought, research into stall and post-stall characteristics of the airfoils in dynamic stall conditions is still limited. This insight into the challenge of stalled and post-stalled flow conditions was also expressed in Butterfield [2], who discussed the challenge in determining wind turbine blade loads at angels of attack between $12°$ and $30°$. For post-stalled conditions, beyond $\alpha = 30°$, flat-plate aerodynamic properties have generally been employed for the design of wind turbine blades [2, 14]. Although flat-plate approximations provide a starting point in the design process of a turbine blade, the method is somewhat flawed and should not completely be depended upon, due to blade thickness variations along the span, and the tendency of stalled, thick airfoil sections to behave in a manner similar to cylinders [15]. Under such conditions the application of flat-plate aerodynamic characteristics becomes invalid.

Similar to steady-state stall, under dynamic-stall conditions and immediately following dynamic stall, application of flat-plate analysis may not fully provide the correct aerodynamic loading on turbine blades. The resulting force fluctuation, outside of those

predicted by flat plate analysis, are of concern to wind engineers and designers of HAWT components due to the over- or under-prediction of the aerodynamic loading during these conditions. In addition, these comments highlight the need for further experimental data relating to the stall characteristics of airfoils, with profiles specific to wind turbines, exposed to elevated angles of attack, and which have undergone dynamic stall and proceeded into a state of fully-separated flow.

Implementation of effective, inexpensive and simple flow-control devices can be a viable means to manipulate and control boundary-layer separation on turbine blades. However, greater understanding of such devices with a minimal drag penalty is still needed for stall and post-stall conditions at elevated angles of attack. Techniques applicable to the control of steady-state boundary layer separation have been investigated for their applicability for dynamic stall conditions. Katz, Nishri and Wygnanski [16] and Lachmann [17] detail the process of laminar and turbulent separation and highlight numerous methods of both active and passive boundary layer control methods, whilst Choudhry et al. [18] review current active and passive control methods utilised for the control of dynamic stall on wind turbines. These flow control techniques have a common objective to delay or reduce the extent of separation by either reducing the surface curvature at the leading edge, thus decreasing the adverse pressure gradient, or by introducing flow momentum within the boundary layer by utilising devices such as blowing or suction.

Active control systems require continuous feedback and often are associated with increased cost and complexity. Active boundary-layer control techniques currently investigated for control of the dynamic stall process include adaptive airfoil geometries [19-26], upper surface blowing [27-32], periodic boundary layer excitation [33-36, 26],

boundary layer suction [37, 38] and more recently, the use of plasma actuators [39-41]. Of these methods, all have been demonstrated to influence dynamic stall to moderately-high angles of attack, although they all consist of highly complex systems that must be tuned to the conditions such that an efficient control of the boundary layer is achieved. In real conditions, less complex systems are preferred due to lower maintenance and installation costs. With an increasing demand for clean, renewable energy, wind turbine size and numbers have increased significantly. Furthermore, placement of the turbines away from urban areas results in increased demand on the turbine due the harsh operating conditions and their remote operating locations [42]. As such, implementation of active boundary layer control systems become increasingly complex and costly to both implement and maintain. For this reason, the use of passive boundary-layer control devices presents a viable means to control dynamic stall, due to simpler installation, lower production cost and ease of use.

Control of separation and increased stall angle of attack on airfoils operating in steady-state conditions have been achieved through the utilisation of devices that generate stream-wise vorticity. Examples include classical vortex generators, airfoils modified with tubercles [43-45], and changes to the wing layout, for example by using undulating-leading edges [46]. Using stream-wise vorticity, significant potential in suppressing separation at moderate angles of attack and increasing the aerodynamic performance at angles of attack close to stall were demonstrated. Although much interest in the application of tubercles for steady-state boundary layer control has been generated, their application has, to an extent, been limited with respect to dynamic stall conditions. One such study into the use of this flow control method under dynamic-stall conditions was undertaken by Hrynuk [47], who concluded that the base flow structure (span-wise to

stream-wise vorticity) was modified for a wing with tubercles, although a single span-wise vortex remained present and shed into the wake once the airfoil transitioned into a deep stalled phase. From the previous literature, tubercles have been shown to be beneficial at pre-stall angles of attack, however in deep-stall flow conditions they do not show any effect on the flow separation process.

Other, more traditional, passive flow-control methods utilise changes in the airfoil geometry via application of flaps and slats at fixed locations [48-50]. Both methods have been proven to delay separation and mitigate the formation of the leading-edge vortex. However, the application of such mechanisms requires complex actuators, where aerodynamic loading and response time are large and thus limit the applicability of the system [51]. Furthermore, passive boundary-layer control devices using leading-edge vortex generators [51] and cylindrical and triangular protrusions mounted on the underside of the leading edge [52], have been shown to reduce the maximum lift, drag, and pitching moment fluctuations at high angles of attacks during dynamic stall. In addition to vortex generators, leading-edge trip wires and span-wise cavities were also investigated by Choudhry [53] for low, quasi-steady rotation rates, such that $\kappa < 0.025$ where $\kappa = \omega c/2U_\infty$, in order to reduce the load fluctuation during the dynamic-stall process. Here ω is the angular velocity in rad/s, c is the airfoil chord length in m and U_∞ is the free-stream velocity in m/s.

In Choudhry et al. [18], a trip wire located at a range of displacements from the leading edge was shown to reduce the stall intensity and improve post-stall flow characteristics, where maximum aerodynamic force was reduced with respect to a clean airfoil. Surface pressure measurements showed that peak lift was reduced by 50% and stall intensity was

also reduced under dynamic-stall conditions for airfoils equipped with the leading-edge trip wire, compared with the clean airfoil case. As the low rotation rates led to reductions in stall intensity [18, 53], the feasibility of investigating the effects of leading-edge trip wires under conditions of high rotation rates is warranted.

This article aims to describe the effects of thin airfoil dynamic stall control where operating conditions are subject to high angles of attack and high rotation rates, typical of high wind shear and gust-like conditions. Control of the dynamic-stall process and post-stall flow characteristics is investigated by utilising a fixed-displacement leading-edge trip wire whereby span-wise vorticity can be introduced to minimise the aerodynamic load variation prior to and after dynamic stall occurrence. Specifically, trip wires with a range of diameters, located at a fixed distance from the leading edge, will be assessed to determine their impact and applicability as a boundary-layer control method for airfoils undergoing constant-pitch-rate dynamic stall. The work herein extends the research conducted in Choudhry, Arjomandi and Kelso [54], where quasi-steady flow conditions ($\kappa = 0.023 \rightarrow 0.038$) were utilised, to the investigation of highly-unsteady operating conditions ($\kappa = 0.025 \rightarrow 0.1$). Additionally, unsteady rotation rate tests will be conducted at elevated angles of attack to determine the effectiveness of the trip wire during dynamic stall and proceeding into post-stall flow states. Mitigation of the post-stall load fluctuation on the blades of horizontal-axis wind turbines will assist the optimisation of turbine control systems, whilst reducing the power fluctuation and blade fatigue developed from the unsteady vortex shedding process

Experimental Procedure

Experiments investigating dynamic stall were conducted in an open-return wind tunnel with a $0.5m \times 0.5m$ test section and a turbulence intensity of $\sim 0.85\%$ [44]. A symmetrical NACA 0012 airfoil of chord $c = 0.1\ m$ and span $b = 0.5\ m$ was fitted with a series of pressure ports distributed along the wing chord at the centre of the wing's span. The arrangement of the pressure ports and the wind tunnel test arrangement are shown in Figure 1.

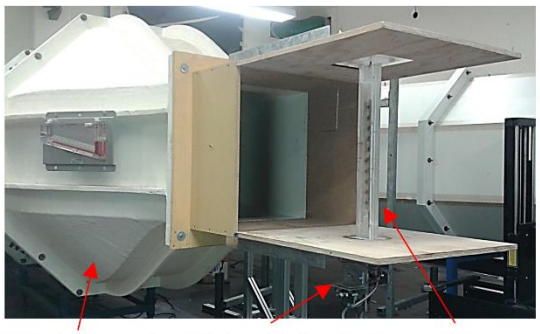

a)

Sensor	% X/C	% Z/C
1	0.00	0.00
2 & 11	3.75	2.17
3 & 12	8.75	5.06
4 & 13	15.00	8.67
5 & 14	22.50	13.00
6 & 15	31.25	18.05
7 & 16	41.25	23.82
8 & 17	52.50	30.32
9 & 18	65.00	37.54
10 & 19	78.75	45.48

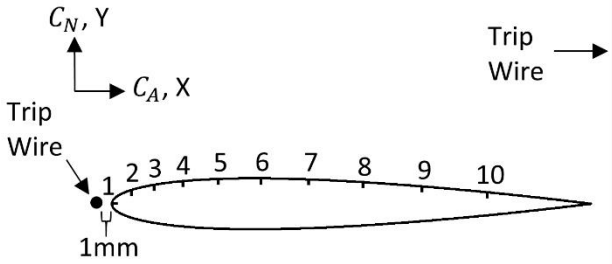

b)

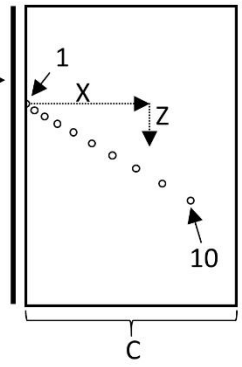

c)

Figure 1: a) Test setup indicating the wind tunnel, wing and motor controller combination employed for dynamic stall testing, b) Chord-wise surface pressure port distribution on the NACA 0012 wing, c) Plan view of the pressure port locations located at the mid-span location of the wing.

The Reynolds number (Re), based on the chord of the wing, was $Re = 20{,}000$. Due to the induced inertial effects developed as a consequence of high rotation rate motion, the influence of Reynolds number can be considered minor when determining the behaviour of major flow structure and the unsteady separation process [55]. Furthermore the Reynolds Number is generally considered to have minimal influence on the unsteady separation process with little impact on the overall characteristics of the separation process [18, 56, 13]. As such the current investigation can be conducted with confidence to identify the variation in performance of the leading-edge trip wire on airfoil exposed to high rotation rate dynamic stall. The surface of the airfoil was CNC machined and post finished using a combination of 600 and 1200 grit emery paper to achieve a uniform and polished surface finish. This resulted in an average surface deviation of $\epsilon = 30\mu m$, or an effective surface roughness of $c/\epsilon = 3.3 \times 10^4$. However, due to the low operating Reynolds Number in the current investigation, a smooth surface could be considered for the current wind tunnel configuration, leading to no observable increases in skin friction drag as a result of surface roughness [57].

The blockage area ratio of the test set-up was approximately 17% at the maximum test angle of attack, $\alpha_{max} = 60°$. Correction of the test data to account for blockage effects in the open section was not performed for the current article due to the minor variation in force generation during the dynamic stall process as described in Granlund et al. [58]. Furthermore, as the airfoil was located 250mm downstream of the wind tunnel opening, free expansion of the wake streamlines was possible further reducing blockage effects [59]. As the current system was limited to a maximum angle of attack of only $\alpha = 60°$ for short periods of time, and due to the absence of side walls limiting free expansion of the wake, blockage corrections were considered insignificant under the present test

configurations. In addition, wind tunnel test at low Reynolds numbers using flat plates in STO [60] indicate minor variation between results obtained from independent wind tunnel facilities with varying blockage ratios. As such, corrections for blockage were not considered significant to manipulate the resulting aerodynamic force generation.

The surface pressure ports were connected directly to $250 \pm 1\%\, Pa$ *Honeywell Truestability®* differential pressure sensors with internal amplification and self-compensation capabilities. The sensors were fixed to a custom-made circuit board mounted in a cavity within the wing and collectively referenced to atmospheric conditions. A *National Instruments®* NI-6210 data acquisition module was utilised, in conjunction with a custom program based on Labview control software, to convert the generated voltage outputs from the pressure sensors into pressure values for both the wing and Pitot tube.

Constant-pitch-rate airfoil motion was provided using a *MaxonMotor®* digital position encoder and DC motor connected to a gear box providing a $28:1$ reduction, coupled directly to a drive shaft located at the mid-chord pivot position of the wing body. The accuracy of rotation was such that the desired angle of attack was controlled to within $\alpha = \pm 0.25°$. The non-dimensional rotation rate was fixed at values of $\kappa = 0.025$, 0.05 and 0.1. Equivalent rotation rates for these reduced frequencies ranged between, $\omega = 1.47 \mathrm{rad/s}$ and $\omega = 5.87\ \mathrm{rad/s}$. The angular displacement with respect to non-dimensional time, T^*, is shown in Figure 2.

Primary evaluation of high $Re - \kappa$ combinations resulted in the introduction of angular displacement errors resulting from the excessive inertial loads placed on the drive motor due to high angular acceleration. To minimise these errors a gradual acceleration was

employed in the first 5° of angular displacement in both the ramp-up and ramp-down stages, thereby achieving an accurate and repeatable trapezoidal velocity profile.

The maximum angle of attack was set to three values of $\alpha = 20°$, $\alpha = 40°$ and $\alpha = 60°$. Once the airfoil reaches the maximum angle of attack, its position was held fixed, to replicate post-stalled flow conditions. The airfoil is held fixed at the maximum angle of attack for a non-dimensional time value of $T^* = 10$, such that $T^* = TU_\infty/c$, where T is the resulting flow time (s).

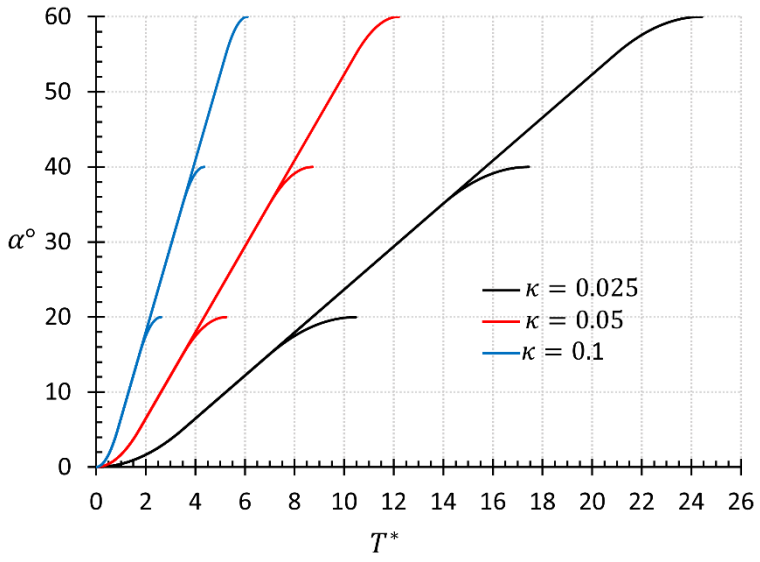

Figure 2: Airfoil angular displacement with respect to non-dimensional time for reduced frequencies of $\kappa = 0.025$, $\kappa = 0.05$ *and* $\kappa = 0.1$ *and for each maximum angle of attack evaluated.*

The aerodynamic force coefficients, with respect to the airfoil coordinate system, were evaluated using a trapezoidal integral [18] of the pressure coefficient, C_P, distribution as described in Equation 1, where P is the measured static pressure, P_0 is the pressure sensor reference pressure, and ρ and V_∞ are the respective free stream density and flow velocity.

$$\mathrm{C}_P = \frac{P - P_0}{1/2\,\rho {V_\infty}^2}, \qquad \mathrm{C}_A = \oint \frac{C_P}{c} dy, \qquad \mathrm{C}_N = -\oint \frac{C_P}{c} dx \tag{2}$$

In Equation(s) 1, C_N and C_A are the respective airfoil normal and axial force coefficients, and dx and dy are the horizontal and vertical displacements between the surface pressure sensors with respect to the x and y coordinate system of the airfoil. Subsequent lift and drag coefficients in the wind tunnel coordinate system were determined using Equations 2.

$$\mathrm{C}_L = C_N \cos\alpha - C_A \sin\alpha, \qquad \mathrm{C}_D = C_N \sin\alpha + C_A \cos\alpha \tag{3}$$

Satisfactory statistical convergence of the measured pressure data was achieved after a total of 100 repeated test cases of the dynamic stall pitch-up simulation. A total of 3000 samples were recorded for each individual surface pressure sensor throughout the duration each test to capture the low-pressure vortex structures developed during the ramp-up and hold motion. As positive benefits were established in Choudhry, Arjomandi and Kelso [54] for the application of a trip wire with fixed diameter, investigations of the sensitivity of the flow to trip wire diameter and its applicability as a turbulence generator at a fixed displacement were investigated in the current article using four test cases of varying diameters. These included, a clean airfoil, where all trip wires were removed, and cases where trip wires of $0.95\mathrm{mm}$, $1.2\mathrm{mm}$, $1.6\mathrm{mm}$ and $2\mathrm{mm}$ diameter were installed at a fixed displacement of $1\ \mathrm{mm}$ forward of the wing leading edge.

Results

Interpretation and Error Analysis

Data from the pressure sensors was post-processed in order to evaluate the variation and average of the generated force coefficients of all pitch-up test cases. The resulting lift coefficients generated from integration of the averaged surface pressure readings, with $\alpha = 20°$ and $\kappa = 0.025$, are displayed in Figure 3.

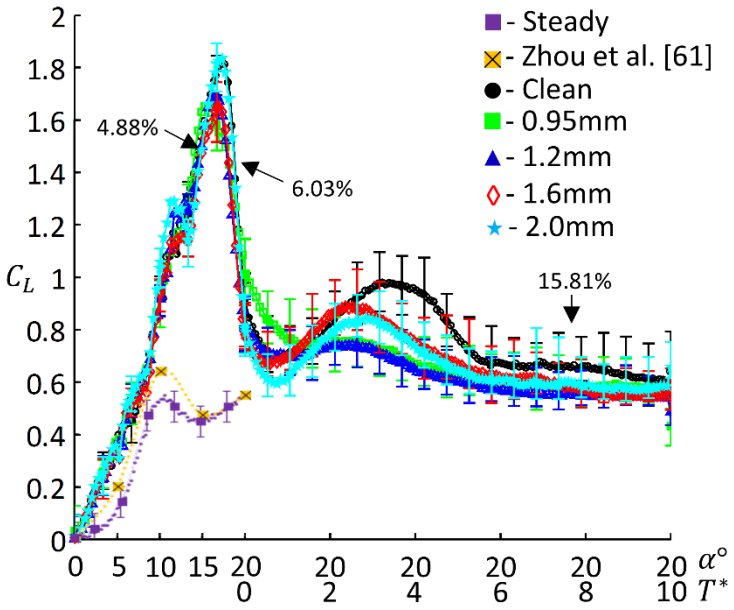

Figure 3: Lift Coefficient of the NACA 0012 airfoil and fluctuations of maximum and minimum forces evaluated for the clean and leading-edge trip wire configurations ranging over the complete dynamic stall test range. $\kappa = 0.025$, $\alpha_{max} = 20°$.

Also shown in Figure 3 are the maximum and minimum variations in force resulting from the fluctuations in the wing surface pressure, plotted with respect to the angle of attack and also T^*. Here T^* represents the flow time after the airfoil has reached its maximum angle of attack and ceased to continue to rotate. To ensure correct operation of the sensors, steady state values evaluated from the current investigation were compared to

results obtained in Zhou et al. [61]. A comparison of the current steady-state results shows good agreement with results in Zhou et al. [61] and provides confidence in further analysing dynamic stall conditions using the test arrangement.

A maximum variation from the mean was found to be approximately 15% in deep-stall regions. Similar observations in force deviation were also observed in Heine et al. [52], where wake vortex shedding during post-stall operation resulted in increased surface pressure and force fluctuation about the airfoil. For regions of attached flow, where $\alpha < 15°$, a maximum deviation from the mean of approximately 6% was obtained. In addition, variability of the mean force coefficient was evaluated to be approximately $\pm 1.2\%$ based on a 95% confidence level of the averaged dynamic stall data recorded. Errors resulting from pressure sensor operation were considered to be minor with regards to the overall pressure measured during dynamic stall. Under such operation, a maximum of 2% variation in pressure measurement was obtained over the entire operating range of the pressure sensors utilised. This equated to a pressure error at the leading edge stagnation point of approximately $0.3Pa$ when operating at $Re = 20{,}000$, or when the measured stagnation pressure was approximately $16Pa$. Large deviations in force coefficient resulted as a consequence of large-scale vortex shedding within post-stall phase and due to unsteady separation of the boundary layer on the upper surface of the airfoil.

Figure 3 indicates the variation in force coefficient errors for the clean wing and for the wing with the leading-edge trip wire attached. Prior to dynamic stall, during the ramp-up phase of the wing, force coefficients for all test cases were seen to be similar, with no statistical significant differences occurring between each of the test data sets. Increasing the angle of attack, where $\alpha > 15°$ and $T^* < 1$, to promote the formation of the leading-

edge vortex results in an error of less than 5% for pre- and post-dynamic-stall phases. Under post-stall conditions, where large vortex structure development and force fluctuation occur, a maximum error of 16%, based on the respective mean lift coefficient value. Post-stall force variation was shown to be a maximum of 5.15%. The fluctuations in surface pressure, resulting in the force coefficient errors, were shown to be the same for all test cases. Due to the subtle changes in force generation for the cases where the leading-edge trip wire was applied, and to increase the visibility of the effects of the trip wire, results for cases utilising the trip wire were normalised such that $C_{LN} = C_{L\,T}/C_{LC}$, where C_{LN} is the variation in lift coefficient generated using the trip wire, $C_{L\,T}$, normalised with respect to the clean airfoil lift coefficient, C_{LC}.

Impact of the Trip Wire

Figure 4 shows the effects of varying the trip wire diameter on the NACA 0012 airfoil lift coefficient and aerodynamic efficiency, C_L/C_D. The figure consists of three pairs of graphs of equal maximum angle of attack, where $\alpha_{max} = 20°$, and increasing the non-dimensional rotation rate, such that $\kappa = 0.025, 0.05, 0.1$ for Figure 4(a, d), Figure 4(b, e) and Figure 4(c, f) respectively. For each case, the angle of attack is indicated along with the non-dimensional time after cessation of the airfoil motion at its maximum angle of attack. Each non-dimensional time unit represents one chord length of travel of the free-stream fluid over the airfoil. For $\kappa = 0.05$, a vortex is observed to develop at the leading edge of the airfoil. This is shown through an increase in lift coefficient, as highlighted in Figure 4b. Similar dynamic stall test conditions were also performed using PIV in a related study, and shown in Figure 4e, which corroborates the presence of the leading-edge vortex and subsequent increase in lift during the pitch-up motion.

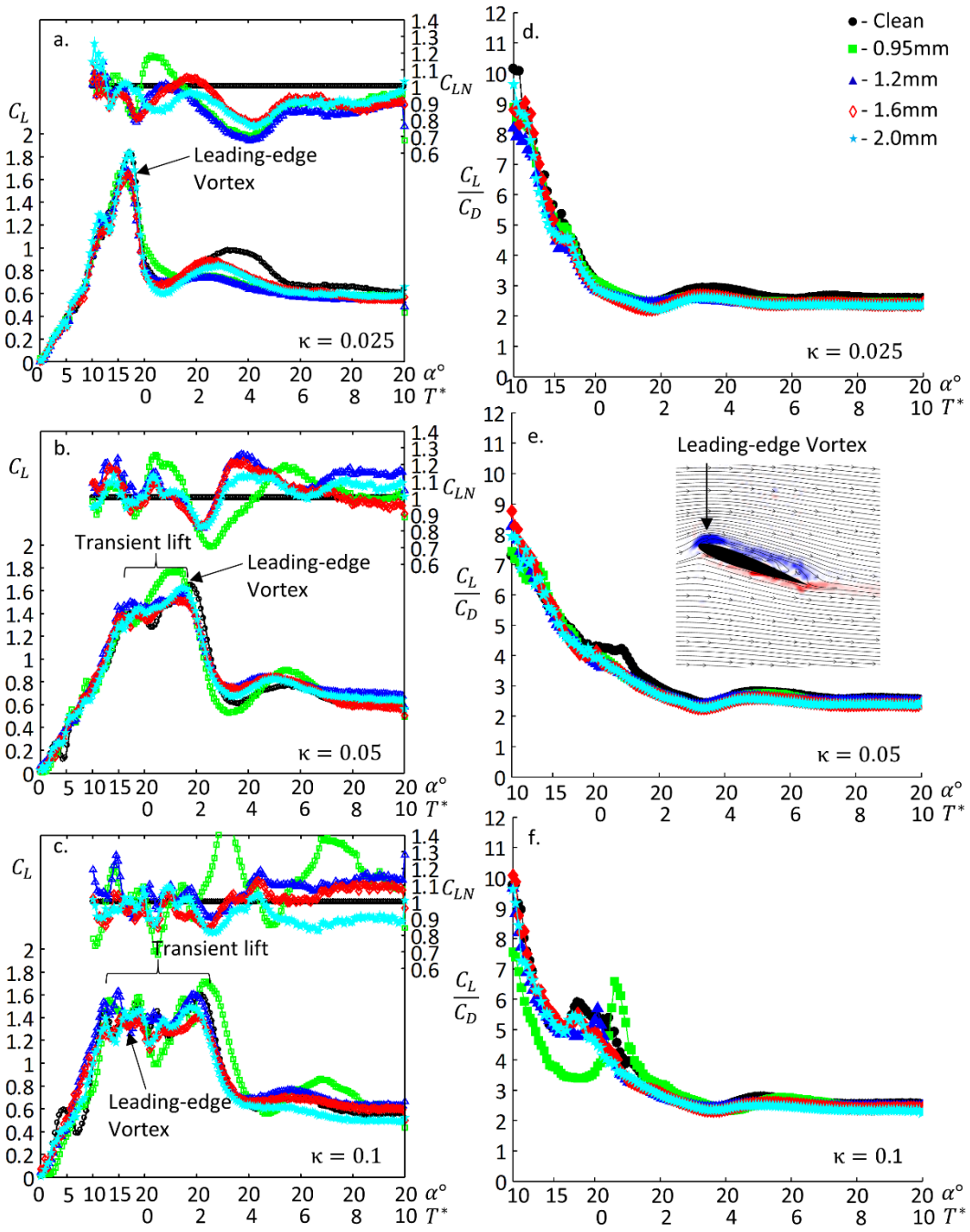

Figure 4: NACA 0012 lift coefficient with normalised trip wire lift coefficient (a, b, c) and lift to drag ratio of post-stall flow conditions (d, e, f) for increasing non-dimensional rotation rate and constant angle of attack, where $\alpha = 20°$.

For $\alpha < 5°$, results indicate that both upper and lower surface pressure distributions are similar with little deviations. This was found to be associated with the increased rotation rate of the airfoil and induced inertial effects at the leading edge leading to decreases in pressure on the lower surface of the airfoil as a result of the pitch-up motion of the airfoil.

Shown in Figure 5 is the surface pressure coefficient of the clean airfoil for increasing angles of attack prior to stall at $\alpha = 20°$.

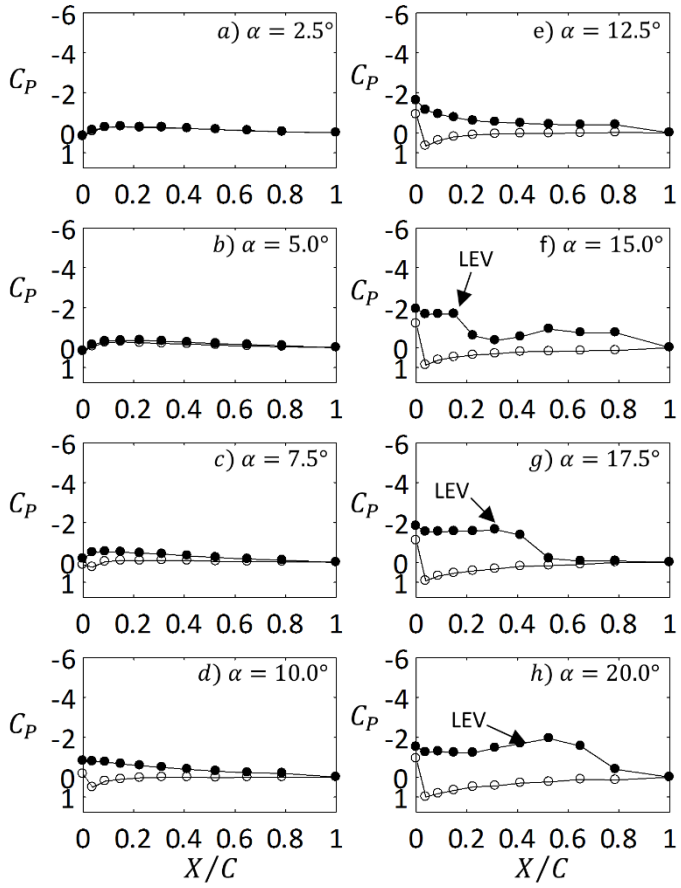

Figure 5: Surface pressure coefficient for the clean NACA 0012 airfoil for $\kappa = 0.025$ indicating the formation of the leading-edge vortex (LEV) and subsequent increased suction resulting in additional lift. ● – Upper Surface, o – Lower surface.

The presence of the leading-edge vortex causes the lift coefficient to increase until the flow fully separates from the airfoil at $\alpha = 20°$, and at which point the lift is seen (Figure 3(a)) to decrease significantly to $C_L = 0.8$. After the leading-edge vortex is shed, and once the airfoil is held fixed at the maximum angle of attack of $20°$, post-stall flow conditions are established. A secondary increase in lift is observed to develop at $T^* = 4$ in Figure 4(a), due to secondary vortex structure development as a result of bluff body separation after the airfoil rotation has ceased. This vortex structure leads to a low-pressure region forming at the leading edge and then extending towards the trailing edge with time. The low-pressure region is indicated in Figure 6, which shows the pressure coefficient developed over the chord of the airfoil with respect to the airfoil angle of attack and T^*. Also indicated in Figure 6 is evidence of a laminar separation bubble prior to $\alpha = 15°$ and the formation of both the leading-edge vortex and secondary vortex structure developed in the post-stall conditions. In regions where the separation bubble exists near the trailing edge, the flow is influenced by the unsteady trailing edge vortex separation combined with shedding and convection of vortices at the leading edge. The net effect of the unsteady vortex shedding leads to unsteady upper-surface pressures, visible by scatter in the pressure contours prior to leading-edge vortex development and aft of the leading-edge vortex once it is formed.

After T^*= 8, a plateau in lift force is observed in Figure 4(a), indicating bluff-body separated flow conditions. Similar force generation profiles can be seen until $20°$ for the cases of $\kappa = 0.05$ and $\kappa = 0.1$, as indicated in Figure 4(b) and Figure 4(c) respectively. However, increasing the non-dimensional rotation rate was shown to increase the duration of maximum lift, where C_L was sustained for periods of $T^* = 0$, $T^* = 2$ and $T^* = 3.5$ for $\kappa = 0.025$, $\kappa = 0.05$ and $\kappa = 0.1$ at the airfoil maximum angle of attack, as shown

in Figure 4(b, c). The increased transient lift can be attributed to the delay in formation of the leading-edge vortex, where for example, with $\kappa = 0.025$, early formation of the leading-edge vortex and its separation are observed. With increased non-dimensional rotation rate, airfoil angular velocity is increased such that separation and roll up of the leading-edge vortex are delayed until the maximum angle of attack is reached.

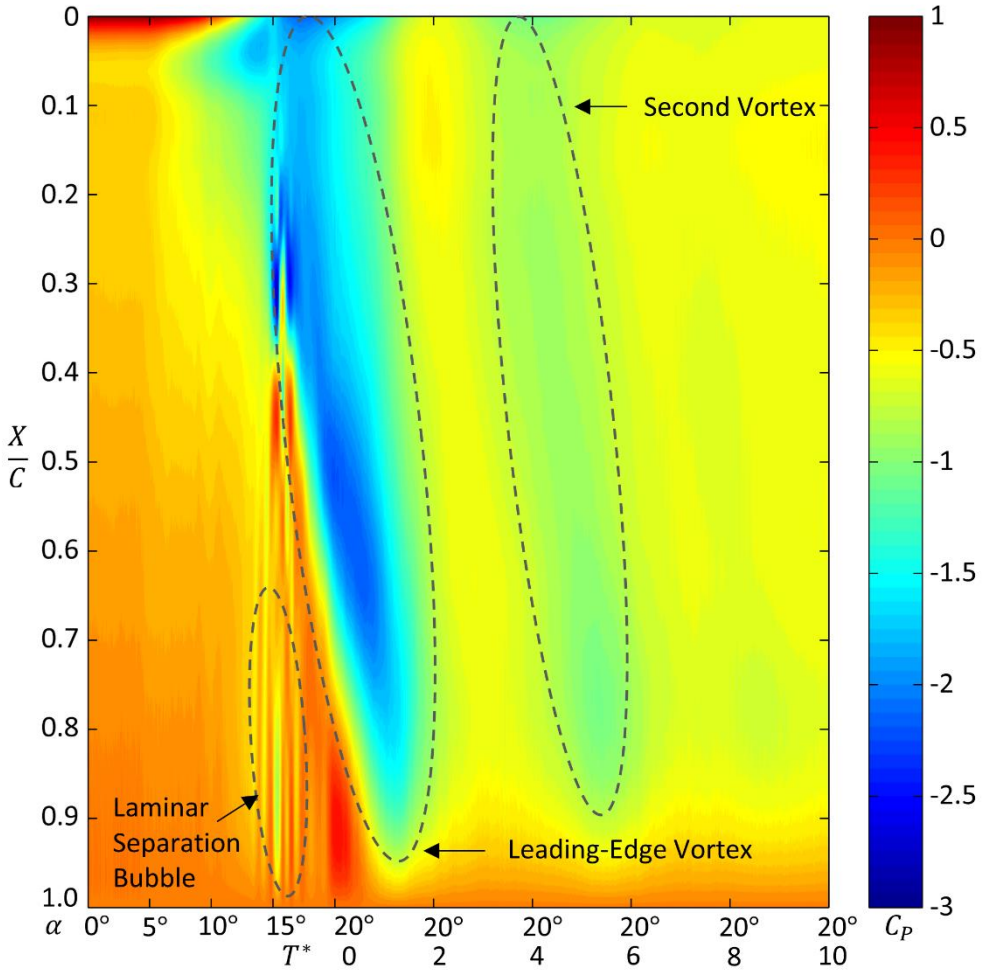

Figure 6: Normalised chord length upper surface pressure contour with respect to angle of attack and normalised time, indicating localised low pressure regions correlating to the laminar separation bubble, leading-edge vortex and second vortex formation. $\kappa = 0.025$ *and* $\alpha_{max} = 20°$.

Once stoppage of the airfoil motion occurs at the maximum angle of attack, large scale separation and roll up of the leading-edge vortex occurs due to the highly adverse pressure gradients at the region of the leading edge. In regions where the separation bubble exists near the trailing edge, the flow is influenced by the unsteady trailing edge vortex separation combined with shedding and convection of vortices at the leading edge. The net effect of the unsteady vortex shedding leads to unsteady upper-surface pressures, visible by scatter in the pressure contours prior to leading-edge vortex development and aft of the leading-edge vortex once it is formed. The effect of the trip wire was demonstrated to be greater at lower reduced frequencies, for example when $\kappa = 0.025$, such that conditions similar to steady-state conditions were replicated [62] and enhanced mixing within the boundary layer could be utilised to control the vortex shedding process and its impact on overall force generation. Under the lowest reduced-frequency test condition, the wake from the trip wire appears to assist with mixing and momentum transfer in the airfoil boundary layer, preventing separation and reducing the build-up of vorticity in the form of the leading edge vortex.

Sensitivity of the airfoil force generation to the trip wires in post-stall conditions was shown to be minimal at all three reduced frequencies, with the normalised lift coefficient trending towards 1 as $T^* \rightarrow 10$ for all cases of varying non-dimensional rotation rate. Once dynamic stall had occurred, post-stall flow conditions were established within 2 shedding cycles of the airfoil. This, however, was difficult to observe for $\kappa = 0.05$ and $\kappa = 0.1$ due to the increased amplitude of fluctuation in C_L and the finite period of data acquisition (up to $T^* = 10$). Figure 4(a, b, c) show that once post-stall flows were established, the lift coefficient asymptotically approached a value of $C_L = 0.6$ for post-stall, fully separated conditions.

To investigate the influence of the trip wires at elevated angles of attack, experiments were performed for the case of $\alpha_{max} = 40°$. Application of the trip wires for this case was shown to lower the maximum lift coefficient relative to the clean airfoil configuration, prior to dynamic stall and shedding of the leading-edge vortex. Figure 7 shows the lift coefficient plotted against the angle of attack and non-dimensional time for ramp-up and hold dynamic stall for the NACA 0012 airfoil.

The normalised lift coefficient (as defined above) of the airfoil fitted with each trip wire at the leading edge is also shown. Overall airfoil efficiency (C_L/C_D) under post-stall conditions is also presented. Similarities in lift generation prior to $\alpha = 20°$ did not show significant differences between each trip wire evaluated, so only the airfoil efficiency during leading-edge vortex growth and in post-stall conditions are indicated.

Dynamic stall was initiated at $\alpha = 25°$ for $\kappa = 0.025$, as observed through the sudden reduction in lift coefficient in Figure 7(a). Due to the lower rotation rate, separation of a second vortex is observed at $\alpha = 37°$. The increase in lift at $\alpha = 37°$ coincides with the reduction in surface pressure as indicated in Figure 8, which shows the pressure coefficient of the upper surface of the NACA 0012 airfoil pitching to $\alpha = 40°$ and maintaining the maximum angle of attack for $T^* = 10$.

As the non-dimensional rotation rate was increased from $\kappa = 0.025$ to $\kappa = 0.05$, the presence of the second vortex structure developed at $\alpha = 20°$ (Figure 6) was no longer observed. Alternatively, for $\kappa = 0.025$, formation of the leading-edge vortex was shown to occur at $\alpha = 20°$, and with the airfoil angle of attack still increasing, a second vortex structure originating at the leading edge was observed to form at $\alpha = 30°$. The peak strength of the second vortex and the associated lift are significantly lower than that of

the leading-edge vortex, which is associated the lowest surface pressures and highest lift over the airfoil as indicated in Figure 8. Formation of a third vortex, for $\kappa = 0.025$, can be associated with the transition into deep stall where periodic vortex shedding occurs.

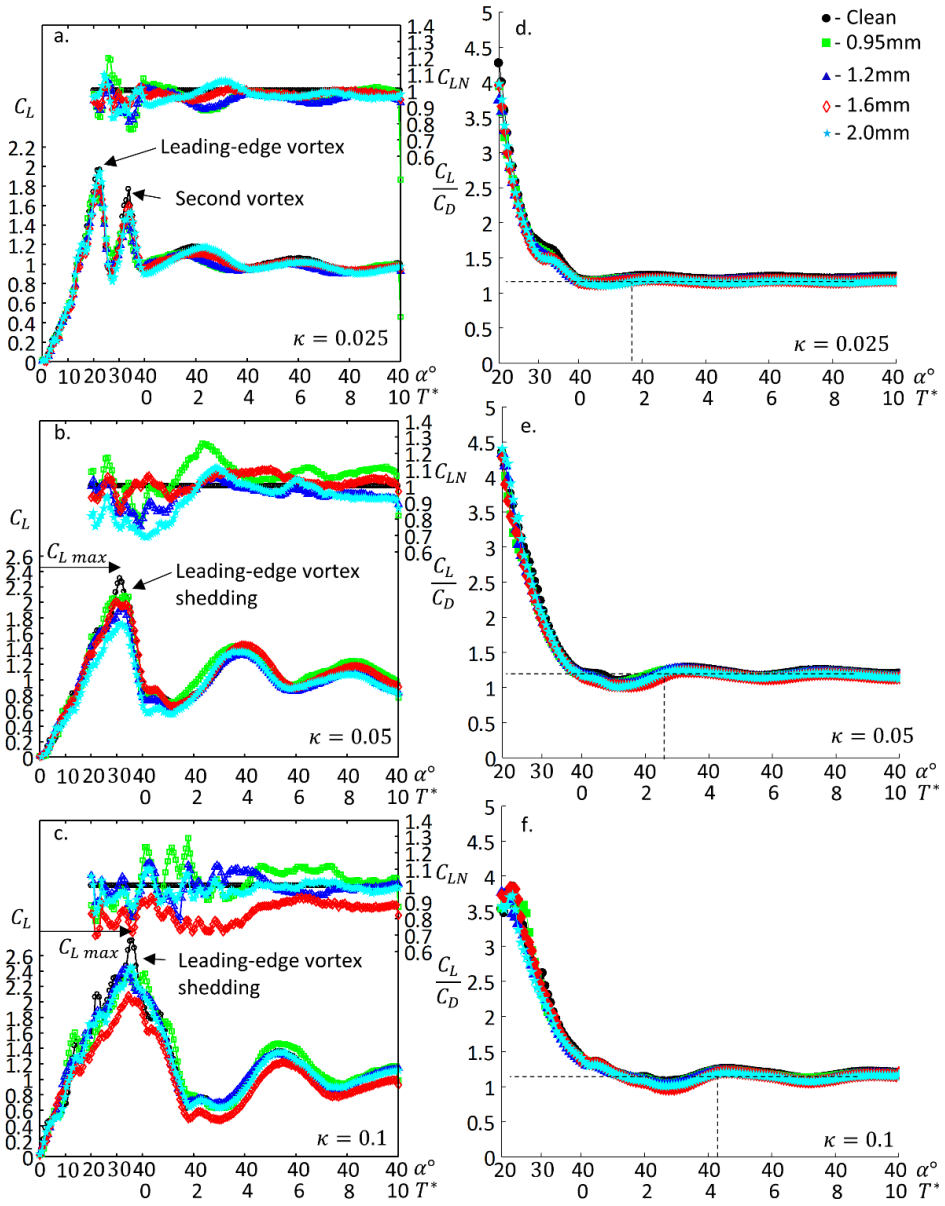

Figure 7: NACA 0012 lift coefficient with normalised trip wire lift coefficient (a, b, c) and lift to drag ratio of post-stall flow conditions (d, e, f) for increasing non-dimensional rotation rate and constant angle of attack, where $\alpha = 40°$.

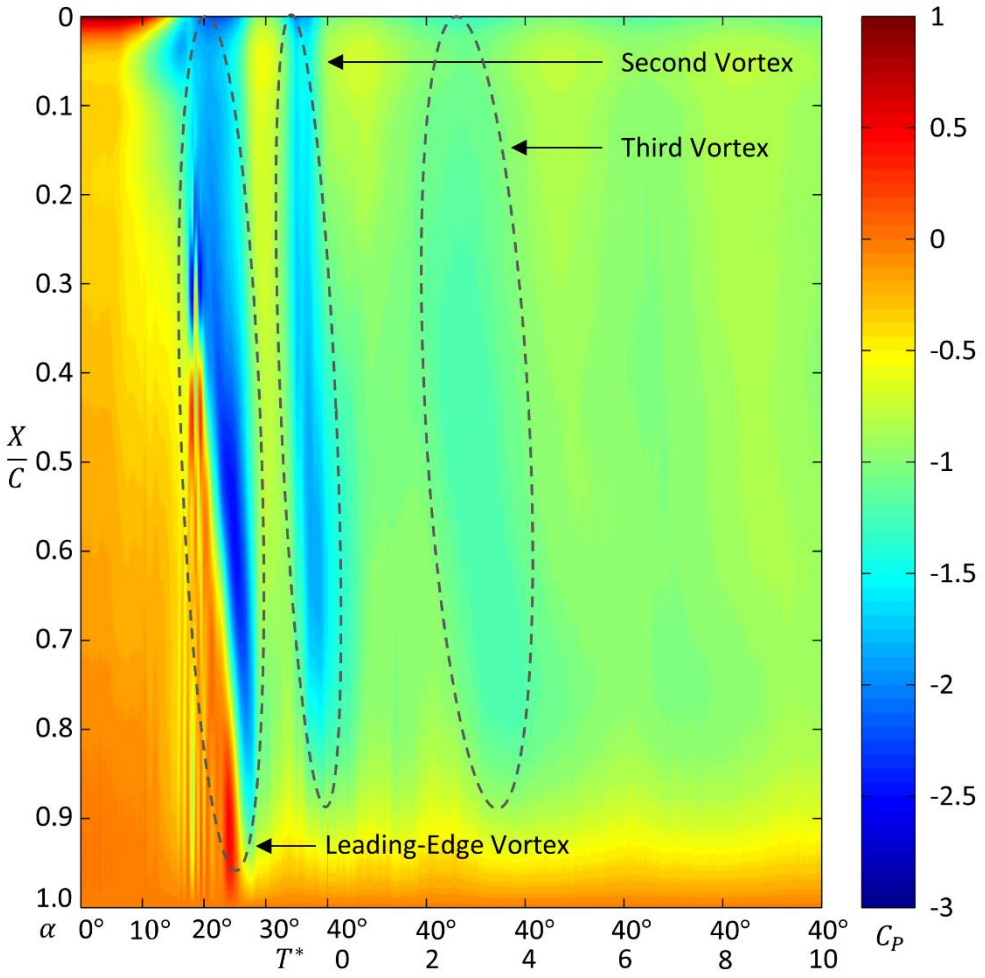

Figure 8: Normalised chord length upper surface pressure contour with respect to angle of attack and normalised time, indicating localised low pressure regions correlating to the leading-edge vortex and subsequent shed vortex structures in post-stall regions. $\kappa = 0.025$ *and* $\alpha_{max} = 40°$.

With increased non-dimensional rotation rate, dynamic stall was shown to occur at $\alpha = 37°$ for $\kappa = 0.05$, and at $\alpha = 40°$ for $\kappa = 0.1$, as indicated in Figure 7(b, c). In conjunction with a delay in the formation of the leading-edge vortex to higher angles of attack, the resulting maximum lift for each non-dimensional rotation rate test case was also increased to values $C_L = 1.8$, to 2.2 and 2.4 for $\kappa = 0.025,\ 0.05$ and 0.1 respectively.

After the onset of dynamic stall, and due to the fixed maximum angle of attack, the airfoil was observed to transition into a state of deep stall where the lift coefficient was observed oscillate about a mean value of $C_L = 1$.

With respect to the influence of the trip wire on the vortex shedding process, increasing the trip wire diameter was shown to lower the maximum lift coefficient of the airfoil during dynamic stall for reduced frequencies of $\kappa = 0.05$ and $\kappa = 0.1$, as shown in Figure 7(b, c). In contrast, the periodic nature of the stall process was not influenced, with vortices rolling up at the same phases of the stall process for each test case. Once post-stall flow conditions were established, no net benefit from the application of the trip wire was observed.

Although the maximum lift coefficient was reduced by the application of the leading-edge trip wires, the impact of the wires on the aerodynamic efficiency was negligible. As shown in Figure 7(d, e, f), the aerodynamic efficiency of the airfoil was shown to decrease and plateau to a value of $C_L/C_D = 1.1$ once post-stall conditions were established. However, the resulting aerodynamic efficiency was shown to be influenced by the non-dimensional rotation rate. Under higher reduced frequencies, increased time intervals were required before a steady-state post-stall characteristics were achieved. This is represented in Figure 7(d, e, f) as indicated by the dashed line for each test case of $\kappa = 0.025$, $\kappa = 0.05$ and $\kappa = 0.1$ where $T^* = 1.5$, $T^* = 2.5$, and $T^* = 4$.

The results for $\alpha_{max} = 60°$ are presented in Figure 9, which shows the lift coefficient, normalised leading-edge trip wire lift coefficient and the overall aerodynamic efficiency of the clean airfoil and the airfoil fitted with the trip wires. Setting the non-dimensional rotation rate to $\kappa = 0.025$ resulted in the formation of three distinct vortex structures,

as highlighted in Figure 9(a). Maximum lift was generated during the initial dynamic stall, where $C_L = 2.0$ for the clean airfoil. Once initial dynamic stall occurred, any further development of vortical structures partially increased lift, although to lower lift coefficient values of $C_L = 1.6$ and $C_L = 1.4$ respectively. Increasing the non-dimensional rotation rate, to $\kappa = 0.05$ and $\kappa = 0.1$ resulted in the formation of a single leading-edge vortex, as indicated in Figure 9(b) and Figure 9(c). Furthermore, the total lift rose with increasing non-dimensional rotation rate, such that $C_L = 2.1$ and $C_L = 2.8$ for the clean configuration at $\kappa = 0.05$ and $\kappa = 0.1$ respectively. Upper surface pressure coefficients for the NACA 0012 pitching to $\alpha_{max} = 60°$ are presented in Figure 10 and show the leading-edge vortex resulting from the dynamic stall process, whilst also highlighting the three vortex structures generated in post-stall conditions.

The leading-edge trip wire was shown to have a similar impact on the lift coefficient as observed in the case of $\alpha_{max} = 40°$, such that until dynamic stall occurs, an overall reduction in the lift coefficient was observed for all three reduced-frequency cases, as shown in Figure 9b and Figure 9c. This reduction in lift was only temporary, with overall lift generation exceeding the clean airfoil configuration in post-stall states. The results indicate that, for the post-stall conditions, minimal influence of the trip wire is achieved once bluff-body flow separation occurs.

Overall aerodynamic efficiency was shown to be independent of the presence of the trip-wire at the leading edge after dynamic stall occurred. As shown in Figure 9(d, e, f), the maximum C_L/C_D ratio was seen to increase from $C_L/C_D = 1.75$ (Figure 9d) to $C_L/C_D = 2.5$ (Figure 9f), although this increase can be attributed to the increase in rotation rate, and delay in separation of the leading-edge vortex (until high angles of attack) with

increased non-dimensional rotation rate. Once the airfoil transitions into a state of deep stall, the overall efficiency of the airfoil decreases to a asymptotic value of $C_L/C_D = 0.6$.

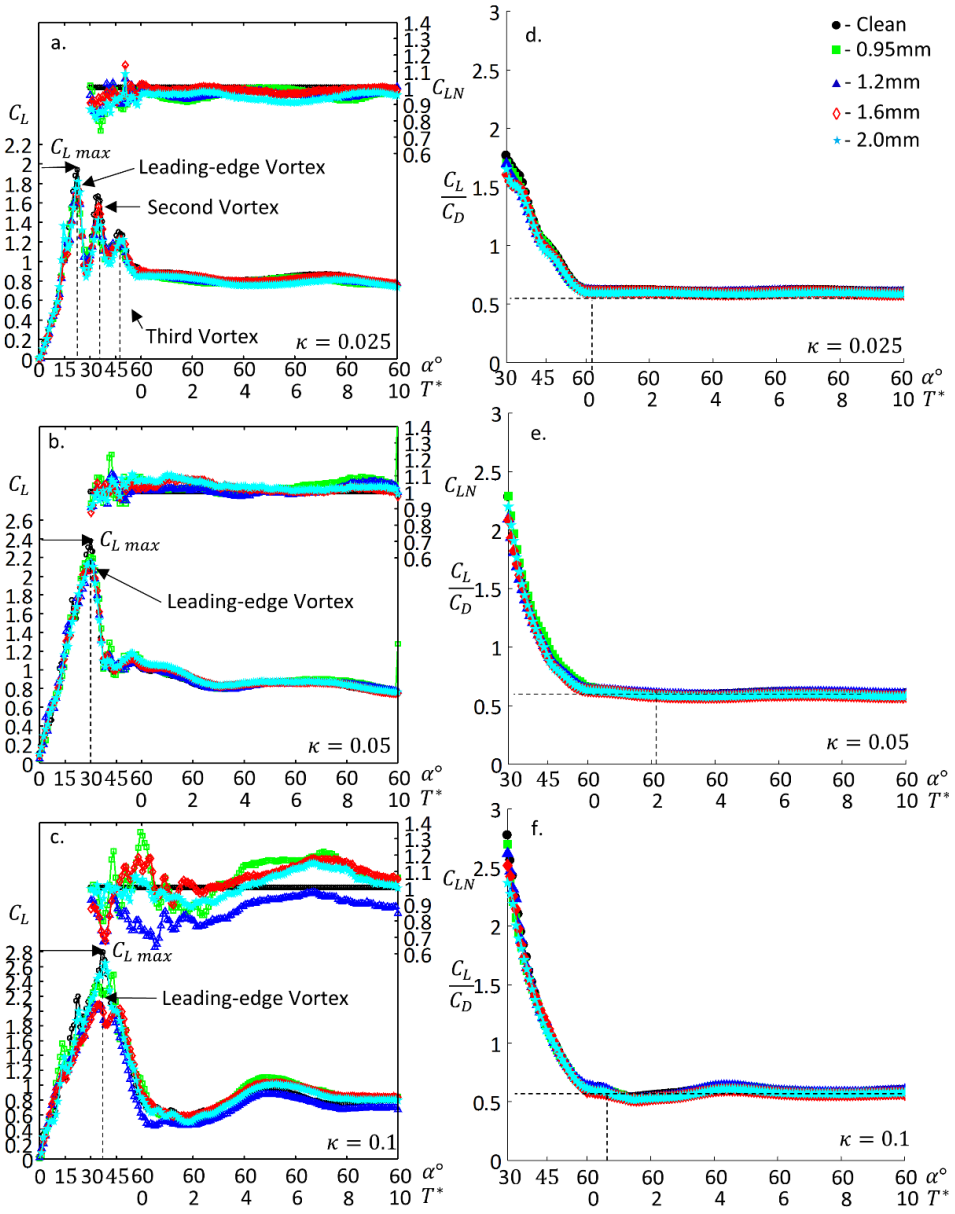

Figure 9: NACA 0012 lift coefficient with normalised trip wire lift coefficient (a, b, c) and lift to drag ratio of post-stall flow conditions (d, e, f) for increasing non-dimensional rotation rate and constant angle of attack, where $\alpha = 60°$.

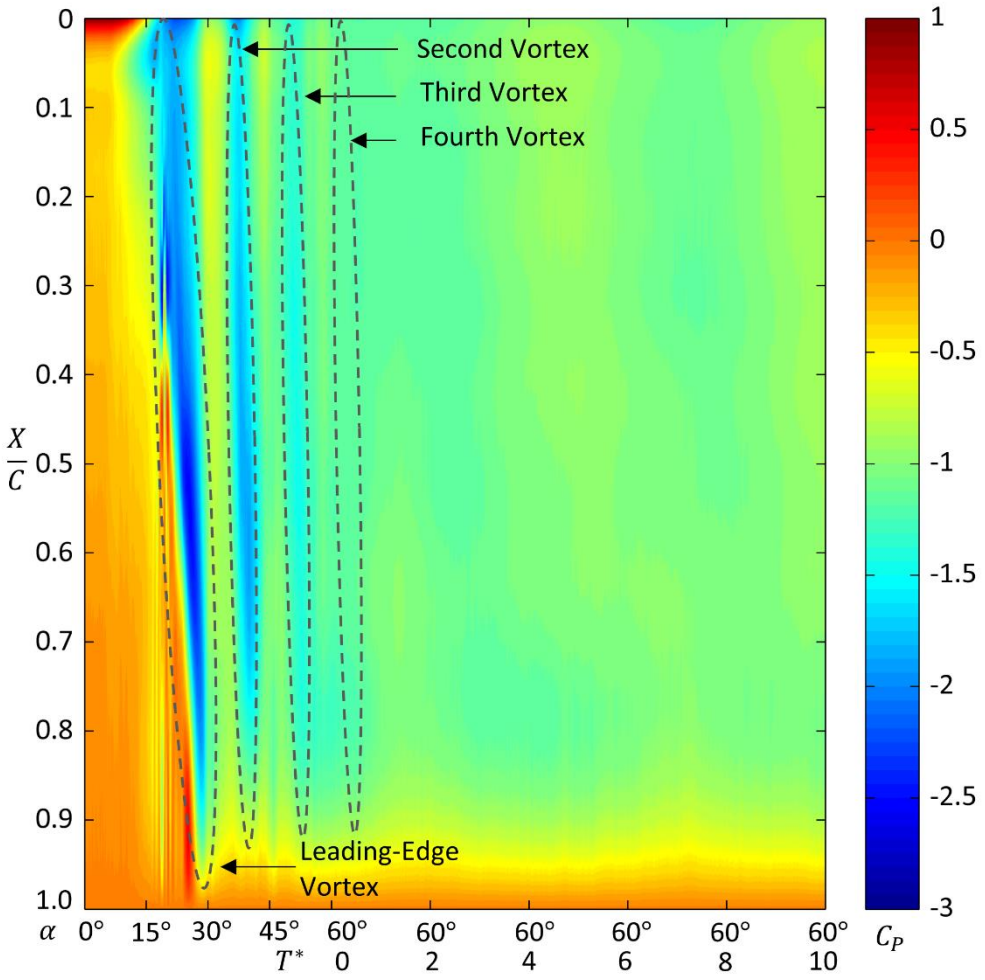

Figure 10: Normalised chord length upper surface pressure contour with respect to angle of attack and normalised time, indicating localised low pressure regions correlating to the leading-edge vortex and subsequent shed vortex structures in post-stall regions. $\kappa = 0.025$ *and* $\alpha_{max} = 60°$.

Comparisons between Test Cases

Collectively, the results show that under quasi-steady reduced frequencies, where $\kappa < 0.025$, the effect of the trip wire was minimal, with the overall force coefficients remaining similar between all test cases at all maximum angles of attack. For the cases where $\alpha_{max} = 40°$ and $60°$, increasing the non-dimensional rotation rate to the unsteady

range resulted in the reduction of the leading-edge vortex lift when the trip wire was applied. Figure 11 shows the resulting pressure coefficient over the airfoil for the clean airfoil and trip wire test cases, where $\alpha = 34°$, $\kappa = 0.05$ and where $\alpha_{max} = 60°$.

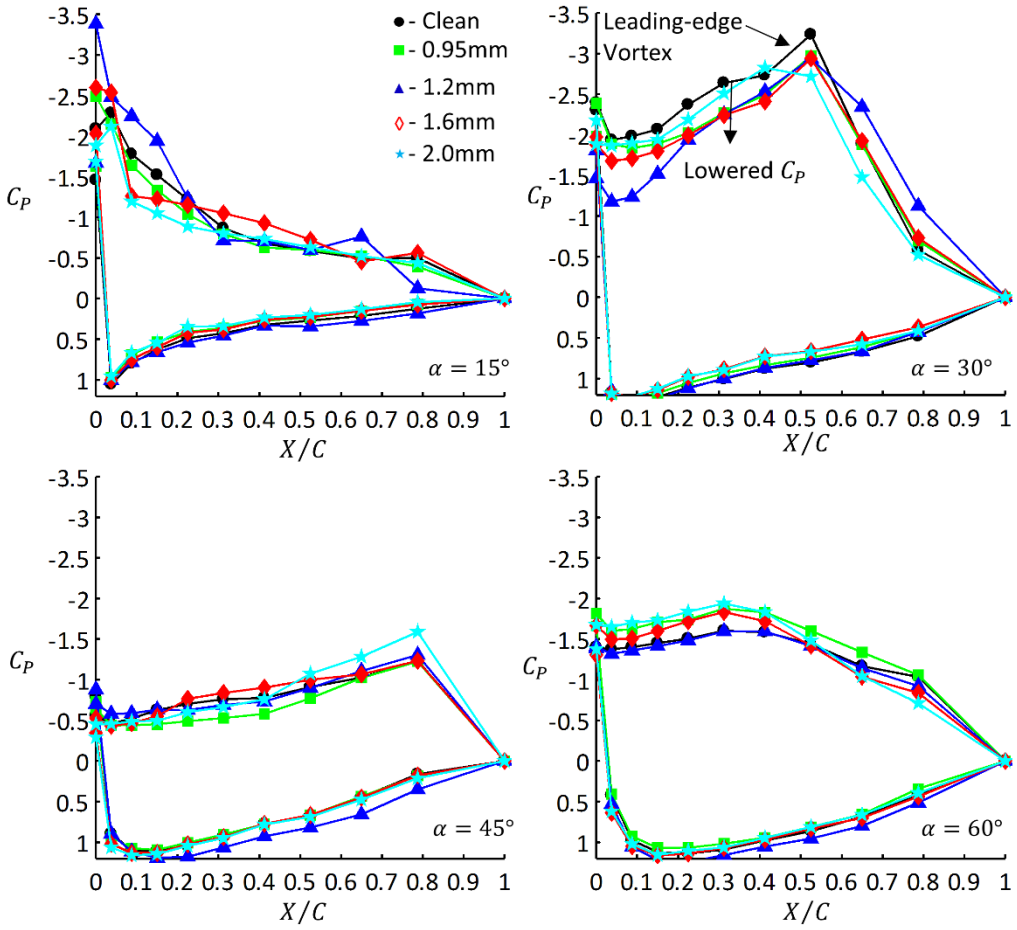

Figure 11: NACA 0012 airfoil surface pressure coefficient distribution during dynamic stall showing the lowering of C_P with the application of the leading-edge trip wire at multiple angles of attack. At $\alpha = 30°$, the leading-edge vortex is seen to convect over the upper surface of the airfoil, however minimal influence of the trip wire is observed to occur at other angles of attack tested. $\kappa = 0.05$ and $\alpha_{max} = 60°$.

Through application of the trip wire, a disruption in the formation of the leading-edge vortex is observed to occur, such that its impact on the airfoil is lowered. This is visible

through the increase in the upper surface pressure coefficient, resulting in a decreased overall maximum lift coefficient, as indicated in Figure 11.

When the airfoil was allowed to transition into a post-stall state at the maximum angle of attack, the effect of the trip wire was found to be negligible. Under post-stall conditions, the large-scale vortex shedding became dominant and any mixing generated by the trip wire wake became ineffective in controlling airfoil separation and vortex shedding. For this Reynolds number, at $\alpha_{max} = 20°$ a laminar separation bubble was observed to form on the clean airfoil, as observed by the reduction in lift coefficient at approximately $\alpha = 10°$ and the pressure distribution history in Figure 6.

For post-stall flow conditions, the lift-to-drag ratio of the airfoil was shown to be unchanged by the application of the trip wire for all three maximum-angle test cases. On the other hand, the high lift-to-drag ratio was sustained for longer durations with increased non-dimensional rotation rate, but lowered by increasing the maximum angle of attack. This effect is due to the delayed separation of the leading-edge vortex at higher reduced frequencies. Although the peak aerodynamic efficiency duration was increased for higher reduced frequencies, force fluctuations increased with increased angular delay in leading-edge vortex formation.

Conclusions

The current article presents the findings of experimental work conducted to evaluate the effectiveness of a leading-edge trip wire as a method of controlling the dynamic-stall process under extreme conditions. A NACA 0012 airfoil was tested over three maximum angle-of-attack values and three reduced frequencies. For each of these the effects of four trip-wire diameters were compared with the clean airfoil case. Surface pressure

measurements were recorded for the pitch-up motion of the airfoil undergoing constant angular velocity rotation from $\alpha = 0° \rightarrow 60°$. The dynamic-stall process was observed through the sudden increase in lift coefficient resulting from the generation of the leading-edge vortex. Once this vortex detached from the airfoil, post-stall flow conditions were established with periodic vortex shedding occurring. The application of the trip wire resulted in the following outcomes for high angle of attack, unsteady dynamic stall:

1) A reduction in lift prior to dynamic stall and a lowering of the post-stall lift fluctuation. Overall, lift was lowered in the post-stall regime with the variation between maximum and minimum lift immediately after dynamic stall being reduced.
2) The trip wire was successful in perturbing the laminar boundary layer at the leading edge due to the entrainment of turbulent, high-momentum flow into the boundary layer.
3) For post-stall flow conditions, maintaining a low angle of attack proved more beneficial in achieving a greater aerodynamic efficiency. Applying the trip wire had a minor positive influence on the aerodynamic efficiency.
4) Increasing the non-dimensional rotation rate, although delaying time to reach a steady-state post stall C_L/C_D values, imposed higher negative load fluctuations on the airfoil.

The findings presented in this article show that trip wires can beneficially manipulate the flow over a large angle-of-attack range and at elevated reduced frequencies, however this is only applicable until dynamic stall occurs. Following dynamic stall, the impact of the trip wire becomes negligible due to the occurrence of bluff-body separation. Although trip

wires are effective under some operating conditions, for the application of wind turbines where random turbulence and wake interactions frequently occur, the trip wire does not appear to be a feasible means of flow control. As such, it is recommended that future research be performed to develop awareness of the fluid-structure interaction and vortex shedding frequency as a result of variations in the trip wire diameter for greater control of the dynamic stall process during unsteady operating conditions. Smoothing the stall process and lowering the force fluctuations on turbine blades during post-stall conditions still requires further investigation if passive control methods are to be implemented. For example, the application of tubercles could be investigated, where energy can be dissipated through means of chord-wise vorticity and where a “softer” stall process occurs.

Acknowledgements

The first author acknowledges the support he has received for this research through the provision of an Australian Government Research Training Program Scholarship. In addition, research undertaken for this article has been assisted by a grant from the Sir Ross and Sir Keith Smith Fund (www.smithfund.org.au). The support is acknowledged and greatly appreciated.

References

[1] Butterfield, C., Hansen A., Simms D., and Scott G., 1991. *Dynamic Stall on Wind Turbine Blades*: National Renewable Energy Lab.

[2] Butterfield, C. P., 1989. *Three-Dimensional Airfoil Performance Measurements on a Rotating Wing*: Solar Energy Research Institute.

[3] Shipley, D. E., Miller M. S., and Robinson M. C., 1995, "Dynamic Stall Occurrence on a Horizontal Axis Wind Turbine Blade". United States: National Renewable Energy Laboratory.

[4] Carr, L. W., 1988, "Progress in Analysis and Prediction of Dynamic Stall," Journal of aircraft, 25 (1):6-17.

[5] Carr, L. W., and Chandrasekhara M., 1996, "Compressibility Effects on Dynamic Stall," Progress in Aerospace Sciences, 32 (6):523-573.

[6] Jumper, E., Dimmick R., and Allaire A., 1989, "The Effect of Pitch Location on Dynamic Stall," Journal of Fluids Engineering, 111 (3):256-262.

[7] Jumper, E., Schreck S., and Dimmick R., 1987, "Lift-Curve Characteristics for an Airfoil Pitching at Constant Rate," Journal of aircraft, 24 (10):680-687.

[8] McCroskey, W., McAlister K., Carr L., and Pucci S., 1982, "An Experimental Study of Dynamic Stall on Advanced Airfoil Sections. Volume 1: Summary of the Experiment."

[9] McAlister, K. W., Carr L. W., and McCroskey W. J., 1978, "Dynamic Stall Experiments on the Naca 0012 Airfoil."

[10] McCroskey, W. J., 1981, "The Phenomenon of Dynamic Stall": DTIC Document.

[11] McCroskey, W. J., Carr L. W., and McAlister K. W., 1976, "Dynamic Stall Experiments on Oscillating Airfoils," AIAA Journal, 14 (1):57-63.

[12] McCroskey, W. J., McAlister K., Carr L., Pucci S., Lambert O., and Indergrand R., 1981, "Dynamic Stall on Advanced Airfoil Sections," Journal of the American Helicopter Society, 26 (3):40-50.

[13] Robinson, M. C., and Wissler J. B., 1988, "Pitch Rate and Reynolds Number Effects on a Pitching Rectangular Wing," AIAA Paper, 88:2577.

[14] Jonkman, J. M., 2001, "Modeling of the Uae Wind Turbine for Refinement of Fastad," Citeseer.

[15] Tangler, J. L., 2004, "Insight into Wind Turbine Stall and Post-Stall Aerodynamics," Wind Energy, 7 (3):247-260.

[16] Katz, Y., Nishri B., and Wygnanski I., 1989, "The Delay of Turbulent Boundary Layer Separation by Oscillatory Active Control," Physics of Fluids A: Fluid Dynamics (1989-1993), 1 (2):179-181.

[17] Lachmann, G. V., 2014. *Boundary Layer and Flow Control: Its Principles and Application*. London: Elsevier.

[18] Choudhry, A., Leknys R., Arjomandi M., and Kelso R., 2014, "An Insight into the Dynamic Stall Lift Characteristics," Experimental Thermal and Fluid Science, 58:188-208.

[19] Chandrasekhara, M., Martin P. B., and Tung C., 2004, "Compressible Dynamic Stall Control Using a Variable Droop Leading Edge Airfoil," Journal of aircraft, 41 (4):862-869.

[20] Chandrasekhara, M., Wilder M., and Carr L., 1998, "Unsteady Stall Control Using Dynamically Deforming Airfoils," AIAA journal, 36 (10):1792-1800.

[21] Feszty, D., Gillies E. A., and Vezza M., 2004, "Alleviation of Airfoil Dynamic Stall Moments Via Trailing-Edge Flap Flow Control," AIAA Journal, 42 (1):17-25.

[22] Geissler, W., Dietz G., Mai H., Junker B., and Lorkowski T., 2004, "Dynamic Stall Control Investigations on a Full Size Chord Blade Section," 30th ERF, Marseille, France.

[23] Greenblatt, D., and Wygnanski I., 2002, "Effect of Leading-Edge Curvature and Slot Geometry on Dynamic Stall Control," AIAA Paper, 3271:2002.

[24] Kerho, M. F., 2007, "Adaptive Airfoil Dynamic Stall Control," Journal of Aircraft, 44 (4):1350-1360.

[25] Lee, T., and Gerontakos P., 2006, "Dynamic Stall Flow Control Via a Trailing-Edge Flap," AIAA Journal, 44 (3):469-480.

[26] Yu, Y. H., Lee S., McAlister K. W., Tung C., and Wang C. M., 1995, "Dynamic Stall Control for Advanced Rotorcraft Application," AIAA Journal, 33 (2):289-295.

[27] Müller-Vahl, H. F., Nayeri C. N., Paschereit C. O., and Greenblatt D., 2016, "Dynamic Stall Control Via Adaptive Blowing," Renewable Energy, 97:47-64.

[28] Müller-Vahl, H. F., Strangfeld C., Nayeri C. N., Paschereit C. O., and Greenblatt D., 2014, "Control of Thick Airfoil, Deep Dynamic Stall Using Steady Blowing," AIAA Journal, 53 (2):277-295.

[29] Sun, M., and Sheikh S., 1999, "Dynamic Stall Suppression on an Oscillating Airfoil by Steady and Unsteady Tangential Blowing," Aerospace Science and Technology, 3 (6):355-366.

[30] Weaver, D., McAlister K., and Tso J., 2004, "Control of Vr-7 Dynamic Stall by Strong Steady Blowing," Journal of Aircraft, 41 (6):1404-1413.

[31] Weaver, D., McAlister K. W., and Tso J., 1996, "Suppression of Dynamic Stall by Steady and Pulsed Upper-Surface Blowing," California Polytechnic State University.

[32] Yen, J., and Ahmed N. A., 2013, "Enhancing Vertical Axis Wind Turbine by Dynamic Stall Control Using Synthetic Jets," Journal of Wind Engineering and Industrial Aerodynamics, 114:12-17.

[33] Gardner, A. D., Richter K., and Rosemann H., 2011, "Numerical Investigation of Air Jets for Dynamic Stall Control on the Oa209 Airfoil," CEAS Aeronautical Journal, 1 (1-4):69-82.

[34] Greenblatt, D., Nishri B., Darabi A., and Wygnanski I., 2001, "Dynamic Stall Control by Periodic Excitation, Part 2: Mechanisms," Journal of Aircraft, 38 (3):439-447.

[35] Greenblatt, D., and Wygnanski I., 2001, "Dynamic Stall Control by Periodic Excitation, Part 1: Naca 0015 Parametric Study," Journal of Aircraft, 38 (3):430-438.

[36] Magill, J. C., and McManus K., 1998, "Control of Dynamic Stall Using Pulsed Vortex Generator Jets," AIAA Paper, 675:1998.

[37] Alrefai, M. d., and Acharya M., 1996, "Controlled Leading-Edge Suction for Management of Unsteady Separation over Pitching Airfoils," AIAA journal, 34 (11):2327-2336.

[38] Karim, M., and Acharya M., 1994, "Suppression of Dynamic-Stall Vortices over Pitching Airfoils by Leading-Edge Suction," AIAA Journal, 32 (8):1647-1655.

[39] Greenblatt, D., Ben-Harav A., and Mueller-Vahl H., 2014, "Dynamic Stall Control on a Vertical-Axis Wind Turbine Using Plasma Actuators," AIAA Journal, 52 (2):456-462.

[40] Lombardi, A. J., Bowles P. O., and Corke T. C., 2013, "Closed-Loop Dynamic Stall Control Using a Plasma Actuator," AIAA Journal, 51 (5):1130-1141.

[41] Post, M. L., and Corke T. C., 2006, "Separation Control Using Plasma Actuators: Dynamic Stall Vortex Control on Oscillating Airfoil," AIAA Journal, 44 (12):3125-3135.

[42] Pao, L. Y., and Johnson K. E., 2009, "A Tutorial on the Dynamics and Control of Wind Turbines and Wind Farms," American Control Conference, 2009. ACC'09.

[43] Fish, F. E., Weber P. W., Murray M. M., and Howle L. E., 2011, "The Tubercles on Humpback Whales' Flippers: Application of Bio-Inspired Technology," Integrative and Comparative Biology, 51 (1):203-213.

[44] Hansen, K. L., Kelso R. M., and Dally B. B., 2011, "Performance Variations of Leading-Edge Tubercles for Distinct Airfoil Profiles," AIAA Journal, 49 (1):185-194.

[45] New, D. T., Wei Z., and Cui Y. D., 2016, "A Time-Resolved Particle-Image Velocimetry Study on the Unsteady Flow Behaviour of Leading-Edge Tubercled Hydrofoils," 18th International Symposium on the Application of Laser and Imaging Techniques to Fluid Mechanics, Portugal.

[46] Rostamzadeh, N., Kelso R., Dally B., and Hansen K., 2013, "The Effect of Undulating Leading-Edge Modifications on Naca 0021 Airfoil Characteristics," Physics of Fluids, 25 (11):117101.

[47] Hrynuk, J., 2015, "The Effect of Leading Edge Tubercles on Dynamic Stall," Ph.D, Clarkson University.

[48] Carr, L., Chandrasekhara M., Wilder M., and Noonan K., 2001, "Effect of Compressibility on Suppression of Dynamic Stall Using a Slotted Airfoil," Journal of Aircraft, 38 (2):296-309.

[49] Joo, W., Lee B.-S., Yee K., and Lee D.-h., 2006, "Combining Passive Control Method for Dynamic Stall Control," Journal of aircraft, 43 (4):1120-1128.

[50] McAlister, K. W., and Tung C., 1993, "Suppression of Dynamic Stall with a Leading-Edge Slat on a Vr-7 Airfoil": DTIC Document.

[51] Geissler, W., Dietz G., Mai H., Bosbach J., and Richard H., 2005, "Dynamic Stall and Its Passive Control Investigations on the Oa209 Airfoil Section," 31st European Rotorcraft Forum, Italy.

[52] Heine, B., Mulleners K., Joubert G., and Raffel M., 2013, "Dynamic Stall Control by Passive Disturbance Generators," AIAA Journal, 51 (9):2086-2097.

[53] Choudhry, A., 2014, "Unsteady Separation Control on Wind Turbine Blades, Phd Thesis," PhD Thesis, School of Mechanical Engineering, The University of Adelaide.

[54] Choudhry, A., Arjomandi M., and Kelso R., 2016, "Methods to Control Dynamic Stall for Wind Turbine Applications," Renewable Energy, 86:26-37.

[55] Shih, C., Lourenco L., and Krothapalli A., 1995, "Investigation of Flow at Leading and Trailing Edges of Pitching-up Airfoil," AIAA Journal, 33 (8):1369-1376.

[56] Choughuri, P. G., and Knight D. D., 1996, "Effects of Compressibility, Pitch Rate, and Reynolds Number on Unsteady Incipient Leading-Edge Boundary Layer Separation over a Pitching Airfoil," Journal of Fluid Mechanics, 308:195-217. doi: 10.1017/S0022112096001450.

[57] Schlichting, H., 1937, "Experimental Investigation of the Problem of Surface Roughness."

[58] Granlund, K., Ol M., Garmann D., Visbal M., and Bernal L., 2010, "Experiments and Computations on Abstractions of Perching," 28th AIAA Applied Aerodynamics Conference, United States.

[59] Sayers, A., and Ball D., 1983, "Blockage Corrections for Rectangular Flat Plates Mounted in an Open Jet Wind Tunnel," Proceedings of the Institution of Mechanical Engineers, Part C: Journal of Mechanical Engineering Science, 197 (4):259-263.

[60] STO, 2016, "Extensions of Fundamental Flow Physics to Practical Mav Aerodynamics": North Atlantic Treaty Organization, Science and Technology Organization.

[61] Zhou, Y., Alam M. M., Yang H., Guo H., and Wood D., 2011, "Fluid Forces on a Very Low Reynolds Number Airfoil and Their Prediction," International Journal of Heat and Fluid Flow, 32 (1):329-339.

[62] Leishman, G. J., 2006. *Principles of Helicopter Aerodynamics*: Cambridge university press.

Chapter 6.

Dynamic Stall Flow Topology

6.1. Chapter 6 Overview

The final chapter of this thesis seeks to investigate the flow characteristics of the dynamic-stall vortex, such that more efficient methods of flow control can be developed for highly-unsteady flow conditions. This is conducted to address the final project objective, and identify the behaviour of the half-saddle point linked to the dynamic-stall vortex. A flat plate fitted with three different leading-edge and trailing-edge geometry combinations are utilised whilst simulating dynamic-stall conditions. A Reynolds number of $Re = 20{,}000$ was replicated in an open jet wind tunnel, where the resulting surface pressures are recorded throughout the duration of the pitch-up process, and for a flow time of $t = 30c/U_\infty$ once rotation had ceased. Regions of low pressure were correlated to the development of the leading-edge vortex. Surface pressure was used to locate the position of the half-saddle point bifurcating streamlines from the leading-edge vortex and the outer free-stream above the upper surface of the airfoil. A strong pressure gradient was observed at the half-saddle location, whilst its position was approximated by the location where the pressure coefficient was approximately $C_P = 0$ and at the location of a severe pressure gradient. Motion of the half-saddle point was linked to the free-stream velocity, plate rotation rate and plate chord length. Knowledge developed in this chapter can allow alternative methods of flow control to be developed that utilise the generated pressure fields to actively apply suitable boundary layer control methods in order to manipulate or reduce the effects of the dynamic stall process.

6.2. Surface Pressure and Flow Topology of a Pitching Plate

Statement of Authenticity

Title of Paper:	Leading-Edge Vortex Development on a Pitching Flat Plate with Multiple Leading Edge Geometries
Publication Status:	☐ Published ☑ Accepted for Publication ☐ Submitted for Publication ☐ Unpublished and Unsubmitted work written in manuscript style
Publication Details:	Leknys, R. R., Arjomandi, M., Kelso, R. M. & Birzer, C. H., 2017, Leading-Edge Vortex Development on a Pitching Flat Plate with Multiple Leading Edge Geometries, *Experimental Thermal and Fluid Science*.

Principal Author

Name of Principal Author:	Ryan Ross Leknys
Contribution to the Paper:	Performed data analysis and interpretation, wrote manuscript and acted as corresponding author.
Overall percentage (%):	70
Certification:	This paper reports on original research I conducted during the period of my Higher Degree by Research candidature and is not subject to any obligations or contractual agreements with a third party that would constrain its inclusion in this thesis. I am the primary author of this paper.

Signature: __ Date: 05 March 2018

Co-Author Contributions

By signing the Statement of Authorship, each author certifies that:

i. the candidate's stated contribution to the publication is accurate (as detailed above);

ii. permission is granted for the candidate in include the publication in the thesis; and

iii. the sum of all co-author contributions is equal to 100% less the candidate's stated contribution.

Name of Co-Author:	Associate Professor Maziar Arjomandi
Contribution to the Paper:	Supervised the development of the research and contributed in academic discussion and the review process of submitted manuscripts.

Signature: _ _____ Date: 05 March 2018

Name of Co-Author:	Associate Professor Richard Kelso
Contribution to the Paper:	Supervised the development of the research and contributed in academic discussion and the review process of submitted manuscripts.

Signature: Date: 05 March 2018

Name of Co-Author:	Dr Cristian Birzer
Contribution to the Paper:	Supervised the development of the research and contributed in academic discussion and the review process of submitted manuscripts.

Signature: __ _____ Date: 05 March 2018

Leading-Edge Vortex Development on a Pitching Flat Plate with Multiple Leading Edge Geometries

R.R. Leknys*, M. Arjomandi, R. M. Kelso and C. H. Birzer

School of Mechanical Engineering.

The University of Adelaide, South Australia, 5005.

*Corresponding Author Contact Email: ryan.leknys@adealide.edu.au

Abstract

This article investigates the dynamic stall of a pitching flat plate in order to facilitate lift control in applications such as flapping wings and micro-aerial vehicles. Constant-pitch-rate rotation, similar to ramp-and-hold, of a flat plate was investigated in an open-jet wind tunnel using embedded surface pressure sensors to assess vortex formation and its impact on aerodynamic characteristics. Three leading edge and trailing edge geometries were investigated, with all demonstrating minor effects on the overall aerodynamic performance for the angles of attack presented. For all leading and trailing edge combinations, increasing the rotation rate increased the magnitude of the localised low pressure on the upper surface the flat plate resulting in increased lift. Separation of the leading-edge vortex was characterised by the motion of a half-saddle flow feature on the upper surface of the flat plate, which in turn was linked to the rotation rate. A critical angle of attack was found whereby further increases in the angle of attack provided no benefit to overall force generation. The surface pressures shown in the current investigation can be utilised for the development of adaptive boundary layer control

devices to either limit or promote the dynamic stall process on a flat plates. This study confirms that vortex lift, which is critical for flight of micro-aerial vehicles and flapping wing devices, is limited by the maximum angle of attack and rotation rate. This is significant for high-lift devices where limited power is available for lift generation.

Keywords

Flat Plate; Dynamic Stall; Particle Image Velocimetry; Surface Pressure; Vortex Dynamics, Lift

Introduction

Unsteady aerodynamics has become a significant research topic in recent years due to its application on micro-aerial vehicles (*MAV*), the understanding of bird and insect flight, high manoeuvrability aircraft, wind turbines and also flat plate structures such as heliostats immersed in the turbulent atmospheric surface layer. Aerodynamic performance in low Reynolds Number (Re) conditions is typically dependent on unsteady aerodynamics of thin airfoil sections, where the generation and interaction of laminar separation bubbles and vortex systems (Ellington, 1984a, Sane, 2003, Shyy et al., 2007) is required for sustained lift. For 60,000 < Re < 200,000, thin flat plate airfoil profiles are often utilised due to their increased performance in steady state conditions (Pelletier and Mueller, 2000). Likewise, for flapping and natural flight behaviour of insects and birds, the study of pitching and stationary flat plates and wings provides insight into the vortex dynamics required for sustained lift (Ellington, 1984b, Dickinson and Gotz, 1993, Dickinson, 1994, Sane, 2003, Pullin and Wang, 2004, Taira and Colonius, 2009, Wilkins and Knowles, 2009, Chen, Colonius and Taira, 2010, Pitt Ford and Babinsky, 2011). Analytical models for rapid analysis of unsteady forces of plates have shown significant development

in assessing the aerodynamic loads on pitching plates (Jones, 2003, Xia and Mohseni, 2012, Ramesh et al., 2014, Narsipur, Gopalarathnam and Edwards, 2018). However, it is critical that results of experimentally obtained force characteristics and flow development be utilised for validation of both analytical and numerical methods. For this reason, the study of the separation process and analysis of upper surface pressure distribution about simplified geometries, such as flat plates, is critical for the development of knowledge relating to lift generation, flow separation and boundary layer control of pitching wings associated with low Reynolds Number flyers, including *MAV*s.

Rival et al. (2013) and Rival et al. (2014) used a flat plate to analyse the development time and lift generation in dynamic stall. In their investigation, a flat plate with four leading-edge and trailing-edge configurations was compared to a NACA 0012 airfoil using both Particle Image Velocimetry (PIV) and force measurements in a free-surface water channel. The reduced frequency (κ) (which is a function of frequency, f (Hz), chord, c (m), and free-stream velocity, $U_\infty(m/s)$) was such that $\kappa = \pi fC/U_\infty = 0.25$, whilst the motion type was pure plunge (i.e. no rotation) and where $Re = 10{,}000$. The leading edge profile was shown to directly influence the onset of leading-edge vortex growth, local shear-layer profiles and lift generation. Similar results were concluded in experiments using PIV in Son and Cetiner (2015) and Son et al. (2016), who showed the difference between both round and square leading-edge and trailing-edge profiles. Conclusions from these works indicated that similar force responses were obtained, however an increase in force fluctuation peak was obtained for the sharp leading-edge profile. Variation in profiles was only shown to influence the onset of vortex development, not its growth rate (Son et al., 2016). Additionally, the detachment of the dynamic-stall vortex, and subsequent lift reduction, was characterised by the 'lift-off' process of the half-saddle

point located aft of the primary leading-edge vortex structure. A similar feature was also identified in Perry and Steiner (1987), who evaluated the flow topology leading to separation of vortex structures behind an inclined plate. The motion of the half-saddle point was only provided for one rotation rate and plate motion type. There remains a gap in literature that addresses the behaviour of the motion of the half-saddle point along the upper surface of the plate with varying rotation rate and motion types.

A comprehensive analysis in Widmann and Tropea (2017) investigated the impact of Re on the dynamic stall process, which showed the Re dependency of the separated shear layer and early detachment of the leading-edge vortex at Re ranging between $Re = 10000$ and $Re = 80000$, and for a fixed reduced frequency, $\kappa = \pi C/U_\infty \tau = 0.25$ (where τ is the period (s) and equal to the inverse of frequency). Although detailing the link between Reynolds number and vortex growth through shear layer roll-up, details of the vortex development and associated flow features connecting the vortex to the plate's upper surface are lacking. Further research is needed to address the knowledge gap associated with flow feature development and their propagation during dynamic stall. Similar to results discussed in Rival et al. (2013) and Rival et al. (2014), Widmann and Tropea (2017) also discussed the importance of critical flow features with respect to vorticity transport between the shear layer and upper-surface vortex structures, and in conjunction with leading-edge vortex separation. Although the characteristics of the vortex development process have been investigated previously, there remains a gap in literature regarding the growth rate of the critical vortex structures with respect to ramp-and-hold, and constant-pitch-rate motion of a wing body. As such, the motivation behind the current investigation is to investigate the motion behaviour and rates of change of the displacement of critical flow features developed on the surface of a pitching plate

undergoing dynamic stall conditions. As previously stated, the knowledge regarding the manipulation of critical flow features can be utilised for more efficient boundary layer flow control techniques, better suited to manipulating the development of the leading-edge vortex (Rival et al., 2013, Rival et al., 2014).

The vortex-formation process of plunging and flapping wings was described in Rival, Prangemeier and Tropea (2009) and Rival, Schönweitz and Tropea (2011), where detailed kinematics of the leading-edge vortex formation process were presented. Vorticity contours provided detail of the vortex growth which led to the identification of convection velocities and positions of the leading-edge and trailing-edge vortices. Due to the time-dependent nature of dynamic stall, variations to the wing kinematics, with respect to rotation rate and motion type, are shown to significantly influence the overall performance and resulting flow structure development. Ol and Babinsky (2016) and Jones et al. (2016) present ranges of testing procedures of the dynamic-stall process applied to flat plates undergoing unsteady motion. In their work, multiple kinematic models are replicated on the flat plate to determine the underlying differences in force generation as a result of motion type and parametric variations in test conditions. This is significant, as their findings indicate the wide range of motion types and their influence on the force development on pitching plates. Ol and Babinsky (2016) presented a decomposition of the fundamental lift generation mechanisms, which included both pressure forces and inertial forces. These results were presented in a bid to better model the force characteristics of low Re dynamic stall on flat plates. The experimental results in Ol and Babinsky (2016) were directly compared with an analytical method using direct force measurements, flow visualisation and PIV, with good agreement being shown between the analytical model and experimental results. Stevens and Babinsky (2017) also utilised

PIV to lift and compare two analytical Wagner models, in order to model vortex growth and lift generation. The position of the leading-edge vortex core above a flat plate undergoing multiple rotation rates was presented in Jones et al. (2016). However, details of near-surface pressures are required for applications utilising boundary layer control methods.

These studies provide beneficial fundamental knowledge of physical parameters and kinematics associated with the vortex separation process of a flat plate in unsteady motion. However, there remains further scope to investigate the development and control of the leading-edge vortex and its influence on surface pressure and forces during dynamic stall at elevated angles of attack and for sustained operating in post-stall conditions.

Research on flat plates undergoing unsteady motion (Granlund, OI and Bernal, 2013, Yu and Bernal, 2013, Buchner and Soria, 2015, North Atlantic Treaty Organization, 2016) have facilitated our understanding of the effects of performance parameters including pitch rate, Reynolds Number, pitch axis location and motion type. These studies utilised load cell measurements and PIV to link the vortex dynamics with associated forces. However, for a greater understanding of the dynamic-stall process, and its related flow structure and critical point development for the design more efficient methods of control, an awareness of the pressure distribution resulting from the vortex-plate interaction is required. Garmann and Visbal (2011) performed numerical modelling of a rapidly-pitching flat plate and presented results of span-averaged surface pressure, although details of the critical points, such as the half-saddle point, on the upper surface of the plate were not discussed. Additionally, as the leading-edge vortex is known to induce a low-pressure

region near the leading edge (McCroskey, 1981, Carr, 1988, Leishman, 1990), the surface pressure coefficients in Garmann and Visbal (2011) were primarily used for validation purposes of their numerical mesh. As such, a weak qualitative link can be deduced between the pressure fields and flow structures developed during dynamic stall.

One way to develop our understanding of unsteady separation is to investigate the control and manipulation of the leading-edge vortex formation. As such, the purpose of the current article is to investigate the aerodynamic performance of a flat-plate wing with a range of leading-edge and trailing-edge geometries, undergoing constant-pitch-rate motion. The article does not attempt to deliver a cost function for the implementation of the specific leading- and trailing-edge geometries, but instead present knowledge of the comparisons in force and surface pressure variation resulting from the application of varying leading- and trailing-edge geometries. In addition, we attempt to determine the impact of the leading-edge geometry variations on the developed separation bubble and leading-edge vortex under multiple pitch-rate conditions. Furthermore, we investigate the near-surface pressure fields and how they are linked to critical flow features developed during unsteady wing motion behaviour. Details of the re-attachment point on the upper surface are investigated in order provide insight into the vortex shedding process of pitching flat plates applicable to *MAV*s, whilst also enhancing the knowledge that can be utilised for the implementation of active flow control devices during dynamic stall, thus helping limit or enhance the unsteady lifting process.

Methods

Dynamic stall was simulated using a flat plate constructed from two aluminium skins secured to front and rear spars, forming a box structure which housed 13 internally-

mounted differential pressure sensors. Due to the internally-mounted pressure sensors, the overall thickness, t, of the flat plate was restricted to, $t = 10$mm. The chord, $c = 100$mm and span, $S = 500$mm provided an overall thickness-to-chord ratio of 0.1 and wing aspect ratio of 5. A 2mm gap between the upper end of the plate and the wind tunnel wall was present. The lower edge of the plate was fixed to a rotating end-plate recessed flush with the wind tunnel wall. The gap on the upper edge was within $0.005 \times S$ to ensure minimal three dimensional effects (Barlow, Rae and Pope, 1999). Both ends of the flat plate were pinned to limit bending and induced vibrations resulting from imposed aerodynamic loads. To evaluate the development of the separation bubble and dynamic-stall vortex, three leading-edge and trailing-edge geometries were constructed using ABS plastic, and used as extensions to the base plate. These comprised of round, square and triangular leading-edge and trailing-edge geometries. Cross sections of the three flat plate profiles are shown in Figure 1a.

Surface pressure was evaluated using $250\,Pa$ *Honeywell Truestability*® differential pressure sensors mounted on a custom-built circuit board fixed within the flat plate structure. Pressure ports of the sensors were connected to copper tubes, with an internal diameter of $0.5mm$, and which were bonded to one side of the flat plate. The sample rate was adjusted such that a minimum $10kHz$ was achieved for each sensor for all tests. A schematic representation of the pressure port location with respect to the wing geometry is provided in Figure 1b and Figure 1c. Harmonic effects in the pressure signals were minimised by reducing the lengths of the tubing connecting the pressure sensor and the surface orifice. The transfer function of the pressure sensor system was such that a linear error of $\pm 1\%$, of the full scale, in pressure fluctuation existed over the operating range of the pressure sensor. However, the error increased to a maximum of $\pm 2.5\%$ in the current

testing due to operation of the pressures sensors at 2.5% of their capacity. The response time of the system was 1ms, which was compensated for in operation of the sensors during flat-plate rotation. In addition, the frequency response of the sensors was significantly higher than the expected vortex shedding frequency of the vortex structures resulting from shear layer separation at both the leading edge and the trailing edge.

a)

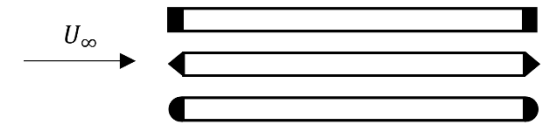

b)

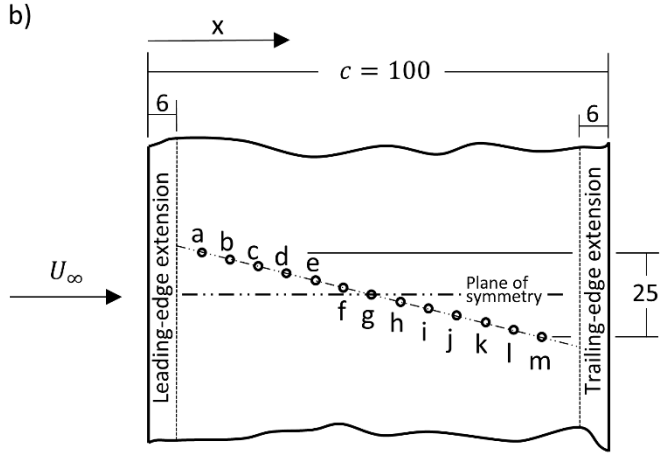

c)

Sensor	Location (x/c)
a	0.11
b	0.17
c	0.23
d	0.29
e	0.36
f	0.42
g	0.48
h	0.54
i	0.60
j	0.66
k	0.73
l	0.79
m	0.85

Figure 1: Geometry of the flat plate used for dynamic stall testing. a) Leading and trailing-edge extension profiles mounted on the leading and trailing edges of the flat plate. b) Pressure port locations on the plate mid-chord location. c) Non-dimensional distance of the pressure sensors from the plate leading edge.

This lowered the sensor error and ensured that sensor noise did not saturate the obtained test results. The limited volume within the flat plate for the internal mounting of the sensors, and the maximum allocation of 14 sensors on the data acquisition system, meant that only one surface of the flat plate could be utilised for surface pressure

measurements. As such, both upper and lower surface pressure measurements were conducted independently and consecutively to obtain both upper and lower surface pressure data. The results for the lower surface pressure were obtained by inverting the flat plate motion to ensure accuracy in the angle of attack and pitch rate motion. Due to the repeatability of the test arrangement a combination of both upper and lower surface readings could be obtained with confidence to evaluate the total forces developed during the pitch-up motion. To further reduce sources of experimental error associated with the use of the pressure sensors, the flat plate was pinned at both ends to limit elastic deflections and vibration. For the anticipated maximum loads, a maximum of 0.01mm of plate deflection was measured on the centreline of the plate.

Data acquisition was achieved through the use of a *National Instruments* NI6210 data acquisition module which was programmed to simultaneously read the wing surface pressure and freestream dynamic pressure within the wind tunnel. The data acquisition system incurred a $10ms$ response time delay, which was subsequently compensated for in custom-designed motion control software which simultaneously controlled pressure sensor recording and motor motion. A trapezoidal displacement motion profile was achieved to simulate constant-pitch-rate motion, whilst a pivot located at the mid-chord point on the flat plate was utilised to minimise virtual mass effects generated through plate rotation (Stevens and Babinsky, 2017).

Ramp-up and ramp-down occurred over the first and last $3°$ of the angular displacement profile in order to initiate smooth start-up and shut-down of the motor. Airfoil motion was provided via a brushless DC motor and gearbox arrangement. The angular displacement, validated using PIV measurements of the same test equipment, was

controlled to within $\alpha = \pm 0.25°$ of the maximum angle of attack (Leknys et al., 2017). The reduced frequency, $\kappa = \dot{\alpha}c/2U_\infty$, where $\dot{\alpha}$ is the flat plate angular velocity (rad/s) and U_∞ is the free-stream velocity (m/s), was adjusted to provide both quasi-steady and unsteady flow conditions such that $\kappa = 0.025, 0.05, 0.1$. The maximum angle of attack, α_{max}, was increased incrementally by $5°$ from $\alpha = 10°$ through to $\alpha = 30°$ and incrementally by $10°$ for $\alpha = 30°$ through to $\alpha = 50°$. The angular displacement with respect to non-dimensional time, $T^* = Tc/U_\infty$, where T is time (s), is shown in Figure 2 for the period of ramp-up and ramp-down motion, and prior to the plate being held fixed at its maximum angle of attack. Constant-pitch-rate motion was achieved by utilising a trapezoidal angular velocity profile as shown in Figure 2b.

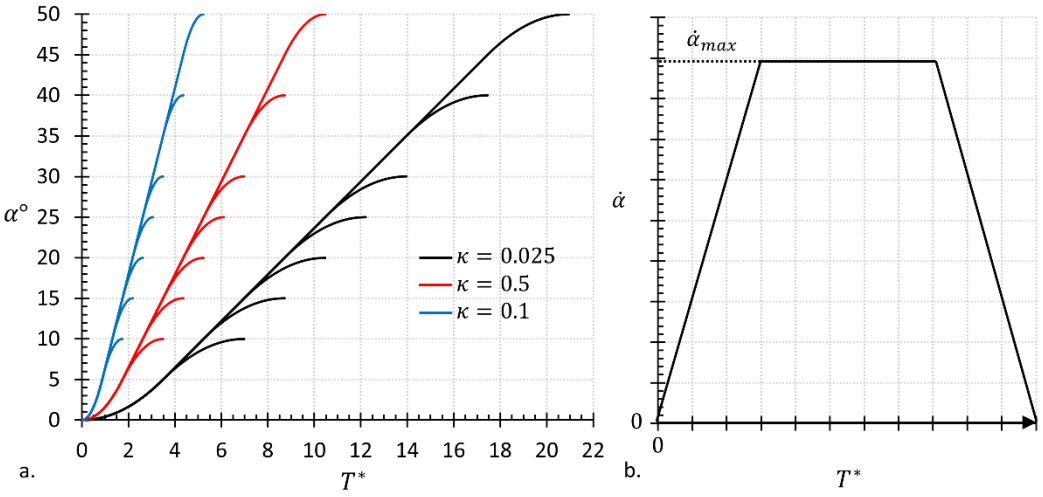

Figure 2: *Airfoil angular displacement with respect to non-dimensional time for reduced frequencies of* $\kappa = 0.025$, $\kappa = 0.05$ *and* $\kappa = 0.1$ *and for each maximum angle of attack evaluated (a) and (b) velocity profile used to simulate constant-pitch-rate motion.*

The maximum angle of attack, $\alpha = 50°$, was specified such that deep stall could be established, whilst also being adequate to simulate flight manoeuvres such as the

perching of birds. The free-stream velocity was $U_\infty = 2.9\ m/s$, corresponding to $Re = 20{,}000$ for all test cases. Individual test cases were repeated 100 times in order to achieve convergence of the resulting surface pressure samples. Stabilised wind tunnel flow was established by allowing the flat plate to return $\alpha = 0°$ after each successive test, where it was held fixed for the equivalent time to travel of 30 chord lengths.

The open-jet wind tunnel (Figure 3a) had a jet cross section of $500mm \times 500mm$, providing a blockage ratio of 15% at the maximum angle of attack, $\alpha = 50°$.

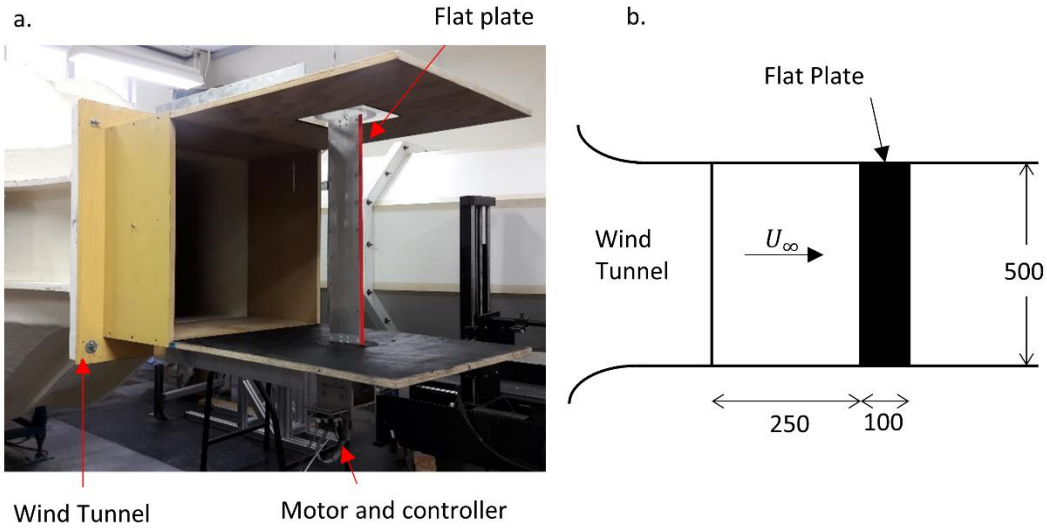

Figure 3: Wind tunnel used for constant-pitch rate dynamic stall simulation. A) Open-jet wind tunnel with motor and flat plate arrangement. B) Diagram of the flat plate in relation to the wind tunnel opening.

Blockage correction of the pressure distribution results was not required due to the minor effects of blockage occurring under dynamic stall conditions (Granlund et al., 2010). Furthermore, the flat plate was positioned $250mm$ downstream of the wind tunnel opening (Figure 3b) to allow sufficient free expansion of the air jet, further reducing blockage effects (Sayers and Ball, 1983). In addition, a collaborative effort, summarised in

North Atlantic Treaty Organization (2016), of five independent test facilities measuring forces on a pitching flat plate, showed minimal impact of blockage effects across the test facilities indicating the insensitive nature of dynamic stall with respect to tunnel blockage.

The normal and axial forces on the flat plate were evaluated through trapezoidal integration of the surface pressures according to:

$$\mathrm{C}_P = \frac{P - P_0}{1/2\,\rho {V_\infty}^2}, \qquad \mathrm{C}_A = \oint \frac{C_P}{c}\,dy, \qquad \mathrm{C}_N = -\oint \frac{C_P}{c}\,dx$$

Where, C_P is the pressure coefficient, $P - P_o$ is the measured (differential) pressure relative to the static reference (Pa), ρ is the fluid density and V_∞ is the wind tunnel free-stream velocity. In addition, C_A and C_N are the axial and normal force coefficients in the flat plate reference plane, as indicated in *Figure 4*, whilst dy and dx are the vector spacings of the surface pressure ports.

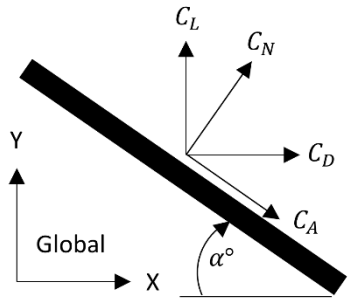

Figure 4: Coordinate system used for force evaluation of the flat plate in the wind tunnel.

Global forces, in the wind tunnel coordinate system were subsequently evaluated according to:

$$\mathrm{C}_L = C_N \cos\alpha - C_A \sin\alpha, \qquad \mathrm{C}_D = C_N \sin\alpha + C_A \cos\alpha$$

Here, C_L and C_D are the respective lift and drag coefficients, whilst α is the flat plate angle of attack.

Results

Investigation of a flat plate undergoing constant-pitch-rate motion was performed to determine the lift development and pressure distribution when the plate was hinged at $x/c = 0.5$, for multiple maximum angles of attack and three reduced frequencies. Noise generated through the use of the data acquisition system was determined by sampling the ambient pressure in still air, and found to be $\pm 0.7Pa$. Figure 5 shows the mean lift coefficient and associated lift fluctuation for the flat plate pitching to a maximum angle of attack of $\alpha_{max} = 50°$, and for reduced frequencies $\kappa = 0.025$, $\kappa = 0.05$ and $\kappa = 0.1$. Error bars represent one standard deviation from the mean of the calculated force. Results from testing showed that the averaged cycle-to-cycle repeatability of the test apparatus was such that one standard deviation,$\emptyset$, achieved a force coefficient error margin of approximately, $\emptyset = 6\%$. The fluctuation in force results are linked to the formation of the leading-edge vortex on the upper surface, resulting in large pressure gradients and surface pressure fluctuations. Similar force fluctuations are discussed in Heine et al. (2013) where fluctuations of lift were shown to be up to $\emptyset = 10\%$ in regions of highly-separated flow. A comparison of the lift coefficient, from direct force measurements, is presented in Rival et al. (2013) and Rival et al. (2014) for a flat plate undergoing constant-velocity plunge motions and shows good agreement with the lift generated for the current test where $\kappa = 0.1$. Maximum pressure fluctuations, which occurred at $\alpha = 50°$, were related to the highly-separated, unsteady flows developed in

the wake of the flat plate. Additionally, similar steady-state values for the drag coefficient were found to compare well with data in Yu (2014) using similar experimental test parameters.

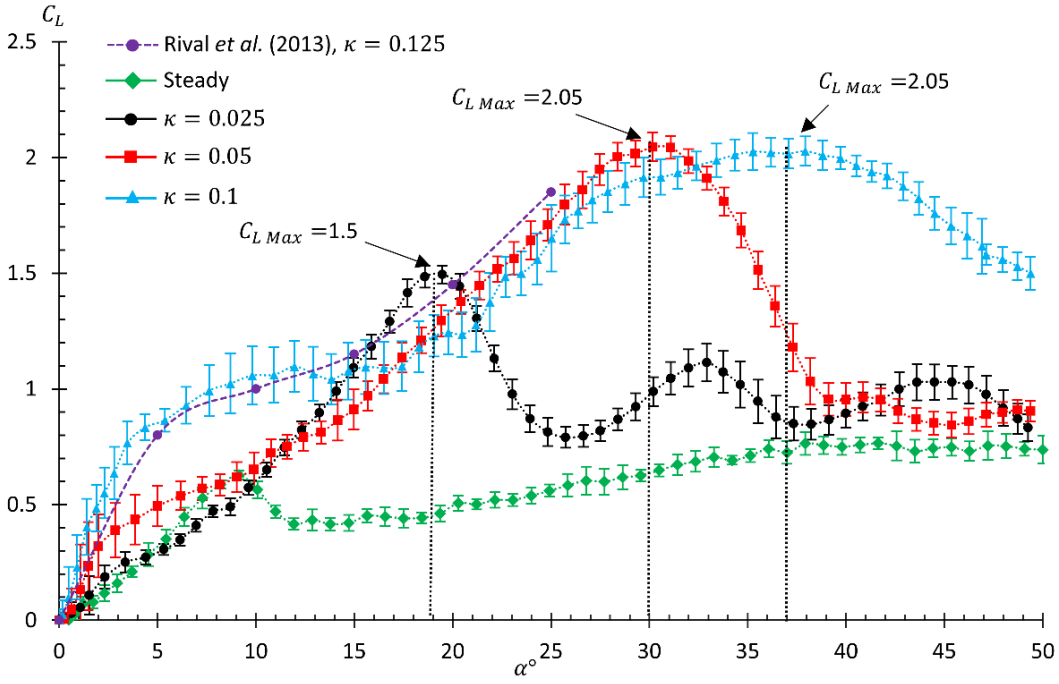

Figure 5: Lift coefficient versus angle of attack for varying κ and α on the pitching flat plate with square leading- and trailing-edge extensions. Error bars represent one standard deviation of the averaged force measurements over 100 repetitions.

Individual surface pressure sensor fluctuations were observed to be minimal in regions of attached flow. However, in regions of high pressure gradient typically associated with the location of the half-saddle point, an increase in pressure fluctuation was observed. Results of the surface pressure fluctuation of sensor 'e', located at $x/c = 0.36$, are shown in Figure 6.

Shown in Figure 6 is the surface pressure coefficient of sensor 'e' on the flat plate undergoing dynamic stall, where $\alpha_{max} = 50°$ and for $\kappa = 0.1$. These operating conditions

led to the highest state of unsteadiness in both operating conditions and recorded surface pressure fluctuations. Lower angles of attack were found to result in lower pressure fluctuations, indicating that the maximum pressure variability occurred during highly separated flows under high rotation rate conditions.

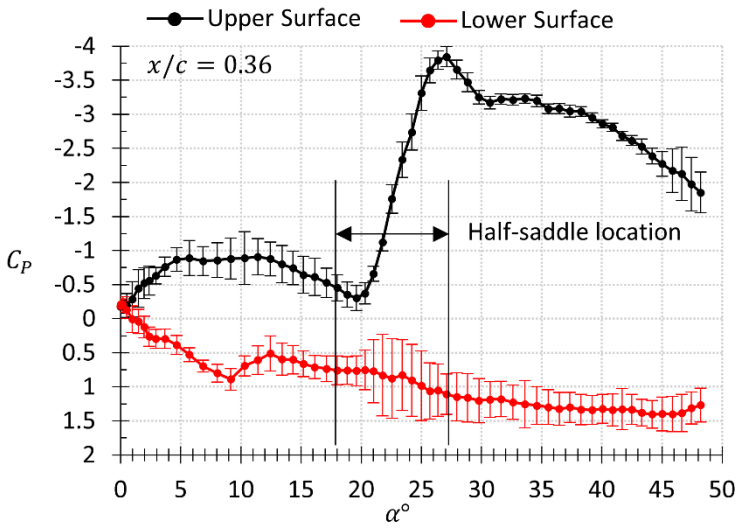

Figure 6: Surface pressure coefficient measured by sensor 'e', located at $x/c = 0.36$ on the flat plate undergoing dynamic stall with $\alpha_{max} = 50°$ and $\kappa = 0.1$. Error bars represent one standard deviation from the mean pressure coefficient.

Greater uncertainties were also observed with low angles of attack and at low flow speeds (hence low dynamic pressure). This led to a low signal/noise ratio of the sensors, however, the overall uncertainty of the averaged force coefficient results was shown to be on average, $\Delta C_L = \pm 0.2$ from the mean lift coefficient and across 100 repeated tests.

Development and shedding of the dynamic-stall vortex, and other upper surface structures, were captured successfully. This allowed the impact of leading and trailing edge geometries to be studied during the pitch-up motion.

Force Generation

The force variation created by the flat plate undergoing constant-pitch-rate motion was shown to vary with both reduced frequency and the type of leading and trailing edge extensions. In addition, the maximum lift was shown to plateau to a point where increasing the angle of attack had a minimal influence on the lift outcome. Figure 7 shows the lift coefficient with respect to the non-dimensional time for multiple angles of attack and the round leading-edge and trailing-edge extensions.

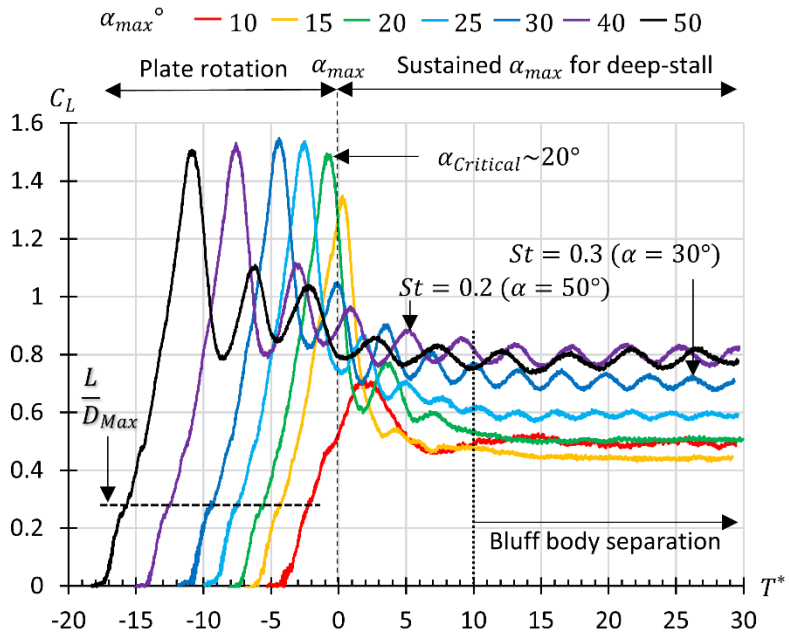

Figure 7: Lift coefficient versus non-dimensional time of the flat plate fitted with a round leading edge profile and exposed to constant-pitch-rate dynamic stall, where $\kappa = 0.025$ and $Re = 20{,}000$. Periods of plate rotation ($T^* < 0$) and sustained α_{max} ($T^* > 0$) periods of flow indicate the critical angle of attack and bluff body separation characteristics respectively.

In Figure 7, lift generated in regions of negative T^* represent stages of increased rotation prior to the flat plate reaching the maximum angle of attack. Positive T^* show lift generated once the flat plate has ceased rotation and is held stationary at the maximum angle of attack. Also shown in Figure 7 is the Strouhal number, $St = fc/U_\infty$, where f is the wake vortex shedding frequency in Hertz for cases where the maximum angle of attack of the plate is $\alpha = 30°$ and $\alpha = 50°$. Strouhal numbers were evaluated only after the plate rotation had ceased and periodic vortex shedding, representing bluff body separation, was established.

From Figure 7, for $\alpha_{max} = 50°$, the period of airfoil rotation is approximately $T^* = 18.5$. Maximum lift is established at $C_L = 1.5$ and when $T^* = -11.5$. As such, a flow time of approximately 7 chord lengths of travel was established between initial plate rotation and establishment of the maximum lift coefficient. Again, T^* represents the non-dimensional flow time, with negative values indicating airfoil rotation and positive values representing period of flow time where the flat has reached its maximum angle of attack and continued to proceed into post-stall at the maximum angle of attack. Peak lift corresponds to the phase in the pitch-up process where the leading-edge vortex has developed and begins to separate from trailing edge on the upper of the flat plate. Once the maximum angle of attack was reached, represented by $T^* = 0$, any benefits of the unsteady lifting process are no longer available. Separation of the leading-edge vortex results in a significant lift reduction. Also shown in Figure 7 is the flow time required to establish bluff-body flow conditions, in this case $T^* = 10$ once the maximum angle of attack is achieved.

Figure 8 shows the lift coefficient with respect to the non-dimensional time for reduced frequencies of $\kappa = 0.025$, $\kappa = 0.05$ and $\kappa = 0.1$. To ensure correct system functions, a

validation case for both lift and rotation rate using Ramesh et al. (2011) where $\kappa = 0.1$ for a flat plate undergoing similar rotation characteristics, was compared to the results obtained from the current investigation.

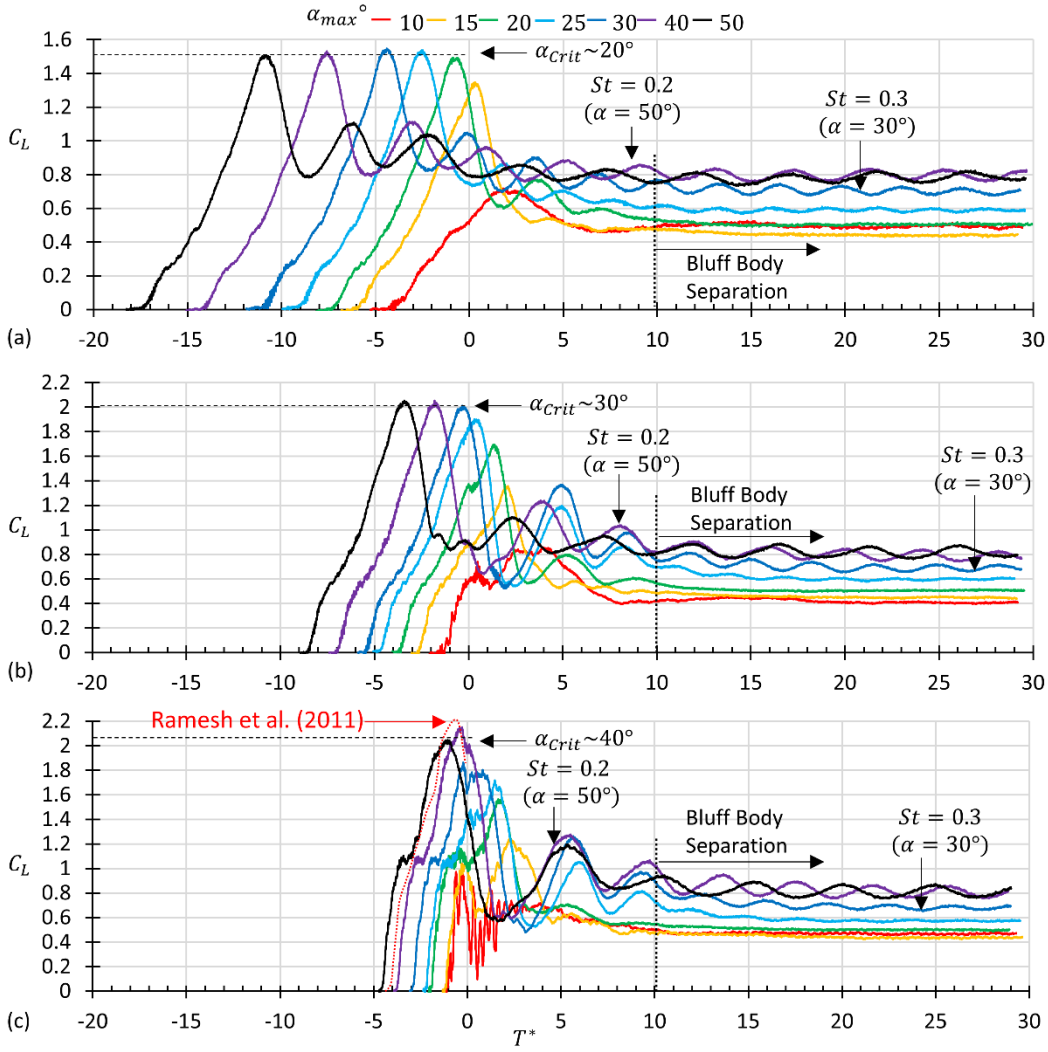

Figure 8: Lift coefficient versus non-dimensional time of the flat plate fitted with round leading and trailing edge extensions and undergoing constant-pitch-rate motion to varying maximum angles of attack. The reduced frequencies were $\kappa = 0.025$ *(a),* $\kappa = 0.05$ *(b) and* $\kappa = 0.1$ *(c).*

The results in Figure 8a demonstrate a delay in lift generation at the beginning of rotation, which are observed as periods of increasing non-linear C_L, and which are attributed to the acceleration of the plate over the first $3°$ of rotation in the pitch-up process. Plotting the lift against the angle of attack resulted in linear increases in lift, as shown in Figure 5, confirming correct operation of the test apparatus. Lift was shown to increase from $C_{L\,max} = 1.5$, for $\kappa = 0.025$ (Figure 8a), to $C_{L\,max} = 2.05$ for both $\kappa = 0.05$ (Figure 8b) and $\kappa = 0.1$ (Figure 8c). This is reflected in an increase in the suction pressure coefficient, over the forward regions and on the upper surface of the flat plate, and also due to an increase in pressure coefficient on the lower surface of the plate with increased rotation rate, as indicated in Figure 9. In Figure 9, T^* is the non-dimensional time from initial plate rotation until the indicated angle of attack is obtained and motions ceased. Increasing the rotation rate of the flat plate is shown to increase the pressure coefficient on the lower surface of the airfoil, resulting in increased lift. This is evident prior to the formation of the leading-edge vortex, as shown in Figure 9c for $\kappa = 0.1$. In Figure 9c, increased suction due to the leading-edge vortex is not observed, indicating that the additional lift is primarily due to the circulation developed about the plate, which is in-turn due to the pressure differential developed from attached flow induced via the pitch-up motion. The absence of the leading-edge vortex, for the case of $\kappa = 0.1$, is attributed to the increase in rotation rate which results in delayed formation of the leading-edge vortex until higher angles of attack. For lower rotation rates, as indicated in Figure 9a and Figure 9b, increases in surface pressure suction peaks are observed to extend along the upper surface with increased angle of attack, due to the growth of the leading-edge vortex.

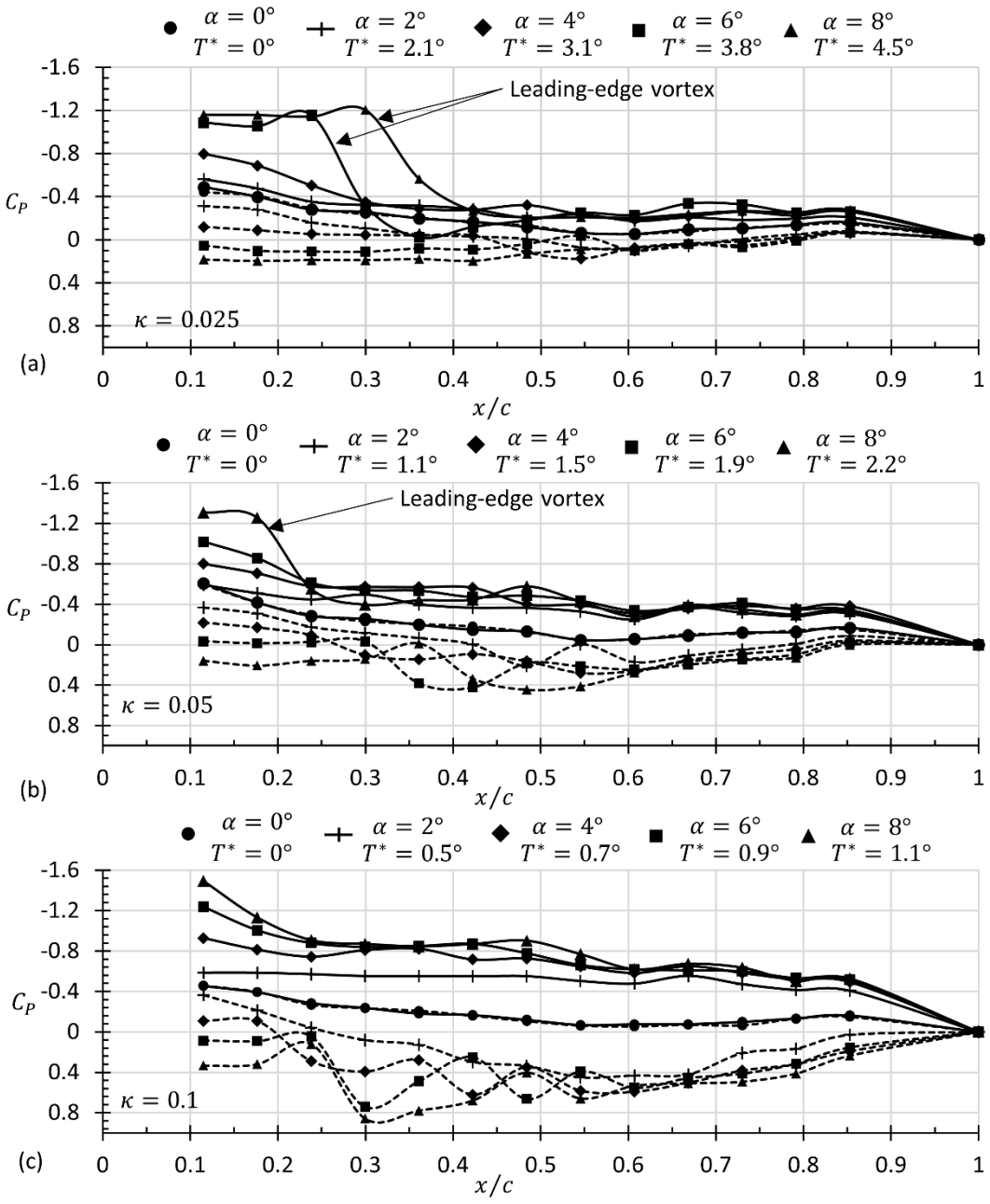

Figure 9: Surface pressure coefficient of the flat plate for $\kappa = 0.025, 0.05$ *and* 0.1 *showing the increase in suction pressure on the forward-upper surface and also increased pressure on the lower-rear surface due to plate rotation. Solid lines represent upper-surface pressure coefficients, whilst broken lines represent lower-surface pressure coefficients.*

However, from Figure 9c, the effects of vortex lift at the indicated angles of attack is limited. This being due to the decreased chord-wise distribution and magnitude of the suction peaks on the upper surface.

Peak lift was delayed to higher angles of attack with an increase in reduced frequency. For example, for $\kappa = 0.025$, increasing the angle of attack beyond $\alpha_{max} = 15°$ resulted in no significant increase in lift generation. Comparatively, with $\kappa = 0.05$, peak lift was established at $\alpha_{max} = 30°$, whilst for $\kappa = 0.1$, maximum lift was obtained at $\alpha_{max} = 37°$. Similar trends in increased lift and delayed stall were also noted in North Atlantic Treaty Organization (2016) The angle of attack where maximum lift is achieved is defined as the critical angle of attack, $\alpha_{critical}$, as beyond this threshold, no additional lift increase is obtained. Increasing the angle of attack above $\alpha_{Critical}$ resulted in an earlier reduction in lift and transition into steady-state (deep) stall. Similar reductions in the aerodynamic force were discussed in Perrotta and Jones (2017) who showed, using PIV, the development of the vortical flow around a flat plate exposed to gust-like disturbances. From the results in Perrotta and Jones (2017), separation of the leading-edge vortex was correlated with significant lift reductions. In the current investigation, complete separation of the leading-edge vortex resulting in deep-stall conditions is expected, and is represented via fluctuations in lift resulting from large scale von-Karman vortex shedding (Fage and Johansen, 1927, Lam and Leung, 2005, Lam and Wei, 2010). The vortex shedding frequency in post-stalled conditions was consistent with steady-state data provided in Chen and Fang (1996). The Strouhal number was $St = 0.3$ for $\alpha = 30°$ and $St = 0.2$ for $\alpha = 50°$. This indicates, for the post-stall flow regime and once rotation has stopped, that deep-stall characteristics and steady-state separation from the plate were not influenced by the flow's previous history and induced flows developed during

the pitch-up motion. As such, the force characteristics revert back to steady-state conditions similar to those observed during von Karman vortex shedding.

Replacing the round leading-edge extension with the square extension was shown to decrease the maximum lift values for all reduced frequency tests. Figure 10(a-c) shows the lift coefficient generated for the flat plate fitted with square extensions for all three reduced frequencies and to varying maximum angles of attack. From observation of the maximum lift coefficient, it is apparent that the lift coefficient of the square extension was reduced by approximately $C_L = 0.1$ when compared with the round leading edge profile. Although this trend is clear, implementation of tests using a higher density pressure array at the leading edge can provide further evidence to focus on the effects of variations in the leading- and trailing-edge profiles. For example, Rival et al. (2013) and Rival et al. (2014) showed the opposite trend, where square leading-edge profiles provided increased aerodynamic performance. However, experiments in Rival et al. (2013) and Rival et al. (2014) were conducted for plunge motion at a varying pitch-rate, and indicating a possible sensitivity of the force response to motion type. These results indicate that the plunge and constant-pitch-rate motion conditions may not be comparable and therefore results from one condition may not be transferable to another for different leading-edge and trailing-edge profiles.

Trends in maximum lift for the square edge cases were observed to be similar to those of the round-extension cases, such that once a critical point in the flat plate angle of attack was reached, then no further increase in lift generation was observed. For the square extension, the critical angle of attack was shown (Figure 10a) to be approximately $\alpha_{Critical} = 10°$ for $\kappa = 0.025$, whilst $\alpha_{Critical} = 20°$ and $\alpha_{Critical} = 40°$ for $\kappa = 0.05$

(Figure 10b) and $\kappa = 0.1$ (Figure 10c) respectively. Increasing the reduced frequency increased the maximum lift capacity such that $C_L = 1.4$ for $\kappa = 0.025$, whilst $C_L = 2.0$ for $\kappa = 0.05$ and $C_L = 2.2$ for $\kappa = 0.1$.

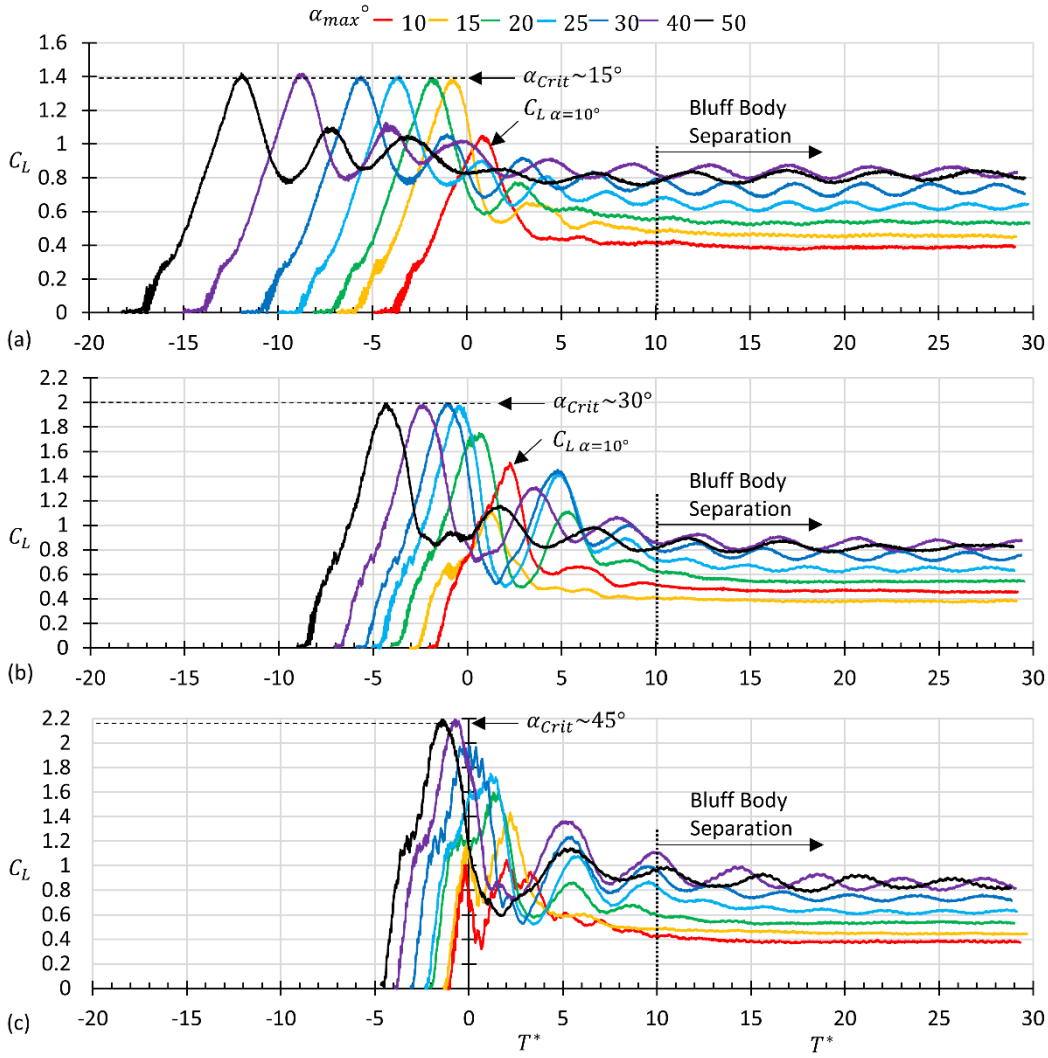

Figure 10: Lift coefficient versus non-dimensional time of the flat plate fitted with a square leading-edge and trailing-edge extensions and undergoing constant-pitch-rate motion to varying maximum angles of attack. The figure shows peak lift generation and the impact of increasing reduced frequency over the range $\kappa = 0.025, 0.05$ *and* 0.1.

Changing the leading-edge and trailing-edge extensions to the triangular geometry showed similar trends in lift generation to those of the round and square geometry extensions, and is shown in Figure 11.

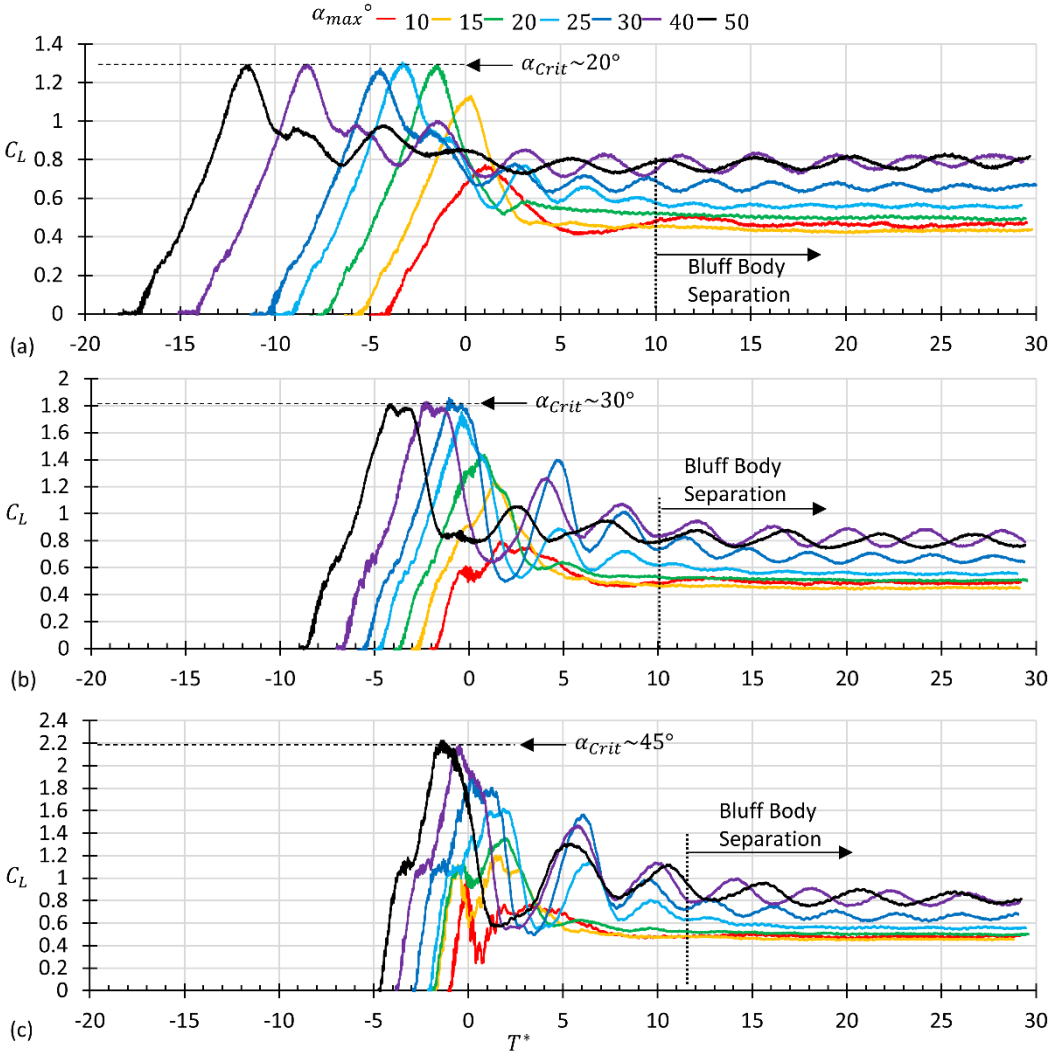

Figure 11: Lift coefficient verses non-dimensional time of the flat plate fitted with triangular leading-edge and trailing-edge extensions and undergoing constant-pitch-rate motion to varying maximum angles of attack. The figure shows peak lift generation and the impact of increasing reduced frequency over the range $\kappa = 0.025,\ 0.05$ *and* 0.1.

As before, delayed lift is observed during flat-plate acceleration, followed by a linear increase in lift prior to leading-edge vortex separation. However, the overall lift was shown to be less compared to both the round and square extensions, which correlates to the observations discussed from results in North Atlantic Treaty Organization (2016) using similar flat plate experiments. The current study indicates that the application of the triangular extensions have little benefits over round extensions in reducing the load fluctuations on plates exposed to transient gust conditions where low-rotation-rate conditions apply. However, for unsteady rotation rates, such as $\kappa = 0.1$, the triangular extensions are shown to have similar performance to both square and round profiles.

The triangular extension results in a reduction of overall lift for the two lowest reduced frequencies, such that $C_L = 1.3$ for $\kappa = 0.025$ (Figure 11a), and $C_L = 1.8$ for $\kappa = 0.05$ (Figure 11b). At the highest reduced frequency, $\kappa = 0.1$, lift was demonstrated to be similar to both the round and square extensions where $C_L = 2.2$ (Figure 11c). Yu and Bernal (2013) show the influence of inertial flows created though high rotation rates, where increased lift and drag was shown to increase with both rotation axis and rotation rate. However in the current investigation, it is shown that the extension profiles do not significantly impact the maximum generated lift at the highest rotation rate investigated ($\kappa = 0.1$). The rotation rate, when compared to leading-edge profile, is shown to have a greater influence on load generation, development of high pressure gradients on the forward upper surface of the plate and increasing pressure on the lower surface of the plate, all of which ultimately result in elevated force generation and flow separation. The presence of flow separation is shown to result from high localised pressure gradients, which in turn are increased with elevated reduced frequencies. These high pressure gradients are present regardless of the leading-edge profile utilised.

Changes in the maximum lift were compared directly for all extension profiles and reduced frequencies, as summarised in Figure 12. It can be seen that increasing the reduced frequency resulted in an overall increase in the lift coefficient for all leading-edge cases. The results from the current work show the round profile extensions generate their maximum lift at higher angles of attack compared to both the square and triangular profiles.

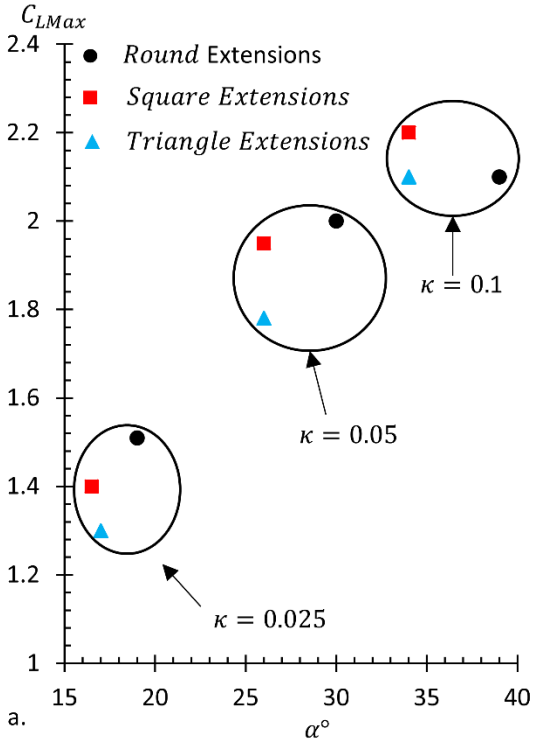

Figure 12: Trend in maximum (a) lift coefficient verses angle of attack verses maximum test angle of attack for the round, square and triangular extension, and for $\kappa = 0.025$, $\kappa = 0.05$ *and* $\kappa = 0.1$.

Leading-edge vortex growth rate

Investigations to identify the growth rate and characteristics of the leading-edge vortex were conducted to determine the impact of varying leading-edge and trailing-edge

geometries and increasing rotation rate on the surface pressure distribution of the flat plate. Moreover, the surface pressure coefficient, C_P, was utilised to determine the change in growth rate of the leading-edge vortex with respect to the reduced frequency. Note that in the current investigation it was not possible to determine the beginning of the leading-edge vortex formation due to the lack of pressure sensors forward of $X/c = 0.11$. However, trends in surface pressure gradient could be utilised for an approximation of the vortex growth once the leading-edge vortex was established. Figure 13a indicates the time history of the upper surface pressure distribution for the flat plate with round extensions, rotating at a reduced frequency of $\kappa = 0.025$ to a maximum angle of attack of $\alpha = 30°$. The location of the half-saddle point, representing the bifurcation between forward and reversed flow on the supper surface, corresponds to the presence of a strong adverse pressure. Although a critical point, in the form of a half saddle, is representative of local maximum pressures (Perry and Fairlie, 1975), where $C_P = 1$, similar behaviour of reduced pressure coefficient at the location of the half-saddle point is also observed in the numerical simulations of Visbal (2011), and in the experimental results of Mueller-Vahl et al. (2014) who measured surface pressures about thick airfoils undergoing pitching motions. This suggests that a change in static pressure results due to the interaction of the leading-edge vortex and motion of the flat plate.

The half-saddle point location, represented by a significant pressure gradient on the plats upper surface, is observed to move aft of the leading edge with increased flow time, as indicated in Figure 13b, until it reaches the trailing edge, prompting complete flow separation. Movement of the half-saddle beyond the trailing edge results in deep stall conditions and loss of suction, as shown in Figure 13a for $\mathrm{T}^* > 2$.

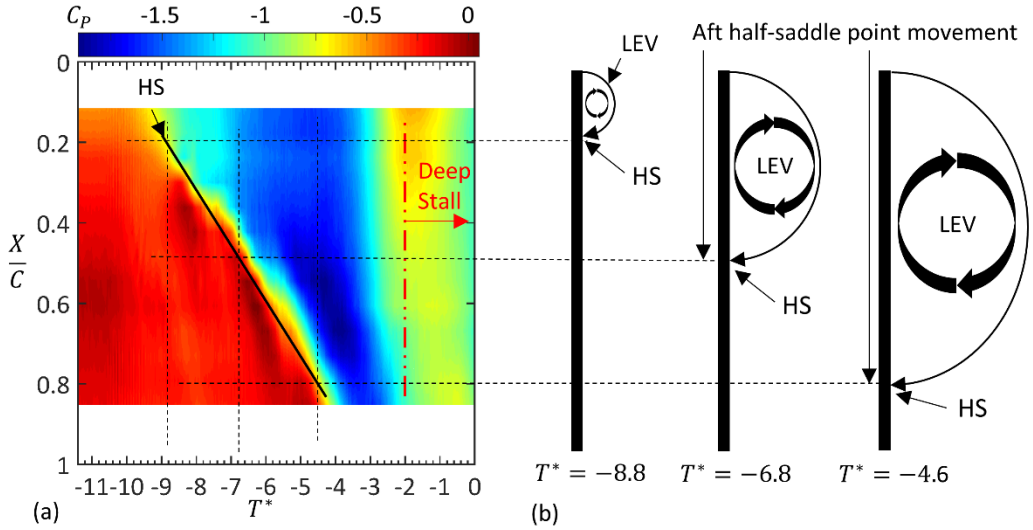

Figure 13: Representation of the leading-edge vortex reattachment point, determined by the half-saddle point defined at a position where a severe pressure gradient is located on the plate upper surface with round profile extensions and pitching to a maximum angle of $\alpha = 30°$ *and for* $\kappa = 0.025$.

Through visual inspection of the pressure coefficient at the half-saddle point, the rate of growth of the leading-edge vortex can be inferred as the reduced frequency is varied. Separation of the saddle point from the trailing edge leading to complete flow separation is also discussed in Rival et al. (2013) and Rival et al. (2014), thus indicating a good agreement with the current analysis linking the evolution of the surface pressure gradient with the motion of the half-saddle point.

From Figure 14, interpretation of the formation of either separation bubbles or the leading-edge vortex is possible. Due to an increase in suction pressure coefficient on the upper surface towards the aft of the flat plate, the formation of a separation bubble is not observed. With the existence of a separation bubble on the upper surface, the pressure coefficient is expected to plateau with increased distance from the leading edge. In the

current analysis, an increase in suction pressure coefficient is observed and can be related to the formation, growth and presence of the leading-edge vortex above the plate's surface.

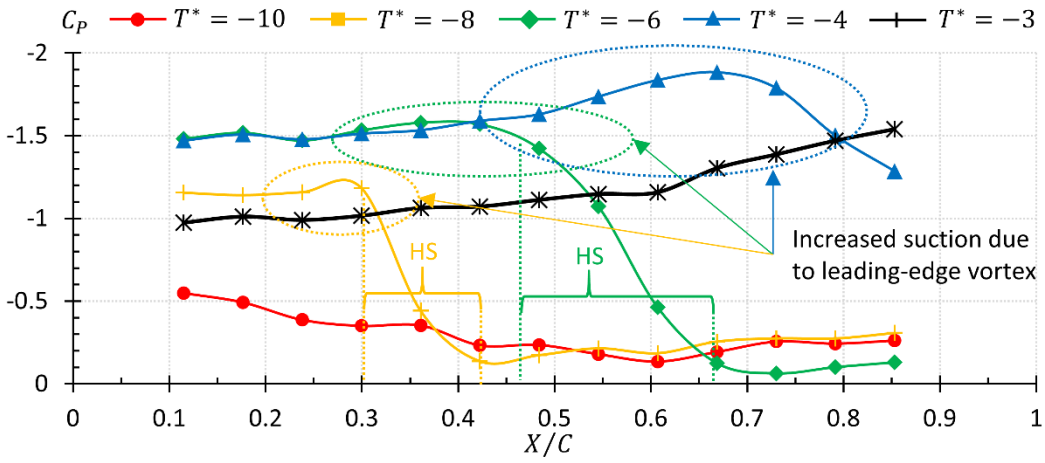

Figure 14: Surface pressure coefficient of the flat plate where $\kappa = 0.025$ and the maximum angle of attack is $\alpha = 30°$. Regions of severe pressure gradient and locations where are utilised for identification of the half-saddle point developed aft of the leading-edge vortex.

Regions of increased suction and leading-edge vortex interaction are highlighted in Figure 14, with locations of increased suction being circled. For example, when $T^* = -4$, an increase in the upper surface suction pressure is observed between $x/c = 0.45$ and $x/c = 0.8$. With the presence of the leading-edge vortex, an increase in induced velocity on the surface occurs, resulting in localised increases in suction pressure (decreased pressure coefficient) and enhanced lift. Additionally, regions approximating the location of the half-saddle

Surface pressure results for $\alpha_{max} = 30°$ are presented in the following analysis as full development of the leading-edge vortex, for all reduced frequency cases investigated was

achieved. Figure 15 shows contours of the upper surface pressure coefficient for $\kappa = 0.025$, $\kappa = 0.05$ and $\kappa = 0.1$ and for the flat plate fitted with round leading-edge and trailing-edge extensions. Here the dimensionless distance along the flat plate's chord length is plotted on the ordinate axis, whilst the non-dimensional time is displayed on the abscissas. Figure 15 also shows the presence of the leading-edge vortex and its growth, which begins at the leading edge and extends to the trailing edge. Initial separation of the boundary layer occurs immediately in the pitch-up process due to the strong adverse pressure gradients created by the leading-edge geometry. With increasing angle of attack and under the presence of rotation, re-attachment of the separated boundary layer occurs, resulting in the formation of an attached leading-edge vortex (Widmann and Tropea, 2015, North Atlantic Treaty Organization, 2016).

Increased lift is attributed to the increased area of the flat plate exposed to low pressure, resulting from the formation and presence of the leading-edge vortex. As the reduced frequency was increased, the magnitude of the suction pressure peak was shown to increase, leading to the increase in lift coefficient as observed in Figure 8(a-c), Figure 10(a-c) and Figure 11(a-c). Increasing the reduced frequency was also shown to result in higher growth rates of the leading-edge vortex. This was identified through the rearward motion of the half saddle-point.

The position of the half-saddle point was shown to progress from the leading edge towards the trailing edge in a linear manner, similar to that of the flat plate motion profile. Once reaching the trailing edge, its separation from the plate surface and departure into the wake lead to deep stall. The position of the half-saddle point, connecting the leading-edge vortex to the upper surface of the flat plate, is approximated in the current work by

the location of a significant pressure gradient aft of the maximum suction location, as indicated in Figure 13b and Figure 15.

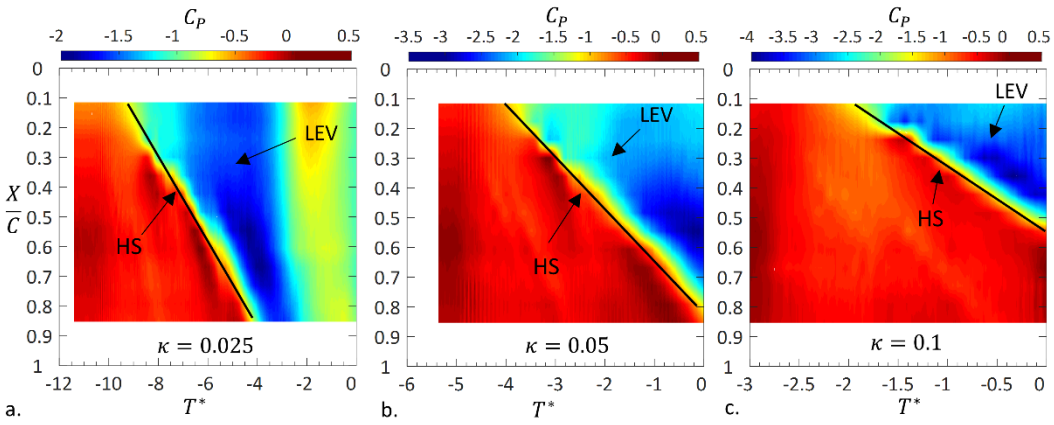

Figure 15: Upper surface pressure coefficient distributions on the pitching flat plate, plotted against non-dimensional time for the cases where the plate is fitted with round extensions and $\alpha_{max} = 30°$. Low pressure regions indicate the formation of the leading-edge vortex.

The locations and definition of the half saddle point, shown in Figure 15, was also identified and discussed in Widmann and Tropea (2017), Rival et al. (2013) and Rival et al. (2014), however, its location was identified as regions of zero surface velocity on the upper surface of the plat during rotation. Rival et al. (2013) and Rival et al. (2014) show the movement of the half saddle for a flat plate with two dissimilar leading-edge profiles and discuss the benefits of knowing its motion with regards to flow control, although only for one test reduced frequency.

In the present text, we have sought to identify the motion of the half saddle point, which directly relates to the growth of the leading-edge vortex, and its variation in growth rate with respect to changes to the reduced frequency to better apply methods of controlling

the growth and development of the leading-edge vortex, and dynamic stall. Movement of the rear half-saddle point attaching the leading-edge vortex to the upper surface is represented by $\dot{X} = X/cT^*$, where $\dot{X}$ is the non-dimensional movement rate determined through interpretation of the surface contours shown in Figure 15, for each reduced frequency and extension profile examined. From analysis of the surface pressures a representation of the reattachment point of the leading-edge vortex could be determined through estimation of the pressure at the location where the significant pressure gradient existed. For the case of the round extensions, the pressure correlating to the location of significant pressure gradient was observed to vary according the flat plate rotation rate, as is shown in Figure 16.

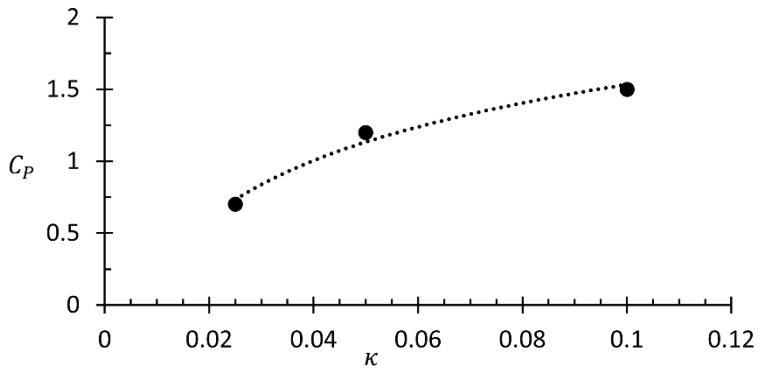

Figure 16: Variation in C_P at the approximation of the half-saddle point location with changes in flat plate rotation rate for the plate with round extensions.

Using the location of the pressure gradient on the upper surface, an approximation of the variation in half-saddle point movement for the constant-pitch-rate motion in the current analysis could be determined. Results of the rate of change of the half-saddle location are shown in Figure 17.

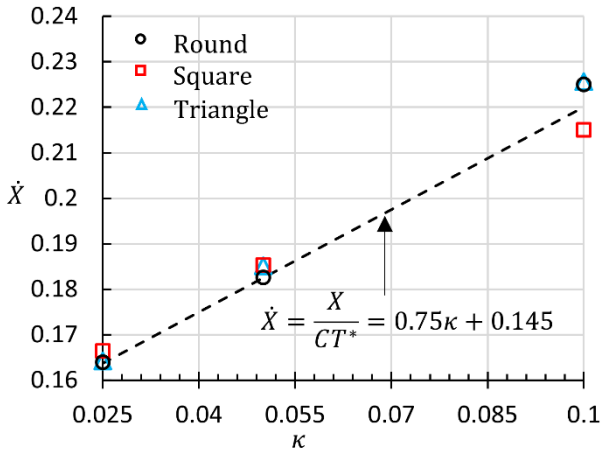

Figure 17: Non-dimensional rate of change of the half-saddle point location from the leading edge with respect to reduced frequency for all three leading edge geometries evaluated on the constant-pitch-rate motion flat plate.

Movement of the half-saddle was observed to correlate closely with the linear pitch-up motion, such that a linear increase in its distance from the leading edge was observed. The normalised movement rate of the vortex half-saddle location was approximated such that $\dot{X} = 0.75\kappa + 0.145$. Substitution of the reduced frequency, free stream velocity and chord length into $\dot{X}$, resulted in the rate of change of the half-saddle location aft of the leading edge, such that $X/T = 0.15(2.5\omega c + U_\infty)$. The movement of the half saddle was shown to be enhanced by the rate of rotation, such that its movement towards the trailing edge increased proportionally with increased reduced frequency and chord length. This indicates the direct relationship between both rotation rate and chord length to the vortex growth for a flat plate exposed to constant-pitch-rate motion, as experienced in the current testing. The current results also agree with observations in Jones et al. (2016), where the leading-edge vortex position was tracked using PIV and increases in the rotation rate were shown to have a similar influence on increasing the velocity of the

leading-edge vortex over the plate's surface. Also noted is that the initial growth rate is solely dependent on the free-stream velocity when the reduced frequency is lowered to $\kappa = 0$. This hypothesis however must be confirmed in future investigations at reduced frequencies where $\kappa < 0.025$, to observe the trend in vortex growth rate as a function of both rotation rate and motion profile.

Conclusions

The edge profile shape was only observed to impact the lift coefficient at low angles of attack of the flat plate, with the lift becoming insensitive to leading-edge and trailing-edge geometry at higher angles of attack. The current work shows the details of variations in leading edge and trailing edge profiles and their influence on the overall lift characteristics. However, future work using additional sensors located at the leading edge can help to provide further evidence, and show the differences between multiple leading edge profiles, for the analysis of lift development and determination of the location and onset of the leading-edge vortex. A critical angle of attack is identified for each of the reduced frequencies, such that beyond this angle no benefit to lift occurs due to continued rotation. The round leading-edge and trailing-edge extensions were demonstrated to generate greater lift when compared to the square and triangular leading-edge and trailing-edge extensions. At the highest rotation rate, where $\kappa = 0.1$, lift was similar between all test cases indicating that the force becomes independent of the plate leading-edge and trailing-edge geometry and more associated with unsteady flows dominated by inertial induced flows. Peak lift was linked to the generation of the leading-edge vortex, which on separation from the flat plate resulted in significant loss of lift.

Detachment of the leading-edge vortex is shown to occur once the location of a half-saddle point, approximated by the location where a significant pressure gradient existed on the upper surface of the flat plate and aft of the low pressure region characterised by the leading-edge vortex, reaches the trailing edge of the flat plate. The half-saddle movement was shown to be independent of leading-edge and trailing edge geometry and also the angle of attack, but directly proportional to the rotation rate, chord length and free-stream velocity. The pressure coefficient at the location of the half-saddle point was shown to be a function of the rotation rate of the plate and increased in a logarithmic manner with increased non-dimensional rotation rate. Although a simple motion type was selected for the current investigation, further work is required to conclude if the motion of the half-saddle point remains linear with changes to the rotation rate profile. This will allow greater flexibility and regulation of boundary layer flow control devices, which may utilise the vortex dynamics for efficient operation. Under post-stalled conditions, the flat plate was observed to exhibit bluff body separation characteristics, where fluctuations in lift are associated with large-scale vortex shedding, and decreased aerodynamic efficiency with increased angle of attack.

Acknowledgements

The first author acknowledges the support provided by an Australian Government Research Training Program Scholarship. In addition, research undertaken for this article has been assisted by a grant from the Sir Ross and Sir Keith Smith Fund (www.smithfund.org.au). The support is acknowledged and greatly appreciated.

References

Barlow, J. B., Rae, W. & Pope, A. 1999. Low-speed wind tunnel testing. *John Wiley & Sons, Canada*.

Buchner, A. & Soria, J. 2015. Measurements of the flow due to a rapidly pitching plate using time resolved high resolution PIV. *Aerospace Science and Technology,* 44**,** 4-17.

Carr, L. W. 1988. Progress in analysis and prediction of dynamic stall. *Journal of aircraft,* 25**,** 6-17.

Chen, J. M. & Fang, Y.-C. 1996. Strouhal numbers of inclined flat plates. *Journal of wind engineering and industrial aerodynamics,* 61**,** 99-112.

Chen, K. K., Colonius, T. & Taira, K. 2010. The leading-edge vortex and quasisteady vortex shedding on an accelerating plate. *Physics of Fluids,* 22**,** 033601.

Dickinson, M. 1994. The effects of wing rotation on unsteady aerodynamic performance at low Reynolds numbers. *Journal of experimental biology,* 192**,** 179-206.

Dickinson, M. H. & Gotz, K. G. 1993. Unsteady aerodynamic performance of model wings at low Reynolds numbers. *Journal of experimental biology,* 174**,** 45-64.

Ellington, C. 1984a. The aerodynamics of hovering insect flight. I. The quasi-steady analysis (I-VI). *Philosophical Transactions of the Royal Society of London B: Biological Sciences,* 305**,** 1-15.

Ellington, C. 1984b. The aerodynamics of hovering insect flight. IV. Aerodynamic mechanisms. *Phil. Trans. R. Soc. Lond. B,* 305**,** 79-113.

Fage, A. & Johansen, F. 1927. On the flow of air behind an inclined flat plate of infinite span. *Proceedings of the Royal Society of London. Series A, Containing Papers of a Mathematical and Physical Character,* 116**,** 170-197.

Garmann, D. J. & Visbal, M. R. 2011. Numerical investigation of transitional flow over a rapidly pitching plate. *Physics of Fluids,* 23**,** 094106.

Granlund, K., Ol, M., Garmann, D., Visbal, M. & Bernal, L. Experiments and computations on abstractions of perching. 28th AIAA Applied Aerodynamics Conference, 2010 United States. 4943.

Granlund, K. O., Ol, M. V. & Bernal, L. P. 2013. Unsteady pitching flat plates. *Journal of Fluid Mechanics,* 733**,** R5.

Heine, B., Mulleners, K., Joubert, G. & Raffel, M. 2013. Dynamic stall control by passive disturbance generators. *AIAA Journal*.

Jones, A. R., Manar, F., Phillips, N., Nakata, T., Bomphrey, R., Ringuette, M. J., Percin, M., van Oudheusden, B. & Palmer, J. Leading edge vortex evolution and lift production on rotating wings. 54th AIAA Aerospace Sciences Meeting, 2016 United States. 0288.

Jones, M. A. 2003. The separated flow of an inviscid fluid around a moving flat plate. *Journal of Fluid Mechanics,* 496**,** 405-441.

Lam, K. & Leung, M. 2005. Asymmetric vortex shedding flow past an inclined flat plate at high incidence. *European Journal of Mechanics-B/Fluids,* 24**,** 33-48.

Lam, K. & Wei, C. 2010. Numerical simulation of vortex shedding from an inclined flat plate. *Engineering Applications of computational fluid mechanics,* 4**,** 569-579.

Leishman, J. 1990. Dynamic stall experiments on the NACA 23012 aerofoil. *Experiments in Fluids,* 9**,** 49-58.

Leknys, R., Arjomandi, M., Kelso, R. & Birzer, C. 2017. Dynamic-and post-stall characteristics of pitching airfoils at extreme conditions. *Proceedings of the*

Institution of Mechanical Engineers, Part G: Journal of Aerospace Engineering, 0954410017710274.

McCroskey, W. J. 1981. The phenomenon of dynamic stall. DTIC Document.

Mueller-Vahl, H., Strangfeld, C., Nayeri, C. N., Paschereit, C. O. & Greenblatt, D. 2014. Thick Airfoil Deep Dynamic Stall. *Wind Energy-Impact of Turbulence*, 35-40.

Narsipur, S., Gopalarathnam, A. & Edwards, J. R. Low-Order Modeling of Airfoils with Massively Separated Flow and Leading-Edge Vortex Shedding. 2018 AIAA Aerospace Sciences Meeting, 2018. 0813.

North Atlantic Treaty Organization, S. T. O. 2016. Extensions of Fundamental Flow Physics to Practical MAV Aerodynamics. North Atlantic Treaty Organization, Science and Technology Organization.

Ol, M. & Babinsky, H. 2016. Extensions of fundamental flow physics to practical MAV aerodynamics. North Atlantic Treaty Organisation.

Pelletier, A. & Mueller, T. J. 2000. Low Reynolds number aerodynamics of low-aspect-ratio, thin/flat/cambered-plate wings. *Journal of Aircraft,* 37, 825-832.

Perrotta, G. & Jones, A. R. 2017. Unsteady forcing on a flat-plate wing in large transverse gusts. *Experiments in fluids,* 58, 101.

Perry, A. & Fairlie, B. 1975. Critical points in flow patterns. *Advances in Geophysics,* 18, 299-315.

Perry, A. & Steiner, T. 1987. Large-scale vortex structures in turbulent wakes behind bluff bodies. Part 1. Vortex formation processes. *Journal of Fluid Mechanics,* 174, 233-270.

Pitt Ford, C. & Babinsky, H. Low Reynolds number experiments on an impulsively started flat plate at high incidence. 49th AIAA Aerospace Sciences Meeting including the New Horizons Forum and Aerospace Exposition, 2011. 475.

Pullin, D. & Wang, Z. J. 2004. Unsteady forces on an accelerating plate and application to hovering insect flight. *Journal of Fluid Mechanics,* 509**,** 1-21.

Ramesh, K., Gopalarathnam, A., Edwards, J., Ol, M. & Granlund, K. Theoretical, computational and experimental studies of a flat plate undergoing high-amplitude pitching motion. 49th AIAA Aerospace Sciences Meeting including the New Horizons Forum and Aerospace Exposition, 2011. 217.

Ramesh, K., Gopalarathnam, A., Granlund, K., Ol, M. V. & Edwards, J. R. 2014. Discrete-vortex method with novel shedding criterion for unsteady aerofoil flows with intermittent leading-edge vortex shedding. *Journal of Fluid Mechanics,* 751**,** 500-538.

Rival, D., Kriegseis, J., Schaub, P., Widmann, A. & Tropea, C. A criterion for vortex separation on unsteady aerodynamic profiles. 51st AIAA Aerospace Sciences Meeting including the New Horizons Forum and Aerospace Exposition, 2013 United States. AIAA, 836.

Rival, D., Prangemeier, T. & Tropea, C. 2009. The influence of airfoil kinematics on the formation of leading-edge vortices in bio-inspired flight. *Experiments in Fluids,* 46**,** 823-833.

Rival, D., Schönweitz, D. & Tropea, C. 2011. Vortex interaction of tandem pitching and plunging plates: a two-dimensional model of hovering dragonfly-like flight. *Bioinspiration & biomimetics,* 6**,** 016008.

Rival, D. E., Kriegseis, J., Schaub, P., Widmann, A. & Tropea, C. 2014. Characteristic length scales for vortex detachment on plunging profiles with varying leading-edge geometry. *Experiments in fluids,* 55**,** 1660.

Sane, S. P. 2003. The aerodynamics of insect flight. *Journal of Experimental Biology,* 206**,** 4191-4208.

Sayers, A. & Ball, D. 1983. Blockage corrections for rectangular flat plates mounted in an open jet wind tunnel. *Proceedings of the Institution of Mechanical Engineers, Part C: Journal of Mechanical Engineering Science,* 197**,** 259-263.

Shyy, W., Lian, Y., Tang, J., Viieru, D. & Liu, H. 2007. *Aerodynamics of low Reynolds number flyers*, Cambridge University Press.

Son, O., Cetiner-Yildirim, O. N., Stevens, R. J., Babinsky, H., Manar, F., Mancini, P., Jones, A. R., Ol, M. V. & Gozukara, A. Parametric Variations in Aspect Ratio, Leading Edge and Planform Shapes for the Rectilinear Pitch Cases of AVT-202. 54th AIAA Aerospace Sciences Meeting, 2016. 0289.

Son, O. & Cetiner, O. Effect of aspect ratio and leading and trailing edge form on the flow around an impulsively pitching flat plate. 53rd AIAA Aerospace Sciences Meeting, 2015. 1296.

Stevens, P. & Babinsky, H. 2017. Experiments to investigate lift production mechanisms on pitching flat plates. *Experiments in Fluids,* 58**,** 7.

Taira, K. & Colonius, T. 2009. Three-dimensional flows around low-aspect-ratio flat-plate wings at low Reynolds numbers. *Journal of Fluid Mechanics,* 623**,** 187-207.

Visbal, M. R. 2011. Numerical investigation of deep dynamic stall of a plunging airfoil. *AIAA J,* 49**,** 2152-2170.

Widmann, A. & Tropea, C. 2015. Parameters influencing vortex growth and detachment on unsteady aerodynamic profiles. *Journal of Fluid Mechanics,* 773**,** 432-459.

Widmann, A. & Tropea, C. 2017. Reynolds number influence on the formation of vortical structures on a pitching flat plate. *Interface Focus,* 7**,** 20160079.

Wilkins, P. & Knowles, K. 2009. The leading-edge vortex and aerodynamics of insect-based flapping-wing micro air vehicles. *The Aeronautical Journal,* 113**,** 253-262.

Xia, X. & Mohseni, K. 2012. Lift evaluation of a 2d flapping flat plate. *arXiv preprint arXiv:1205.6853*.

Yu, H.-T. 2014. *Unsteady Aerodynamics of Pitching Flat Plate Wings.* Doctor of Philosophy, The University of Michigan.

Yu, H.-T. & Bernal, L. Effect of pivot point on aerodynamic force and vortical structure of pitching flat plate wings. 51st AIAA aerospace sciences meeting including the new horizons forum and aerospace exposition, 2013 United States. AIAA, 792.

Chapter 7.

Conclusions and Future Work

Dynamic stall on airfoils exposed to constant-pitch-rate motion was investigated for its associated effects, such as increased force and moment fluctuation, on the blades of rotary machines. The research herein utilises PIV and surface pressure analysis to examine fluid flow formation and load generation at low Reynolds numbers, in order to address the overall thesis objectives. This leads to knowledge that can be utilised for more efficient control of the boundary layer during dynamic stall. Airfoil thickness was shown to have a minor influence on the flow structure and force at elevated rotation rates and high angles of attack. Furthermore, in post-stalled conditions, dynamic stall had little effect on the force generation, although separation of the leading-edge vortex was delayed to higher angles of attack with increasing pitch rate. Under high rotation rates and high angles of attack, the leading-edge trip wire did not perform adequately, due to high inertial loads imposed during airfoil rotation. The trip wire was not observed to provide beneficial flow control properties under the highly accelerated flow conditions. The thesis shows the formation of a half-saddle point on the surface of the flat plate aft of the leading-edge vortex, which can potentially be utilised for control of boundary layer separation. The following subsections outline major outcomes and conclusions drawn from each of the research aims developed at the initiation of the project.

7.1. Dynamic Stall on Thick and Thin Airfoils

Through application of PIV and surface pressure measurements, the extent of load generation and flow separation developed about two wings of different thicknesses were investigated during constant-pitch-rate dynamic stall. The two airfoils consisted of a thin NACA 0012 and a thick NACA 0021 airfoil. Test parameters include constant angular velocity, reduced frequencies of $\kappa = 0.05$, 0.1 and 0.2, and a Reynolds number for $Re = 20{,}000$. The wings were rotated to a maximum angle of attack of $\alpha = 90°$ and remained fixed at this angle prior to returning to $\alpha = 0°$. The presence of vortex formations was shown to be similar between the two airfoils. However, the airfoil thickness and rotation rate were shown to influence the growth and strength of the developed separation bubble and leading-edge vortex on the suction side of the wing. Increases in rotation rate were linked to a delay in flow separation and leading-edge vortex formation, resulting in increased lift production of both airfoils to significantly higher angles of attack in comparison to steady-state operation. Fully-separated flow conditions were achieved once the stagnation point on the upper surface of the airfoil transitioned from the trailing edge of the airfoil into the wake.

Geometry and reduced frequency variations did not appear to influence deep-stall flow characteristics. Both airfoils exhibited bluff-body separation characteristics, distinguished by large-scale von-Karman vortex shedding once deep stall was established. Decreases in pressure at the leading edge on the suction surface were observed to occur with increasing rotation rate. The reduced pressure at the leading edge, prior to leading-edge vortex formation, combined with the presence of a separation bubble on the aft of the airfoil, resulted in a reduction in the lift-curve slope. During ramp-up of the wings, periodic

fluctuations in lift were observed with the presence of the leading-edge vortex. The fluctuations in lift were linked to vortices shed at the trailing edge, which in turn increased in magnitude with increased rotation rate.

7.2. Deep Stall Effects

Post-stall characteristics of a NACA 0021 airfoil was investigated to determine the effect of dynamic stall on the flow structure and force, proceeding departure of the leading-edge vortex. Three maximum angles of attack of $\alpha = 20°$, $\alpha = 40°$ and $\alpha = 60°$ were investigated at $Re = 20{,}000$. Multiple vortex structures developed on the airfoil upper surface due to the breakdown of a separation bubble located over the rear of the airfoil prior to leading-edge vortex formation.

Merging of the leading-edge vortex and vortex structures over the rear of the airfoil resulted in the generation of the dynamic-stall vortex. Subsequently, the vortices were shown to induce low pressure regions on the upper surface of the airfoil resulting in an increase in lift. The fluctuation in force prior to periodic bluff-body separation were primarily due to the unsteady vortex shedding process. Fully separated flows were observed when the dynamic-stall vortex separated from the airfoil. Separated flows were shown to be minimally influenced by the rotation rate and angle of attack. As such, bluff body separated flow characteristics were established within six chord-lengths of the airfoil reaching the maximum angle of attack. Convection of the vortex structures towards the trailing edge resulted in a significant movement of the airfoil centre of pressure, prior to the establishment of periodic bluff-body separated flow characteristics. With an increasing angle of attack, the centre of pressure is shown to move aft of the leading edge.

Variation in location of the centre of pressure is minimal once bluff-body separation had developed.

7.3. Dynamic Stall Control

The effectiveness of a leading-edge trip wire for boundary layer flow control in highly unsteady flow conditions was examined for three maximum angle-of-attack values and three reduced frequencies using a NACA 0012 airfoil. Maximum angles of attack were $\alpha = 20°$, $40°$ and $60°$, whilst reduced frequencies were $\kappa = 0.025$, 0.05 and 0.1. Internally-mounted pressure transducers were utilised to record fluctuations in flat plate surface pressure during the pitch-up process and for 10 chord-lengths of travel, relative to the flow, after reaching the maximum angle of attack. Surges in lift resulted from increased suction on the upper surface of the airfoil resulting from the leading-edge vortex. Post-stall flow conditions were established with separation of the leading-edge vortex and observation of periodic force fluctuations resulting from von-Karman vortex shedding.

The application of the trip wire was shown to reduce the lift during pre- and post-dynamic stall, whilst also diminishing the formation of laminar separation bubbles due to increased boundary layer mixing. Maintaining lower airfoil angles of attack reduced force fluctuations and generated greater overall performance. The trip wires were ineffective in controlling boundary layer separation at high reduced frequencies. In such operating conditions, increased periods of load fluctuation occurred prior to steady-state conditions being established.

The results from this investigation show the limited applicability of a leading-edge trip wire as a passive flow control technique under highly unsteady operating conditions.

Although the trip wire demonstrated some positive benefits to force control at low rotation rates and prior to dynamic-stall vortex development, its effects at high rotation rates and angles of attack were limited.

7.4. Dynamic Stall Flow Topology

Major flow structure topology and surface pressures generated about a pitching flat plate were studied to develop knowledge of surface pressure variation for future dynamic stall control purposes. Round, square and triangular leading edge profiles were evaluated for their effect on the dynamic-stall process. Variations in leading edge geometries are shown to be critical prior to leading-edge vortex formation and at low angles of attack. High rotation rate operating conditions resulted in high inertial loads which dominated flow development. This led to no significant visible effect of the leading edge geometry on the generated forces. Continued rotation resulted in the observation of a critical angle of attack, from which, continued increase of the angle of attack resulted in no advantageous increases in lift. Higher lift characteristics were established for the combination of the round leading- and trailing-edge profiles during low ration rates. Under high rotation rates, where $\kappa = 0.1$, no distinct advantage of was observed to result from varying the leading- and trailing-edge extensions.

A half-saddle point was identified in the region of high pressure gradient on the surface of the plate and aft of the leading-edge vortex. The half-saddle was linked to the attachment of the leading-edge vortex and was represented by the attachment point on the plate surface of the streamline bifurcating the outer free-stream and the flow within the lead-edge vortex. Whilst the half-saddle was present on the upper surface, increases

in vortex lift were observed. After the half-saddle moved into the wake, fully separated flows were developed. Leading-edge and trailing-edge geometries were demonstrated to have a minor influence, whilst movement of the half-saddle point aft of the leading edge was shown to be linearly dependent on the free-stream velocity, chord length and rotation rate. Results herein links pressure fields and critical flow topology for enhanced knowledge of dynamic stall control.

7.5. Significance of the Present Work

Wind turbines, helicopters, micro-aerial vehicles and natural flyers are all subjected to high rotation rates and high angles of attack, which results in dynamic stall and unsteady force generation characteristics. These conditions leads to high inertial loads, enhanced vibration and increased structural fatigue. Development of knowledge associated with the dynamic-stall process during these operating conditions can lead to more efficient boundary layer control devices to assist with dynamic stall suppression, in order to reduced fatigue and structural loading on rotary machines, or enhance lift for increased control and manoeuvrability of micro-aerial vehicles and natural flyers.

The research in the current thesis demonstrates increased load development at extreme operating conditions. Additionally, the thesis details major contributions towards research into dynamic stall and includes:

1. Demonstrating the presence of load fluctuations for increased periods of time following dynamic stall and during post-stall conditions.

2. Showing the minimal influence of variations in airfoil thickness on the flow development characteristics during highly-unsteady rotation rate airfoil pitch-up motions.

This is significant to the operation of wind turbines, where stalled conditions are often used as a simple method to control over-speed operation of the rotors in high-gust configurations.

3. Presenting the effects of a leading-edge trip wire on airfoils which are undergoing highly unsteady flow conditions.

4. The trip wire had a minor effect on flow development during high rotation rate, high angle of attack flow conditions. Furthermore, in post-stall conditions the trip wire was demonstrated to have a minor influence on the overall aerodynamic efficiency of the airfoil.

This is significant, as it indicates that the leading-edge trip wire is an ineffective boundary layer control technique when used in highly unsteady operating conditions.

5. The presence of a half-saddle point location was identified, through surface pressure investigations, on a flat plate undergoing dynamic stall. The motion of the half-saddle point was linked to performance parameters such as airfoil rotation rate, free-stream velocity and the airfoil chord length.

This is significant as pressure data generated from a flat plate undergoing dynamic stall can potentially be combined with more advanced adaptive control devices to control and manipulate the presence of the leading-edge vortex.

7.6. Recommendations for Future Work

The results of this research provide detail of the dynamic-stall process where highly unsteady flow conditions and high angles of attack are experimentally investigated. Details such as the dynamic-stall separation, post-stall flow behaviour, a passive flow control method and surface pressure development over a flat plate exposed to dynamic stall conditions are presented. Throughout the research, future recommendations have been identified to advance the state of knowledge of the dynamic-stall process. Some of these recommendations include:

- Developing more effective passive flow control devices for highly unsteady flow environments. From the literature, it was identified that many of the flow control techniques have been applied to helicopter applications. Under these operating conditions, the angle of attack seldom exceeds $\alpha = 30°$, whilst the rotation rate is typically quasi-steady ($\kappa < 0.05$). As such, there is still significant work to be done to develop flow control methods that are effective at controlling large-scale separation at high angles of attack, and also during high-rotation-rate motions. A potential avenue of investigation includes developing a control system that dissipates or transfers the momentum from the leading-edge vortex into other flow features, such as chord-wise vortices, to sustain lift or to lead to more controlled stall characteristics.

- Further evaluation of the characteristics in the motion profile of the half-saddle point on the airfoil upper surface. Identification of the half-saddle location led to the awareness of the aft motion being a function of rotation rate, chord length and free-stream velocity. More testing should be conducted to further explore these

relationships, and to determine if the motion of the half-saddle point is dependent on the airfoil rotation rate profile.

- Developing more advanced active boundary layer control methods for suppression of lift formed during highly-unsteady dynamic stall. For example, the flow rate of suction ports located at the leading edge can be tuned using feedback from additional pressure ports located along the chord of the airfoil sensing the half-saddle point location. Active feedback control of the boundary layer can potentially be utilised for manipulation and control of the leading-edge vortex. As such, variations in load fluctuation can be controlled in order to prevent blade load oscillation and increased vibration.

- Determination of the rate of flow entrainment into the leading-edge vortex. Through investigation of the flow rate into the leading-edge vortex, suitable suction devices can be implemented to actively draw flow towards the airfoil surface to inhibit large-scale flow separation and load oscillation. Further work is therefore required to understand the entrainment rate for the application of more specific and targeted boundary layer control methods.

- Apply highly-unsteady flow conditions at higher Reynolds numbers. Increasing the Reynolds number to higher values may lead to variations in force characteristics from those achieved in this thesis. As such, it is recommended that additional work be conducted to investigate the dynamic-stall process and post-stall characteristics under high Reynolds number conditions representative of rotary machine applications.

Appendix - Dynamic Stall Velocity Profiles Using PIV

The experimental study of the flow field velocity developed about two symmetrical airfoils with differing thickness-chord ratios and undergoing dynamic stall was carried out in the water channel located with the School of Mechanical Engineering, The University of Adelaide. The results from the work were presented at the 20th Australasian Fluid Mechanics Conference held in Perth, Western Australia. The results complement the vorticity contours presented in Chapter 1 of this thesis which are used to compare flow dynamics of NACA 0012 and NACA 0021 airfoils undergoing unsteady dynamic stall.

Statement of Authenticity

Title of Paper:	Dynamic stall on Airfoils Exposed to Constant-Pitch-Rate Motion
Publication Status:	☑ Published ☐ Accepted for Publication ☐ Submitted for Publication ☐ Unpublished and Unsubmitted w ork w ritten in manuscript style
Publication Details:	Leknys, R. R., Arjomandi, M., Kelso, R. M. & Birzer, C. H., 2016, dynamic stall on Airfoils Exposed to Constant-Pitch-Rate Motion, 20th Australasian Fluid Mechanics Conference, Perth, Western Australia.

Principal Author

Name of Principal Author:	Ryan Ross Leknys
Contribution to the Paper:	Performed data analysis and interpretation, wrote manuscript and acted as corresponding author.
Overall percentage (%):	70
Certification:	This paper reports on original research I conducted during the period of my Higher Degree by Research candidature and is not subject to any obligations or contractual agreements with a third party that would constrain its inclusion in this thesis. I am the primary author of this paper.

Signature: _ _ Date: 05 March 2018

Co-Author Contributions

By signing the Statement of Authorship, each author certifies that:

i. the candidate's stated contribution to the publication is accurate (as detailed above);

ii. permission is granted for the candidate in include the publication in the thesis; and

iii. the sum of all co-author contributions is equal to 100% less the candidate's stated contribution.

Name of Co-Author:	Associate Professor Maziar Arjomandi
Contribution to the Paper:	Supervised the development of the research and contributed in academic discussion and the review process of submitted manuscripts.

Signature: _____ _____ Date: 05 March 2018

Name of Co-Author:	Associate Professor Richard Kelso
Contribution to the Paper:	Supervised the development of the research and contributed in academic discussion and the review process of submitted manuscripts.

Signature: Date: 05 March 2018

Name of Co-Author:	Dr Cristian Birzer
Contribution to the Paper:	Supervised the development of the research and contributed in academic discussion and the review process of submitted manuscripts.

Signature: _____ _____ Date: 05 March 2018

20th Australasian Fluid Mechanics Conference
Perth, Australia
5-8 December 2016

Dynamic Stall on Airfoils Exposed to Constant Pitch-Rate Motion

R.R. Leknys, M. Arjomandi, R.M. Kelso and C. Birzer

School of Mechanical Engineering, the University of Adelaide, Adelaide, South Australia 5005, Australia

Abstract

Gust-like flow behavior is simulated using pitching airfoils to represent the unpredictable nature of atmospheric turbulence on the blades of wind turbines. Angle of attack, reduced frequency and both NACA 0021 and NACA 0012 airfoils are investigated using particle image velocimetry to assess their influence on the developed flow structure resulting from the ramp-up constant angular velocity motion. The pitch motion was shown to delay the onset of the stall vortex to high angles of attack, which is linked to increased lift. Moreover, increasing the reduced frequency reduced the rate of vortex growth as the angle of attack was increased. Development of a rear separation bubble with low velocity is noted during initial development of the dynamic stall process. Once the critical angle of attack is reached, initiation of the formation of the dynamic stall vortex is observed. Increased angular displacement resulted in the annihilation of the trailing edge vortices, by the initial stall vortex, which also coincided with vortex-induced separation leading to bluff body separation. Results from the current work show the presence of delayed separation and vortex formation on the upper surface of the airfoil characteristic to the dynamic stall process. The current work highlights the flow features responsible for enhanced lift, whilst shedding light on the development process for constant-pitch-rate motion about thick and thin airfoil sections.

Introduction

Dynamic stall is the phenomenon of delayed stall whereby large increases in aerodynamic loading are achieved past typical steady state angles of attack. The process of dynamic stall is typically associated with retreating blade stall of helicopters and unsteady atmospheric operation of vertical and horizontal axis wind turbines. For these machines, the additional loading generated by blade pitching leads to excessive fatigue and reduced performance. Furthermore, dynamic stall has been associated with natural flyers including birds and insects where vortex lift is utilised for predatory avoidance, hover and perching manoeuvres [22]. Dynamic stall is characterised by the delay in boundary layer separation followed by the rapid formation of a leading-edge vortex on airfoils undergoing pitching or heaving motions. The delay in boundary layer separation has been attributed to an overall decrease in surface pressure coefficient and delayed collapse of the leading-edge suction peaks resulting in periodic lift generation [8]. Once the leading-edge vortex forms, further lift is generated until the vortex finally departs from the airfoil surface, resulting in deep stall conditions [14].

The awareness of unsteady performance characteristics associated with dynamic stall was first realised through the work of Kramer [9] who identified the additional lift over aircraft wings due to gusts. Proceeding from this initial study and due to the technical advancements of rotorcraft and the requirement for increased speed and manoeuvrability, a wealth of research [2, 3, 11-13, 15] was undertaken to further identify the performance advantages and disadvantages of dynamic stall. Various parametric studies investigating pitch rate, Reynolds number, airfoil geometry and Mach number [4, 6] all seek to identify key performance characteristics associated with each major influencing operating parameter.

Physical parameters that significantly influence the development of dynamic stall include the reduced frequency, $\kappa = \omega C/2U_\infty$, where ω is the rotation rate in deg/sec taken about the mid-chord location, C is the airfoil chord in meters and U_∞ is the free stream velocity in m/s, other parameters are Reynolds number, Re, based on the airfoil chord; the angle of attack, α; airfoil geometry and non-dimensional pitch location, $\overline{x} = x / C$ where x is the chord-wise location from the leading edge of the airfoil.

Multiple investigations, using surface pressure measurements and smoke-wire flow visualisation, discuss the effects of reduced frequency on dynamic stall [7, 8, 17]. The outcomes of these studies suggest that increasing the reduced frequency leads to the delay in formation of the leading-edge vortex and subsequent enhanced, temporary lift generation. Although reduced frequency has been shown to have a dramatic effect on the development of the dynamic stall and associated forces, research is still required to determine the variations in flow structure across multiple reduced frequencies that are associated with quasi-steady and unsteady flow conditions.

Through the use of surface pressure, [17] conducted systematic studies over Reynolds numbers ranging between 59,000 and 223,000. Decreases in pressure at the leading edge were observed and could be correlated with the formation of a primary and secondary leading edge vortex, however, the development of these structures and overall increase in normal force coefficient was not influenced by Reynolds number. A similar study using surface pressure measurements by Conger and Ramaprian [7], although conducted in a water channel, demonstrates the effects of Reynolds number on a NACA 0015 airfoil undergoing dynamic stall. In this study, the magnitudes of surface pressure peaks were shown to be significantly influenced by the Reynolds number, although the net force coefficient was shown to be minimally affected by variations in Reynolds number. As such, minimal force changes on an airfoil are observed due to the effects of Reynolds number [7, 17, 18]. This suggests that the dynamic stall phenomenon is more sensitive to pitch-induced inertial effects and vortex-induced flows rather than the state of the laminar or turbulent boundary layers.

The above studies were primarily conducted to evaluate the effects of dynamic stall on helicopter rotors where limitations in performance were discovered due to the unsteady flow structures. In recent years, advancements and the urge for cleaner energy production through the application of wind turbines has led to further investigations of dynamic stall [1, 5, 10, 19, 21]. Wind turbine blades are exposed to multiple sources of unsteadiness including atmospheric turbulence, tower shadow and upstream turbulent wakes [10]. The result of these unsteady velocity fluctuation exposes the turbine to dynamic stall conditions. In addition, due to structural and aerodynamic requirements, turbine blade thickness can vary as much as 12% along the total span [20]. Although other performance parameters are heavily investigated, the effects of airfoil geometry have been given less attention. One

comprehensive study [12] investigated eight airfoil sections specific for helicopter applications. This study focused on the effects of dynamic stall with blades thickness ratios varying between 9.5% and 16.5%. In a separate study to overcome performance degradation on wind turbine blades due to leading edge contamination and blade twist, a new family of airfoil profiles was developed specifically for wind turbine applications with thickness ratios varying between 11% and 21% [23]. Although these sections have been utilised in industry, the various aerodynamic properties developed as a result of dynamic stall due to the variation in airfoil thickness has not been fully investigated.

Although the dominating leading-edge vortex is associated with the dynamic stall process, investigation of its development across varying thickness airfoils at extreme angles of attack requires further investigation. The current work sets out to identify the flow structures and velocity variation generated about two symmetrical airfoil geometries with dissimilar thickness ratios relevant to wind turbine operation. Moreover, multiple pitch rates are investigated at extreme angles of attack to establish dynamic-stall conditions.

Experimental Setup

Particle image velocimetry (PIV) was performed in a water channel at the University of Adelaide. A schematic representation of the test apparatus is provided in Figure 1 showing the arrangement of the laser and water channel facility.

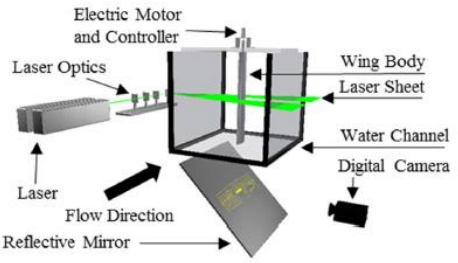

Figure 1. Experimental setup showing the arrangement of the laser, airfoil and camera used for PIV measurements.

A Nd:YAG double-pulsed laser with 532nm wavelength was utilised to create a 3mm thick light sheet for observation of 50μm polyamide seeding particles with a specific gravity of 1.03. Phase-averaged PIV was performed using the combination 200 image pairs of both upper and lower velocity data sets generated, using PIVView V1.7. This provided complete velocity data sets around the airfoil and eliminated shadow created by single-sided evaluation. Constant-pitch-rate motion about the mid-chord location of the wing was supplied via a brushless DC motor with an integrated position encoder and reduction gear box. Reduced frequency values of $\kappa = 0.05, 0.1, 0.2$ were used to simulate quasi-steady and unsteady flows about each of the test airfoils [10]. The airfoil pitch velocity profile was adjusted such that 5° of rotation was allocated for acceleration and deceleration of the test wing with chord, $C = 0.07$m, and span, $S = 0.5$m. Two symmetrical airfoils, with dissimilar thickness ratios, a NACA 0012 and NACA 0021, were selected for testing flow structure development and variation during the dynamic stall process. The water channel velocity was such that a Reynolds number, $Re = 20000$, based on the airfoil characteristic length was achieved.

Quasi-Steady Dynamic Stall

Figure 2 shows the normalised velocity contours and streamline plots of the NACA 0012 and NACA 0021 undergoing dynamic stall between $\alpha = 0° - 60°$ and for a reduced frequency of $\kappa = 0.05$. *For the current flow conditions, quasi-steady conditions are achieved whilst* $\kappa = 0.05$.

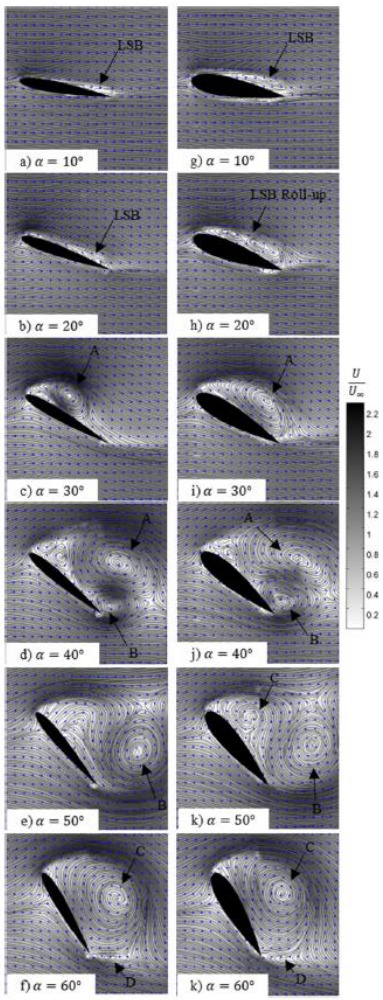

Figure 2. Normalised velocity contours and streamline plots of NACA 0012 (left) and NACA 0021 (right) airfoils undergoing constant-pitch-rate dynamic stall. $\kappa = 0.05$. Shown is the presence of the laminar separation bubble (LSB), leading edge vortex (A), trailing edge vortex (B) and secondary leading edge vortex (C). At this quasi-steady reduced frequency, the airfoil is seen to transition into fully-separated flow at $\alpha = 40°$.

The presence of the laminar separation bubble at the test low Reynolds number is observed in Figure 2(a-b) and Figure 2(g-h) with the leading edge vortex (A) only forming at $\alpha = 30°$ for both airfoils. The laminar separation bubble is shown to be thicker over the NACA 0021, and in addition, the leading edge vortex is shown to form and occupy the total chord length of the airfoil. Comparing this to the NACA 0012 where the leading edge vortex is more defined with higher velocity and only occupies the forward half of the airfoil chord. The presence of a stagnation point at the trailing edge, even after leading edge vortex formation, suggests that the bound circulation continues to grow as a result of vortex generation. Surface pressure measurements in [16] show the

decrease in surface pressure due to the presence of the vortex structures. Also shown in [16] using PIV is the decreased and more intense distribution of surface pressure resulting from a region of high vorticity at the leading edge, compared to a lower broader pressure distribution resulting from a lower vorticity trailing-edge vortex. Relating the flow pattern and surface pressure from [16] to the current work suggests that the NACA 0012 develops a much stronger pressure reduction at the leading edge with comparison to the NACA 0021 where the pressure distribution is expected to be much broader and to a high value. The resulting vortex distribution indicates that for the lower, quasi-steady reduced frequencies, the NACA 0012 will generate a high pitching moment due to the intense vortex adjacent to the forward region of the airfoil. Due to the attachment of the vortex structure, and as suggested in [5], an apparent camber effect and artificial geometry is generated which in addition can be attributed to increased aerodynamic force. The observation of the maximum 'displaced' velocity away from the airfoil boundary itself suggests that an increase in lift is possible even though the boundary layer over the airfoil is seen to break down and form into the dominating vortex structures as indicated in Figure 2c and Figure 2i. Once the leading-edge vortex transitions into the freestream and depart from the surface of both airfoils, as shown from Figure 2d and Figure 2j, initiation of fully-separated flow is achieved. The point at which the leading-edge vortex transitions into the free-stream marks the initiation of deep-stall flow conditions where any further pitching would lead to the formation of a secondary trailing edge vortex (B) and subsequent periodic vortex shedding.

Unsteady Dynamic Stall

For the case of $\kappa = 0.1$, representing unsteady dynamic stall, each of the airfoils was subject to constant-pitch-rate motion to a maximum angle of attack of $\alpha = 60°$. The thickness of the airfoil is shown to directly influence the development of the leading edge vortex in conjunction with the process of laminar separation bubble roll-up on the upper surface of both airfoils. Normalised velocity contours and streamline plots are presented in Figure 3 and can be used to identify the regions of flow separation about both the NACA 0012 and NACA 0021.

As indicated in Figure 3, flow features developed during the pitch-up process are presented and include the laminar separation bubble formed of the upper-rear of the airfoil, as shown in Figure 3(a-b) and Figure 3(g-h) for $\alpha = 10°$ and $\alpha = 20°$. During this period of rotation, the laminar separation bubble is observed to be considerably thinner for the NACA 0012, with comparison to the NACA 0012, whilst the upstream attachment point of the laminar separation bubble is shown to move toward the leading edge until $\alpha = 30°$, Figure 3c, where the formation of the leading edge vortex is observed. At $\alpha = 30°$, the NACA 0021 generates four vortex structures within the laminar separation region whilst the NACA 0012 generates a forward region of vorticity combined with a trailing edge re-circulation zone beginning the process of leading edge vortex formation. Once the leading-edge vortex formed, as shown in Figure 3d and Figure 3j, the effects of flow structure development are seen to become independent of airfoil geometry such that a single leading edge (vortex A) and single trailing edge vortex (vortex B), both of clockwise circulation are formed. In addition, geometry is shown to influence the maximum velocity such that the NACA 0012 generates higher normalised velocity with the leading edge vortex, suggesting that lower pressure coefficients are produced, contributing to high pitching-moment and increased lift compared to the NACA 0021.

Continued rotation results in the amalgamation of the forward two vortex structures and rear vortex structures such that a single dynamic stall vortex (vortex C) exists over the upper surface of the airfoil.

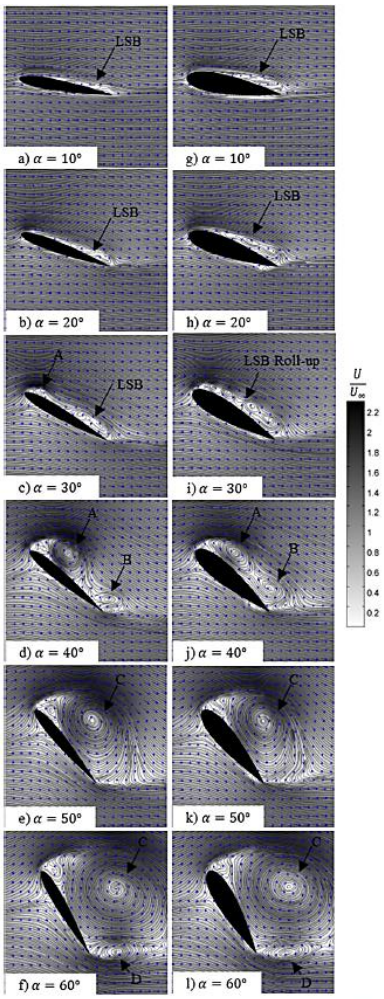

Figure 3. Normalised velocity contours and streamlines of NACA 0012 (left) and NACA 0021 (right) airfoils undergoing constant-pitch-rate dynamic stall. $\kappa = 0.1$. Shown is the presence of the laminar separation bubble (LSB), leading edge vortex (A), counter clock-wise trailing edge vortex (B) and amalgamated leading and trailing edge vortex (C) leading to fully separated flows. A secondary trailing-edge vortex (D) is observed to form as a result of complete stall.

As for the case of the quasi-steady reduced frequency, Figure 2, deep stall is initiated with the presence of a secondary counter-clockwise vortex (vortex D) forming at the trailing edge of both airfoils as indicated in Figure 3f and Figure 3l, suggesting the independence of airfoil geometry with respect to deep stall flow structure. Following $\alpha = 60°$, the airfoil transitions into a phase of fully-separated flow where large-scale bluff body separation in observed.

Leading-Edge Vortex Growth

Growth of the leading edge vortex is shown to be a function of both the maximum angle of attack and the reduced frequency. Figure 4 shows the non-dimensional leading-edge vortex core radius, $\bar{r} = r_{Vort}/C$, as a function of the angle of attack and

reduced frequency where r_{Vort} is the leading edge vortex core radius prior to separation from the airfoil. The leading-edge vortex is approximated using the Lamb-Oseen vortex whereby the maximum vortex-core radius can be defined as the radius at which maximum tangential velocity occurs. Results of vortex core radius as functions of angle of attack and reduced frequency as shown in Figure 4. As observed in Figure 4, regardless of the reduced frequency, the airfoil angle of attack allowed for the growth of the leading edge vortex to continue. However, increased reduced frequency is shown not only to delay the formation of the leading edge vortex to higher angles of attack, but also to decrease the rate of vortex growth.

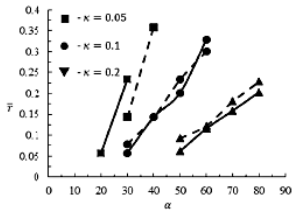

Figure 4. Non-dimensional leading-edge vortex core radius as a function of both angle of attack and reduced frequency. Growth rate is observed to decrease with reduced frequency whilst the onset of vortex formation is delayed. Solid lines represent the NACA 0021 whilst dashed lines represent the NACA 0012.

Conclusion

Flow structure development of the dynamic stall process is presented for unsteady reduced frequencies on multiple airfoils with varying thickness ratios. The thicker airfoil developed broader laminar separation bubble and dynamic stall vortex during reduced frequencies specific to quasi-steady conditions, whilst the thinner airfoil was shown to be more susceptible to abrupt separation resulting in leading edge vortex formation. For unsteady reduced frequencies the flow structure development was similar, although higher velocity gradients were observed about the NACA 0012. Deep stall about both test airfoils was observed to occur once the primary leading-edge vortex transitioned into the free stream and a secondary trailing edge vortex with counter-clockwise circulation was generated. The combination of the attached vortex and airfoil geometry suggests that an artificially-generated profile governs the lift properties of the airfoil due to the additional circulation created by the vortex structure prior to fully separated flow. Observation of velocity contours indicated that the maximum velocity was displaced away from the surface of the airfoil and located between the alleyway separating the leading-edge vortex and the free-stream. Furthermore, increasing the reduced frequency was shown to not only inhibit the initiation of leading edge vortex formation, but it also varied its growth rate where decreased rates of expansion were observed. The developed flow structure and associated forces can be directly related to the unsteady operation of wind turbines, where increased blade fatigue and higher operating costs are incurred, due to the dynamic stall process.

Acknowledgements

Research undertaken for this report has been assisted with a grant from the Sir Ross and Sir Keith Smith Fund (Smith Fund) (www.smithfund.org.au). The support is acknowledged and greatly appreciated.

References

[1] Butterfield, C.P., A.C. Hansen, D. Simms, and G. Scott, *Dyanamic stall on wind turbine blades,* 1991, National Renewable Energy Laboratory.

[2] Carr, L.W., Progress in analysis and prediction of dynamic stall. *Journal of Aircraft*, 1988. **25**(1): p. 6-17.

[3] Carr, L.W., K.W. McAlister, and W.J. McCroskey, Analysis of the development of dynamic stall based on oscillating airfoil experiments. 1977.

[4] Chandrasekhara, M., M. Wilder, and L. Carr, Boundary-layer-tripping studies of compressible dynamic stall flow. *AIAA Journal*, 1996. **34**(1): p. 96-103.

[5] Choudhry, A., R. Leknys, M. Arjomandi, and R. Kelso, An insight into the dynamic stall lift characteristics. *Experimental Thermal and Fluid Science*, 2014. **58**: p. 188-208.

[6] Choughuri, P.G. and D.D. Knight, Effects of compressibility, pitch rate, and reynolds number on unsteady incipient leading-edge boundary layer separation over a pitching airfoil. *Journal of Fluid Mechanics*, 1996. **308**: p. 195-217.

[7] Conger, R.N. and B.R. Ramaprian, Pressure measurements on a pitching airfoil in a water channel. *AIAA Journal*, 1994. **32**(1): p. 108-115.

[8] Jumper, E.J., S.J. Schreck, and R.L. Dimmick, Lift-curve characteristics for an airfoil pitching at constant rate. *Journal of Aircraft*, 1987. **24**(10): p. 680-687.

[9] Kramer, M., Increase in the Maximum Lift of an Airplane Wing due to a Sudden Increase in its Effective Angle of Attack Resulting from a Gust. 1932.

[10] Leishman, J.G., *Principles of helicopter aerodynamics*. 2 ed. 2000, New York: Cambridge Aerospace Press.

[11] McAlister, K.W. and L.W. Carr, Water tunnel visualisations of dynamic stall. *Journal of Fluids Engineering*, 1979. **101**(3): p. 376-380.

[12] McCroskey, W., K. McAlister, L. Carr, and S. Pucci, An experimental study of dynamic stall on advanced airfoil sections. Volume 1: Summary of the experiment. 1982.

[13] McCroskey, W., K. McAlister, L. Carr, S. Pucci, O. Lambert, and R. Indergrand, Dynamic stall on advanced airfoil sections. *Journal of the American Helicopter Society*, 1981. **26**(3): p. 40-50.

[14] McCroskey, W.J., *The phenomenon of dynamic stall,* 1981, DTIC Document.

[15] McCroskey, W.J., L.W. Carr, and K.W. McAlister, Dynamic stall experiments on oscillating airfoils. *Aiaa Journal*, 1976. **14**(1): p. 57-63.

[16] Mueller-Vahl, H., C. Strangfeld, C.N. Nayeri, C.O. Paschereit, and D. Greenblatt, *Thick Airfoil Deep Dynamic Stall*, in *Wind Energy-Impact of Turbulence*. 2014, Springer. p. 35-40.

[17] Robinson, M.C. and J.B. Wissler, Pitch rate and Reynolds number effects on a pitching rectangular wing. *AIAA Journal*, 1988. **88**: p. 2577.

[18] Schreck, S.J., W.E. Faller, and H.E. Helin, Pitch rate and Reynolds number effects on unsteady boundary-layer transition and separation. *Journal of Aircraft*, 1998. **35**(1): p. 46-52.

[19] Schreck, S.J., M.C. Robinson, M. Maureen Hand, and D. Simms, A, Blade dynamic stall vortex kinematics for a horizontal axis wind turbine in yawed conditions. *Journal of Solar Energy Engineering*, 2001. **123**(4): p. 272-281.

[20] Schubel, P.J. and R.J. Crossley, Wind turbine blade design. *Energies*, 2012. **5**(9): p. 3425-3449.

[21] Shipley, D.E., M.S. Miller, and M.C. Robinson, *Dynamic stall occurance on a horizontal axis wind turbine,* 1995, National Renewable Energy Laboratory.

[22] Shyy, W., Y. Lian, J. Tang, D. Viieru, and H. Liu, *Aerodynamics of low reynolds number flyers*. Vol. 22. 2007: Cambridge University Press.

[23] Tangler, J.L. and D.M. Somers, *NREL airfoil families for HAWTs*. 1995: Citeseer.